MECHANIK

FORSCHUNGSBERICHT

Theoretical modeling and parallel programming of a nonlinear composite finite shell element based on a mixed global-local variational principle

Marco Schürg

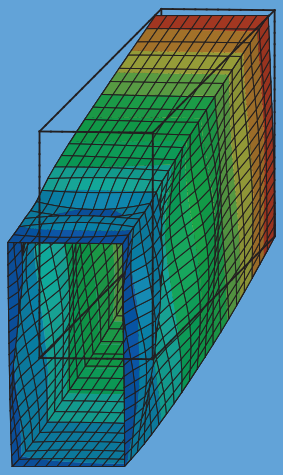

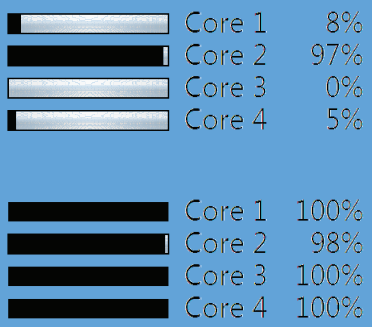

TECHNISCHE UNIVERSITÄT DARMSTADT

Band 27

Theoretical modeling and parallel programming of a nonlinear composite finite shell element based on a mixed global-local variational principle

Vom Fachbereich Bauingenieurwesen und Geodäsie
der Technischen Universität Darmstadt
zur Erlangung des akademischen Grades eines
Doktor-Ingenieurs
(Dr.-Ing.)

genehmigte Dissertation
von

Dipl.-Ing. Marco Schürg

aus Mainz

Erstreferent:	Prof. Dr.-Ing. habil. F. Gruttmann
Korreferenten:	Prof. Dr.-Ing. habil. W. Wagner
	Dr.-Ing. J. Wackerfuß
Tag der Einreichung:	02.07.2012
Tag der mündlichen Prüfung:	22.08.2012

Darmstadt 2013
D17

Schürg, Marco

Theoretical modeling and parallel programming of a nonlinear composite finite shell element based on a mixed global-local variational principle

Forschungsberichte des Instituts für Mechanik der Technischen Universität Darmstadt
Band 27

Herausgeber:

Studienbereich Mechanik
Technische Universität Darmstadt
Hochschulstr. 1
D-64289 Darmstadt
Germany

URN: urn:nbn:de:tuda-tuprints-33070
URI: http://tuprints.ulb.tu-darmstadt.de/id/eprint/3307

ISBN 978-3-935868-27-3

Acknowledgement

This dissertation is a result of my research work at the division of Solid Mechanics, Technische Universität Darmstadt. I would like to express my gratitude to all those that had a part in the success of this work. In particular, I extend my thanks to Professor Dr.-Ing. Friedrich Gruttmann for his support, professional guidance, supervision of this work and successful collaboration in a research project funded by the German Research Foundation (DFG). Further, I thank Professor Dr.-Ing. Werner Wagner for his interest in and co-supervision of this thesis and helpful suggestions. I also owe special thanks to Dr.-Ing. Jens Wackerfuß for co-supervising this work. He always took the time to answer my questions and provided much insight. Additionally, I want to use this opportunity to thank my colleagues for scientific discussions and creating a pleasant working atmosphere. I especially thank C. Fell, with whom I shared an office after graduation. I am also grateful to the DFG for providing the funds to support my research work. Particular thanks I extend to my family for their support and patience, especially to my wife, Sandra, and to my daughter, Hannah.

Darmstadt, August 2012 Marco Schürg

Contents

Nomenclature

This nomenclature provides a list of important symbols used in this thesis. Symbols used in this work that do not appear here are explained as they appear in the text.

Latin symbols

$\mathrm{d}a$	Infinitesimal area element in the current configuration
$\mathrm{d}\mathbf{a}$	Vector element of an infinitesimally small area in the current configuration
$\mathbf{a}$	Unit vector indicating the fiber direction in the current configuration
$\mathbf{a}_0$	Unit vector indicating the fiber direction in the reference configuration
$\mathbf{a}_i$	Covariant base system on Ω_t
$\mathbf{a}^i$	Contravariant base system on Ω_t
$\mathrm{d}A$	Infinitesimal area element in the reference configuration
$\mathrm{d}\mathbf{A}$	Vector element of an infinitesimally small area in the reference configuration
$\mathbf{A}$	Assembly matrix
$\mathbf{A}_G$	Global assembly matrix
$\mathbf{A}_L$	Local assembly matrix
$\mathbf{A}_i$	Covariant base system on Ω_0
$\mathbf{A}^i$	Contravariant base system on Ω_0
$\tilde{\mathbf{A}}$	Global-local assembly matrix
$\mathbf{b}$	Left Cauchy-Green tensor
$\mathbf{b}_0$	External body force
$\mathbf{B}$	Matrix containing interpolation functions for independent field $\tilde{\mathbf{v}}$
$\mathcal{B}$	Continuum body
$\partial\mathcal{B}$	Boundary of continuum body
$\mathcal{B}_0$	Continuum body in the reference configuration
$\partial\mathcal{B}_0$	Boundary of continuum body in the reference configuration
$\mathcal{B}_t$	Continuum body in the current configuration
$\partial\mathcal{B}_t$	Boundary of continuum body in the current configuration
C_{ij}^G	Components of $\mathbf{C}_G$
C_{ij}^F	Components of $\mathbf{C}_F$
$\mathbf{C}$	Right Cauchy-Green tensor
$\mathbf{C}_F$	Elasticity matrix related to $\mathbf{t}_i$
$\mathbf{C}_G$	Elasticity matrix related to $\hat{\mathbf{t}}_i$
$\mathbf{C}_m$	Submatrix of $\mathbf{C}_G$
$\mathbf{C}_s$	Submatrix of $\mathbf{C}_G$

$\mathbb{C}$	Elasticity tensor
$\mathbf{d}$	Director vector in the current configuration
$\mathbf{D}$	Director vector in the reference configuration
$\bar{\mathbf{D}}$	Material tangent matrix
$\tilde{\mathbf{D}}$	Global-local material tangent matrix
$\mathbf{D}_G$	Global material tangent matrix
$\mathbf{D}_L$	Local material tangent matrix
$\mathbf{D}_{GL}$	Global-local material tangent matrix
e_0	Internal mechanical energy
$\mathbf{e}_i$	Base system of Cartesian coordinate system
E	Efficiency
E_{ij}^F	Components of the Green-Lagrange strain tensor related to $\mathbf{t}_i$
E_{ij}^G	Components of the Green-Lagrange strain tensor related to $\hat{\mathbf{t}}_i$
$\mathbf{E}$	Green-Lagrange strain tensor
$\bar{\mathbf{E}}$	Vector of Green-Lagrange strains
$\bar{\mathbf{E}}_G$	Vector of global Green-Lagrange strains
$\bar{\mathbf{E}}_L$	Vector of local Green-Lagrange strains
$\hat{\mathbf{E}}$	Surface-related Green-Lagrange strain tensor
$\mathcal{E}$	Internal energy
$\mathbf{f}$	Force vector
$\mathrm{d}\mathbf{f}$	Infinitesimal force vector
$\mathbf{f}_0$	Resultant force due to external sources
$\mathbf{F}$	Deformation gradient
$\hat{\mathbf{F}}$	Deformation gradient at the reference surface of the shell
g_{ij}	Covariant metric coefficients in the current configuration
g^{ij}	Contravariant metric coefficients in the current configuration
$\mathbf{g}_i$	Covariant base system in the reference configuration
$\mathbf{g}^i$	Contravariant base system in the reference configuration
G_{ij}	Covariant metric coefficients in the current configuration
G^{ij}	Contravariant metric coefficients in the current configuration
$\mathbf{G}_i$	Covariant base system in the reference configuration
$\mathbf{G}^i$	Contravariant base system in the reference configuration
h	Thickness of the shell
h^-	Bottom coordinate of the shell
h^+	Top coordinate of the shell
H_j	Linear shape functions
$\mathbf{H}$	Displacement gradient
$\mathbf{H}_u$	Vector containing linear shape functions in ξ^1-direction
$\mathbf{H}_v$	Vector containing linear shape functions in ξ^2-direction
$\mathbf{H}_w$	Vector containing linear shape functions in ξ^3-direction
I_i	Hierarchic quadratic shape functions
$\mathbf{I}_u$	Vector containing hierarchic quadratic shape functions in ξ^1-direction
$\mathbf{I}_v$	Vector containing hierarchic quadratic shape functions in ξ^2-direction
$\mathbf{I}_w$	Vector containing hierarchic quadratic shape functions in ξ^3-direction
j	Mid-surface Jacobian
J	Jacobian determinant

J_i	Hierarchic cubic shape functions
$\mathbf{J}$	Angular momentum
$\mathbf{J}_u$	Vector containing hierarchic cubic shape functions in ξ^1-direction
$\mathbf{J}_v$	Vector containing hierarchic cubic shape functions in ξ^2-direction
$\mathbf{J}_w$	Vector containing hierarchic cubic shape functions in ξ^3-direction
$\mathcal{K}$	Kinetic energy
$\mathbf{L}$	Linear momentum
m	Mass
$\tilde{m}^{\alpha\beta}$	Effective stress couple resultants
$\mathbf{m}$	Vector containing displacements through the thickness
$\mathbf{m}_G$	Vector containing global displacements and rotations
$\mathbf{m}_L$	Vector containing local displacements
$\mathbf{m}_0$	Resultant moment due to external sources
$\mathbf{m}_u$	Vector containing displacements in ξ^1-direction
$\mathbf{m}_v$	Vector containing displacements in ξ^2-direction
$\mathbf{m}_w$	Vector containing displacements in ξ^3-direction
$\mathbf{m}^\alpha$	Shell stress couple resultant
$\tilde{\mathbf{m}}^\alpha$	Shell director stress couple resultant
$\mathbf{M}$	Matrix containing shape functions
$\mathbf{M}_u$	Vector containing shape functions in ξ^1-direction
$\mathbf{M}_v$	Vector containing shape functions in ξ^2-direction
$\mathbf{M}_w$	Vector containing shape functions in ξ^3-direction
n	Number of layers in the laminate
$\tilde{n}^{\alpha\beta}$	Effective membrane stress resultants
$\mathbf{n}$	Normal unit vector on the cutting plane in the current configuration
$\mathbf{n}_0$	Normal unit vector on the cutting plane in the reference configuration
$\mathbf{n}^\alpha$	Shell stress resultant
N_k	Ansatz functions
$\mathbf{N}_{\varepsilon G}$	Matrix containing interpolation functions for independent field $\boldsymbol{\varepsilon}_G$
$\mathbf{N}_{\varepsilon L}$	Matrix containing interpolation functions for independent field $\boldsymbol{\varepsilon}_L$
$\mathbf{N}_\sigma$	Matrix containing interpolation functions for independent field $\boldsymbol{\sigma}_G$
p	Number of processors
$\bar{\mathbf{p}}$	Surface loads acting on Ω_0
$\mathbf{P}$	First Piola-Kirchhoff stress tensor
$\mathcal{P}_{\text{ext}}$	External mechanical power
$\mathcal{P}_{\text{int}}$	Stress power
$\tilde{q}^\alpha$	Effective shear stress resultants
$\mathbf{q}_0$	Cauchy heat flux
$\mathbf{q}$	Shell across-the-thickness stress resultant
$\mathbf{Q}$	Orthogonal tensor describing arbitrary rigid body motion
$\mathcal{Q}$	Thermal power
$\tilde{\mathcal{Q}}$	Rate of entropy input
r_0	Heat source
$\mathbf{R}$	Rotation tensor
s_0	Entropy per unit volume
$\mathrm{d}s$	Line increment of the shell boundary
S	Speedup

$\mathbf{S}$	Second Piola-Kirchhoff stress tensor
$\hat{\mathbf{S}}$	Surface-related second Piola-Kirchhoff stress tensor
$\bar{\mathbf{S}}$	Vector of second Piola-Kirchhoff stresses
$\mathcal{S}$	Entropy
t	Time
t_i	Thickness of layer i
$\mathbf{t}$	Cauchy traction vector
$\mathbf{t}_0$	External traction vector
$\bar{\mathbf{t}}_0$	Prescribed external traction vector
$\bar{\mathbf{t}}$	Boundary loads acting on $\Gamma_{\sigma 0}$
$\mathbf{t}_i$	Local base system of the composite shell
$\hat{\mathbf{t}}_i$	Global fixed base system of the composite shell
t_i^-	Bottom coordinate of layer i
t_i^+	Top coordinate of layer i
T_p	Runtime of the simulation with p processors
T_s	Runtime of the simulation with one processor
$\mathbf{T}$	Cauchy stress tensor
$\bar{\mathbf{T}}$	Transformation matrix
$\hat{\mathbf{T}}$	Transformation matrix
u	Displacement in ξ^1-direction
$\mathbf{u}$	Displacement vector
$\tilde{\mathbf{u}}$	Displacement vector in the extended product ansatz
$\mathbf{u}_G$	Global displacement vector
$\mathbf{u}_L$	Local displacement vector
$\bar{\mathbf{u}}$	Prescribed displacement vector
$\mathbf{U}$	Right stretch tensor
v	Displacement in ξ^2-direction
$\mathrm{d}v$	Infinitesimal volume element in the current configuration
$\mathbf{v}$	Left stretch tensor
$\tilde{\mathbf{v}}$	Field of displacements and rotational parameters
$\mathbf{v}_0$	Velocity in the reference configuration
$\mathrm{d}V$	Infinitesimal volume element in the reference configuration
w	Displacement in ξ^3-direction
$\delta\mathbf{w}$	Variation of the axial vector associated with $\delta\mathbf{R}\mathbf{R}^T$
δW_{int}	Internal virtual mechanical work
δW_{ext}	External virtual mechanical work
$\mathbf{W}$	Skew symmetric tensor associated with $\mathbf{d}$
$\mathbf{x}$	Position vector in the current configuration
$\mathrm{d}\mathbf{x}$	Infinitesimal line element in the current configuration
$\mathbf{x}_0$	Position vector of a reference point
$\mathbf{X}$	Position vector in the reference configuration
$\mathrm{d}\mathbf{X}$	Infinitesimal line element in the reference configuration
$\mathbf{Z}$	Shifter tensor in the reference configuration
$\bar{\mathbf{Z}}$	Shifter tensor in the current configuration

Greek symbols

$\tilde{\boldsymbol{\alpha}}_u$	Vector of parameters added to the shape functions, ξ^1-direction
$\tilde{\boldsymbol{\alpha}}_v$	Vector of parameters added to the shape functions, ξ^2-direction
β_i	Rotational parameters associated with $\mathbf{a}_i$
$\boldsymbol{\beta}$	Vector of rotational parameters associated with $\mathbf{a}_i$
$\tilde{\boldsymbol{\beta}}_u$	Vector of parameters added to the shape functions, ξ^1-direction
$\tilde{\boldsymbol{\beta}}_v$	Vector of parameters added to the shape functions, ξ^2-direction
γ_α	Shell shear strains
$\tilde{\boldsymbol{\gamma}}_u$	Vector of parameters added to the shape functions, ξ^1-direction
$\tilde{\boldsymbol{\gamma}}_v$	Vector of parameters added to the shape functions, ξ^2-direction
Γ	Total production of entropy
Γ_0	Boundary of the reference surface of the shell in the reference configuration
Γ_t	Boundary of the reference surface of the shell in the current configuration
δ^i_j	Kronecker symbol
$\tilde{\boldsymbol{\delta}}_u$	Vector of parameters added to the shape functions, ξ^1-direction
$\tilde{\boldsymbol{\delta}}_v$	Vector of parameters added to the shape functions, ξ^2-direction
ε	Scalar parameter
$\varepsilon_{\alpha\beta}$	Shell membrane strains
$\boldsymbol{\varepsilon}$	Vector of shell strains
$\boldsymbol{\varepsilon}_g$	Vector of geometric shell strains
$\boldsymbol{\varepsilon}_G$	Vector of global shell strains
$\boldsymbol{\varepsilon}_L$	Vector of local displacements and their derivatives
$\tilde{\boldsymbol{\varepsilon}}$	Vector containing $\boldsymbol{\varepsilon}_G$ and $\boldsymbol{\varepsilon}_L$
ζ_i	Normalized thickness coordinate of layer i
$\boldsymbol{\eta}$	Test function
Θ	Absolute temperature
$\boldsymbol{\theta}$	Vector containing the three fields $\tilde{\mathbf{v}}$, $\boldsymbol{\varepsilon}$ and $\boldsymbol{\sigma}$
$\kappa_{\alpha\beta}$	Shell curvatures
λ_0	Stretch
$\bar{\mu}$	Determinant of the shifter tensor
$\boldsymbol{\nu}$	Normal vector on the shell boundary
ξ^i	Convective coordinates
ξ^3_{si}	Distance of the middle of the layer i to the reference surface
Π	Total potential energy
Π_{ext}	External potential energy
Π_{int}	Internal potential energy
ρ	Mass density in the current configuration
ρ_0	Mass density in the reference configuration
$\rho_{\alpha\beta}$	Second order shell curvatures
$\boldsymbol{\sigma}$	Vector of effective shell stress resultants
$\boldsymbol{\sigma}_G$	Vector of global effective shell stress resultants
$\boldsymbol{\sigma}_L$	Vector of local higher-order shell stress resultants
$\boldsymbol{\tau}$	Kirchhoff stress tensor
$\hat{\varphi}$	Bijective transformation
φ	Fiber angle in the composite shell

φ_x	Warping function
φ_y	Warping function
$\boldsymbol{\phi}$	Position vector of a point in the deformed shell space
$\boldsymbol{\Phi}$	Position vector of a point in the undeformed shell space
Ψ	Helmholtz free-energy function or strain-energy function
$\hat{\Psi}$	Strain-energy function in terms of the shell strains
ω	Length of pseudo-rotation vector
ω_i	Rotational parameters
$\boldsymbol{\omega}$	Pseudo-rotation vector
Ω_0	Reference surface of the shell in the reference configuration
Ω_t	Reference surface of the shell in the current configuration
$\boldsymbol{\Omega}$	Skew-symmetric tensor associated with $\boldsymbol{\omega}$

Kurzfassung

Dünnwandige Strukturen aus Faserverbundwerkstoffen sind in verschiedenen Ingenieurdisziplinen sehr gefragt. Diese Arbeit leistet einen Beitrag zur theoretischen und numerischen Modellierung dieser Materialien. Das vorgestellte global-lokale finite Schalenelement entwickelt ein nichtlineares finites Schalenelement weiter, das aus einem gemischten Variationsprinzip hervorgeht. Das zugrundeliegende Schalenmodell wird in dieser Arbeit das globale Modell genannt, da die zugehörigen Feldgleichungen für die gesamte Struktur erfüllt sein müssen. Das Variationsprinzip wird um eine lokale Feldgleichung erweitert, die in einem bestimmten Punkt der Struktur erfüllt sein muss. Innerhalb der Finite-Elemente-Methode bedeutet dies, dass die lokale Gleichung in einem Integrationspunkt erfüllt wird. Die lokale Feldgleichung ist die Gleichgewichtsbedingung, mit deren Hilfe die interlaminaren Spannungen ermittelt werden. Dieser Teil des Modells wird in dieser Arbeit das lokale Modell genannt. Die Schnittstelle zwischen dem globalen und lokalen Modell ist klar definiert. Der Verlauf der interlaminaren Spannungen wird als Teil der variationellen Formulierung berechnet. Der globale und lokale Teil des Modells sind nicht unabhängig voneinander. Die Einführung des lokalen Modells führt daher zu veränderten Ergebnissen der effektiven Schnittgrößen. Um dies zu umgehen wird eine Orthogonalitätsbedingung eingeführt, die verlangt, dass der Beitrag des lokalen Schalenmodells nicht zu zusätzlichen Normalkräften und Momenten führt. Für Simulationen mit der Finite-Elemente-Methode werden die unabhängigen Felder innerhalb des linearisierten global-lokalen Variationsprinzips mit geeigneten Interpolationsfunktionen approximiert. Das global-lokale finite Schalenelement hat fünf oder sechs Freiheitsgrade, drei Verschiebungen und zwei oder drei Rotationsparameter, da alle weiteren unabhängigen Felder durch numerische Verfahren auf Elementebene eliminiert werden. Zusätzlich wird in dieser Arbeit eine alternative Möglichkeit vorgeschlagen, um die interlaminaren Schubspannungen zu ermitteln, die in Plattenelementen oder Schalenelementen in einem Post-Processing Verfahren angewandt werden kann. Die Wirkungsweisen des global-lokalen Schalenelements und des Post-Processing Verfahrens werden mit Hilfe einiger numerischer Beispiele illustriert. Die Einführung des lokalen Modells führt durch die auf Elementebene eingebrachten zusätzlichen Unbekannten zu einer wesentlichen Erhöhung der Rechenzeit. Aus diesem Grund wird die bei der Implementierung des Schalenelements verwendete Finite-Elemente-Software an moderne Rechnerarchitekturen mit mehreren Prozessoren und einem gemeinsamen Speicher angepasst, indem der implementierte Code parallelisiert wird. Mehrere auf einem modernen Desktop-Computer durchgeführte Beispiele werden dargestellt, um die Effektivität der Parallelisierung zu veranschaulichen.

Abstract

Thin-walled structures made of fiber-reinforced composites possess properties which are in high demand in various engineering fields. In this thesis, a contribution is made to the theoretical and numerical modeling of such materials. The global-local finite shell element presented further develops a nonlinear finite shell element emanating from a mixed variational principle. The underlying shell model is called the global model in this work, since the associated field equations have to be fulfilled for the structure as a whole. The variational principle is extended with a local field equation, which is to be fulfilled at a specific point in the structure. In the context of the finite element formulation this means that the local equation is fulfilled in an integration point. The local field equation is the local equilibrium equation, by which the local displacements and the interlaminar stresses are derived. This part of the model is called the local part. A clearly defined interface between the global and the local part of the model is provided. The path of the interlaminar stresses is computed as part of the variational formulation. The global and local part of the model are not independent of each other. Thus, through the addition of the local model the results of the effective stress resultants are manipulated. In order to circumvent this, an orthogonality condition is introduced, which requires that the addition of the local model to the effective membrane stress resultants and the effective stress couple resultants vanishes. For simulations with the finite element method, the independent fields in the linearized global-local variational principle are approximated with suitable interpolation functions. The global-local finite shell element has five or six global degrees of freedom, three displacements and two or three rotational parameters, since all other fields are eliminated by numeric procedures on the element level. Additionally, an alternative possibility to derive the interlaminar shear stresses is proposed, which can be applied in shell and plate elements and is a post-processing procedure. The capabilities of the global-local finite shell element and the post-processing procedure are illustrated with the help of numerical examples. The addition of the local part of the model leads to a significant increase in computation time, due to the unknowns introduced on the element level. For this reason, the finite element software used in the implementation of the finite shell element is adapted to modern computer architectures with multiple cores and shared memory by parallelizing the implemented code. A number of examples carried out on a modern desktop computer are presented to illustrate the effectiveness of the implemented parallelized code.

Chapter 1

Introduction

Materials with properties such as low weight together with high stiffness and strength are in high demand in different engineering fields. Thin-walled structures made of fiber-reinforced composites possess these properties together with reduced noise and vibration characteristics and good corrosion resistance. Such materials increasingly replace metal parts in automotive and aerospace engineering. In civil engineering, they are applied in bridge constructions and increase the load capacity of old structures by means of retrofitting. Figure 1.1 shows two examples of practical application, an Airbus 350 (figure 1.1a) and a fiber-reinforced composite box beam (figure 1.1b). The box beam was constructed in the framework of a joint scientific study investigating highly loaded fiber-reinforced composite beams[1].

Because of their anisotropic material properties, the interaction between loads and deformation states in fiber-reinforced composites is more complicated than in isotropic materials, such as steel. Thus, more sophisticated design concepts must be developed to predict the behavior of a structure made of this material. This thesis deals with theoretical modeling of fiber-reinforced composites. An overview of manufacturing and fabrication processes involved with such materials is given in [10, 52, 107].

1.1 Current state of the research and objectives

The shell model has proven to be an auspicious mathematical concept for thin-walled structures, including fiber-reinforced composites, given that it is adapted to their characteristics. It has therefore found wide acceptance in different engineering fields. Using it to represent a structure when solving a boundary value problem constitutes a simplification of reality, which necessitates a number of assumptions. The partial differential equations

[1] This research project with the title "Große, hochbelastbare Biegeträger aus Faser-Kunststoff-Verbunden" was funded by the German Research Foundation (DFG). The project partners are three research groups at TU Darmstadt, "Fachgebiet Festkörpermechanik" (Professor Dr.-Ing. Gruttmann), "Fachgebiet Konstruktiver Leichtbau und Bauweisen" (Professor Dr.-Ing. Schürmann), and "Fachgebiet Strukturmechanik" (Professor Dr.-Ing. Becker). The work done in this research project contributed to the development of the global-local finite shell element and the results presented in this thesis.

(a) Airbus A350 – © Airbus SAS 2013

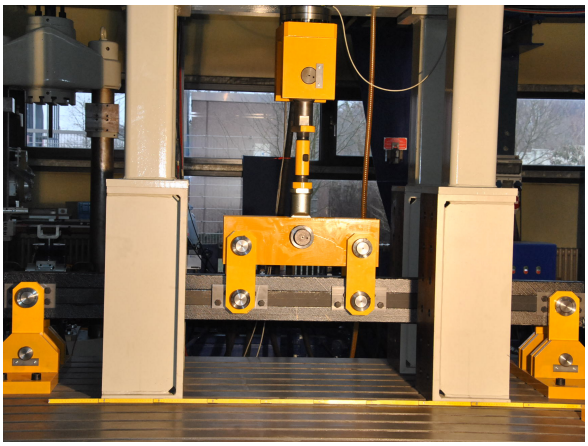

(b) Box beam with test setup – © Fachgebiet KLUB, TU Darmstadt

Figure 1.1: Examples of thin-walled structures made of fiber-reinforced composites

that emerge when using the shell model to predict the behavior of thin-walled structures can often only be solved by numerical techniques such as the finite element method.

In order to achieve good results, suitable finite shell elements must be developed. It is possible to discretize the complete structure with three-dimensional elements, but even with computing power still growing exponentially, this leads to unacceptably large computation times, especially for geometrically and physically non-linear problems, where the systems of equations have to be solved a large number of times.

Thin-walled structures are often very sensitive to a loss of stability. The stability behavior of these constructions is therefore crucial. When designing a thin-walled structure made of a fiber-reinforced composite, the finite element method can be used to perform stability analysis. So as to be able to perform a comprehensive stability analysis it is desirable that the model of the structure is based on a geometrically nonlinear theory.

In order to be able to simulate failure modes such as cracking, the finite shell element developed must be able to model physically nonlinear behavior. The finite element method can also be used to investigate delamination. Delamination occurs due to the jumps of the elastic constants in adjacent layers of a laminate, which leads to high interlaminar stresses. If such a failure mode is the subject of investigation using the finite element method, an interface to three-dimensional non-linear material models must be provided. This requires knowledge of the complete three-dimensional stress state, because interlaminar stresses are the driving forces behind delamination. Numerical simulations in this field often lead to numerical difficulties. The finite element models developed thus have to be as accurate and robust as possible.

Although many underlying concepts remain the same, there is a vast array of different variations in different shell theories and derived finite shell elements due to the fact that there is a large variety of different applications. If the theory is to be as generalized for as many physical problems as possible, accuracy and efficiency may suffer. On the other hand, some assumptions may increase accuracy and efficiency but only have a small number of applications. The large variety of shell models makes it difficult to classify them, as

there are many similarities and intersections. A complete overview and a classification of different shell theories is not the subject of this work[2]. Nevertheless, a short review of some different shell models will be presented, in order to be able to classify the global-local finite shell element that was developed in this project.

To develop shell models suitable for computational formulations a number of assumptions have to be made. Two important theoretical approaches are the Kirchhoff-Love theory and the Reissner-Mindlin theory. In the Kirchhoff-Love theory, the assumptions are made that cross sections remain normal to the mid-surface, inextensible and straight. The transverse shear strains are set to zero, so that only membrane and bending effects can be considered with the help of this model. When developing finite shell elements based on this theory, C^1 continuity requirements need to be met. The Reissner-Mindlin theory, which is a first order shear deformation theory (FSDT), in contrast, eliminates the requirement that cross sections remain normal to the mid-surface. The transverse shear strains are no longer set to zero. The Reissner-Mindlin theory leads to constant transverse shear strains and, for this reason, also constant transverse shear stresses through the thickness. These assumptions demand a modification of the constitutive law to a two-dimensional form through plane stress or plane strain conditions.

Giving up the assumption that the cross section is inextensible in thickness direction leads to formulations with seven parameters or more. Such so-called 3d-shell models are derived from a three-dimensional continuum. As finite shell elements with seven parameters are to model the three-dimensional behavior of the shell structure, three-dimensional constitutive equations are used. Two different paths can be taken in developing shell models with seven parameters or more. The first necessitates a quadratic distribution of the displacements through the thickness, in order to meet the requirement that the normal strain in thickness direction be represented at least linearly. The consequences for the finite element formulation are at least two additional parameters at the nodes, namely two through-the-thickness stretching parameters [21, 98]. In the second procedure the thickness strains are enhanced by applying the enhanced assumed strain (EAS) method, leading to displacement-like parameters at the nodes and a strain-like variable describing the thickness, which are eliminated on the element level [15, 18, 19]. A drawback of extensibility in thickness direction is that it leads to problems at shell intersections. This follows from the continuity of the extensible director vector or thickness strain at the intersection node, leading to wrong results [71]. Research in finite shell elements that account for strains in the direction perpendicular to the shell surface is discussed, for example, in [55], where an update of the thickness change at the end of each equilibrium iteration is used to enforce the zero normal stress condition in thickness direction. Another model to enforce the stress condition is suggested in [32]. A further approach involves a quadratically convergent iteration at each integration point [34, 68].

The assumption of cross sections remaining straight is given up in multi-layer or multi-director theories, thus allowing warping. These models yield good results for the paths of the transverse shear stresses, and when allowing thickness strains also for the interlaminar normal stresses [39, 75]. They are based on a multiplicative decomposition of the displacement field, so that the number of unknowns depends on the number of layers in

[2] A comprehensive overview of past and recent developments in the shell concept and an attempt at a classification are, for example, given in [65, 134, 135].

the composite shell.

A popular approach in computational shell analysis is the degenerated solid approach [1]. In this model, finite shell elements can be directly derived from fundamental equations of continuum mechanics, but they have the disadvantage of being computationally expensive [135]. Surveys of this approach are provided in [12, 54]. A comparison between the degenerated approach and more conventional shell theory is given in [23].

In stress resultant-based formulations, the shell is treated as a surface with oriented directors, which is an approach developed in [36] following the concept of a Cosserat continuum [30]. A geometrically exact shell model formulated in stress resultants is presented in [109–114, 117]. Further examples are expounded in [73, 86].

Additionally, solid shells elements have been developed, for example in [67], where the structure is discretized with a three-dimensional mesh and assumptions pertaining to the shell theory are introduced. The solid shell element only has displacement degrees of freedom and does not have rotational degrees of freedom.

To date, 4-node shell elements with bilinear shape functions are mostly used when solving problems involving shell structures [66]. Such elements without modifications usually suffer from the phenomena of locking, meaning that the calculated behavior is too stiff. Two types of locking that occur in shell elements with low-order interpolations are transverse shear locking, where nearly all the energy is stored in transverse shear terms and membrane locking, where the energy is stored in membrane terms.

A remedy to avoid locking is reduced integration [57, 137], which has the drawback that it causes a rank deficiency of the element stiffness matrix and therefore leads to zero energy modes for certain boundary conditions. This in turn, has motivated the development of stabilization techniques [17, 77, 127]. Some of these elements have been sensitive to the ad hoc hourglass control parameters. This has been overcome by a three-field Hu-Washizu formulation in [16]. A procedure to specifically avoid shear locking is the implementation of an assumed shear strain field, that was first suggested in [78] and further developed in [14, 33, 58, 79]. Additional information regarding assumed strain methods is given in [13, 20, 115].

Low-order finite shell elements based on the first-order shear deformation theory yield satisfactory results for a wide class of structural problems and constitute a good compromise between the quality of the results and computational costs. However, due to the underlying assumptions, they are often not able to predict the correct paths of interlaminar stresses, which can lead to interlaminar failure modes, such as delamination, in fiber-reinforced composites. A large number of different procedures have been proposed to derive the interlaminar stresses. A general survey on the computation of interlaminar stress concentrations is given in [84].

Procedures to compute interlaminar stresses can be based on the use of brick elements or solid shell elements, such as the ones proposed in [69, 70, 82]. The disadvantage of such methods is that each layer must be discretized with several elements in thickness direction, leading to large computation times.

The formulation of layer-wise theories is a different approach to compute the interlaminar

stresses, for example the procedure proposed in [93], where the displacement field is represented separately in each layer. Piecewise polynomial distributions of the membrane displacements in thickness direction are developed in so-called zig-zag theories by means of introducing additional variables for each layer. An overview of zig-zag theories for shells with multiple layers is given in [25] and two such theories are presented in [22, 24]. Procedures based on the multi-director theory are presented in [42–44, 48]. Because in these procedures additional unknowns are introduced, they also lead to large computation times.

Another possibility is the development of higher-order shear deformation theories (HSDT). A parabolic distribution for the transverse shear strains through the thickness of the plate is introduced in [92]. A second-order theory is developed in [35]. Many other finite elements are based on higher-order shear deformation theories. The shape functions in these elements often need to meet the C^1-continuity requirement, which has numerical disadvantages.

Other procedures employ post-processing approaches to derive the interlaminar stresses. A predictor corrector approach is taken in [87]. A different approach is to exploit the equilibrium equations [88]. Because the second derivatives of the in-plane stresses are needed in the procedure, often higher-order shape functions need to be used, for example in [81]. In order to use bilinear shape functions, further assumptions need to be made. For example, the equilibrium equations are exploited assuming cylindrical bending and neglecting membrane forces in [96]. In [7], a 4-node element based on a mixed-enhanced approach is presented. The results for the in-plane deformation are improved by means of enhanced incompatible modes and by means of bubble functions for the rotational degrees of freedom.

This thesis contributes to further developing a finite shell element well-suited for nonlinear analysis of composite structures, based on a three-field Hu-Washizu variational principle [45–47, 71, 131]. The element allows large load steps, which is important for nonlinear simulations as large systems of equations have to be solved a high number of times. The three independent fields are the field of displacements and rotational parameters, the stress resultant field and the strain field. The global number of degrees of freedom is not enlarged by the interpolation of the strain and stress fields because they are eliminated on the element level by means of static condensation. However, this procedure leads to increased memory capacity requirements due to the additional unknowns. An effective method is employed in order to avoid numerically expensive matrix inversions. An interface to nonlinear three-dimensional constitutive laws is provided. A number of techniques are applied to avoid the phenomena of locking.

The shell element has five or six global degrees of freedom, which makes it possible to consider shell structures with intersections. If rotations about the normal to the shell surface are excluded, this leads to a model with five degrees of freedom, three displacements and two local rotations. This requires the construction of special coordinate systems for the rotational parameters. The inclusion of the additional rotational degree of freedom leads to a finite element discretization with six nodal parameters. The advantage of this is that a global coordinate frame is associated with the displacement and rotational parameters, while the disadvantage lies in the larger system of equations that has to be solved. The drilling degree of freedom is fixed in every node that is not located on an intersection,

while all nodes that lie on an intersection have three global displacement components and three global rotations.

The finite shell element yields good results in the nonlinear analysis of composite structures, for example for the displacements and stress resultants. However, the assumptions made in the first-order shear deformation theory are detrimental to the computation of the interlaminar stresses. By forbidding warping of the cross section, the computed interlaminar shear strains are constant through the thickness of the composite and the interlaminar shear stresses are constant in each layer and only correct on an average. The assumption of inextensibility of the cross section leads to vanishing thickness strains and thus also vanishing interlaminar normal stresses. In this thesis, the capabilities of the finite shell element are extended by the following features.

(i) Supplementary to the field equations, that can be derived from the three-field variational principle and that yield good results for a wide class of structural problems, an additional field equation is included in the variational formulation. The preexisting field equations are formulated for the structure as a whole, and thus are said to belong to the global part of the shell model. The additional field equation requires that an equilibrium equation is to be fulfilled at a specific point in the structure, and therefore belongs to the local part of the model. In the context of the finite element formulation, this means that the local equation must be fulfilled in an integration point. The composite finite shell element is therefore based on a global-local mixed variational principle.

(ii) Additional unknowns, the number of which depends on the number of layers, are introduced through the local part of the model. These unknowns are the local displacements across the thickness of the shell and their derivatives, with the goal of making it possible to compute warping of the cross section and thickness changes. They are introduced into the model by means of a multiplicative decomposition of the displacement field. A clearly defined interface between the global and the local part of the model is provided. The path of the interlaminar stresses is therefore computed as part of the variational formulation. The quadratic path of the interlaminar shear stresses is displayed. In particular, the interlaminar shear stresses equal zero at the top and the bottom of the shell, in the absence of boundary conditions that require otherwise, and the continuity at the layer boundaries is given. The local part of the model is introduced in a geometrically linear way, which is permissible for the classes of problems investigated. It can be extended to a nonlinear model. In the finite element formulation, two different procedures for the interpolation of the local quantities in the domain are proposed. The additional unknowns are eliminated on the element level by means of static condensation, so that the global number of unknowns remains unchanged.

(iii) Due to the coupling of the global and the local model, the stress resultants are altered through the addition of the local model. Since the global model already yields satisfactory results for the stress resultants, different orthogonalization procedures for the local model are introduced.

(iv) As an alternative to the global-local model, a procedure is proposed for the computation of interlaminar shear stresses. It is based on an enhanced FSDT model, which

can be applied in plate and shell elements. Two warping functions are introduced. Furthermore, the equilibrium equations are exploited in a post-processing procedure to set up a coupled system of ordinary differential equations. In the procedure, the derivatives of the membrane strains and the curvatures are needed. In 4-node elements, they can be determined by means of a regularized minimum problem, while in 9-node elements, they can be computed from the field of displacements and rotations. Assumptions such as cylindrical bending and neglect of membrane forces are not made.

(v) By means of the local model, a large number of unknowns in the finite element computation is introduced on the element level, thus leading to an increase in computation time. Therefore, the available computation power needs to be used efficiently. For this purpose, the finite element software used in the implementation of the finite shell element was adapted to modern computer architectures by parallelizing the implemented code. Since the software is to run on modern desktop computers with multiple cores, the parallelization was carried out for shared memory processing systems. The implemented parallelization leads to a significant decrease in computation time.

1.2 Outline of this work

In **chapter 2**, some basics of continuum mechanics, that have a bearing on the work done in this thesis, are presented. The kinematics of a continuum body is expounded. Further, some tensors to describe the deformation of a continuum body and to measure the strain are defined. In order to describe the internal forces, that result from a deformation process, some traction vectors and stress tensors are introduced. After naming some axiomatic balance laws that are valid for all kinds of materials, it is explained how the relation between the stresses and the strains can be established by constitutive laws for specific materials. Numerical solution techniques such as the finite element method are usually applied to variational principles. The principle of virtual work is introduced as a single-field variational principle, where the single field is the displacement field. A generalization of the principle of virtual work is provided by a Hu-Washizu variational principle with independent field of displacements and rotational parameters, stress resultant field and strain field. As variational principles are usually nonlinear functions the concept of linearization is exemplified with the principle of virtual work.

The definitions of continuum mechanics are applied to a nonlinear shell model for fiber-reinforced composites in **chapter 3**, called the global model. The kinematics of the shell continuum body is explicated and so-called shell strains are defined and related to the Green-Lagrange strain tensor, a primary strain measure in continuum mechanics. Work-conjugate to the shell strains, effective stress resultants are introduced with the components of the second Piola-Kirchhoff stress tensor. The principle of virtual work is used to derive the equilibrium equations and boundary conditions of the shell and a three-dimensional transversely isotropic constitutive law for small strains is specified. The Hu-Washizu variational principle with independent displacements and rotational parameters, stress resultants and strains for the shell is specified. Its linearization, needed

when conducting nonlinear simulations with the finite element method, is derived.

The local addition to the shell model is defined in **chapter 4** by means of a multiplicative decomposition of the displacement field. A clearly defined interface between the global and the local part of the shell model is derived and the coupling between the two parts is shown. Different orthogonalization procedures needed in the local model are proposed. The mixed variational principle is extended with the local model, introducing the local displacements and their derivatives. It is shown that the additional field equation introduced by the local model is the local equilibrium equation. The linearization of the coupled global-local variational principle is specified.

In **chapter 5**, the finite element implementation of the global-local variational formulation is discussed. The interpolations of the independent fields in the variational formulation, the field of displacements and rotational parameters, the stress resultant field and the field of strains and local quantities are interpolated by appropriate functions. Two different procedures to interpolate the local displacements and their derivatives are suggested. After inserting the interpolated fields into the linearized variational formulation, it is shown how the independent field of local quantities, the strain field and the stress resultant field can be eliminated on the element level using static condensation. Thus, a global-local finite shell element with five or six global degrees of freedom is derived.

The alternative procedure based on an enhanced FSDT model to compute interlaminar shear stresses is introduced in **chapter 6**. It is a post-processing procedure and can be applied in plate or shell elements. After making some basic definitions including the definition of two warping functions, it is shown how the derivatives of the membrane strains and curvatures needed in the procedure can be derived in a 4-node element and a 9-node element. A solution for the system of ordinary differential equations is derived, in order to compute the interlaminar shear stresses.

It was already mentioned that the addition of the local model introduces a large number of unknowns on the element level, leading to a significant increase in computation time, especially if the finite element software is executed sequentially. In **chapter 7**, the procedure of adapting the finite element software to modern computer architectures by parallelizing the code is described. An overview of parallel computing, computer architectures and programming techniques to implement parallelization is provided. Some performance characteristics are defined, by means of which the effectiveness of a parallelized code can be evaluated. The development environment and the finite element software used are described and the software is analyzed for portions of the code, which lend themselves well to parallelization. Subsequently, a suitable parallel programming technique is chosen and the parallel implementation is explicated.

In **chapter 8**, the performance of the global-local finite shell element and the capability of the procedure based on an enhanced FSDT model to compute interlaminar shear stresses are illustrated by means of numerical examples. A simulation of a simply supported plate subjected to a constant area load is conducted for a number of different stacking sequences. The results for the displacements, stress resultants and stresses are given. The contribution of the local part of the model is shown through the specification of the altered results for warping of the cross section and interlaminar stresses. The results of some geometrically nonlinear simulations of box beams and double-T girders are shown. The effectiveness of

the implemented parallelization of the finite element software is illustrated by comparing the computation times of some simulations executed sequentially and in parallel with different compiler options turned on or off.

The results of this thesis are summarized in **chapter 9**. Areas are specified where additional research is needed and an outlook is given.

Chapter 2

Continuum mechanics - basic equations

In this work, the behavior of the materials under investigation, thin-walled composites made up of fibers and a matrix material, is modeled as a continuum with equations formulated on a global and a local level. The global equations are valid for the structure as a whole, while the local equations are to be satisfied at a specific point in the structure.

In the approach of continuum mechanics, physical phenomena are modeled not on a microscopic level, but by treating the object as a continuous medium characterized by certain field quantities that are averages over dimensions [53]. This is less accurate, but more computationally feasible and sufficiently accurate for most engineering problems. When modeling an object in this way, the model is considered a macroscopic system, having dimensions much larger than the dimensions on the microscopic scale and possessing certain macroscopic quantities.

Some basics of continuum mechanics are summarized in this chapter. The goal of this summary is not to present a comprehensive overview of continuum mechanics. For this purpose the reader is referred to fundamental works such as [3, 53, 83, 120, 124]. Rather, some pertinent definitions are made to facilitate the development of a finite shell element based on a global-local variational principle, which can be used to model the behavior of thin-walled structures. After expounding the kinematics of a continuum body and defining the notion of stress, some balance laws independent of a specific material are introduced. Thereafter, some constitutive equations within a phenomenological approach are presented. The chapter concludes with the explanation of some variational principles which are well-suited to serve as a starting point for a discretization technique such as the finite element method. Since the variational principles are usually nonlinear functions, their linearizations are specified, so that they can be used in numerical solution techniques.

2.1 Configuration and motion

In continuum mechanics, the aforementioned macroscopic system is made up of a continuous system of material points, which is called a continuum body and denoted by $\mathcal{B}$ with boundary $\partial\mathcal{B}$. The continuum body is parametrized in Euclidean space throughout a

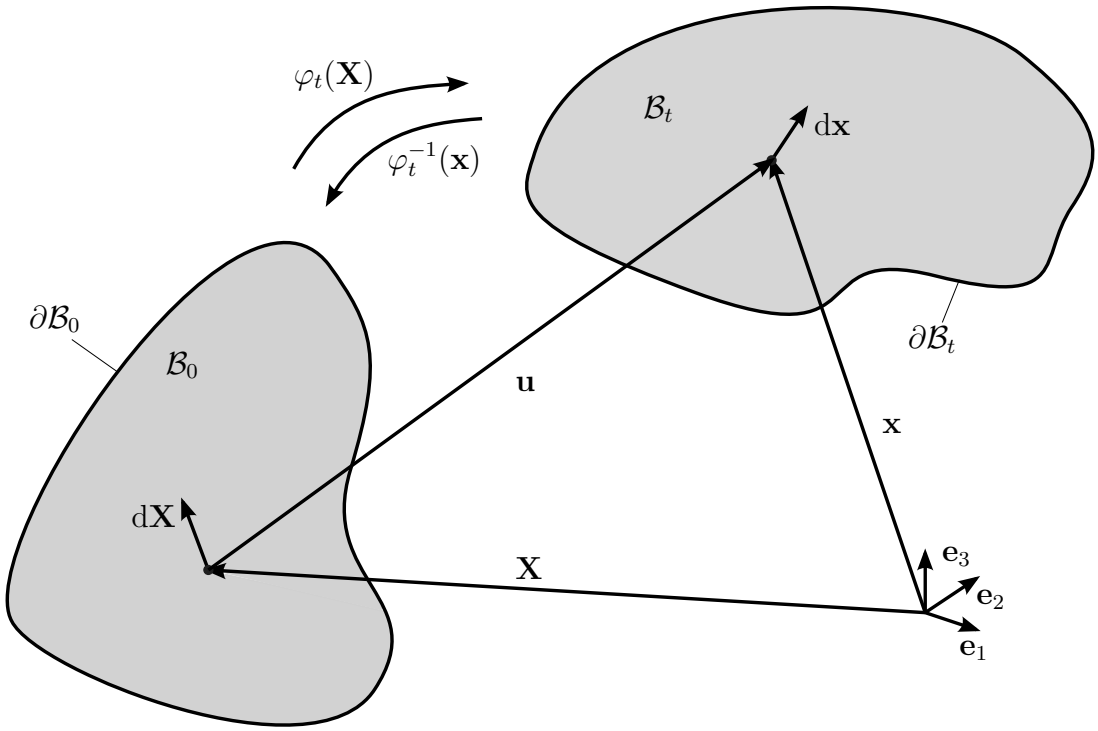

Figure 2.1: Continuum body in the reference configuration and the current configuration

certain time period $t > 0$. By defining the origin of a base system as a reference frame, every material point can be clearly identified by means of a position vector at every point in time.

To describe the change or deformation process of the continuum body through time, a reference configuration is defined at time $t = t_0$, at which the continuum body and its boundary are denoted by $\mathcal{B}_0$ and $\partial\mathcal{B}_0$, as illustrated on the left in figure 2.1. A material point of the body in the reference configuration can be described by position vector $\mathbf{X}$ relative to the fixed origin of the base system $\mathbf{e}_i$ with $i = 1, 2, 3$. In the following, repeated Latin indices in equations underlie the sum convention. The so-called current configuration at subsequent time $t > 0$ is the configuration of the body in its changed or deformed state, where the continuum body and its boundary are denoted by $\mathcal{B}_t$ and $\partial\mathcal{B}_t$, as illustrated in figure 2.1 on the right. The material point in the current configuration is described by position vector $\mathbf{x}$ relative to the fixed origin of the base system. The base system of the reference and current configurations do not have to be identical, but are assumed to be so in this work.

In order to be able to uniquely map the state of the continuum body in the reference configuration to the state in the current configuration, a bijective transformation

$$\hat{\varphi}\left(\mathbf{X}, t\right) : \mathcal{B}_0 \rightarrow \mathcal{B}_t \tag{2.1}$$

as a function of the position vector in the reference configuration $\mathbf{X}$ and the time t is introduced, which maps material points in the reference configuration to the current configuration. The vector field $\hat{\varphi}\left(\mathbf{X}, t\right)$ is often referred to as the motion of the continuum body. The bijective transformation is uniquely invertible, so that points in the current

configuration can be mapped to the reference configuration by means of

$$\hat{\varphi}^{-1}(\mathbf{x}, t) : \mathcal{B}_t \to \mathcal{B}_0 \quad . \tag{2.2}$$

For simplicity, $\hat{\varphi}(\mathbf{X}, t)$ and $\hat{\varphi}^{-1}(\mathbf{x}, t)$ are often abbreviated as $\hat{\varphi}_t(\mathbf{X})$ and $\hat{\varphi}_t^{-1}(\mathbf{x})$. In continuum mechanics, it is assumed that the transformation possesses continuous derivatives with respect to its variables. In the following, quantities in the reference configuration are denoted by uppercase letters or a subscript index $(\bullet)_0$ and quantities in the current configuration are denoted by lowercase letters.

In some cases, for example in shell theory, it can be advantageous to introduce curved convective coordinates denoted by ξ^i to parametrize the continuum body. The convective coordinate lines are deformed along with the continuum body. The tangential vectors at the coordinate lines form a covariant base system defined by

$$\mathbf{G}_i = \frac{\partial \mathbf{X}}{\partial \xi^i} \qquad \text{and} \qquad \mathbf{g}_i = \frac{\partial \mathbf{x}}{\partial \xi^i} \tag{2.3}$$

in the reference and current configurations, respectively. The corresponding reciprocal vectors form contravariant base systems and can be derived from the orthogonality conditions

$$\mathbf{G}^i \cdot \mathbf{G}_j = \delta^i_j \qquad \text{and} \qquad \mathbf{g}^i \cdot \mathbf{g}_j = \delta^i_j \quad , \tag{2.4}$$

where δ^i_j denotes the Kronecker symbol. The covariant metric coefficients G_{ij} and g_{ij} and contravariant metric coefficients G^{ij} and g^{ij} can be derived from the scalar products of the corresponding base vectors.

The displacement of a material point from the reference to the current configuration is described by the vector $\mathbf{u} = \mathbf{x} - \mathbf{X}$, as illustrated in figure 2.1. The displacement field $\mathbf{u}$ is the primary quantity in solid mechanics used to describe the behavior of a continuum body.

Having defined two different configurations to study the behavior of a continuum body, they can now be used to define other quantities that help to describe the deformation process of the continuum body. If a quantity is related to the reference configuration the so-called material or Lagrangian description is used, whereas if a quantity is related to the current configuration the so-called spatial or Eulerian description is used. Even though both descriptions are viable, in this work the quantities will be defined mainly in the material description, which is more common in solid mechanics.

2.2 Deformation and strain

The definitions made in the preceding section are used to describe the deformation process of a continuum body with the help of the material deformation gradient, specified by

$$\mathbf{F} = \operatorname{Grad} \mathbf{x} \quad , \tag{2.5}$$

where the material gradient operator has been introduced, which is defined by

$$\mathrm{Grad}\,(\bullet) = \frac{\partial(\bullet)}{\partial \mathbf{X}} \quad . \tag{2.6}$$

By means of the displacement gradient $\mathbf{H} = \mathrm{Grad}\,\mathbf{u}$, an equivalent representation to (2.5) can be introduced by

$$\mathbf{F} = \mathbf{H} + \mathbf{1} \quad , \tag{2.7}$$

where $\mathbf{1}$ is the second-order identity tensor. When using convective coordinates to parametrize the continuum body, another useful representation of the deformation gradient can be specified in terms of the covariant and contravariant base vectors with

$$\mathbf{F} = \mathbf{g}_i \otimes \mathbf{G}^i \quad . \tag{2.8}$$

The deformation gradient $\mathbf{F}$ transforms an undeformed line element $\mathrm{d}\mathbf{X}$ attached to a position vector $\mathbf{X}$ of a typical point in the reference configuration to the deformed line element $\mathrm{d}\mathbf{x}$ attached to a position vector $\mathbf{x}$ of the related typical point in the reference configuration,

$$\mathrm{d}\mathbf{x} = \mathbf{F}\,\mathrm{d}\mathbf{X} \quad . \tag{2.9}$$

The deformation gradient is a two-point tensor field because it involves both the reference and current configurations and it is a primary measure of deformation. Since the transformation between the reference and current configurations is assumed to be uniquely invertible, the inverse $\mathbf{F}^{-1}$ of the deformation gradient that transforms an infinitesimal spatial line element to an infinitesimal material line element exists. Because of this, and to avoid self-penetration of the continuum body during the deformation process,

$$J = \det \mathbf{F} > 0 \tag{2.10}$$

holds. The determinant of the deformation gradient J is called the Jacobian determinant or volume ratio. It is a measure for the change in the volume during the deformation process. By means of the Jacobian determinant, an infinitesimal material volume element $\mathrm{d}V$ is mapped to an infinitesimal spatial volume element $\mathrm{d}v$, so that

$$\mathrm{d}v = J\,\mathrm{d}V \quad . \tag{2.11}$$

The relation that maps a vector element $\mathrm{d}\mathbf{A} = \mathrm{d}A\mathbf{n}_0$ of an infinitesimally small area in the reference configuration to a vector element $\mathrm{d}\mathbf{a} = \mathrm{d}a\mathbf{n}$ of an infinitesimally small area in the current configuration can be derived to be

$$\mathrm{d}\mathbf{a} = J\mathbf{F}^{-T}\,\mathrm{d}\mathbf{A} \quad . \tag{2.12}$$

The unit vectors $\mathbf{n}_0$ and $\mathbf{n}$ are normal to an infinitesimal area element in the reference configuration and the current configuration, respectively. In (2.12) and in the following,

the abbreviation $(\bullet)^{-T} := \left[(\bullet)^{-1}\right]^T$ is used. The deformation gradient $\mathbf{F}$ can be separated into a proper orthogonal tensor $\mathbf{R}$ called the rotation tensor and either the right stretch tensor $\mathbf{U}$ or the left stretch tensor $\mathbf{v}$, so that

$$\mathbf{F} = \mathbf{R}\mathbf{U} = \mathbf{v}\mathbf{R} \quad . \tag{2.13}$$

The multiplicative decomposition (2.13) is unique and is often referred to as the right polar decomposition or the left polar decomposition respectively. Thus, the deformation of the line element $\mathrm{d}\mathbf{X}$ to the line element $\mathrm{d}\mathbf{x}$ can be interpreted as a sequence of a rotation and a stretching or vice versa.

Since the deformation gradient includes the rigid body motion, it is unsuitable as a strain measure. Two deformation tensors that are important strain measures are referred to as the right Cauchy-Green tensor $\mathbf{C}$ and the left Cauchy-Green tensor $\mathbf{b}$, which are defined by

$$\mathbf{C} = \mathbf{F}^T\mathbf{F} = \mathbf{U}^2 \qquad \text{and} \qquad \mathbf{b} = \mathbf{F}\mathbf{F}^T = \mathbf{v}^2 \tag{2.14}$$

respectively. A further strain measure is the Green-Lagrange strain tensor $\mathbf{E}$ defined by

$$\mathbf{E} = \frac{1}{2}\left(\mathbf{F}^T\mathbf{F} - \mathbf{1}\right) = \frac{1}{2}\left(\mathbf{C} - \mathbf{1}\right) \quad , \tag{2.15}$$

which results from the difference of the squares of the infinitesimal spatial and material line elements. The Green-Lagrange strain tensor is symmetric and invariant towards rigid body motions. With the help of the displacement gradient introduced in (2.7), an alternative representation to (2.15) can be specified to be

$$\mathbf{E} = \frac{1}{2}\left(\mathbf{H}^T + \mathbf{H} + \mathbf{H}^T\mathbf{H}\right) \quad . \tag{2.16}$$

The alternative representation (2.16) can easily be separated into a linear and nonlinear part. This can be advantageous in the case of small strains, where the nonlinear part can be neglected. When using convective coordinates, the Green-Lagrange strain tensor can be specified by

$$\mathbf{E} = \frac{1}{2}\left(g_{ij} - G_{ij}\right)\mathbf{G}^i \otimes \mathbf{G}^j \quad . \tag{2.17}$$

The Green-Lagrange strain tensor is symmetric. If the continuum body undergoes a rigid-body motion, the Green-Lagrange strain tensor vanishes, meaning that the size and shape of the body do not change.

2.3 Traction vectors and stress tensors

When the continuum body undergoes a deformation process, this leads to inner reaction forces and stresses. The internal forces can be made accessible by imagining a cut through

the continuum body along a plane surface. A normal unit vector $\mathbf{n}$ pointing outward is located on the cut surface at a particular point $\mathbf{x}$. The Cauchy traction vector $\mathbf{t}$ is defined by

$$\mathbf{t} = \frac{\mathrm{d}\mathbf{f}}{\mathrm{d}a} \quad , \tag{2.18}$$

and thus acts across the infinitesimal surface element $\mathrm{d}a$ associated with $\mathbf{x}$ on the cut surface with normal $\mathbf{n}$. In (2.18), $\mathrm{d}\mathbf{f}$ is the infinitesimal force vector that acts on the infinitesimal surface element $\mathrm{d}a$.

The traction vector depends on the orientation of the cutting surface and therefore on the normal unit vector $\mathbf{n}$. By means of Cauchy's stress theorem, there exists a relation between the surface traction and a stress tensor, so that

$$\mathbf{t} = \mathbf{T}\mathbf{n} \quad , \tag{2.19}$$

where $\mathbf{T}$ denotes the Cauchy stress tensor. The principle of balance of angular momentum introduced in chapter 2.4.2 can be used to prove that the Cauchy stress tensor is symmetric. The Cauchy stress tensor is defined in the current configuration and thus represents the true stresses. On the other hand, the nominal stresses are represented by the first Piola-Kirchhoff stress tensor $\mathbf{P}$, which is defined in the reference configuration. It can be written in terms of the Cauchy stress tensor as

$$\mathbf{P} = J\mathbf{T}\mathbf{F}^{-T} \quad . \tag{2.20}$$

Another useful stress tensor defined in the current configuration is the Kirchhoff stress tensor $\boldsymbol{\tau}$ specified by

$$\boldsymbol{\tau} = J\mathbf{T} \quad . \tag{2.21}$$

A definition of a stress tensor in the reference configuration that is practical for computational mechanics and will be extensively referred to later is the second Piola-Kirchhoff stress tensor $\mathbf{S}$, given with

$$\mathbf{S} = J\mathbf{F}^{-1}\mathbf{T}\mathbf{F}^{-T} \quad . \tag{2.22}$$

When using convective coordinates the second Piola-Kirchhoff stress tensor can be expressed by means of

$$\mathbf{S} = S^{ij}\mathbf{G}_i \otimes \mathbf{G}_j \quad . \tag{2.23}$$

The second Piola-Kirchhoff stress tensor $\mathbf{S}$ does not have a physical interpretation, but unlike the first Piola-Kirchhoff stress tensor, it is symmetric and it forms a work conform stress power with the time derivative $\dot{\mathbf{E}}$ of the Green-Lagrange strain tensor (see chapter 2.4.3). A large number of other definitions of stress tensors exist.

Besides the internal forces, which act on an imaginary surface within the continuum body, external forces act on the whole or parts of the boundary surface of the body. Additionally, volume forces or body forces, that are usually defined per unit volume, such as gravitation forces that act on a particle in the continuum body, must be regarded. External forces drive the deformation process.

2.4 Balance laws

In the field of continuum mechanics, a number of axiomatic balance laws that are valid for all materials exist. They will be briefly named and explained in this section. The emphasis will be placed on balance laws formulated with regards to the reference configuration, which is more practical in solid mechanics, with the exception of the conservation of mass, since this principle relates the mass of the reference configuration to the current configuration.

2.4.1 Conservation of mass

Every continuum body possesses a mass, which is a measure for the amount of material contained in the continuum body and is continuously distributed. The principle of conservation of mass in the global form,

$$m = \int_{\mathcal{B}_0} \rho_0(\mathbf{X}) \, \mathrm{d}V = \int_{\mathcal{B}_t} \rho(\mathbf{x}, t) \, \mathrm{d}v = \text{const} > 0 \quad , \tag{2.24}$$

postulates that the mass of each particle in the continuum body and therefore also the total mass stays the same during a motion or a deformation process of the body. In (2.24), $\rho_0(\mathbf{X})$ is the reference mass density related to $\mathrm{d}V$ and $\rho(\mathbf{x}, t)$ is the spatial mass density related to $\mathrm{d}v$. If the density does not depend on the position vectors $\mathbf{X}$ or $\mathbf{x}$ the continuum body is considered homogeneous.

Considering (2.11), the continuity of mass equation can be specified by

$$J = \frac{\rho_0}{\rho} \quad . \tag{2.25}$$

Apart from being a measure for the change in volume, the Jacobian determinant J thus is also a measure for the change of density from the reference configuration to the current configuration.

2.4.2 Balance of linear and angular momentum

The global form of the balance of linear momentum in the material description,

$$\dot{\mathbf{L}} = \mathbf{f}_0 \qquad \text{or} \qquad \frac{\mathrm{d}}{\mathrm{d}t} \int_{\mathcal{B}_0} \rho_0 \mathbf{v}_0 \, \mathrm{d}V = \int_{\mathcal{B}_0} \mathbf{b}_0 \, \mathrm{d}V + \int_{\partial\mathcal{B}_0} \mathbf{t}_0 \, \mathrm{d}A \quad , \tag{2.26}$$

postulates that the time derivative $\dot{\mathbf{L}}$ of the linear momentum is equal to the resultant force due to external sources $\mathbf{f}_0$. In (2.26), $\mathbf{v}_0$ is the velocity, $\mathbf{b}_0$ is an external body force

such as a gravitational force, and $\mathbf{t}_0$ is an external traction vector that acts on the surface of the body. In the static case, time derivatives vanish and (2.26) is reduced to

$$\int_{\mathcal{B}_0} \mathbf{b}_0 \, \mathrm{d}V + \int_{\partial\mathcal{B}_0} \mathbf{t}_0 \, \mathrm{d}A = \mathbf{0} \quad . \tag{2.27}$$

Using Cauchy's stress theorem and applying the divergence theorem, Cauchy's first equation of motion in the global form for the static case can be derived relating to the reference configuration and written as

$$\int_{\mathcal{B}_0} (\mathrm{Div}\, \mathbf{P} + \mathbf{b}_0) \, \mathrm{d}V = \mathbf{0} \quad . \tag{2.28}$$

Since the volume is arbitrary, a local form of (2.28) can be derived, so that

$$\mathrm{Div}\, \mathbf{P} + \mathbf{b}_0 = \mathbf{0} \quad . \tag{2.29}$$

The global form of the balance of angular momentum in the material description,

$$\dot{\mathbf{J}} = \mathbf{m}_0 \qquad \text{or} \qquad \frac{\mathrm{d}}{\mathrm{d}t} \int_{\mathcal{B}_0} \mathbf{r} \times \rho_0 \mathbf{v}_0 \, \mathrm{d}V = \int_{\mathcal{B}_0} \mathbf{r} \times \mathbf{b}_0 \, \mathrm{d}V + \int_{\partial\mathcal{B}_0} \mathbf{r} \times \mathbf{t}_0 \, \mathrm{d}A \quad , \tag{2.30}$$

postulates that the time derivative of the angular momentum $\dot{\mathbf{J}}$ is equal to the resultant moment due to external sources $\mathbf{m}_0$. The vector $\mathbf{r}$ in (2.30) denotes a position vector defined by $\mathbf{r} = \mathbf{x} - \mathbf{x}_0$, where $\mathbf{x}_0$ denotes the position vector of a reference point. The balance of angular momentum can be used to prove the symmetry of the Cauchy stress tensor $\mathbf{T}$ and therefore also the second Piola-Kirchhoff stress tensor $\mathbf{S}$.

2.4.3 Balance of energy

The balance of energy is introduced considering solely mechanical and thermal energy. It is also referred to as the first law of thermodynamics and can be specified by

$$\dot{\mathcal{K}} + \dot{\mathcal{E}} = \mathcal{P}_{\mathrm{ext}} + \mathcal{Q} \quad . \tag{2.31}$$

The first law of thermodynamics states that the rate of change of the total energy of the system, which is separated into the kinetic energy $\mathcal{K}$ and the internal energy $\mathcal{E}$ in (2.31), equals the total external power, which is separated into the external mechanical power $\mathcal{P}_{\mathrm{ext}}$ due to surface tractions and body forces and the thermal power $\mathcal{Q}$. Inserting the explicit forms of these quantities, (2.31) becomes

$$\frac{\mathrm{d}}{\mathrm{d}t} \int_{\mathcal{B}_0} \left(\frac{1}{2} \rho_0 \mathbf{v}_0^2 + e_0 \right) \mathrm{d}V = \int_{\mathcal{B}_0} (\mathbf{b}_0 \cdot \mathbf{v}_0 + r_0) \, \mathrm{d}V + \int_{\partial\mathcal{B}_0} (\mathbf{t}_0 \cdot \mathbf{v}_0 - \mathbf{q}_0 \cdot \mathbf{n}_0) \, \mathrm{d}A \quad , \tag{2.32}$$

where e_0 denotes the internal mechanical energy defined per unit reference volume, r_0 denotes a heat source, $\mathbf{q}_0$ denotes the Cauchy heat flux, and $\mathbf{n}_0$ denotes the normal unit vector on the cutting surface in the reference configuration.

If thermal power is neglected by setting $\mathcal{Q}$ to zero in (2.31), the terms in (2.32) that emanate from the heat flux and the heat source can be neglected. In this case, the rate of the internal energy $\mathcal{E}$ equals the stress power $\mathcal{P}_{\text{int}}$, which corresponds to the rate of internal mechanical work $\dot{W}$,

$$\dot{W} = \mathcal{P}_{\text{int}} = \dot{\mathcal{E}} = \frac{\mathrm{d}}{\mathrm{d}t} \int_{\mathcal{B}_0} e_0 \, \mathrm{d}V = \int_{\mathcal{B}_0} \mathbf{P} : \dot{\mathbf{F}} \, \mathrm{d}V = \int_{\mathcal{B}_0} \mathbf{S} : \dot{\mathbf{E}} \, \mathrm{d}V \quad . \tag{2.33}$$

The rate of internal mechanical work $\dot{W}$ describes the response of the continuum body to the stress field at a particular time. The stress power can be expressed with the help of a number of different work conjugate pairs, two of which are specified in (2.33) for the reference configuration. By means of the double contractions in (2.33), the rate of internal mechanical work per unit reference volume is described. Work conjugate pairs are important when constructing constitutive equations, which interrelate state variables. The external mechanical power expended by the forces $\mathbf{b}_0$ and $\mathbf{t}_0$ can be expressed by

$$\mathcal{P}_{\text{ext}} = \int_{\mathcal{B}_0} \mathbf{b}_0 \cdot \mathbf{v}_0 \, \mathrm{d}V + \int_{\partial\mathcal{B}_0} \mathbf{t}_0 \cdot \mathbf{v}_0 \, \mathrm{d}A \quad . \tag{2.34}$$

In this context, it makes sense to introduce the external potential energy Π_{ext} and the internal potential energy Π_{int} of a continuum body. The total potential energy Π results from the sum of the external and internal potential energy,

$$\Pi = \Pi_{\text{int}} + \Pi_{\text{ext}} \quad . \tag{2.35}$$

The internal and external potential will be further defined in chapter 2.6. The external mechanical power $\mathcal{P}_{\text{ext}}$ and internal mechanical power $\mathcal{P}_{\text{int}}$ can be expressed as the time derivative of the external and internal potential energy, so that

$$\mathcal{P}_{\text{ext}} = -\frac{\mathrm{d}\Pi_{\text{ext}}}{\mathrm{d}t} \qquad \text{and} \qquad \mathcal{P}_{\text{int}} = \frac{\mathrm{d}\Pi_{\text{int}}}{\mathrm{d}t} \quad , \tag{2.36}$$

if the system is conservative, which means that the total potential energy Π and the kinetic energy $\mathcal{K}$ are conserved when the body undergoes a deformation process. In many mechanical problems, such as plasticity problems, energy dissipates and, in such cases, the continuum bodies therefore cannot be viewed as conservative systems.

2.4.4 Entropy inequality

The entropy inequality is also referred to as the second law of thermodynamics and is responsible for the direction of an energy transfer process [53]. A continuum body possesses

an entropy denoted by $\mathcal{S}$ and defined by

$$\mathcal{S} = \int_{\mathcal{B}_0} s_0 \, \mathrm{d}V \quad , \tag{2.37}$$

where s is the entropy per unit volume. The second law of thermodynamics can be specified by

$$\Gamma = \dot{\mathcal{S}} - \tilde{\mathcal{Q}} \geq 0 \quad . \tag{2.38}$$

It states that the total production of entropy denoted by Γ cannot be negative. The total production of entropy consists of the difference between the rate of change of the entropy $\mathcal{S}$ and the rate of entropy input denoted by $\tilde{\mathcal{Q}}$, which is made up the entropy that is transferred across its boundary surface and the entropy that is produced inside the body. The second law of thermodynamics determines the direction of the energy transfer. For example, heat will always flow from a warmer region to a colder region in the continuum body. If $\Gamma = 0$, the process is reversible, whereas if $\Gamma > 0$, energy has dissipated and the process is said to be irreversible.

A number of other representations of the second law of thermodynamics can be derived. One example is a form of the Clausius-Planck inequality given by

$$\mathbf{P} : \dot{\mathbf{F}} - \dot{\Psi} - s_0 \dot{\Theta} \geq 0 \quad , \tag{2.39}$$

where Θ denotes the absolute temperature and Ψ is called the Helmholtz free-energy function. Ignoring thermal effects leads to a purely mechanical theory and (2.39) becomes

$$\mathbf{P} : \dot{\mathbf{F}} - \dot{\Psi} \geq 0 \quad , \tag{2.40}$$

where Ψ corresponds to the internal energy e_0 (2.32). From (2.40) it can be concluded, that for reversible processes, the stress power per unit reference volume (2.33) is equal to the rate $\dot{\Psi}$ of the Helmholtz free-energy function.

2.5 Constitutive law

In order to solve boundary problems in continuum mechanics, it is indispensable to establish the connection between stresses and strains by means of appropriate constitutive laws, because the previously considered equations are not sufficient to determine the material response of deformable bodies. Constitutive laws approximate the observed physical behavior of a real material [53]. The development of constitutive laws is a very important and extensive research field. Considerable information on the development of nonlinear constitutive equations is for example provided in [124]. The purpose of this section merely is to provide a basis for a constitutive law suitable for using in the development of the finite element for fiber-reinforced composite materials, the subject of this research work.

When developing constitutive laws, a number of important principles must be considered. They are listed in the following without going into further detail: principle of causality,

principle of determinism, principle of equipresence, principle of material frame-indifference, principle of material symmetry, principle of local effect, principle of declining memory and principle of admissibility.

For the scope of this work, a phenomenological approach is taken, meaning that the macroscopic nature of a material is described. This is reasonable since the macroscopic properties of the composite material to be investigated are known. The macroscopic model employs a continuum approach to describe the behavior of the material.

In the context of hyperelastic materials the existence of a Helmholtz free-energy function Ψ introduced in (2.39) in connection with the second law of thermodynamics is assumed. The second law of thermodynamics can be helpful when developing constitutive laws for hyperelastic materials, where the deformation process is reversible and the dissipation is equal to zero. There also exist hyperelastic material models that are physically motivated. In general, the Helmholtz free-energy Ψ can be established as a function of the deformation gradient $\mathbf{F}$ or some other strain tensor. For hyperelastic materials, it is often defined as a function of the right Cauchy-Green tensor $\mathbf{C}$ or the left Cauchy-Green tensor $\mathbf{b}$. In this context, the Helmholtz free-energy function is commonly referred to as the strain-energy function. The strain-energy function must meet a number of requirements, which are briefly described here. Further comprehensive descriptions can be found in the cited references.

One requirement is that the so-called growth conditions need to be met [28, 53]. These imply that in order for the structure under investigation to be infinitely expanded or infinitely compressed, an infinite amount of strain-energy is needed ($\Psi \to +\infty$ when $J \to +\infty$ and $J \to +0$ with (2.10)).

Also, the stress in the undeformed state, the so-called residual stress, has to vanish, so that

$$\Psi(\mathbf{F}) = 0 \qquad \text{when} \qquad \mathbf{F} = \mathbf{1} \quad . \tag{2.41}$$

On the other hand, following from the fact that the strain-energy must increase with deformation,

$$\Psi(\mathbf{F}) \geq 0 \tag{2.42}$$

holds. Additionally, the strain-energy function should be polyconvex, which is a central concept in the theory of existence of solutions [8, 9, 28, 83]. The advantage of such functions is that they guarantee the existence of minimizers for simulations of boundary value problems using numerical solution techniques.

An important distinction that plays a large role in the development of strain-energy functions for different material types is their classification into homogeneous or heterogeneous materials. The strain-energy function takes the form

$$\Psi = \Psi(\mathbf{F}) \qquad \text{or} \qquad \Psi = \Psi(\mathbf{X}, \mathbf{F}) \tag{2.43}$$

for homogeneous or heterogeneous materials respectively. When modeling homogeneous materials, such as materials that show the same behavior in any direction, it makes sense to assume that the strain-energy function depends solely on the deformation gradient or a

strain tensor. On the other hand, for heterogeneous materials, such as the composites made up of fibers and a matrix material with arbitrary stacking sequences under investigation in this work, the strain-energy function depends on the deformation gradient or a strain tensor and the position in the structure under consideration.

In order to fulfill the principle of material frame indifference (also referred to as the principle of material objectivity), the constitutive equations must be invariant when subjected to a rigid body motion. Accordingly, the same holds true for the strain-energy, so that the restrictions

$$\Psi(\mathbf{F}) = \Psi(\mathbf{QF}) \qquad \text{and} \qquad \Psi(\mathbf{X}, \mathbf{F}) = \Psi(\mathbf{X}, \mathbf{QF}) \tag{2.44}$$

apply, where $\mathbf{Q}$ is an orthogonal tensor, which describes an arbitrary rigid body motion. In order to meet this requirement, the strain-energy must be independent of the rotational part of the polar decomposition $\mathbf{F} = \mathbf{RU}$, so that

$$\Psi(\mathbf{F}) = \Psi(\mathbf{U}) \qquad \text{and} \qquad \Psi(\mathbf{X}, \mathbf{F}) = \Psi(\mathbf{X}, \mathbf{U}) \tag{2.45}$$

hold. Since the right Cauchy-Green tensor $\mathbf{C}$ (2.14) and the Green-Lagrange strain tensor $\mathbf{E}$ (2.15) can be expressed with the help of the material stretch tensor,

$$\Psi(\mathbf{F}) = \Psi(\mathbf{C}) = \Psi(\mathbf{E}) \qquad \text{and} \qquad \Psi(\mathbf{X}, \mathbf{F}) = \Psi(\mathbf{X}, \mathbf{C}) = \Psi(\mathbf{X}, \mathbf{E}) \tag{2.46}$$

hold. Materials can further be classified into isotropic and anisotropic materials. If the reference configuration is subjected to a rigid body motion superimposed on a deformation process and the strain-energy function does not change, a material is said to be isotropic. Such a material has the same properties in every direction. On the other hand, if the strain-energy function changes, the material is said to be anisotropic.

The response of the material to the deformation process can be given in terms of the first Piola-Kirchhoff stress tensor $\mathbf{P}$ (2.20) by

$$\mathbf{P}(\mathbf{F}) = \frac{\partial \Psi(\mathbf{F})}{\partial \mathbf{F}} \qquad \text{and} \qquad \mathbf{P}(\mathbf{X}, \mathbf{F}) = \frac{\partial \Psi(\mathbf{X}, \mathbf{F})}{\partial \mathbf{F}} \quad , \tag{2.47}$$

so that in homogeneous materials, $\mathbf{P}$ is a function of the deformation gradient or a strain tensor, whereas in heterogeneous materials it is a function of the deformation gradient or a strain tensor and the position of interest. Materials whose stress field depends only on the state of deformation (2.47) and not on the deformation history are referred to as Cauchy-elastic.

For homogeneous materials, where the strain-energy does not depend on the position of interest, other stress tensors can be expressed with the strain-energy as a function of several strain tensors by means of standard algebra and defined stress relations. The first Piola-Kirchhoff stress tensor $\mathbf{P}$ (2.20) and the second Piola-Kirchhoff stress tensor $\mathbf{S}$ (2.22) can be derived from the strain-energy function by

$$\mathbf{P} = \frac{\partial \Psi(\mathbf{F})}{\partial \mathbf{F}} = 2\,\mathbf{F}\,\frac{\partial \Psi(\mathbf{C})}{\partial \mathbf{C}} \qquad \text{and} \qquad \mathbf{S} = 2\,\frac{\partial \Psi(\mathbf{C})}{\partial \mathbf{C}} = \frac{\partial \Psi(\mathbf{E})}{\partial \mathbf{E}} \quad , \tag{2.48}$$

respectively, while the Cauchy stress tensor $\mathbf{T}$ (2.19) can be derived from

$$\mathbf{T} = J^{-1}\,\mathbf{F}\left(\frac{\partial \Psi(\mathbf{F})}{\partial \mathbf{F}}\right)^{T} = 2\,J^{-1}\,\mathbf{F}\left(\frac{\partial \Psi(\mathbf{C})}{\partial \mathbf{C}}\right)\mathbf{F}^{T} \tag{2.49}$$

and the Kirchhoff stress tensor $\boldsymbol{\tau}$ (2.21) from

$$\boldsymbol{\tau} = 2\,\mathbf{F}\left(\frac{\partial \Psi(\mathbf{C})}{\partial \mathbf{C}}\right)\mathbf{F}^{T} \quad . \tag{2.50}$$

It is now assumed that the strain-energy function is expressed in terms of the right Cauchy-Green tensor. When modeling isotropic materials, the strain-energy function needs to meet the requirement for an isotropic tensor function,

$$\Psi(\mathbf{C}) = \Psi\left(\mathbf{Q}\mathbf{C}\mathbf{Q}^{T}\right) \quad . \tag{2.51}$$

Based on the representation theorem for invariants [49, 95, 124] the strain-energy function for isotropic materials can be expressed in terms of the independent strain invariants of the right Cauchy-Green tensor $\mathbf{C}$, so that

$$\Psi = \Psi\left[I_1(\mathbf{C}), I_2(\mathbf{C}), I_3(\mathbf{C})\right] \quad , \tag{2.52}$$

where I_1, I_2 and I_3 are the three invariants of $\mathbf{C}$,

$$I_1 = \operatorname{tr}\mathbf{C} \quad , \qquad I_2 = \frac{1}{2}\left[(\operatorname{tr}\mathbf{C})^2 - \operatorname{tr}\left(\mathbf{C}^2\right)\right] \qquad \text{and} \qquad I_3 = \det\mathbf{C} \quad . \tag{2.53}$$

When modeling the behavior of an isotropic material, the three invariants of $\mathbf{C}$ thus are sufficient to meet requirement (2.51). In order to derive the material response to a deformation in the form of the second Piola-Kirchhoff stress tensor in terms of the invariants the constitutive equation defined in (2.48 b) can be exploited. Applying the chain rule, the derivative of the strain-energy function $\Psi = \Psi(\mathbf{C})$ with respect to $\mathbf{C}$,

$$\frac{\partial \Psi(\mathbf{C})}{\partial \mathbf{C}} = \frac{\partial \Psi}{\partial I_1}\frac{\partial I_1}{\partial \mathbf{C}} + \frac{\partial \Psi}{\partial I_2}\frac{\partial I_2}{\partial \mathbf{C}} + \frac{\partial \Psi}{\partial I_3}\frac{\partial I_3}{\partial \mathbf{C}} \quad , \tag{2.54}$$

can be specified and after some algebra, the constitutive law that yields the response of an isotropic material, in the form of the second Piola-Kirchhoff stress tensor, can be derived to be

$$\mathbf{S} = 2\left[\left(\frac{\partial \Psi}{\partial I_1} + I_1\frac{\partial \Psi}{\partial I_2}\right)\mathbf{1} - \frac{\partial \Psi}{\partial I_2}\mathbf{C} + I_3\frac{\partial \Psi}{\partial I_3}\mathbf{C}^{-1}\right] \quad . \tag{2.55}$$

Defining the strain-energy as a function of the three invariants of the right Cauchy-Green tensor $\mathbf{C}$ is a suitable strategy when modeling isotropic materials. However, this form of the strain-energy function is not applicable to anisotropic materials such as composites made up of fibers and a matrix material. As already pointed out, in such a material the

strain-energy function must depend not only on the deformation gradient $\mathbf{F}$ or a strain tensor but additionally on the point of interest $\mathbf{X}$.

However, the special properties of composites made up of fibers that have a preferred direction and are enclosed by a matrix material can be used to construct a strain-energy function that complies with the principle of material objectivity. Such a material is called transversely isotropic, which is the simplest case of an anisotropic material. In this model, it is assumed that the presence of the fibers is the sole reason for the anisotropic behavior of the structure and that the material behaves isotropically along directions orthogonal to the preferred direction.

When modeling the behavior of transversely isotropic materials, the strain-energy can be constructed as a function depending on the deformation gradient $\mathbf{F}$ or a strain tensor and on the fiber direction at a particular point. Accordingly, the unit vector field $\mathbf{a}_0(\mathbf{X})$ is introduced, which determines the direction of the fiber at a certain point of interest in the reference configuration. The direction of the same fiber in the current configuration is determined by the unit vector field $\mathbf{a}$. Introducing the stretch λ_0 of the fiber along its direction $\mathbf{a}_0$, the relation $\lambda_0\mathbf{a} = \mathbf{F}\mathbf{a}_0$ holds. The square of the stretch λ_0 can thus be determined to be

$$\lambda_0^2 = \mathbf{a}_0 \cdot \mathbf{F}^T\mathbf{F}\mathbf{a}_0 = \mathbf{a}_0 \cdot \mathbf{C}\mathbf{a}_0 \quad . \tag{2.56}$$

The strain-energy for a transversely isotropic material can therefore be established as a function of $\mathbf{C}$ and the fiber direction $\mathbf{a}_0$,

$$\Psi = \Psi\left(\mathbf{C}, \mathbf{a}_0 \otimes \mathbf{a}_0\right) \quad . \tag{2.57}$$

The principle of material objectivity is met by (2.57) because $\mathbf{C}$ and $\mathbf{a}_0 \otimes \mathbf{a}_0$ are defined with respect to the reference configuration and are therefore unaffected by transformations of the current configuration. Analogous to (2.51), for isotropic materials a requirement,

$$\Psi(\mathbf{C}, \mathbf{a}_0 \otimes \mathbf{a}_0) = \Psi\left(\mathbf{Q}\mathbf{C}\mathbf{Q}^T, \mathbf{Q}\mathbf{a}_0 \otimes \mathbf{a}_0\mathbf{Q}^T\right) \quad , \tag{2.58}$$

can be set up that transversely isotropic materials need to meet. In order to meet requirement (2.58), two additional invariants to the three strain invariants of $\mathbf{C}$ defined in (2.53) specified by

$$I_4 = \mathbf{a}_0 \cdot \mathbf{C}\mathbf{a}_0 \qquad \text{and} \qquad I_5 = \mathbf{a}_0 \cdot \mathbf{C}^2\mathbf{a}_0 \tag{2.59}$$

have to be introduced. They are called the pseudo-invariants of $\mathbf{C}$ and $\mathbf{a}_0$ [119].

Similarly to (2.52) for isotropic materials, the strain-energy function for anisotropic materials can be expressed in terms of the three independent invariants of the right Cauchy-Green tensor $\mathbf{C}$ and the two pseudo-invariants, so that

$$\Psi = \Psi\left[I_1(\mathbf{C}), I_2(\mathbf{C}), I_3(\mathbf{C}), I_4(\mathbf{C}, \mathbf{a}_0), I_5(\mathbf{C}, \mathbf{a}_0)\right] \quad . \tag{2.60}$$

For the phenomenological description of anisotropic elasticity at large strains, some anisotropic polyconvex [8] free-energy functions are proposed in [101, 102]. A discussion of polyconvex strain-energy functions particularly for shell structures is conducted in [11].

Analogous to (2.54) and (2.55) for isotropic materials, in order to derive the second Piola-Kirchhoff stress tensor in terms of the invariants the chain rule is utilized to determine the derivative of the strain-energy function for transversely isotropic materials $\Psi = \Psi(\mathbf{C}, \mathbf{a}_0 \otimes \mathbf{a}_0)$ with respect to $\mathbf{C}$,

$$\frac{\partial \Psi(\mathbf{C}, \mathbf{a}_0 \otimes \mathbf{a}_0)}{\partial \mathbf{C}} = \sum_{n=1}^{5} \frac{\partial \Psi(\mathbf{C}, \mathbf{a}_0 \otimes \mathbf{a}_0)}{\partial I_n} \frac{\partial I_n}{\partial \mathbf{C}} \quad . \tag{2.61}$$

The constitutive law that yields the second Piola-Kirchhoff stress tensor for transversely isotropic materials can be specified by

$$\begin{aligned} \mathbf{S} = 2 \Bigg[& \left(\frac{\partial \Psi}{\partial I_1} + I_1 \frac{\partial \Psi}{\partial I_2} \right) \mathbf{1} - \frac{\partial \Psi}{\partial I_2} \mathbf{C} + I_3 \frac{\partial \Psi}{\partial I_3} \mathbf{C}^{-1} \\ & + \frac{\partial \Psi}{\partial I_4} \mathbf{a}_0 \otimes \mathbf{a}_0 + \frac{\partial \Psi}{\partial I_5} \left(\mathbf{a}_0 \otimes \mathbf{C}\mathbf{a}_0 + \mathbf{a}_0 \mathbf{C} \otimes \mathbf{a}_0 \right) \Bigg] \quad . \end{aligned} \tag{2.62}$$

With (2.55) and (2.62) constitutive laws in terms of invariants have been established for isotropic and transversely isotropic materials, if suitable strain-energy functions can be constructed.

When solving nonlinear problems with numerical procedures such as the finite element method, iterative solution techniques of Newton's type are applied to solve a series of linearized equations. In this context, the linearized constitutive equation needs to be derived, which yields for hyperelasticity the so-called elasticity tensor $\mathbb{C}$, which can be derived from the second derivative of the strain-energy function and thus can be specified by

$$\mathbb{C} = 4 \frac{\partial^2 \Psi}{\partial \mathbf{C} \partial \mathbf{C}} = 2 \frac{\partial \mathbf{S}}{\partial \mathbf{C}} \quad , \tag{2.63}$$

where the strain-energy function and second Piola-Kirchhoff stress tensor are given by (2.52) and (2.55) for isotropic materials and by (2.60) and (2.62) for transversely isotropic materials. The elasticity tensor $\mathbb{C}$ is a tensor of rank four and because it possesses the so-called minor and major symmetries, it cannot have more than 21 independent components.

2.6 Variational principles and their linearizations

A starting point for a discretization technique such as the finite element method that yields good approximations is often a variational principle based on the weak form of field equations and derived from the stationary condition of a functional. Variational principles can be based on one or more field quantities. In the following, a variational principle based on one field, the displacement vector $\mathbf{u}$, will be derived.

The starting point is the static, local form of Cauchy's first equation of motion specified with regard to the reference configuration in (2.29). Multiplying (2.29) with an arbitrary

vector-valued test function denoted by $\boldsymbol{\eta}$ and integrating over the volume of the body leads to the weak form of the equation of motion,

$$g\left(\mathbf{u},\boldsymbol{\eta}\right)=\int\limits_{\mathcal{B}_0}\left(\operatorname{Div}\mathbf{P}+\mathbf{b}_0\right)\cdot\boldsymbol{\eta}\,\mathrm{d}V=0\quad . \tag{2.64}$$

The weak form (2.64) is equivalent to the static form of the equation of motion (2.29), as the latter can be derived out of the former by means of the fundamental lemma of variational calculus. An equation derived out of a weak form is often referred to as an Euler-Lagrange equation. The test function $\boldsymbol{\eta}$ must meet the kinematic boundary conditions on the boundary surface and $\boldsymbol{\eta}=\mathbf{0}$ holds on the boundary surface denoted by $\partial\mathcal{B}_{0u}$. The boundary surface $\partial\mathcal{B}_{0u}$ is distinct from the boundary surface $\partial\mathcal{B}_{0\sigma}$ and together they make up the total boundary surface $\partial\mathcal{B}_0$ illustrated in figure 2.1. Applying the product rule and the divergence theorem, (2.64) can be rewritten as

$$g\left(\mathbf{u},\boldsymbol{\eta}\right)=\int\limits_{\mathcal{B}_0}\left(\mathbf{P}:\operatorname{Grad}\boldsymbol{\eta}-\mathbf{b}_0\cdot\boldsymbol{\eta}\right)\,\mathrm{d}V-\int\limits_{\partial\mathcal{B}_{0\sigma}}\bar{\mathbf{t}}_0\cdot\boldsymbol{\eta}\,\mathrm{d}A=0\quad . \tag{2.65}$$

Since it is required that $\boldsymbol{\eta}$ fulfills the kinematic boundary conditions $\mathbf{u}=\bar{\mathbf{u}}$, with $\bar{\mathbf{u}}$ being a prescribed displacement field, no integration over $\partial\mathcal{B}_{0u}$ is needed. The stress boundary conditions $\mathbf{t}_0=\mathbf{P}\mathbf{N}=\bar{\mathbf{t}}_0$, with $\bar{\mathbf{t}}_0$ being a prescribed traction vector, however, are part of the weak form in (2.65).

As a test function, a virtual displacement field $\delta\mathbf{u}$ can be chosen, which is independent of the displacement field $\mathbf{u}$ and represents an infinitesimal, imaginary change of the continuum body as opposed to $\mathrm{d}\mathbf{u}$, which represents an infinitesimal, actual change of the body. The so-called variational operator $\delta(\bullet)$ is a linear operator for which the usual properties of differentiation apply. With relation $\delta\mathbf{F}=\operatorname{Grad}\delta\mathbf{u}$, the weak form (2.65) can then be rewritten as

$$g\left(\mathbf{u},\delta\boldsymbol{u}\right)=\int\limits_{\mathcal{B}_0}\left(\mathbf{P}:\delta\mathbf{F}-\mathbf{b}_0\cdot\delta\boldsymbol{u}\right)\,\mathrm{d}V-\int\limits_{\partial\mathcal{B}_{0\sigma}}\bar{\mathbf{t}}_0\cdot\delta\boldsymbol{u}\,\mathrm{d}A=0\quad , \tag{2.66}$$

which is referred to as the principle of virtual work. The terms in (2.66) can be separated into a part called the internal virtual work δW_{int},

$$\delta W_{\mathrm{int}}=\int\limits_{\mathcal{B}_0}\mathbf{P}:\delta\mathbf{F}\,\mathrm{d}V=\int\limits_{\mathcal{B}_0}\mathbf{S}:\delta\mathbf{E}\,\mathrm{d}V\quad , \tag{2.67}$$

and a part called the external virtual work δW_{ext},

$$\delta W_{\mathrm{ext}}=\int\limits_{\mathcal{B}_0}\mathbf{b}_0\cdot\delta\boldsymbol{u}\,\mathrm{d}V+\int\limits_{\partial\mathcal{B}_{0\sigma}}\bar{\mathbf{t}}_0\cdot\delta\boldsymbol{u}\,\mathrm{d}A\quad . \tag{2.68}$$

The internal virtual work equals the external virtual work in the static case, so that

$$g(\mathbf{u}, \delta\boldsymbol{u}) = \delta W_{\text{int}} - \delta W_{\text{ext}} = 0 \quad . \tag{2.69}$$

In many continuum mechanics problems, it can be assumed that the direction of the loads in (2.68) stays parallel and their values do not change during the deformation process. Loads that behave in this way are referred to as conservative loads.

The principle of virtual work applies to all materials, since it does not require the existence of a potential Π, which was introduced in chapter 2.4.3 as the sum of the internal and external potential energy (2.35). However, if the system is conservative, an energy functional describing the potential energy exists, from which the principle of virtual work can be derived. Assuming that a potential energy exists has benefits when developing numerical methods to find a solution of the variational formulation.

The internal potential energy Π_{int} and external potential energy Π_{ext} are defined by

$$\Pi_{\text{int}} = \int_{\mathcal{B}_0} \Psi \, \mathrm{d}V \qquad \text{and} \qquad \Pi_{\text{ext}} = -\int_{\mathcal{B}_0} \mathbf{b}_0 \cdot \boldsymbol{u} \, \mathrm{d}V - \int_{\partial\mathcal{B}_{0\sigma}} \bar{\mathbf{t}}_0 \cdot \boldsymbol{u} \, \mathrm{d}A \quad , \tag{2.70}$$

where Ψ is the strain-energy as a function of the deformation gradient $\mathbf{F}$ or a strain tensor discussed in the previous section. If the sum of internal and external potential (2.35) is stationary, an equilibrium state has been reached. It can be derived by invoking the directional derivative of Π with respect to the displacements $\mathbf{u}$, so that

$$\delta\Pi(\mathbf{u}, \delta\mathbf{u}) = D[\Pi(\mathbf{u})] \cdot \delta\mathbf{u} = \frac{d}{d\varepsilon}\Pi(\mathbf{u} + \varepsilon\delta\mathbf{u})\,|_{\varepsilon=0} = 0 \quad , \tag{2.71}$$

where ε is a scalar parameter. The variational principle in (2.71) is called the principle of stationary potential energy and requires that the directional derivative with respect to $\mathbf{u}$ vanishes in all directions $\delta\mathbf{u}$. In (2.71), $D[\bullet]$ is a directional derivation operator known as the Gâteaux operator. Applying the directional derivative to (2.35) with (2.70) leads to the principle of virtual work (2.66), so that

$$\delta\Pi(\mathbf{u}, \delta\mathbf{u}) = \delta\Pi_{\text{int}} + \delta\Pi_{\text{ext}} = \delta W_{\text{int}} - \delta W_{\text{ext}} = 0 \quad . \tag{2.72}$$

Thus, if (2.66) is satisfied, the total potential energy Π is stationary for arbitrary variations $\delta\mathbf{u}$.

The principle of virtual work (2.66) is usually nonlinear in $\mathbf{u}$. Analytical solutions are often difficult or impossible to derive. Thus, numerical techniques based on the finite element method, such as the iterative solution techniques of Newton's type, need to be employed to achieve an approximate solution. In this technique, the nonlinear problem is separated into a number of successive linear problems, requiring a consistent linearization of the quantities in the nonlinear problem. A further discussion on a consistent linearization is carried out in [56]. Thus, the function $g(\mathbf{u}, \delta\boldsymbol{u})$ (3.85) is linearized based on a first-order Taylor expansion specified by

$$L[g(\mathbf{u}, \delta\boldsymbol{u}), \Delta\mathbf{u}] = g(\mathbf{u}, \delta\boldsymbol{u}) + D[g(\mathbf{u}, \delta\boldsymbol{u})] \cdot \Delta\mathbf{u} \quad , \tag{2.73}$$

where $D[\bullet]$ is the Gâteaux operator mentioned earlier in this section and $L[\bullet]$ is a linearization operator. The operator $\Delta(\bullet)$ is similar to the operator $\delta(\bullet)$ in that it also is a linear operator for which the usual properties of differentiation apply. Similar to $\delta\mathbf{u}$, the incremental displacement field $\Delta\mathbf{u}$ also represents an infinitesimal, imaginary change of the continuum body. The second term in (2.73) is the directional derivative of the principle of virtual work and can be derived by evaluating

$$D\left[g\left(\mathbf{u},\delta\boldsymbol{u}\right)\right]\cdot\Delta\mathbf{u}=\frac{d}{d\varepsilon}\left[g\left(\mathbf{u}+\varepsilon\Delta\mathbf{u},\delta\mathbf{u}\right)\right]|_{\varepsilon=0}\quad . \tag{2.74}$$

If the loads in (2.66) are considered dead loads, the linearization of the external virtual work vanishes so that

$$D\left[\delta W_{\text{ext}}\left(\mathbf{u},\delta\boldsymbol{u}\right)\right]\cdot\Delta\mathbf{u}=0\quad . \tag{2.75}$$

Thus, in this case, only the linearization of the internal virtual work needs to be considered. Formulated in terms of the second Piola-Kirchhoff stress tensor $\mathbf{S}$ and the Green-Lagrange strain tensor $\mathbf{E}$ it can be derived as

$$D\left[g\left(\mathbf{u},\delta\mathbf{u}\right)\right]\cdot\Delta\mathbf{u}=D\left[\delta W_{\text{int}}\left(\mathbf{u},\delta\boldsymbol{u}\right)\right]\cdot\Delta\mathbf{u}=\int_{\mathcal{B}_0}\left[\mathbf{S}:\Delta\delta\mathbf{E}+\delta\mathbf{E}:\mathbb{C}:\Delta\mathbf{E}\right]\,\mathrm{d}V\quad , \tag{2.76}$$

where $\mathbf{S}$ is a function of $\mathbf{E}$ and $\mathbf{E}$ is a function of $\mathbf{u}$. In (2.76), $\mathbb{C}$ denotes the elasticity tensor introduced in (2.63). Other forms of (2.76) can be derived. By means of the linearized principle of virtual work, a starting point for the implementation of the finite element method has been provided. In such a procedure, the term $g\left(\mathbf{u},\delta\boldsymbol{u}\right)$ in (2.73) constitutes the residuum and the incremental displacements $\Delta\mathbf{u}$ are calculated in every iteration, so that $L\left[g\left(\mathbf{u},\delta\boldsymbol{u}\right),\Delta\mathbf{u}\right]=0$ is fulfilled. The displacements are then updated and the procedure is repeated until the residuum vanishes, meaning that a solution for $\mathbf{u}$ has been found.

A variational principle based on only one field, usually the displacement field $\mathbf{u}$, such as the principle of virtual work just described, does not always perform well when used as a basis for numerical simulations with the finite element method. In certain physical problems so-called locking phenomena occur, where the discretized system behaves too stiff and the results become highly inaccurate. This is especially the case for low-order finite elements. An example for a physical problem that leads to locking in finite element simulations are bending dominated problems, in which plate and shell elements are used.

One possible remedy for locking is using a variational principle that depends on multiple fields, often called a mixed variational principle. An example for a two-field variational principle that is often used in nonlinear theories of plates is the Hellinger-Reissner variational principle [51, 94], where besides the displacements the stresses are an independent field variable. A disadvantage of this principle is that the inverse form of the constitutive equation needs to be derived, which is numerically costly or in some cases impossible.

A three-field variational principle that often performs well when using it in numerical simulations is the Hu-Washizu variational principle, where the displacements, stresses and

strains are independent field variables. One general form of a Hu-Washizu principle [53] is

$$\begin{aligned}\Pi(\mathbf{u},\mathbf{F},\mathbf{P}) = &\int_{\mathcal{B}_0} \left(\Psi(\mathbf{F}) - \mathbf{P}:\mathbf{F} - \mathbf{b}_0\cdot\mathbf{u} - \operatorname{Div}\mathbf{P}\cdot\mathbf{u}\right)\,\mathrm{d}V \\ &+ \int_{\partial\mathcal{B}_{0\sigma}} \mathbf{u}\cdot(\mathbf{t}_0 - \bar{\mathbf{t}}_0)\,\mathrm{d}A - \int_{\partial\mathcal{B}_{0u}} \mathbf{t}_0\cdot(\mathbf{u}-\bar{\mathbf{u}})\,\mathrm{d}A \quad .\end{aligned} \tag{2.77}$$

The Hu-Washizu variational principle can be viewed as a generalization of the principle of virtual work. By invoking the stationary of (2.77) with respect to the three independent fields the Euler-Lagrange equations and the boundary conditions of Π,

$$\left.\begin{aligned}\operatorname{Div}\mathbf{P} + \mathbf{b}_0 &= \mathbf{0} \\ \mathbf{P} &= \frac{\partial\Psi(\mathbf{F})}{\mathbf{F}} \\ \mathbf{F} &= \operatorname{Grad}\mathbf{u}\end{aligned}\right\} \text{in } \mathcal{B}_0 \qquad \text{and} \qquad \begin{aligned}\mathbf{u} &= \bar{\mathbf{u}} \text{ on } \partial\mathcal{B}_{0u} \\ \mathbf{t}_0 = \mathbf{P}\mathbf{n}_0 &= \bar{\mathbf{t}}_0 \text{ on } \partial\mathcal{B}_{0\sigma}\end{aligned} \tag{2.78}$$

respectively, can be derived. The three Euler-Lagrange equations are the static equilibrium equation, a field equation that contains the strain-energy function and the geometric field equation. In a similar way, a modified version of the Hu-Washizu variational principle is used in the shell formulation developed in this work, which will be discussed in the following chapters.

Chapter 3

Nonlinear composite shell theory - the global model

In this chapter, the equations of a nonlinear shell model for fiber-reinforced composites, which is the basis for a nonlinear mixed finite shell element, will be presented. The model discussed here is based on the work of Gruttmann et al. [45–47, 71, 131]. It is called the global model in this work to differentiate it from the local addition to the model, which is the main subject of this thesis and will be discussed in chapter 4.

When using the shell model, the three-dimensional continuum is approximated by a two-dimensional reference surface and a director vector. A common assumption in shell theory is that the deformation in thickness direction is much smaller than the other strain measures and therefore can be neglected. It is further often assumed that originally plane cross sections remain plane during the deformation process. These assumptions are also made in the global shell model presented in this chapter, but they are given up to some extent in the local model introduced in chapter 4.

In this chapter, the term shell model applies to the global shell formulation presented. In the following sections, some of the definitions of continuum mechanics discussed in the preceding chapter will be adapted to the shell model. At first, the kinematics of the shell model is presented. Accounting for the special geometry of shell structures, the continuum mechanical assumptions described in chapter 2 are transformed into shell kinematics, leading to so-called shell strains. Thereafter, the stresses in the body are used to define shell stress resultants. The equilibrium equations of the shell are derived with the help of the principle of virtual work and a constitutive law for small strains is introduced. As mentioned in the preceding chapter, numerical simulations with the finite element method based on a three-field variational principle often yield excellent results. This chapter thus concludes by introducing such a mixed variational principle based on a Hu-Washizu principle adapted for shells.

3.1 Kinematics of the shell

In order to describe the kinematics of the shell some definitions regarding its geometry have to be made. Subsequently, the shell strains can be derived.

3.1.1 Geometry of the shell

The shell model is based on the choice of an arbitrary reference surface in the plane of the shell and a director vector that is perpendicular to the plane of the shell in the reference configuration, as illustrated in figure 3.1. To elucidate the notation used, a three-dimensional Euclidean space denoted by $\mathcal{B}_0$ and occupied by the shell in the reference configuration is introduced. The reference surface is denoted by Ω_0, while the boundary of the shell reference surface is denoted by Γ_0. The deformed shell space, its boundary and its reference surface are denoted by $\mathcal{B}_t$, Γ_t and Ω_t, respectively. Similar to the notation in the preceding chapter, in the following uppercase letters denote quantities in the reference configuration, while lowercase letters reside in the current configuration. It is assumed that the thickness of the shell is much smaller than the smallest curvature radius.

The Euclidean space is defined using a Cartesian coordinate system, where the base system is denoted by $\mathbf{e}_i$ and the convected coordinate system of the body by ξ^i, the index i running from 1 to 3. In the following, Latin indices run from 1 to 3, while Greek indices run from 1 to 2. Repeated indices underlie the sum convention. Although this does not generally have to be the case, the global Cartesian coordinate system is the same for the reference and the current configuration.

The position vector $\mathbf{\Phi}$ of an arbitrary point in the undeformed shell space $\mathcal{B}_0$ can be expressed by a combination of a position vector $\mathbf{X}$ of a point on the reference surface of the shell and a director vector $\mathbf{D}$, as illustrated in figure 3.1. Both vectors depend solely on the in-plane coordinates ξ^1 and ξ^2, so that

$$\mathbf{\Phi}(\xi^1, \xi^2, \xi^3) = \Phi^i \, \mathbf{e}_i = \mathbf{X}(\xi^1, \xi^2) + \xi^3 \, \mathbf{D}(\xi^1, \xi^2) \quad . \tag{3.1}$$

In an analogous manner, the position vector $\boldsymbol{\phi}$ of any point on the deformed shell space $\mathcal{B}_t$ can be expressed by

$$\boldsymbol{\phi}(\xi^1, \xi^2, \xi^3) = \phi^i \, \mathbf{e}_i = \mathbf{x}(\xi^1, \xi^2) + \xi^3 \, \mathbf{d}(\xi^1, \xi^2) \quad . \tag{3.2}$$

The vector $\mathbf{u}$ is introduced by

$$\mathbf{u}(\xi^1, \xi^2) = \mathbf{x}(\xi^1, \xi^2) - \mathbf{X}(\xi^1, \xi^2) \quad , \tag{3.3}$$

which describes the displacement of a point on the shell reference surface from the reference configuration to the current configuration and is illustrated in figure 3.2. With the displacement vector $\mathbf{u}$ three translational degrees of freedom are permitted for the shell, namely the three translations along the ξ^1-, ξ^2- and ξ^3-axis.

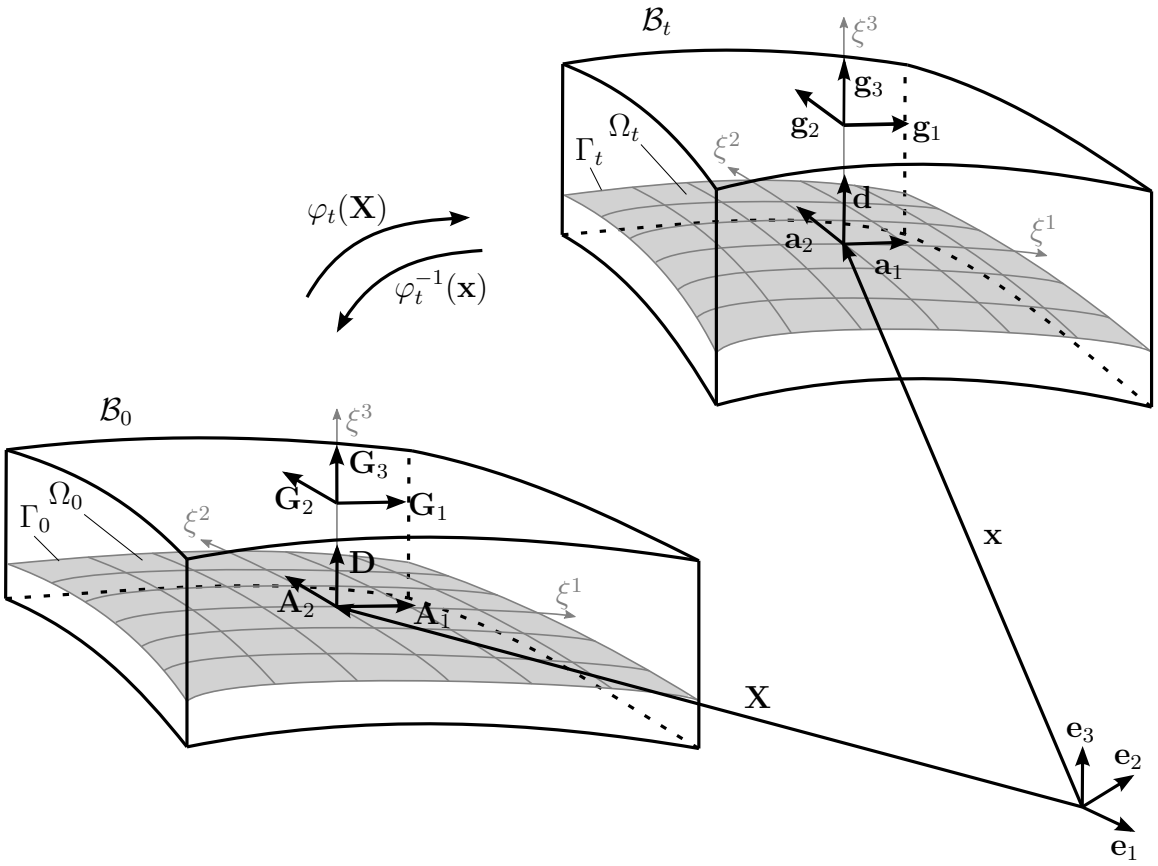

Figure 3.1: Model of the shell in the reference configuration and the current configuration

In (3.1), the symbol $\mathbf{D}(\xi^1, \xi^2)$ with $|\mathbf{D}(\xi^1, \xi^2)| = 1$ has been introduced to denote the aforementioned director vector in the reference configuration. By postulating $|\mathbf{d}(\xi^1, \xi^2)| = 1$ in (3.2) for the director vector in the current configuration, a change in the length of the director vector from the reference configuration to the current configuration is not permitted, representing inextensibility in thickness direction.

The director vector $\mathbf{d}(\xi^1, \xi^2)$ in the current configuration does not have to remain normal to the reference plane in the current configuration ($\mathbf{d} \cdot \mathbf{x}_{,\alpha} \neq 0$), so that the model allows for transverse shear strains, corresponding to a Reissner-Mindlin kinematic. For the finite element formulation, this means that the difficulties caused by C^1 requirements of the classical Kirchhoff theory are avoided [123, 136]. Here and in the following, the symbol $(\bullet)_{,i}$ denotes a partial derivative with respect to the coordinate ξ^i.

Before it is shown how the vector $\mathbf{d}$ can be derived, some further definitions have to be made. The coordinate systems $\mathbf{G}_i$ and $\mathbf{g}_i$ were already introduced as tangential vectors at coordinate lines that form a covariant base system in (2.3) for the continuum body. Here they represent covariant base systems, whose reference points lie in a certain material point of the shell. The covariant base vectors for the reference configuration can be derived from the partial derivatives of the position vectors $\mathbf{\Phi}$, so that

$$\mathbf{G}_\alpha = \frac{\partial \mathbf{\Phi}}{\partial \xi^\alpha} = \mathbf{X}_{,\alpha} + \xi^3 \, \mathbf{D}_{,\alpha} \qquad \text{and} \qquad \mathbf{G}_3 = \frac{\partial \mathbf{\Phi}}{\partial \xi^3} = \mathbf{D} \quad . \tag{3.4}$$

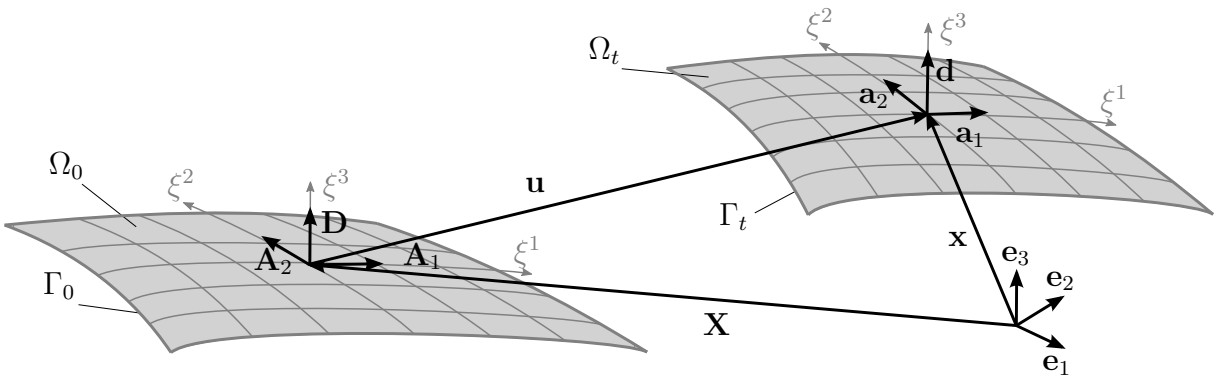

Figure 3.2: Shell reference surfaces and displacement vector $\mathbf{u}$

The covariant base vectors for the current configuration can be derived from the partial derivatives of the position vectors $\boldsymbol{\phi}$, leading to

$$\mathbf{g}_\alpha = \frac{\partial \boldsymbol{\phi}}{\partial \xi^\alpha} = \mathbf{x}_{,\alpha} + \xi^3 \, \mathbf{d}_{,\alpha} \qquad \text{and} \qquad \mathbf{g}_3 = \frac{\partial \boldsymbol{\phi}}{\partial \xi^3} = \mathbf{d} \quad . \tag{3.5}$$

The contravariant base vectors can be derived from (2.4). Additionally, the volume element can be specified by

$$\mathrm{d}V = \sqrt{G} \, \mathrm{d}\xi^1 \, \mathrm{d}\xi^2 \, \mathrm{d}\xi^3 \qquad \text{with} \qquad \sqrt{G} = (\mathbf{G}_1 \times \mathbf{G}_2) \cdot \mathbf{G}_3 \quad . \tag{3.6}$$

The vectors $\mathbf{A}_\alpha$ and $\mathbf{a}_\alpha$ are introduced to provide a space tangent to the shell reference surface, so that $\mathbf{A}_\alpha = \mathbf{G}_\alpha \, (\xi^\beta, \xi^3 = 0)$ and $\mathbf{a}_\alpha = \mathbf{g}_\alpha \, (\xi^\beta, \xi^3 = 0)$. The contravariant base vectors are given with $\mathbf{A}_\alpha \cdot \mathbf{A}^\beta = \delta_\alpha^\beta$ in the reference configuration and analogously in the current configuration. The area element is defined by

$$\mathrm{d}A = j \, \mathrm{d}\xi^1 \, \mathrm{d}\xi^2 \qquad \text{with} \qquad j = \sqrt{A} = |\mathbf{A}_1 \times \mathbf{A}_2| \quad , \tag{3.7}$$

where j denotes the mid-surface Jacobian. Perpendicular to the base vectors $\mathbf{A}_\alpha$ located in the shell reference surface, the director vector $\mathbf{D} = \mathbf{A}_3$ is defined as a unit vector. With the help of the shifter tensor $\mathbf{Z} = \mathbf{G}_i \otimes \mathbf{A}^i$ and $\bar{\mathbf{Z}} = \mathbf{g}_i \otimes \mathbf{a}^i$, the relationship between the base vectors $\mathbf{G}_i$ in the shell space and the base vectors $\mathbf{A}_i$ on the reference surface can be specified by

$$\mathbf{G}_i = \mathbf{Z}\mathbf{A}_i \qquad \text{and} \qquad \mathbf{g}_i = \bar{\mathbf{Z}}\mathbf{a}_i \quad . \tag{3.8}$$

The determinant $\bar{\mu} = \sqrt{G/A}$ of the shifter tensor is important for subsequent integrations over the volume, because

$$\frac{\mathrm{d}V}{\mathrm{d}A} = \frac{\sqrt{G} \, \mathrm{d}\xi^1 \, \mathrm{d}\xi^2 \, \mathrm{d}\xi^3}{\sqrt{A} \, \mathrm{d}\xi^1 \, \mathrm{d}\xi^2} = \bar{\mu} \, \mathrm{d}\xi^3 \quad . \tag{3.9}$$

In the context of the finite element formulation, numerical tests have shown that $\bar{\mu} = 1$ can be set for the whole finite shell element and convergence against the correct solution is given [47].

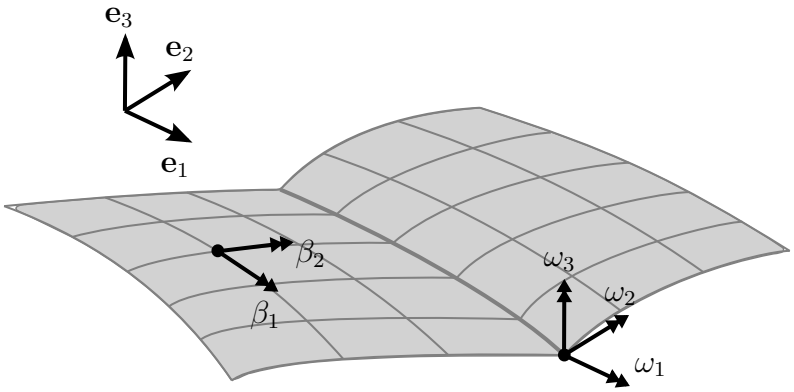

Figure 3.3: Shell model with intersection and rotational parameters

Having introduced the base vectors of the shell, the vector $\mathbf{d}$ can be obtained from $\mathbf{D}$ by means of an orthogonal transformation specified by

$$\mathbf{d} = \mathbf{R}\mathbf{D} = (\mathbf{a}_i \otimes \mathbf{A}_i)\mathbf{D} \quad . \tag{3.10}$$

In the same way the base vectors $\mathbf{a}_\alpha$ in the deformed state of the shell can be identified by a transformation of the base vectors $\mathbf{A}_\alpha$ in the undeformed state with the help of the transformation tensor $\mathbf{R}$. Different forms of the orthogonal tensor $\mathbf{R}$ in (3.10) can be given, for example by parametrizations with Euler angles, Cardan angles or quaternions. An overview is given in [23]. Here the Euler-Rodrigues formula, for example discussed in [5],

$$\mathbf{R} = \mathbf{a}_i \otimes \mathbf{A}_i = \mathbf{1} + \frac{\sin\omega}{\omega}\boldsymbol{\Omega} + \frac{1-\cos\omega}{\omega^2}\boldsymbol{\Omega}^2 \quad , \tag{3.11}$$

is used for the representation of the rotation tensor. A pseudo-rotation vector $\boldsymbol{\omega}$ with $\omega = |\boldsymbol{\omega}|$ containing the independent rotational parameters and a corresponding skew-symmetric tensor $\boldsymbol{\Omega}$ with $\boldsymbol{\omega} \times \mathbf{h} = \boldsymbol{\Omega}\mathbf{h}$ are introduced. The vector $\mathbf{h}$ can be any vector $\mathbf{h} \in R^3$. The vector $\boldsymbol{\omega}$ is defined as a vector describing a rotation about a unit axis multiplied with the angle of the rotation. Both $\boldsymbol{\omega}$ and $\boldsymbol{\Omega}$ contain rotational parameters and are specified by

$$\boldsymbol{\omega} = \begin{bmatrix} \omega_1 \\ \omega_2 \\ \omega_3 \end{bmatrix} \qquad \text{and} \qquad \boldsymbol{\Omega} = \begin{bmatrix} 0 & -\omega_3 & \omega_2 \\ \omega_3 & 0 & -\omega_1 \\ -\omega_2 & \omega_1 & 0 \end{bmatrix} \tag{3.12}$$

in matrix notation. The parameters ω_1, ω_2 and ω_3 in (3.12) are the rotational parameters with respect to the global coordinate system $\mathbf{e}_i$, so that

$$\boldsymbol{\omega} = \omega_i\, \mathbf{e}_i \quad . \tag{3.13}$$

With the pseudo-rotation vector $\boldsymbol{\omega}$, three additional rotational degrees of freedom are permitted for the shell, namely three rotations around the ξ^1-, ξ^2-, and ξ^3-axis. With the three translational degrees of freedom introduced by the displacement vector in (3.3), the

shell has six degrees of freedom. This is advantageous when thin-walled structures with intersections, illustrated in figure 3.3, are to be investigated. When the finite element method is applied, the three rotational degrees of freedom need to be available for nodes on shell intersections. Examples for such structures are box girders and double T-girders such as the ones examined in chapter 8.1.3. On the other hand, when the shell surface is smooth the local drilling degree of freedom perpendicular to the shell surface can be set to zero in the finite element formulation via boundary conditions. This will be further explained in chapter 3.3.1.

The chosen procedure is singularity-free for $\omega < 2\pi$, and a combination with multiplicative update procedures is possible, making it well-suited to be used in the transformation of the director vector.

3.1.2 Green-Lagrange strains and shell strains

When the shell is moved from $\mathcal{B}_0$ to $\mathcal{B}_t$ (figure 3.1), it undergoes a deformation process. To capture this process, some deformation magnitudes, analogous to chapter 2, are introduced. It was already shown in (2.8), how the deformation gradient $\mathbf{F}$ can be expressed by means of covariant base vectors, such as the ones introduced in (3.4) and (3.5) for the shell, and their contravariant counterparts. Using (3.8), the deformation gradient can be expressed with the shifter tensor, so that

$$\mathbf{g}_i = \mathbf{F}\mathbf{G}_i = \left(\bar{\mathbf{Z}}\hat{\mathbf{F}}\mathbf{Z}^{-1}\right)\mathbf{G}_i \qquad \text{and} \qquad \mathbf{F} = \bar{\mathbf{Z}}\hat{\mathbf{F}}\mathbf{Z}^{-1} \quad , \tag{3.14}$$

where $\hat{\mathbf{F}} = \mathbf{F}(\xi^3 = 0)$, and therefore $\hat{\mathbf{F}} = \mathbf{a}_i \otimes \mathbf{A}^i$ and $\mathbf{a}_i = \hat{\mathbf{F}}\mathbf{A}_i$.

Using the definition of the Green-Lagrange strain tensor for convective coordinates (2.17) the derivatives of the position vectors (3.4) can be used to derive the Green-Lagrange strain tensor for the shell, resulting in

$$\mathbf{E} = E_{ij}\mathbf{G}^i \otimes \mathbf{G}^j \qquad \text{with} \qquad E_{ij} = \frac{1}{2}\left(\boldsymbol{\phi}_{,i}\cdot\boldsymbol{\phi}_{,j} - \boldsymbol{\Phi}_{,i}\cdot\boldsymbol{\Phi}_{,j}\right) \quad . \tag{3.15}$$

The Green-Lagrange strains are thus derived from the difference between the squares of line elements in the deformed and the undeformed state. It is expedient to express the Green-Lagrange strains in terms of the base vectors $\mathbf{A}_i$ of the shell with the help of the shifter tensor by means of

$$\mathbf{E} = \mathbf{Z}^{-T}\hat{\mathbf{E}}\mathbf{Z}^{-1} \quad . \tag{3.16}$$

Here, the surface-related Green-Lagrange strain tensor $\hat{\mathbf{E}}$ is defined by

$$\hat{\mathbf{E}} = \hat{E}_{ij}\mathbf{A}^i \otimes \mathbf{A}^j = \left(\mathbf{E}^0 + \xi^3\mathbf{E}^1 + (\xi^3)^2\mathbf{E}^2\right) \quad , \tag{3.17}$$

where $\mathbf{E}^0$, $\mathbf{E}^1$ and $\mathbf{E}^2$ are defined as

$$\begin{aligned}
\mathbf{E}^0 &= E^0_{ij}\mathbf{A}^i \otimes \mathbf{A}^j = \varepsilon_{\alpha\beta}\mathbf{A}^\alpha \otimes \mathbf{A}^\beta + \frac{1}{2}\gamma_\alpha \left(\mathbf{A}^\alpha \otimes \mathbf{A}^3 + \mathbf{A}^3 \otimes \mathbf{A}^\alpha\right) \quad , \\
\mathbf{E}^1 &= E^1_{ij}\mathbf{A}^i \otimes \mathbf{A}^j = \kappa_{\alpha\beta}\mathbf{A}^\alpha \otimes \mathbf{A}^\beta \quad , \\
\mathbf{E}^2 &= E^2_{ij}\mathbf{A}^i \otimes \mathbf{A}^j = \rho_{\alpha\beta}\mathbf{A}^\alpha \otimes \mathbf{A}^\beta \quad .
\end{aligned} \tag{3.18}$$

In (3.18), the shell membrane strains $\varepsilon_{\alpha\beta}$, curvatures $\kappa_{\alpha\beta}$, shear strains γ_α, and second order curvatures $\rho_{\alpha\beta}$ have been introduced with

$$\begin{aligned}
\varepsilon_{\alpha\beta} &= \frac{1}{2}\left(\mathbf{x}_{,\alpha}\cdot\mathbf{x}_{,\beta} - \mathbf{X}_{,\alpha}\cdot\mathbf{X}_{,\beta}\right) \quad , \\
\kappa_{\alpha\beta} &= \frac{1}{2}\left(\mathbf{x}_{,\alpha}\cdot\mathbf{d}_{,\beta} + \mathbf{x}_{,\beta}\cdot\mathbf{d}_{,\alpha} - \mathbf{X}_{,\alpha}\cdot\mathbf{D}_{,\beta} - \mathbf{X}_{,\beta}\cdot\mathbf{D}_{,\alpha}\right) \quad , \\
\gamma_\alpha &= \mathbf{x}_{,\alpha}\cdot\mathbf{d} - \mathbf{X}_{,\alpha}\cdot\mathbf{D} \quad , \\
\rho_{\alpha\beta} &= \frac{1}{2}\left(\mathbf{d}_{,\alpha}\cdot\mathbf{d}_{,\beta} - \mathbf{D}_{,\alpha}\cdot\mathbf{D}_{,\beta}\right) \quad .
\end{aligned} \tag{3.19}$$

Because of the inextensibility condition $|\mathbf{D}| = |\mathbf{d}| = 1$, the terms $\mathbf{D}_{,\alpha}\cdot\mathbf{D}$, $\mathbf{d}_{,\alpha}\cdot\mathbf{d}$ and $(\mathbf{d}\cdot\mathbf{d} - \mathbf{D}\cdot\mathbf{D})$ vanish. The second order curvatures $\rho_{\alpha\beta}$ can be neglected for thin shells. It is pointed out that with the transverse shear strains emanating from the Reissner-Mindlin theory, standard patch tests are not passed in the context of a finite element formulation [45]. For this reason, the shear strains are approximated with independent interpolation functions as described in chapter 5.1.1.

For a simpler notation, the components of the Green-Lagrange strains are collected in a vector denoted $\bar{\mathbf{E}}$,

$$\bar{\mathbf{E}} = \left[E_{11}, E_{22}, E_{33}, 2E_{12}, 2E_{13}, 2E_{23}\right]^T \quad , \tag{3.20}$$

and the components of the shell strains in a vector denoted $\boldsymbol{\varepsilon}$,

$$\boldsymbol{\varepsilon} = \left[\varepsilon_{11}, \varepsilon_{22}, 2\varepsilon_{12}, \kappa_{11}, \kappa_{22}, 2\kappa_{12}, \gamma_1, \gamma_2\right]^T \quad . \tag{3.21}$$

The relation between the Green-Lagrange strains and the shell strains is given with the help of the assembly matrix $\mathbf{A}$ by means of

$$\bar{\mathbf{E}} = \mathbf{A}\boldsymbol{\varepsilon} \qquad \text{or} \qquad \begin{bmatrix} E_{11} \\ E_{22} \\ E_{33} \\ 2E_{12} \\ 2E_{13} \\ 2E_{23} \end{bmatrix} = \begin{bmatrix} 1 & 0 & 0 & \xi^3 & 0 & 0 & 0 & 0 \\ 0 & 1 & 0 & 0 & \xi^3 & 0 & 0 & 0 \\ 0 & 0 & 0 & 0 & 0 & 0 & 0 & 0 \\ 0 & 0 & 1 & 0 & 0 & \xi^3 & 0 & 0 \\ 0 & 0 & 0 & 0 & 0 & 0 & 1 & 0 \\ 0 & 0 & 0 & 0 & 0 & 0 & 0 & 1 \end{bmatrix} \begin{bmatrix} \varepsilon_{11} \\ \varepsilon_{22} \\ 2\varepsilon_{12} \\ \kappa_{11} \\ \kappa_{22} \\ 2\kappa_{12} \\ \gamma_1 \\ \gamma_2 \end{bmatrix} \quad . \tag{3.22}$$

It is important to point out that due to the assumptions in shell theory, the normal strain E_{33} equals zero, which is why the third row in $\mathbf{A}$ contains only zeros. Nevertheless, it has been included because an interface to a three-dimensional material law is to be provided by the shell formulation. A procedure of how to incorporate nonlinear three-dimensional constitutive equations without modifying (3.22) by including independent thickness strains is proposed in [71]. A different procedure will be discussed in chapter 4 with the introduction of the local part of the shell model. It is pointed out that the definition of the assembly matrix $\mathbf{A}$ can be adapted if E_{33} is not to be considered, for example if the constitutive law is based on the assumption of plane stress, as it is done in [47].

3.2 Second Piola-Kirchhoff stresses, stress resultants

The work conjugated tensor to the Green-Lagrange strain tensor $\mathbf{E}$, the second Piola-Kirchhoff stress tensor $\mathbf{S}$ introduced in (2.22), can be expressed in terms of the covariant base vectors of the shell (3.4) by means of (2.23). Similar to the Green-Lagrange strain tensor in (3.16) and (3.17), the second Piola-Kirchhoff stress tensor can be expressed with help of the shifter tensor and the surface-related tensor $\hat{\mathbf{S}}$, so that

$$\mathbf{S} = \mathbf{Z}\hat{\mathbf{S}}\mathbf{Z}^T \qquad \text{with} \qquad \hat{\mathbf{S}} = S^{ij}\mathbf{A}_i \otimes \mathbf{A}_j \quad . \tag{3.23}$$

Based on the work presented in [110], the stress resultant $\mathbf{n}^\alpha$ and the stress couple resultant $\mathbf{m}^\alpha$ are defined by

$$\mathbf{n}^\alpha = \int_{h^-}^{h^+} \mathbf{T}\mathbf{g}^\alpha \bar{\mu}\, \mathrm{d}\xi^3 \qquad \text{and} \qquad \mathbf{m}^\alpha = \mathbf{d} \times \tilde{\mathbf{m}}^\alpha = \mathbf{d} \times \int_{h^-}^{h^+} \mathbf{T}\mathbf{g}^\alpha \xi^3 \bar{\mu}\, \mathrm{d}\xi^3 \quad , \tag{3.24}$$

where here and in the following, the bottom and the top of the shell, as illustrated in figure 3.6, are denoted by h^- and h^+, $\mathbf{T}$ denotes the Cauchy stress tensor defined in (2.19) and $\tilde{\mathbf{m}}^\alpha$ denotes the director stress couple resultant. Further, the across-the-thickness stress resultant $\mathbf{q}$ is defined by

$$\mathbf{q} = \int_{h^-}^{h^+} \mathbf{T}\mathbf{g}^3 \bar{\mu}\, \mathrm{d}\xi^3 \quad . \tag{3.25}$$

Dividing the stress resultant $\mathbf{n}^\alpha$ and the director stress couple resultant $\tilde{\mathbf{m}}^\alpha$ into components along $\mathbf{x}_{,\alpha}$ and $\mathbf{d}$ yields[3]

$$\mathbf{n}^\alpha = n^{\beta\alpha}\mathbf{x}_{,\beta} + q^\alpha \mathbf{d} \qquad \text{and} \qquad \tilde{\mathbf{m}}^\alpha = \tilde{m}^{\beta\alpha}\mathbf{x}_{,\beta} \quad . \tag{3.26}$$

[3] In [110], the component of $\mathbf{m}^\alpha$ along $\mathbf{d}$ denoted $\tilde{m}^{3\alpha}$ is included in the definition of the director stress couple resultant. However, it does not enter the subsequent formulations explicitly and in the same publication, a suggestion is made how it can be eliminated. A separation of $\mathbf{q}$ into components along $\mathbf{x}_{,\alpha}$ and $\mathbf{d}$ is likewise carried out in [110].

In (3.26), the components $\tilde{m}^{\beta\alpha}$ are the effective stress couple resultants. They are part of the work conjugate vector to the vector of shell strains $\boldsymbol{\varepsilon}$ (3.21), which is the effective stress resultant vector denoted $\boldsymbol{\sigma}$ (3.32). It also contains the effective membrane stress resultants $\tilde{n}^{\beta\alpha}$ and the effective shear stress resultants $\tilde{q}^{\alpha}$, which can be established with the help of the stress power defined in (2.33), and thus

$$\dot{W} = \mathcal{P}_{\text{int}} = \int_{\mathcal{B}_0} \text{tr}\left(\dot{\mathbf{E}}\mathbf{S}^T\right) \, \text{d}V \quad . \tag{3.27}$$

The shifted quantities in terms of the reference surface defined in (3.17) and (3.23) can be used to express (3.27) and therefore with (3.9),

$$\dot{W} = \mathcal{P}_{\text{int}} = \int_{\mathcal{B}_0} \text{tr}\left[\left(\dot{\mathbf{E}}^0 + \xi^3\dot{\mathbf{E}}^1\right)\hat{\mathbf{S}}\right] \bar{\mu} \, \text{d}\xi^3 \, \text{d}A \tag{3.28}$$

holds. Inserting (3.23) leads to the definition of the stress resultant tensors

$$\begin{aligned}
\tilde{\mathbf{N}} &= \int_{h^-}^{h^+} S^{\alpha\beta}\bar{\mu} \, \text{d}\xi^3 \mathbf{A}_\alpha \otimes \mathbf{A}_\beta = \tilde{n}^{\alpha\beta}\mathbf{A}_\alpha \otimes \mathbf{A}_\beta \quad , \\
\tilde{\mathbf{Q}} &= \int_{h^-}^{h^+} S^{\alpha 3}\bar{\mu} \, \text{d}\xi^3 \mathbf{A}_\alpha = \tilde{q}^{\alpha}\mathbf{A}_\alpha \quad , \\
\tilde{\mathbf{M}} &= \int_{h^-}^{h^+} S^{\alpha\beta}\xi^3\bar{\mu} \, \text{d}\xi^3 \mathbf{A}_\alpha \otimes \mathbf{A}_\beta = \tilde{m}^{\alpha\beta}\mathbf{A}_\alpha \otimes \mathbf{A}_\beta \quad .
\end{aligned} \tag{3.29}$$

The stress resultant $\mathbf{n}^\alpha$ can be expressed with the effective membrane stress resultants $\tilde{n}^{\beta\alpha}$ and the effective shear stress resultants $\tilde{q}^{\alpha}$ as components of the vectors $\mathbf{x}_{,\alpha}$, $\mathbf{d}$ and $\mathbf{d}_{,\alpha}$ by means of

$$\mathbf{n}^\alpha = \tilde{n}^{\beta\alpha}\mathbf{x}_{,\beta} + \tilde{q}^{\alpha}\mathbf{d} + \tilde{m}^{\beta\alpha}\mathbf{d}_{,\beta} \quad . \tag{3.30}$$

The components of the stress resultant $\mathbf{n}^\alpha$ in (3.26 a) can be expressed with the help of the effective stress resultants. To accomplish this, the vectors $\mathbf{d}_{,\alpha}$ must be represented as linear combinations of the vectors $\mathbf{x}_{,\alpha}$ and $\mathbf{d}$ considering $\mathbf{a}^i \cdot \mathbf{a}_j = \delta^i_j$, $\mathbf{a}_\alpha = \mathbf{x}_{,\alpha}$ and $\mathbf{a}_3 = \mathbf{d}$ and introducing $b^j_\alpha = \mathbf{d}_{,\alpha} \cdot \mathbf{a}^j$, and thus,

$$n^{\beta\alpha} = \tilde{n}^{\beta\alpha} + \tilde{m}^{\alpha\gamma}b^\beta_\gamma \qquad \text{and} \qquad q^\alpha = \tilde{q}^\alpha + \tilde{m}^{\alpha\gamma}b^3_\gamma \tag{3.31}$$

hold. It is noted that $\tilde{n}^{12} = \tilde{n}^{21}$, but $n^{12} \neq n^{21}$.

To simplify the notation, the components of the second Piola-Kirchhoff stresses are collected in a vector denoted $\bar{\mathbf{S}}$,

$$\bar{\mathbf{S}} = \left[S^{11}, S^{22}, S^{33}, S^{12}, S^{13}, S^{23}\right]^T \quad , \tag{3.32}$$

and the components of the effective shell stress resultants in a vector denoted $\boldsymbol{\sigma}$,

$$\boldsymbol{\sigma} = \left[\tilde{n}^{11}, \tilde{n}^{22}, \tilde{n}^{12}, \tilde{m}^{11}, \tilde{m}^{22}, \tilde{m}^{12}, \tilde{q}^{1}, \tilde{q}^{2}\right]^{T} \quad . \tag{3.33}$$

The relation between the vector of the second Piola-Kirchhoff stresses $\bar{\mathbf{S}}$ and the effective shell stress resultants $\boldsymbol{\sigma}$ can be given in matrix notation with the help of the assembly matrix $\mathbf{A}$ (3.22) by means of

$$\boldsymbol{\sigma} = \frac{\partial \hat{\Psi}(\boldsymbol{\varepsilon})}{\partial \boldsymbol{\varepsilon}} = \int_{h^-}^{h^+} \mathbf{A}^T \bar{\mathbf{S}} \bar{\mu} \, \mathrm{d}\xi^3 \quad , \tag{3.34}$$

where $\hat{\Psi}(\boldsymbol{\varepsilon})$ has been introduced as an arbitrary strain-energy function of the shell strains, which is further defined in (3.78).

It is important to note that since the effective stress resultants are integrals of the components of the second Piola-Kirchhoff stress tensor $\mathbf{S}$, they have no physical meaning. Analogous to the explanation given at the end of chapter 3.1.2, the interlaminar normal stress S_{33} has been included allowing the employment of three-dimensional material laws, which will be discussed in chapter 4.

3.3 Equilibrium equations

In this section, the resultant form of the equilibrium equations is derived from the principle of virtual work. In order to do so, the variation of the shell strains $\delta\boldsymbol{\varepsilon}$ and the variation of the orthogonal transformation need to be determined.

3.3.1 Variation of the shell strains

The variation of the shell strains $\delta\boldsymbol{\varepsilon}$ can be derived by applying the directional derivative in a standard way, so that

$$\begin{aligned}
\delta\varepsilon_{\alpha\beta} &= \frac{1}{2}\left(\delta\mathbf{x}_{,\alpha}\cdot\mathbf{x}_{,\beta} + \delta\mathbf{x}_{,\beta}\cdot\mathbf{x}_{,\alpha}\right) \quad , \\
\delta\kappa_{\alpha\beta} &= \frac{1}{2}\left(\delta\mathbf{x}_{,\alpha}\cdot\mathbf{d}_{,\beta} + \delta\mathbf{x}_{,\beta}\cdot\mathbf{d}_{,\alpha} + \delta\mathbf{d}_{,\alpha}\cdot\mathbf{x}_{,\beta} + \delta\mathbf{d}_{,\beta}\cdot\mathbf{x}_{,\alpha}\right) \quad , \\
\delta\gamma_{\alpha} &= \delta\mathbf{x}_{,\alpha}\cdot\mathbf{d} + \delta\mathbf{d}\cdot\mathbf{x}_{,\alpha} \quad ,
\end{aligned} \tag{3.35}$$

with the variation of the membrane strains $\delta\varepsilon_{\alpha\beta}$, the variation of the curvatures $\delta\kappa_{\alpha\beta}$ and the variation of the transverse shear strains $\delta\gamma_{\alpha}$. The variations of the shell strains are collected in a vector denoted $\delta\boldsymbol{\varepsilon}$ analogous to (3.21). Because, as already pointed out, the shear strains are approximated with independent interpolation functions in the

finite element formulation, the variation of the assumed strain interpolation needs to be determined, which will be done in chapter 5.

The variation of the director vector $\delta\mathbf{d}$ and the variation of the axial vector $\delta\mathbf{w}$, which is associated with the skew symmetric tensor $\delta\mathbf{R}\mathbf{R}^T$, are derived to be

$$\delta\mathbf{d} = \delta\mathbf{R}\mathbf{D} = \delta\mathbf{R}\mathbf{R}^T\mathbf{d} = \delta\mathbf{w} \times \mathbf{d} \qquad \text{and} \qquad \delta\mathbf{w} = \mathbf{H}\delta\boldsymbol{\omega} \quad , \tag{3.36}$$

respectively. Hereby, (3.10), (3.11) and (3.12), as well as the definitions

$$\mathbf{H} = \mathbf{1} + c_1\boldsymbol{\Omega} + c_2\boldsymbol{\Omega}^2 \quad , \qquad c_1 = \frac{1-\cos\omega}{\omega^2} \qquad \text{and} \qquad c_2 = \frac{\omega - \sin\omega}{\omega^3} \tag{3.37}$$

are used. For scalar products of the form $\mathbf{h}\cdot\delta\mathbf{d}$, where $\mathbf{h}$ can be any vector $\mathbf{h} \in R^3$, which occur in (3.35),

$$\mathbf{h}\cdot\delta\mathbf{d} = (\mathbf{d}\times\mathbf{h})\cdot\delta\mathbf{w} \tag{3.38}$$

holds. An alternative notation for the variation of the director vector $\delta\mathbf{d}$ (3.36) for later reference when discussing the finite element approximation is introduced by defining

$$\delta\mathbf{d} = \delta\mathbf{w}\times\mathbf{d} = \mathbf{W}^T\delta\mathbf{w} \qquad \text{with} \qquad \mathbf{W} = \operatorname{skew}\mathbf{d} \quad . \tag{3.39}$$

As was already mentioned, if the shell surface is smooth, the local drilling degree of freedom can be set to zero (see figure 3.3). For this purpose, the variation of the pseudo-rotation vector is expressed with the help of the base vectors $\mathbf{a}_i$. The variations of the rotational parameters corresponding to the bases system $\mathbf{a}_i$ are denoted with $\delta\beta_i$. Thus, if the shell is smooth, the pseudo-rotation vector can also be expressed by

$$\boldsymbol{\omega} = \delta\beta_i\mathbf{a}_i = \delta\beta_\alpha\mathbf{a}_\alpha \quad . \tag{3.40}$$

If the shell surface is smooth, the shell therefore has five degrees of freedom, three translations and two rotations.

The variation of the rotational parameters collected in $\delta\boldsymbol{\omega}$ related to the global coordinate system can thus be derived by means of

$$\delta\boldsymbol{\omega} = \bar{\mathbf{T}}\delta\boldsymbol{\beta} \quad , \tag{3.41}$$

where the transformation matrix denoted by $\bar{\mathbf{T}}$ is defined by

$$\bar{\mathbf{T}} = \begin{cases} \mathbf{1}_3 & \text{for positions on shell intersections} \\ [\mathbf{a}_1, \mathbf{a}_2]_{(3x2)} & \text{for all other positions} \quad , \end{cases} \tag{3.42}$$

with $\mathbf{1}_3$ denoting the 3x3 unit-matrix. Additionally, the vector $\delta\boldsymbol{\beta}$ is defined as

$$\delta\boldsymbol{\beta} = \begin{cases} [\delta\omega_1, \delta\omega_2, \delta\omega_3] & \text{for positions on shell intersections} \\ [\delta\beta_1, \delta\beta_2] & \text{for all other positions} \quad , \end{cases} \tag{3.43}$$

in which the variation of the rotational parameters are collected. By means of (3.36), (3.37) and (3.41), relation (3.39) can thus be rewritten as

$$\delta \mathbf{d} = \mathbf{W}^T \mathbf{H} \bar{\mathbf{T}} \delta \boldsymbol{\beta} \quad . \tag{3.44}$$

The variation of the base vectors $\mathbf{a}_\alpha$ in the deformed state of the shell can be performed in the same way.

3.3.2 Principle of virtual work

In this section, the principle of virtual work (2.69) introduced in chapter 2.6 will be adapted to the shell model, which yields the resultant form of the equilibrium equations for the shell. To derive the internal virtual work, a strain-energy function $\Psi(\mathbf{C})$, introduced in (2.57), for a transversely isotropic material is employed. The second argument of Ψ, $\mathbf{a}_0 \otimes \mathbf{a}_0$, is dropped in this chapter and the following chapters to simplify the notation. Considering (2.70) with (2.72) the internal virtual work of the shell is defined as the integration over the shell body of the variation of the strain-energy function, so that

$$\delta W_{\text{int}} = \int_{\mathcal{B}_0} \delta \Psi(\mathbf{C}) \, \mathrm{d}V \quad . \tag{3.45}$$

From (2.15), $\delta \mathbf{C} = 2\delta \mathbf{E}$ is obvious and with (2.48 b), the variation of Ψ yields

$$\delta \Psi(\mathbf{C}) = 2\delta \mathbf{E} : \frac{\partial \Psi(\mathbf{C})}{\partial \mathbf{C}} = \delta \mathbf{E} : \mathbf{S} \quad , \tag{3.46}$$

so that, corresponding to (2.67), the internal virtual work in terms of the Green-Lagrange strains $\mathbf{E}$ and the second Piola-Kirchhoff stresses $\mathbf{S}$ can be given by

$$\delta W_{\text{int}} = \int_{\mathcal{B}_0} \delta \mathbf{E} : \mathbf{S} \, \mathrm{d}V \quad . \tag{3.47}$$

Similar to (3.28), the shifted quantities in terms of the reference surface can be used to express (3.47) with (3.7) and (3.9) , so that

$$\begin{aligned} \delta W_{\text{int}} &= \int_{\Omega_0} \int_{h^-}^{h^+} \operatorname{tr}\left[\left(\delta \mathbf{E}^0 + \xi^3 \delta \mathbf{E}^1 \right) \hat{\mathbf{S}} \right] \bar{\mu} \, \mathrm{d}\xi^3 \, \mathrm{d}A \\ &= \int_{\Omega_0} \left(\tilde{n}^{\alpha\beta} \delta \varepsilon_{\alpha\beta} + \tilde{m}^{\alpha\beta} \delta \kappa_{\alpha\beta} + \tilde{q}^{\alpha} \delta \gamma_{\alpha} \right) \mathrm{d}A \quad . \end{aligned} \tag{3.48}$$

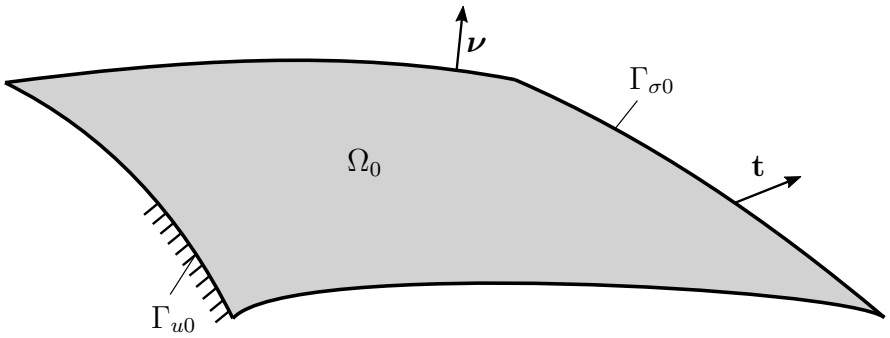

Figure 3.4: Boundary conditions and normal vector $\boldsymbol{\nu}$

In matrix notation, (3.47) can be expressed by

$$\delta W_{\text{int}} = \int_{\mathcal{B}_0} \delta\bar{\mathbf{E}}^T \bar{\mathbf{S}} \, \mathrm{d}V = \int_{\Omega_0} \delta\boldsymbol{\varepsilon}^T \int_{h^-}^{h^+} \mathbf{A}^T \bar{\mathbf{S}} \bar{\mu} \, \mathrm{d}\xi^3 \, \mathrm{d}A \quad . \tag{3.49}$$

Thus, the internal virtual work can be expressed in terms of the effective stress resultants $\boldsymbol{\sigma}$, so that

$$\delta W_{\text{int}} = \int_{\Omega_0} \delta\boldsymbol{\varepsilon}^T \boldsymbol{\sigma} \, \mathrm{d}A = \int_{\Omega_0} \delta\boldsymbol{\varepsilon}^T \frac{\partial \hat{\Psi}(\boldsymbol{\varepsilon})}{\partial \boldsymbol{\varepsilon}} \, \mathrm{d}A \tag{3.50}$$

holds. With (3.35) and the use of some mathematical relations, the internal virtual work can be expressed in terms of the stress resultant $\mathbf{n}^\alpha$ and the stress couple resultant $\mathbf{m}^\alpha$ (3.24) with

$$\delta W_{\text{int}} = \int_{\Omega_0} \left(\mathbf{n}^\alpha \cdot \delta\mathbf{x}_{,\alpha} + \tilde{q}^\alpha \mathbf{x}_{,\alpha} \cdot \delta\mathbf{d} + \tilde{\mathbf{m}}^\alpha \cdot \delta\mathbf{d}_{,\alpha} \right) \mathrm{d}A \quad . \tag{3.51}$$

Similar to the approach described in chapter 2.6 for the continuum body, the boundary of the shell Γ_0 is separated into the boundary Γ_{u0} and the boundary surface $\Gamma_{\sigma 0}$. Admissible variations must meet the kinematic boundary conditions and fulfill the requirements $\delta\mathbf{x} = \delta\mathbf{u} = 0$ and $\delta\mathbf{d} = 0$ on Γ_{u0}. By means of integration by parts and (3.24) the internal virtual work can be expressed by

$$\begin{aligned} \delta W_{\text{int}} = &- \int_{\Omega_0} \left[\frac{1}{j} \left(j\mathbf{n}^\alpha \right)_{,\alpha} \cdot \delta\mathbf{u} + \left(\frac{1}{j} \left(j\mathbf{m}^\alpha \right)_{,\alpha} + \mathbf{x}_{,\alpha} \times \mathbf{n}^\alpha \right) \cdot \delta\mathbf{w} \right] \mathrm{d}A \\ &+ \int_{\Gamma_{\sigma 0}} \left[\left(j\mathbf{n}^\alpha \nu_\alpha \right) \cdot \delta\mathbf{u} + \left(j\mathbf{m}^\alpha \nu_\alpha \right) \cdot \delta\mathbf{w} \right] \mathrm{d}s \quad , \end{aligned} \tag{3.52}$$

where the vector $\boldsymbol{\nu} = [\nu_1, \nu_2]^T$ denotes the normal vector on the shell boundary (see figure 3.4) and $\mathrm{d}s$ denotes the line increment of the shell boundary.

The external virtual work[4] δW_{ext} performed by the surface loads $\bar{\mathbf{p}}$ acting on the shell reference surface Ω_0 and the boundary loads $\bar{\mathbf{t}}$ acting on the shell boundary $\Gamma_{\sigma 0}$ can be expressed by

$$\delta W_{\text{ext}} = \int_{\Omega_0} \bar{\mathbf{p}} \cdot \delta \mathbf{u} \, \mathrm{d}A + \int_{\Gamma_{\sigma 0}} \bar{\mathbf{t}} \cdot \delta \mathbf{u} \, \mathrm{d}s \quad . \tag{3.53}$$

The kinematic boundary conditions $\mathbf{u} = \bar{\mathbf{u}}$ on Γ_{u0} with the prescribed displacements $\bar{\mathbf{u}}$ are fulfilled as constraints through the choice of the variational field $\delta\mathbf{u}$. The static boundary condition $\mathbf{t} = \bar{\mathbf{t}}$ must be fulfilled on $\Gamma_{\sigma 0}$ and is part of the variational formulation. Based on (2.69), the principle of virtual work for the shell in the static case becomes

$$g\left(\tilde{\mathbf{v}}, \delta\tilde{\mathbf{v}}\right) = \delta W_{\text{int}} - \delta W_{\text{ext}} = 0 \quad , \tag{3.54}$$

with $\tilde{\mathbf{v}} = [\mathbf{u}, \boldsymbol{\omega}]^T$. Inserting (3.52) and (3.53) into (3.54),

$$\begin{aligned} g\left(\tilde{\mathbf{v}}, \delta\tilde{\mathbf{v}}\right) = & \int_{\Omega_0} \left[\left(\frac{1}{j} \left(j\mathbf{n}^\alpha\right)_{,\alpha} + \bar{\mathbf{p}} \right) \cdot \delta\mathbf{u} + \left(\frac{1}{j} \left(j\mathbf{m}^\alpha\right)_{,\alpha} + \mathbf{x}_{,\alpha} \times \mathbf{n}^\alpha \right) \cdot \delta\mathbf{w} \right] \mathrm{d}A \\ & + \int_{\Gamma_{\sigma 0}} \left[\left(j\mathbf{n}^\alpha \nu_\alpha - \bar{\mathbf{t}}\right) \cdot \delta\mathbf{u} + \left(j\mathbf{m}^\alpha \nu_\alpha\right) \cdot \delta\mathbf{w} \right] \mathrm{d}s \end{aligned} \tag{3.55}$$

holds. Applying the fundamental lemma of variational calculus to (3.55) yields the static equilibrium equations, which in this case are the resultant form of the balance of linear and angular momentum, and the static boundary equations, specified by

$$\left.\begin{aligned} \frac{1}{j}\left(j\mathbf{n}^\alpha\right)_{,\alpha} + \bar{\mathbf{p}} &= \mathbf{0} \\ \frac{1}{j}\left(j\mathbf{m}^\alpha\right)_{,\alpha} + \mathbf{x}_{,\alpha} \times \mathbf{n}^\alpha &= \mathbf{0} \end{aligned}\right\} \text{ in } \Omega_0 \qquad \text{and} \qquad \left.\begin{aligned} j\left(\mathbf{n}^\alpha \nu_\alpha\right) - \bar{\mathbf{t}} &= \mathbf{0} \\ j\left(\mathbf{m}^\alpha \nu_\alpha\right) &= \mathbf{0} \end{aligned}\right\} \text{ on } \Gamma_{\sigma 0} \quad , \tag{3.56}$$

respectively[5]. As already mentioned, requiring admissible variations to meet the kinematic boundary conditions on Γ_{u0} leads to their implicit fulfillment and they therefore do not appear in the weak form.

3.4 Linear elastic constitutive law for fiber-reinforced composites

In chapter 2.5, it was shown how constitutive laws that establish the connection between stresses and strains can be constructed based on the second law of thermodynamics and

[4] In this work the contribution to the external virtual work is restricted to surface loads acting on the shell surface and prescribed forces acting on the shell boundary, while external couples acting on the shell surface and prescribed torques acting on the shell boundary are excluded.

[5] Alternatively, the balance equations can be derived from the three-dimensional integral balance laws. A concise discussion is given in [110] and a review in the context of Cosserat surfaces in [86].

the concept of the strain-energy function Ψ. Hence, a phenomenological approach is taken to describe the material's macroscopic behavior. For fiber-reinforced composites, the phenomenological approach to fit mathematical equations to experimental data has proven to be efficient in modeling the material behavior, but it is incapable of describing the microscopic structure and therefore fails to accurately represent the mechanism of deformation. An alternative approach is to consider microscopic properties of the material and to describe the interaction of fiber and matrix. These considerations are then used to derive material constants by means of a homogenization procedure [39][6].

In the following the assumption is made that even though the rotations can be large, the body undergoes only small strains[7]. This leads to a linear elastic constitutive law, where the strain-energy is a quadratic function of the strains. In connection with isotropic material behavior, this material model is often called the Saint-Venant Kirchhoff material law [124]. The simplest definition of such a strain-energy function is

$$\Psi = \frac{1}{2}\mathbf{E}^T : \mathbb{C} : \mathbf{E} \quad . \tag{3.57}$$

In (2.60), the strain-energy function for anisotropic materials was introduced as a function of five invariants based on the representation theorem for invariants. A definition of the strain-energy function that depends on the Green-Lagrange strain tensor $\mathbf{E}$ (2.46) and is valid for transversely isotropic materials and small strains is introduced as a function of the five invariants of $\mathbf{E}$ and $\mathbf{a}_0$ by means of

$$\begin{aligned} \Psi(\mathbf{E}) =& \frac{1}{2}\lambda\left(\mathrm{tr}\mathbf{E}\right)^2 + \mu_T \mathrm{tr}\left(\mathbf{E}^2\right) + \alpha\left(\mathbf{a}_0 \cdot \mathbf{E}\mathbf{a}_0\right)\mathrm{tr}\mathbf{E} \\ &+ 2\left(\mu_L - \mu_T\right)\left(\mathbf{a}_0 \cdot \mathbf{E}^2\mathbf{a}_0\right) + \frac{1}{2}\beta\left(\mathbf{a}_0 \cdot \mathbf{E}\mathbf{a}_0\right)^2 \quad , \end{aligned} \tag{3.58}$$

where λ, μ_T, μ_L, α and β are elasticity constants. The strain-energy function (3.58) is based on an extension of the small strain theory to the case of finite deformations and is not constructed as a polyconvex strain-energy function [102]. It is valid for strains of up to about five percent [39]. Considering (2.48), the constitutive law that furnishes the relation between the Green-Lagrange strains and the second Piola-Kirchhoff stresses is derived from the strain-energy function (3.58), and thus

$$\begin{aligned} \mathbf{S} = \frac{\partial \Psi(\mathbf{E})}{\partial \mathbf{E}} =& \lambda \mathrm{tr}\mathbf{E}\mathbf{1} + 2\mu_T\mathbf{E} + \alpha\left[\mathrm{tr}\mathbf{E}\left(\mathbf{a}_0 \otimes \mathbf{a}_0\right) + \left(\mathbf{a}_0 \cdot \mathbf{E}\mathbf{a}_0\right)\mathbf{1}\right] \\ &+ 2\left(\mu_L - \mu_T\right)\left(\mathbf{a}_0 \otimes \mathbf{E}\mathbf{a}_0 + \mathbf{E}\mathbf{a}_0 \otimes \mathbf{a}_0\right) \\ &+ \beta\left(\mathbf{a}_0 \cdot \mathbf{E}\mathbf{a}_0\right)\left(\mathbf{a}_0 \otimes \mathbf{a}_0\right) \quad . \end{aligned} \tag{3.59}$$

The linearized constitutive equation needs to be derived when employing iterative solution techniques of Newton's type. For linear elasticity, this yields the elasticity tensor $\mathbb{C}$, and,

[6] More information regarding the homogenization procedure is given in [2, 31, 74, 125].

[7] Further information on constitutive laws considering small elastic strains for transversely isotropic materials is provided in [31, 52, 61, 125].

analogous to (2.63), it can be specified by

$$\begin{aligned}\mathbb{C} = \frac{\partial^2 \Psi(\mathbf{E})}{\partial \mathbf{E} \partial \mathbf{E}} =& \lambda \mathbf{1} \otimes \mathbf{1} + 2\mu_T \mathbf{I} + \alpha \left[\mathbf{1} \otimes (\mathbf{a}_0 \otimes \mathbf{a}_0) + (\mathbf{a}_0 \otimes \mathbf{a}_0) \otimes \mathbf{1}\right] \\ &+ 2(\mu_L - \mu_T)\left(\mathbf{a}_0 \otimes \mathbf{I}^{(2)}\mathbf{a}_0\right) + \left(\mathbf{I}^{(2)}\mathbf{a}_0 \otimes \mathbf{a}_0\right) \\ &+ \beta (\mathbf{a}_0 \otimes \mathbf{a}_0) \otimes (\mathbf{a}_0 \otimes \mathbf{a}_0) \quad .\end{aligned} \tag{3.60}$$

In (3.60), $\mathbf{I}$ is the rank four unit tensor with $\mathbf{I} = \frac{1}{2}(\delta_{ik}\delta_{jl} + \delta_{il}\delta_{jk})\,\mathbf{e}_i \otimes \mathbf{e}_j \otimes \mathbf{e}_k \otimes \mathbf{e}_l$ and $\mathbf{I}^{(2)}\mathbf{a}_0$ is a tensor of rank three with $\mathbf{I}^{(2)}\mathbf{a}_0 = \frac{1}{2}(\delta_{ik}\delta_{jl} + \delta_{il}\delta_{jk})\,a_j\,(\mathbf{e}_i \otimes \mathbf{e}_k \otimes \mathbf{e}_l)$.

In the following it is assumed that the fiber direction coincides with the first vector of the shell's base system. In order to simplify the notation, a matrix-vector representation is introduced. The vector of Green-Lagrange strains $\bar{\mathbf{E}}$ defined in (3.20) is linked to the vector of the second Piola-Kirchhoff stresses $\bar{\mathbf{S}}$ defined in (3.32) by means of

$$\bar{\mathbf{S}} = \mathbf{C}_F \bar{\mathbf{E}} \quad , \tag{3.61}$$

where $\mathbf{C}_F$ denotes the matrix containing the elasticity constants,

$$\mathbf{C}_F = \begin{bmatrix} \lambda + 2\alpha + 4\mu_L - 2\mu_T + \beta & \lambda + \alpha & \lambda + \alpha & 0 & 0 & 0 \\ \lambda + \alpha & \lambda + 2\mu_T & \lambda & 0 & 0 & 0 \\ \lambda + \alpha & \lambda & \lambda + 2\mu_T & 0 & 0 & 0 \\ 0 & 0 & 0 & \mu_L & 0 & 0 \\ 0 & 0 & 0 & 0 & \mu_L & 0 \\ 0 & 0 & 0 & 0 & 0 & \mu_T \end{bmatrix} \quad . \tag{3.62}$$

The strain-energy function corresponding to the transversely isotropic constitutive law for small strains in matrix vector notation (3.61) is

$$\Psi(\bar{\mathbf{E}}) = \frac{1}{2}\bar{\mathbf{E}}^T \mathbf{C}_F \bar{\mathbf{E}} \quad . \tag{3.63}$$

Using the elasticity constants E_1, E_2, ν_{12}, ν_{23} and G_{12} that are more common in the linear theory the matrix of elasticity constants can also be written as

$$\mathbf{C}_F = \begin{bmatrix} E_1^*(1-\nu_{23}^2) & E_2^*\nu_{12}(1+\nu_{23}) & E_2^*\nu_{12}(1+\nu_{23}) & 0 & 0 & 0 \\ E_2^*\nu_{12}(1+\nu_{23}) & E_2^*(1-\nu_{12}\nu_{21}) & E_2^*(\nu_{23}+\nu_{12}\nu_{21}) & 0 & 0 & 0 \\ E_2^*\nu_{12}(1+\nu_{23}) & E_2^*(\nu_{23}+\nu_{12}\nu_{21}) & E_2^*(1-\nu_{12}\nu_{21}) & 0 & 0 & 0 \\ 0 & 0 & 0 & G_{12} & 0 & 0 \\ 0 & 0 & 0 & 0 & G_{12} & 0 \\ 0 & 0 & 0 & 0 & 0 & G_{23} \end{bmatrix} , \tag{3.64}$$

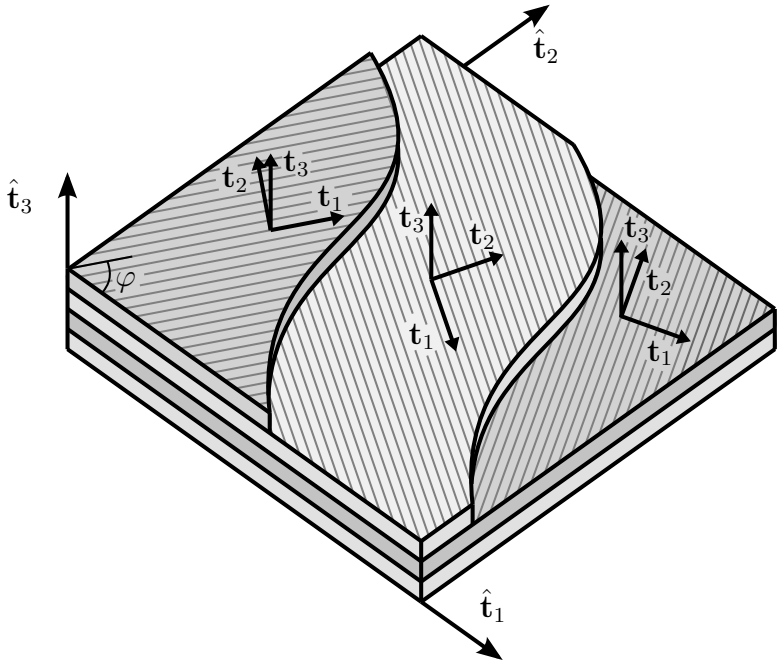

Figure 3.5: Global and fiber-oriented base systems

where the constants E_1^*, E_2^*, G_{23} and ν_{21} are defined by

$$\begin{aligned} E_1^* &= \frac{E_1}{(1+\nu_{23})\,(1-\nu_{23}-2\nu_{12}\nu_{21})} \quad , & G_{23} &= \frac{E_2}{2\,(1+\nu_{23})} \quad , \\ E_2^* &= \frac{E_1}{(1+\nu_{23})\,(1-\nu_{23}-2\nu_{12}\nu_{21})} \quad , & \nu_{21} &= E_2 \frac{\nu_{12}}{E_1} \quad . \end{aligned} \tag{3.65}$$

In order for the constitutive model to be physically sound the elasticity constants must meet a number of requirements. Because of requirement (2.42) for the strain-energy function the matrix of elasticity constants $\mathbf{C}_F$ must be positive definite and therefore have only positive eigenvalues. The requirements $E_1 > 0$, $E_2 > 0$, $G_{12} > 0$ and $G_{23} > 0$ hold. Additionally, $(1 - \nu_{12}\nu_{21}) > 0$, $(1 - \nu_{23}^2) > 0$, and $(1 - \nu_{23} - 2\nu_{12}\nu_{21}) > 0$ apply.

Fiber-reinforced composites usually consist of a number of different layers with arbitrary stacking sequences. Thus, in the general case, the fiber direction does not coincide with the first vector or the base system of the shell $\hat{\mathbf{t}}_i$ called the global base system in the following. In order to transform the constitutive law (3.61) from the fiber-oriented base system to the global base system, an additional base system $\mathbf{t}_i$, called the fiber-oriented base system, is therefore introduced. In it, the fiber direction coincides with the first vector. The base systems are illustrated in figure 3.5. The planar rotation between $\hat{\mathbf{t}}_i$ and $\mathbf{t}_i$ can be carried out by means of

$$\mathbf{t}_i = \bar{\mathbf{T}}\hat{\mathbf{t}}_i \quad , \tag{3.66}$$

where $\bar{\mathbf{T}}$ denotes a transformation tensor that describes the planar rotation between $\hat{\mathbf{t}}_i$ and $\mathbf{t}_i$. Since the rotation is planar an angle denoted φ between the base vectors in the plane $\hat{\mathbf{t}}_1$ and $\mathbf{t}_1$, and, correspondingly, between $\hat{\mathbf{t}}_2$ and $\mathbf{t}_2$, can be used to describe it. The

components of the transformation tensor $\bar{T}_{ij}$ are specified by

$$\bar{T}_{ij} = \hat{\mathbf{t}}_i \cdot \mathbf{t}_j \qquad \text{and} \qquad \left[\bar{T}_{ij}\right] = \begin{bmatrix} \cos\varphi & -\sin\varphi & 0 \\ \sin\varphi & \cos\varphi & 0 \\ 0 & 0 & 1 \end{bmatrix} \quad . \tag{3.67}$$

The Green-Lagrange strain tensor can be expressed in terms of the global and the fiber-oriented base systems by means of

$$\mathbf{E} = E^F_{ij}\, \mathbf{t}_i \otimes \mathbf{t}_j = E^G_{ij}\, \hat{\mathbf{t}}_i \otimes \hat{\mathbf{t}}_j \quad . \tag{3.68}$$

The superscripts F and G in (3.68) are introduced to indicate that the components E^F_{ij} and E^G_{ij} are associated with the local fiber-oriented base system $\mathbf{t}_i$ and the fixed global base system $\hat{\mathbf{t}}_i$. They will be used in the following as superscripts or subscripts to denote quantities expressed in terms of the respective base systems. The global components can be transformed to the local components by means of

$$E^F_{ij} = \mathbf{t}_i \cdot \mathbf{E}\mathbf{t}_j = \bar{T}_{ik} E^G_{kl} \bar{T}_{jl} \quad . \tag{3.69}$$

Reverting to matrix notation, the transformation of the Green-Lagrange strains associated with the global reference base system to the fiber-oriented fiber-oriented base system can be derived by exploiting (3.69), so that

$$\bar{\mathbf{E}}_F = \hat{\mathbf{T}} \bar{\mathbf{E}}_G \qquad \text{with} \qquad \hat{\mathbf{T}} = \begin{bmatrix} c^2 & s^2 & 0 & sc & 0 & 0 \\ s^2 & c^2 & 0 & -sc & 0 & 0 \\ 0 & 0 & 1 & 0 & 0 & 0 \\ -2sc & 2sc & 0 & c^2 - s^2 & 0 & 0 \\ 0 & 0 & 0 & 0 & c & s \\ 0 & 0 & 0 & 0 & -s & c \end{bmatrix} \quad , \tag{3.70}$$

where $\hat{\mathbf{T}}$ denotes a transformation matrix and the definitions $c = \cos\varphi$ and $s = \sin\varphi$ have been made. Considering the principle of material objectivity, the strain-energy function for small strains defined in (3.57) must be invariant towards the change in the reference system from $\hat{\mathbf{t}}_i$ to $\mathbf{t}_i$, so that

$$\Psi = \frac{1}{2} \bar{\mathbf{E}}^T_F \mathbf{C}_F \bar{\mathbf{E}}_F = \frac{1}{2} \left(\hat{\mathbf{T}}^i \bar{\mathbf{E}}_G \right)^T \mathbf{C}_F \hat{\mathbf{T}}^i \bar{\mathbf{E}}_G = \frac{1}{2} \bar{\mathbf{E}}^T_G \mathbf{C}^i_G \bar{\mathbf{E}}_G \quad , \tag{3.71}$$

where the superscript i has been inserted to make it clear that the respective matrix is associated with a particular layer i in an arbitrary stacking sequence of n layers, as illustrated in figure 3.6. It is pointed out that in (3.71) and (3.72) there is no summation

over i. The elasticity matrix $\mathbf{C}_G^i$ of a particular layer in terms of the reference base system can thus be determined from the local elasticity matrix $\mathbf{C}_F$ by means of

$$\mathbf{C}_G^i = \left(\hat{\mathbf{T}}^i\right)^T \mathbf{C}_F \hat{\mathbf{T}}^i \quad . \tag{3.72}$$

Dropping the layer index for convenience, the components C_{ij}^G of $\mathbf{C}_G$ can be analytically determined [39] and are specified by

$$\begin{aligned}
C_{11}^G &= c^4 C_{11}^F + 2c^2 s^2 \left(C_{12}^F + 2C_{44}^F\right) + s^4 C_{22}^F \quad , \\
C_{12}^G &= c^2 s^2 \left(C_{11}^F + C_{22}^F - 4C_{44}^F\right) + \left(c^4 + s^4\right) C_{12}^F \quad , \\
C_{13}^G &= c^2 C_{13}^F + s^2 C_{23}^F \quad , \\
C_{14}^G &= c^3 s \left(C_{11}^F - C_{12}^F - 2C_{44}^F\right) + cs^3 \left(C_{12}^F - C_{22}^F + 2C_{44}^F\right) \quad , \\
C_{22}^G &= s^4 C_{11}^F + 2c^2 s^2 \left(C_{12}^F + 2C_{44}^F\right) + c^4 C_{22}^F \quad , \\
C_{23}^G &= s^2 C_{13}^F + c^2 C_{23}^F \quad , \\
C_{24}^G &= cs^3 \left(C_{11}^F - C_{12}^F - 2C_{44}^F\right) + c^3 s \left(C_{12}^F - C_{22}^F + 2C_{44}^F\right) \quad , \\
C_{33}^G &= C_{33}^F \quad , \\
C_{34}^G &= cs \left(C_{31}^F - C_{32}^F\right) \quad , \\
C_{44}^G &= c^2 s^2 \left(C_{11}^F + C_{22}^F - 2C_{12}^F - 2C_{44}^F\right) + \left(c^4 + s^4\right) C_{44}^F \quad , \\
C_{55}^G &= c^2 C_{55}^F + s^2 C_{66}^F \quad , \\
C_{56}^G &= cs \left(C_{55}^F - C_{66}^F\right) \quad , \\
C_{66}^G &= s^2 C_{55}^F + c^2 C_{66}^F \quad .
\end{aligned} \tag{3.73}$$

The matrix must be symmetrically completed and all other missing components are zero. Therefore, analogous to (3.61), when allowing alternating fiber orientations in the composite shell model, the vector of Green-Lagrange strains $\bar{\mathbf{E}}$ is linked to the vector of the second Piola-Kirchhoff stresses $\bar{\mathbf{S}}$ by means of the global elasticity matrix $\mathbf{C}_G$, and thus

$$\bar{\mathbf{S}} = \mathbf{C}_G \bar{\mathbf{E}} \quad . \tag{3.74}$$

The vectors $\bar{\mathbf{S}}$ and $\bar{\mathbf{E}}$ in (3.74) contain the components related to the global, fixed base system, but the superscript G is omitted for both vectors to simplify the notation, which is also done in the following without being explicitly mentioned. For later considerations, two subparts of $\mathbf{C}_G$ are defined by

$$\mathbf{C}_m = \begin{bmatrix} C_{11}^G & C_{12}^G & C_{14}^G \\ C_{21}^G & C_{22}^G & C_{24}^G \\ C_{41}^G & C_{42}^G & C_{44}^G \end{bmatrix} \qquad \text{and} \qquad \mathbf{C}_s = \begin{bmatrix} C_{55}^G & C_{56}^G \\ C_{65}^G & C_{66}^G \end{bmatrix} \quad . \tag{3.75}$$

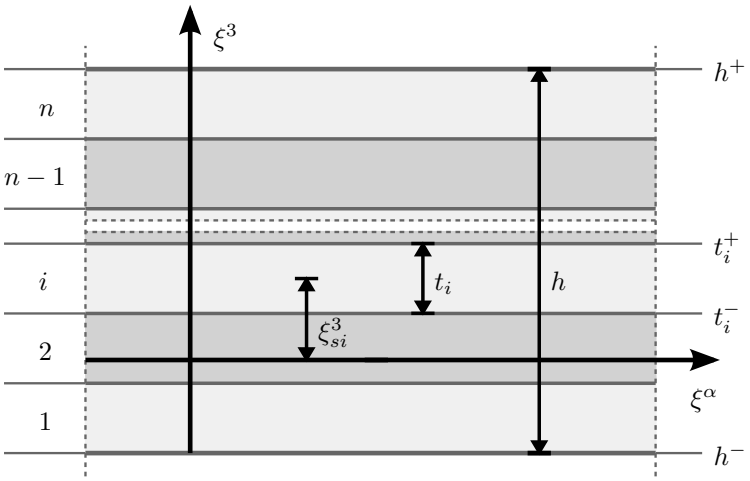

Figure 3.6: Layer numbering and some specifications for the composite shell

The submatrix $\mathbf{C}_m$ is associated with the in-plane stresses of the shell, and the submatrix $\mathbf{C}_s$ is associated with the interlaminar shear stresses. It is noted that for all angles $\varphi \neq 0°$ and $\varphi \neq 90°$ the matrices $\mathbf{C}_m$ and $\mathbf{C}_s$ are dense, while otherwise the components C_{14}^G, C_{24}^G, C_{41}^G, and C_{42}^G in $\mathbf{C}_m$ and the components C_{56}^G and C_{65}^G in $\mathbf{C}_s$ are zero. The common reduction of the constitutive laws to a two-dimensional form is foregone here, as the shell model is to accommodate for three-dimensional constitutive laws by the addition of a local part. It was already mentioned that a procedure of how to incorporate three-dimensional constitutive equations into the global shell model is proposed in [71].

Considering (3.34), it is possible to define the strain-energy $\hat{\Psi}(\boldsymbol{\varepsilon})$ as a function of the shell strains and thereby to introduce a constitutive law in terms of the effective shell stress resultants with (3.74) and (3.22), so that

$$\boldsymbol{\sigma} = \frac{\partial \hat{\Psi}(\boldsymbol{\varepsilon})}{\partial \boldsymbol{\varepsilon}} = \int_{h^-}^{h^+} \mathbf{A}^T \mathbf{C}_G \mathbf{A} \bar{\mu} \, \mathrm{d}\xi^3 \, \boldsymbol{\varepsilon} \quad . \tag{3.76}$$

Thus the vector of shell strains defined in (3.21) is linked to the vector of effective shell stress resultants defined in (3.33) by means of

$$\boldsymbol{\sigma} = \bar{\mathbf{D}} \boldsymbol{\varepsilon} \qquad \text{with} \qquad \bar{\mathbf{D}} = \int_{h^-}^{h^+} \mathbf{A}^T \mathbf{C}_G \mathbf{A} \bar{\mu} \, \mathrm{d}\xi^3 \quad , \tag{3.77}$$

where $\bar{\mathbf{D}}$ is the material tangent matrix. The corresponding strain-energy function in terms of the shell strains for transversely isotropic materials with small strains is

$$\hat{\Psi}(\boldsymbol{\varepsilon}) = \frac{1}{2} \boldsymbol{\varepsilon}^T \bar{\mathbf{D}} \boldsymbol{\varepsilon} \quad . \tag{3.78}$$

The integration over the thickness of the shell in (3.77) can be carried out analytically,

since $\mathbf{C}_G$ is constant in each layer, and thus, (3.77) can be rewritten as

$$\begin{bmatrix} \tilde{\mathbf{n}} \\ \tilde{\mathbf{m}} \\ \tilde{\mathbf{q}} \end{bmatrix} = \begin{bmatrix} \mathbf{D}_m & \mathbf{D}_{mb} & \mathbf{0} \\ \mathbf{D}_{mb}^T & \mathbf{D}_b & \mathbf{0} \\ \mathbf{0} & \mathbf{0} & \mathbf{D}_s \end{bmatrix} \begin{bmatrix} \bar{\boldsymbol{\varepsilon}} \\ \bar{\boldsymbol{\kappa}} \\ \bar{\boldsymbol{\gamma}} \end{bmatrix} \quad , \tag{3.79}$$

where the effective shell stress resultants are collected in the vectors

$$\tilde{\mathbf{n}} = \begin{bmatrix} \tilde{n}^{11} \\ \tilde{n}^{22} \\ \tilde{n}^{12} \end{bmatrix} \quad , \qquad \tilde{\mathbf{m}} = \begin{bmatrix} \tilde{m}^{11} \\ \tilde{m}^{22} \\ \tilde{m}^{12} \end{bmatrix} \quad , \qquad \tilde{\mathbf{q}} = \begin{bmatrix} \tilde{q}^{1} \\ \tilde{q}^{2} \end{bmatrix} \quad , \tag{3.80}$$

and the shell membrane strains, curvatures, and transverse shear strains are collected in the vectors

$$\bar{\boldsymbol{\varepsilon}} = \begin{bmatrix} \varepsilon_{11} \\ \varepsilon_{22} \\ \varepsilon_{12} \end{bmatrix} \quad , \qquad \bar{\boldsymbol{\kappa}} = \begin{bmatrix} \kappa_{11} \\ \kappa_{22} \\ \kappa_{12} \end{bmatrix} \quad , \qquad \bar{\boldsymbol{\gamma}} = \begin{bmatrix} \gamma_{1} \\ \gamma_{2} \end{bmatrix} \quad . \tag{3.81}$$

The submatrices in (3.79) contain the evaluated analytical integrations and are defined by

$$\begin{aligned} \mathbf{D}_m &= \sum_{i=1}^{n} \mathbf{C}_m^i t_i \quad , & \mathbf{D}_b &= \sum_{i=1}^{n} \mathbf{C}_m^i \left[\frac{(t_i)^3}{12} + t_i (\xi_{si}^3)^2 \right] \quad , \\ \mathbf{D}_{mb} &= \sum_{i=1}^{n} \mathbf{C}_m^i t_i \xi_{si}^3 \quad , & \mathbf{D}_s &= \sum_{i=1}^{n} \mathbf{C}_s^i t_i \quad , \end{aligned} \tag{3.82}$$

where i denotes the layer number and runs from one to the number of layers n. The thickness of the layer i is denoted by t_i and the distance of the middle of the layer i to the reference surface is denoted by ξ_{si}^3, both of which are illustrated in figure 3.6 along with the thickness of the shell h, the coordinates of the bottom and the top of the composite shell, h^- and h^+, and the coordinates of the bottom and the top of layer i, t_i^- and t_i^+. It is noted that from (3.79), it is obvious that for general inhomogeneous behavior there is a coupling of the membrane and bending terms.

3.5 Mixed variational principle

As was pointed out in chapter 2.6, using a mixed variational principle as the basis for a finite element formulation avoids numerical difficulties such as locking phenomena, which are problematic when using shell formulations with low-order finite elements based on a single-field variational principle. In this work a modified Hu-Washizu formulation is used as a variational basis. The advantages of using such a three-field variational principle were described in chapter 2.6.

The three-field Hu-Washizu functional is given in the form[8]

$$\Pi(\tilde{\mathbf{v}}, \boldsymbol{\sigma}, \boldsymbol{\varepsilon}) = \int_{\Omega_0} [\hat{\Psi}(\boldsymbol{\varepsilon}) + \boldsymbol{\sigma}^T(\boldsymbol{\varepsilon}_g(\tilde{\mathbf{v}}) - \boldsymbol{\varepsilon})]\, \mathrm{d}A - \int_{\Omega_0} \mathbf{u}^T \bar{\mathbf{p}}\, \mathrm{d}A - \int_{\Gamma_{\sigma 0}} \mathbf{u}^T \bar{\mathbf{t}}\, \mathrm{d}s \quad , \tag{3.83}$$

the independent field $\tilde{\mathbf{v}} = [\mathbf{u}, \boldsymbol{\omega}]^T$ containing the displacement vector $\mathbf{u}$ and the vector $\boldsymbol{\omega}$ of rotational parameters of the shell middle surface, the independent strain field $\boldsymbol{\varepsilon}$, and the independent stress resultant field $\boldsymbol{\sigma}$. The subscript g in $\boldsymbol{\varepsilon}_g$ indicates that these are geometric strains as a function of the field of displacements and rotational parameters $\tilde{\mathbf{v}}$. To derive the stationary condition of (3.83), the directional derivative is invoked following (2.71) with respect to the three independent fields $\tilde{\mathbf{v}}$, $\boldsymbol{\varepsilon}$, and $\boldsymbol{\sigma}$, so that

$$\begin{aligned} \delta\Pi = g(\boldsymbol{\theta}, \delta\boldsymbol{\theta}) = \int_{\Omega_0} \left[\delta\boldsymbol{\varepsilon}^T \left(\frac{\partial \hat{\Psi}(\boldsymbol{\varepsilon})}{\partial \boldsymbol{\varepsilon}} - \boldsymbol{\sigma} \right) + \delta\boldsymbol{\sigma}^T (\boldsymbol{\varepsilon}_g - \boldsymbol{\varepsilon}) + \delta\boldsymbol{\varepsilon}_g^T \boldsymbol{\sigma} \right] \mathrm{d}A \\ - \int_{\Omega_0} \delta\mathbf{u}^T \bar{\mathbf{p}}\, \mathrm{d}A - \int_{\Gamma_{\sigma 0}} \delta\mathbf{u}^T \bar{\mathbf{t}}\, \mathrm{d}s = 0 \quad , \end{aligned} \tag{3.84}$$

with $\boldsymbol{\theta} = [\tilde{\mathbf{v}}, \boldsymbol{\sigma}, \boldsymbol{\varepsilon}]^T$ and $\delta\boldsymbol{\theta} = [\delta\tilde{\mathbf{v}}, \delta\boldsymbol{\sigma}, \delta\boldsymbol{\varepsilon}]^T$. The entries in the vector $\delta\boldsymbol{\varepsilon}_g$ in (3.84) can be gathered from (3.35). The vectors $\delta\boldsymbol{\varepsilon}$ and $\delta\boldsymbol{\sigma}$ are the variation of the independent shell strains and independent effective shell stress resultants. The strain-energy $\hat{\Psi}(\boldsymbol{\varepsilon})$ in (3.84) is a function of the independent shell strains, while in (3.34) it is a function of the strains derived from the field of displacements and rotational parameters. The three-field variational formulation (3.84) is the basis of the finite element implementation. The geometric boundary conditions $\mathbf{u} = \bar{\mathbf{u}}$ are fulfilled as constraints through the choice of the variational field $\delta\mathbf{u}$.

The term in (3.84) that contains the variation of the geometric strains $\delta\boldsymbol{\varepsilon}_g^T$ corresponds to the internal virtual work (3.50 a) and can thus be brought into the form (3.52) by means of integration by parts, and thus, (3.84) can be rewritten as

$$\begin{aligned} g(\boldsymbol{\theta}, \delta\boldsymbol{\theta}) = \int_{\Omega_0} \left[\delta\boldsymbol{\varepsilon}^T \left(\frac{\partial \hat{\Psi}(\boldsymbol{\varepsilon})}{\partial \boldsymbol{\varepsilon}} - \boldsymbol{\sigma} \right) + \delta\boldsymbol{\sigma}^T (\boldsymbol{\varepsilon}_g - \boldsymbol{\varepsilon}) \right] \mathrm{d}A \\ - \int_{\Omega_0} \left[\left(\frac{1}{j} (j\mathbf{n}^\alpha)_{,\alpha} + \bar{\mathbf{p}} \right) \cdot \delta\mathbf{u} + \left(\frac{1}{j} (j\mathbf{m}^\alpha)_{,\alpha} + \mathbf{x}_{,\alpha} \times \mathbf{n}^\alpha \right) \cdot \delta\mathbf{w} \right] \mathrm{d}A \\ + \int_{\Gamma_{\sigma 0}} \left[(j\mathbf{n}^\alpha \nu_\alpha - \bar{\mathbf{t}}) \cdot \delta\mathbf{u} + (j\mathbf{m}^\alpha \nu_\alpha) \cdot \delta\mathbf{w} \right] \mathrm{d}s \quad . \end{aligned} \tag{3.85}$$

[8] In the form it is specified here, the mixed variational formulation is implemented with a two-dimensional constitutive law assuming the plane stress condition in [47]. In this thesis, it constitutes the global part of the coupled global-local shell model outlined in the next section with an interface to three-dimensional constitutive equations.

From (3.85) the static field equations can be derived. When comparing (3.85) to (3.55) and applying the fundamental lemma of variational calculus, it becomes evident that additionally to the resultant form of the balance of linear and angular momentum and the boundary conditions (3.56), two further Euler-Lagrange equations can be derived,

$$\left.\begin{aligned} \frac{\partial \hat{\Psi}(\boldsymbol{\varepsilon})}{\partial \boldsymbol{\varepsilon}} - \boldsymbol{\sigma} &= \mathbf{0} \\ \boldsymbol{\varepsilon}_g - \boldsymbol{\varepsilon} &= \mathbf{0} \end{aligned}\right\} \text{in } \Omega_0 \quad . \tag{3.86}$$

These are a field equation that contains the strain-energy function (3.86 a) and can thus be used to implement a constitutive law, and the geometric field equation (3.86 b).

3.6 Linearization of the mixed variational principle

The variational formulation (3.84) is a nonlinear function in $\boldsymbol{\theta}$. In chapter 2.6 it was explained that to apply solution techniques of Newton's type a consistent linearization of the quantities in the nonlinear problem must be performed and the linearization procedure of a variational principle was demonstrated. Thus, analogous to (2.73), the function $g\left(\boldsymbol{\theta}, \delta\boldsymbol{\theta}\right)$ is linearized based on a first-order Taylor expansion specified by

$$L\left[g(\boldsymbol{\theta}, \delta\boldsymbol{\theta}), \Delta\boldsymbol{\theta}\right] = g(\boldsymbol{\theta}, \delta\boldsymbol{\theta}) + D\left[g(\boldsymbol{\theta}, \delta\boldsymbol{\theta})\right] \cdot \Delta\boldsymbol{\theta} \quad , \tag{3.87}$$

where the operators $L[\bullet]$, $D[\bullet]$ and $\Delta(\bullet)$ were introduced in chapter 2.6 and $\Delta\boldsymbol{\theta} = [\Delta\tilde{\mathbf{v}}, \Delta\boldsymbol{\sigma}, \Delta\boldsymbol{\varepsilon}]^T$. Analogous to (2.74), the second term in (3.87) is the directional derivative of the principle of virtual work and can be derived by evaluating

$$D\left[g(\boldsymbol{\theta}, \delta\boldsymbol{\theta})\right] \cdot \Delta\boldsymbol{\theta} = \frac{d}{d\varepsilon}\left[g\left(\boldsymbol{\theta} + \varepsilon\Delta\boldsymbol{\theta}, \delta\boldsymbol{\theta}\right)\right]\big|_{\varepsilon=0} \quad . \tag{3.88}$$

With conservative external loads $\bar{\mathbf{p}}$ and $\bar{\mathbf{t}}$, the linearization of terms in (3.84) containing them vanish, and the directional derivative of the variational formulation becomes

$$\begin{aligned} D\left[g(\boldsymbol{\theta}, \delta\boldsymbol{\theta})\right] \cdot \Delta\boldsymbol{\theta} = \int_{\Omega_0} \Bigg[\delta\boldsymbol{\varepsilon}^T \left(\frac{\partial^2 \hat{\Psi}(\boldsymbol{\varepsilon})}{\partial\boldsymbol{\varepsilon}\partial\boldsymbol{\varepsilon}} \Delta\boldsymbol{\varepsilon} - \Delta\boldsymbol{\sigma} \right) + \delta\boldsymbol{\sigma}^T(\Delta\boldsymbol{\varepsilon}_g - \Delta\boldsymbol{\varepsilon}) \\ + \delta\boldsymbol{\varepsilon}_g^T \Delta\boldsymbol{\sigma} + \Delta\delta\boldsymbol{\varepsilon}_g^T \boldsymbol{\sigma} \Bigg] \, \mathrm{d}A \quad . \end{aligned} \tag{3.89}$$

In (3.89), the material tangent matrix defined in (3.77) enters as the second derivative of the strain-energy function, so that

$$\bar{\mathbf{D}} = \frac{\partial \boldsymbol{\sigma}}{\partial \boldsymbol{\varepsilon}} = \frac{\partial^2 \hat{\Psi}(\boldsymbol{\varepsilon})}{\partial\boldsymbol{\varepsilon}\partial\boldsymbol{\varepsilon}} \quad . \tag{3.90}$$

Analogous to the determination of the variation of the shell strains (3.35), applying the directional derivative leads to the linearized shell strains

$$\begin{aligned}
\Delta\varepsilon_{\alpha\beta} &= \frac{1}{2}\left(\Delta\mathbf{x}_{,\alpha}\cdot\mathbf{x}_{,\beta}+\Delta\mathbf{x}_{,\beta}\cdot\mathbf{x}_{,\alpha}\right) \quad , \\
\Delta\kappa_{\alpha\beta} &= \frac{1}{2}\left(\Delta\mathbf{x}_{,\alpha}\cdot\mathbf{d}_{,\beta}+\Delta\mathbf{x}_{,\beta}\cdot\mathbf{d}_{,\alpha}+\Delta\mathbf{d}_{,\alpha}\cdot\mathbf{x}_{,\beta}+\Delta\mathbf{d}_{,\beta}\cdot\mathbf{x}_{,\alpha}\right) \quad , \\
\Delta\gamma_{\alpha} &= \Delta\mathbf{x}_{,\alpha}\cdot\mathbf{d}+\Delta\mathbf{d}\cdot\mathbf{x}_{,\alpha} \quad ,
\end{aligned} \tag{3.91}$$

with the linearized membrane strains $\Delta\varepsilon_{\alpha\beta}$, the linearized curvatures $\Delta\kappa_{\alpha\beta}$, and the linearized transverse shear strains $\Delta\gamma_{\alpha}$.

Applying the directional derivative to the variation of the strains yields the linearized virtual shell strains

$$\begin{aligned}
\Delta\delta\varepsilon_{\alpha\beta} &= \frac{1}{2}\left(\Delta\mathbf{x}_{,\alpha}\cdot\delta\mathbf{x}_{,\beta}+\Delta\mathbf{x}_{,\beta}\cdot\delta\mathbf{x}_{,\alpha}\right) \quad , \\
\Delta\delta\kappa_{\alpha\beta} &= \frac{1}{2}\left(\delta\mathbf{x}_{,\alpha}\cdot\Delta\mathbf{d}_{,\beta}+\delta\mathbf{x}_{,\beta}\cdot\Delta\mathbf{d}_{,\alpha}+\delta\mathbf{d}_{,\alpha}\cdot\Delta\mathbf{x}_{,\beta}\right. \\
&\quad \left.+\,\delta\mathbf{d}_{,\beta}\cdot\Delta\mathbf{x}_{,\alpha}+\mathbf{x}_{,\alpha}\cdot\Delta\delta\mathbf{d}_{,\beta}+\mathbf{x}_{,\beta}\cdot\Delta\delta\mathbf{d}_{,\alpha}\right) \quad , \\
\Delta\delta\gamma_{\alpha} &= \delta\mathbf{x}_{,\alpha}\cdot\Delta\mathbf{d}+\delta\mathbf{d}\cdot\Delta\mathbf{x}_{,\alpha}+\mathbf{x}_{,\alpha}\cdot\Delta\delta\mathbf{d} \quad ,
\end{aligned} \tag{3.92}$$

with the linearized variation of the membrane strains $\Delta\delta\varepsilon_{\alpha\beta}$, the linearized variation of the curvatures $\Delta\delta\kappa_{\alpha\beta}$, and the linearized variation of the transverse shear strains $\Delta\delta\gamma_{\alpha}$.

The linearization of the variation of the director vector $\Delta\delta\mathbf{d}$ can be determined after extensive algebraic manipulations [40, 47] and is summarized here. For scalar products of the form $\mathbf{h}\cdot\Delta\delta\mathbf{d}$, where $\mathbf{h}$ can be any vector $\mathbf{h}\in R^3$, that occur in (3.92),

$$\mathbf{h}\cdot\Delta\delta\mathbf{d} = \mathbf{h}\cdot\Delta\left(\delta\mathbf{w}\times\mathbf{d}\right) = \delta\mathbf{w}\cdot\mathbf{M}\Delta\mathbf{w} \tag{3.93}$$

holds, where, analogous to (3.37), $\Delta\mathbf{w} = \mathbf{H}\Delta\boldsymbol{\omega}$ and

$$\mathbf{M} = \frac{1}{2}\left(\mathbf{d}\otimes\mathbf{h}+\mathbf{h}\otimes\mathbf{d}\right)+\frac{1}{2}\left(\mathbf{t}\otimes\boldsymbol{\omega}+\boldsymbol{\omega}\otimes\mathbf{t}\right)+c_1\mathbf{1} \quad . \tag{3.94}$$

In (3.94), the vector $\mathbf{t}$ is defined by

$$\mathbf{t} = -c_2\left(\mathbf{d}\times\mathbf{h}\right)+c_3\left[\left(\mathbf{d}\times\mathbf{h}\right)\cdot\boldsymbol{\omega}\right]\boldsymbol{\omega} \quad , \tag{3.95}$$

and the constant c_1 has been introduced with

$$c_1 = \frac{\sin\omega-\omega}{2\,\omega\left(\cos\omega-1\right)}\left[\left(\mathbf{d}\times\mathbf{h}\right)\cdot\boldsymbol{\omega}\right]-\left(\mathbf{d}\cdot\mathbf{h}\right) \quad , \tag{3.96}$$

where further constants c_2 and c_3 are specified by

$$c_2 = \frac{\omega \sin\omega + 2\cos\omega - 2}{\omega^2 (\cos\omega - 1)} \qquad \text{and} \qquad c_3 = \frac{4(\cos\omega - 1) + \omega^2 + \omega \sin\omega}{2\,\omega^4 (\cos\omega - 1)} \quad . \tag{3.97}$$

The pseudo-rotation vector $\boldsymbol{\omega}$ and $\omega = |\boldsymbol{\omega}|$ were introduced in chapter 3.1.1, while the axial vector $\mathbf{w}$ and the tensor $\mathbf{H}$ were defined in chapter 3.3.1. The linearization of the rotational parameters collected in $\Delta\boldsymbol{\omega}$ related to the global coordinate system can be derived by evaluating

$$\Delta\boldsymbol{\omega} = \bar{\mathbf{T}} \Delta\boldsymbol{\beta} \quad , \tag{3.98}$$

where $\bar{\mathbf{T}}$ is defined in (3.42) and $\Delta\boldsymbol{\beta}$ is defined by

$$\Delta\boldsymbol{\beta} = \begin{cases} [\Delta\omega_1, \Delta\omega_2, \Delta\omega_3] & \text{for positions on shell intersections} \\ [\Delta\beta_1, \Delta\beta_2] & \text{for all other positions} \quad . \end{cases} \tag{3.99}$$

Because the shear strains are approximated with independent interpolation functions in the finite element formulation, the variation of the assumed strain interpolation needs to be determined separately (see chapter 5).

Chapter 4

Extension of the global shell theory - the coupled global-local model

The nonlinear shell model presented in chapter 3 is well-suited for the nonlinear analysis of thin structures, if one is interested in the displacements of the structure and its stress resultants. It is not able, however, to compute the exact paths of the interlaminar stresses. In the context of the Reissner-Mindlin kinematic, the interlaminar shear stresses are only correct on an average, while peaks in the stresses cannot be computed. As already pointed out, the interlaminar stresses are the driving force behind failure modes such as delamination. In this work, the nonlinear shell model of chapter 3 is referred to as the global model. In this section an addition to the global model called the local model is introduced. The equations of the global model are formulated for the structure as a whole, while the local model introduces equations that have to be fulfilled at a specific point in the structure. In the implementation of the finite element formulation, this means that the local equations must be fulfilled in an integration point. With the local model, warping of the cross section can be determined, thus supplying local displacements through the thickness of the shell. Thus, the assumption made in the global model that plane cross sections remain plane during a deformation process is not valid in the local model.

The addition of the local model to the global nonlinear shell model is implemented based on a geometrically linear theory. This is permissible for the simulations performed in this work, allowing large displacements and rotations, but small strains. It is noted, however, that the interface to the global model is derived in a way that makes it possible to implement the local model based on a geometrically nonlinear theory without further modifications of the global model. As a starting point to derive the local model and the interface between the global and the local model the conventional kinematics of the shell is extended. The procedure will be discussed in the following section. Then, an orthogonalization procedure will be introduced, so as to avoid falsifying the original results of the global shell model. Subsequently, the local model will be introduced into the mixed variational formulation and the linearized form will be derived.

4.1 Extended kinematics of the shell

In order to derive the extended kinematics of the shell, an extended product ansatz is made for the displacements of the shell. Subsequently, the associated strain field and the stress resultants are derived.

4.1.1 Generalized displacement field

An integral part of the coupled global-local model is a multiplicative decomposition of the displacement field. Interpolations are made for the distribution of the displacements with respect to the thickness coordinate ξ^3. The local model introduces unknowns into the shell model, the number of which depends on the number of layers of the composite shell. The additional unknowns are eliminated on the element level by means of static condensation in the context of the finite element formulation. Similar work is carried out for a beam model in [128, 129].

The way the interpolation functions in the thickness direction are chosen is facilitated by the finite element method for one-dimensional elements with linear ansatz functions. In this case, the appendant quantities are the displacements at virtual nodes at the layer boundaries and hierarchic quadratic and cubic functions where the appendant quantities are the relative displacements of the additional virtual nodes displayed in figures 4.2, 4.3 and 4.4. Thus the same interpolation functions are chosen for the displacements u, v and w in the ξ^1-, ξ^2- and ξ^3-direction respectively. The coordinates ξ^1 and ξ^2 are the in-plane coordinates of the shell and ξ^3 is the coordinate perpendicular to the shell plane, as introduced in figure 3.1. A profile of the composite shell with n layers is shown in figure 4.1. Consistent with the preceding chapter, the bottom and the top of the shell are denoted by h^- and h^+, while the bottom and the top of layer i are denoted by t^- and t^+, the thickness of the composite shell is denoted by h and the thickness of layer i by t_i. The multiplicative decomposition of the displacements for layer i of the composite shell is given with

$$\begin{aligned} u_i(\xi^1,\xi^2,\xi^3) &= \sum_{k=1}^{4} N_k(\xi^3)\,\bar{u}_k(\xi^1,\xi^2) \quad , \\ v_i(\xi^1,\xi^2,\xi^3) &= \sum_{k=1}^{4} N_k(\xi^3)\,\bar{v}_k(\xi^1,\xi^2) \quad , \\ w_i(\xi^1,\xi^2,\xi^3) &= \sum_{k=1}^{4} N_k(\xi^3)\,\bar{w}_k(\xi^1,\xi^2) \quad , \end{aligned} \tag{4.1}$$

where the ansatz functions N_k are defined by

$$\begin{aligned} N_1 &= \frac{1}{2}(1-\zeta_i) \quad , & N_2 &= \frac{1}{2}(1+\zeta_i) \quad , \\ N_3 &= 1-\zeta_i^2 \quad , & N_4 &= \frac{8}{3}\zeta_i\left(1-\zeta_i^2\right) \quad . \end{aligned} \tag{4.2}$$

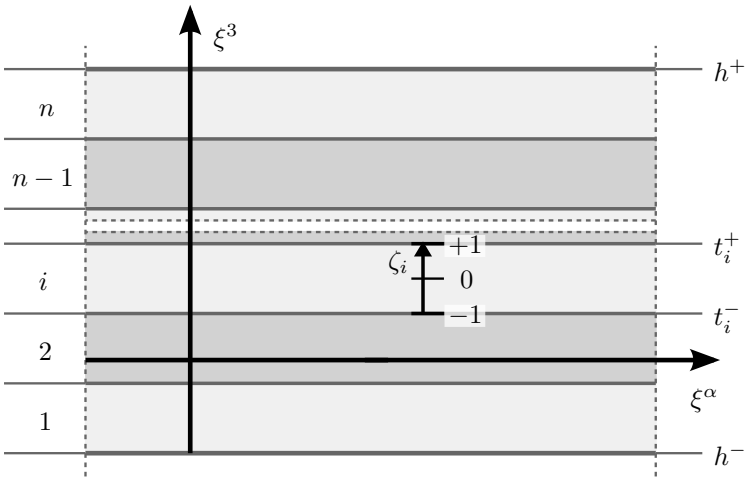

Figure 4.1: Layers in the composite shell

The index variable i runs from 1 to the number of layers n. The normalized thickness coordinate ζ_i of layer i in (4.2) is denoted by $-1 \leq \zeta_i \leq 1$ and illustrated in figure 4.1. The extended product ansatz of the complete composite shell with an arbitrary number of layers n is thus defined by[9]

$$\tilde{\mathbf{u}}(\xi^1, \xi^2, \xi^3) = \mathbf{M}(\xi^3)\, \mathbf{m}(\xi^1, \xi^2) \quad , \tag{4.3}$$

so that in the global-local shell model, the displacements $\tilde{\mathbf{u}}$ are expressed as the product of a matrix $\mathbf{M}$ and a vector $\mathbf{m}$. The matrix $\mathbf{M}$ contains the shape functions that depend on the coordinate perpendicular to the shell ξ^3, and the vector $\mathbf{m}$ contains the displacements at virtual nodes described earlier through the thickness of the shell, which depend on the coordinates in the plane of the shell ξ^1 and ξ^2. The matrix $\mathbf{M}$ and vector $\mathbf{m}$ are specified by

$$\tilde{\mathbf{u}} = \begin{bmatrix} \tilde{u}(\xi^1, \xi^2, \xi^3) \\ \tilde{v}(\xi^1, \xi^2, \xi^3) \\ \tilde{w}(\xi^1, \xi^2, \xi^3) \end{bmatrix} = \begin{bmatrix} \mathbf{M}_u(\xi^3) & \mathbf{0} & \mathbf{0} \\ \mathbf{0} & \mathbf{M}_v(\xi^3) & \mathbf{0} \\ \mathbf{0} & \mathbf{0} & \mathbf{M}_w(\xi^3) \end{bmatrix} \begin{bmatrix} \mathbf{m}_u(\xi^1, \xi^2) \\ \mathbf{m}_v(\xi^1, \xi^2) \\ \mathbf{m}_w(\xi^1, \xi^2) \end{bmatrix} \quad , \tag{4.4}$$

where the vectors $\mathbf{M}_u$, $\mathbf{M}_v$, and $\mathbf{M}_w$ are defined by

$$\begin{aligned} \mathbf{M}_u &= [\mathbf{H}_u, \quad \mathbf{I}_u, \quad \mathbf{J}_u] \\ \mathbf{M}_v &= [\mathbf{H}_v, \quad \mathbf{I}_v, \quad \mathbf{J}_v] \\ \mathbf{M}_w &= [\mathbf{H}_w, \quad \mathbf{I}_w, \quad \mathbf{J}_w] \quad . \end{aligned} \tag{4.5}$$

[9] Instead of expressing the extended product ansatz with the matrix and vector in (4.3) a notation with a summation over all layers could be used.

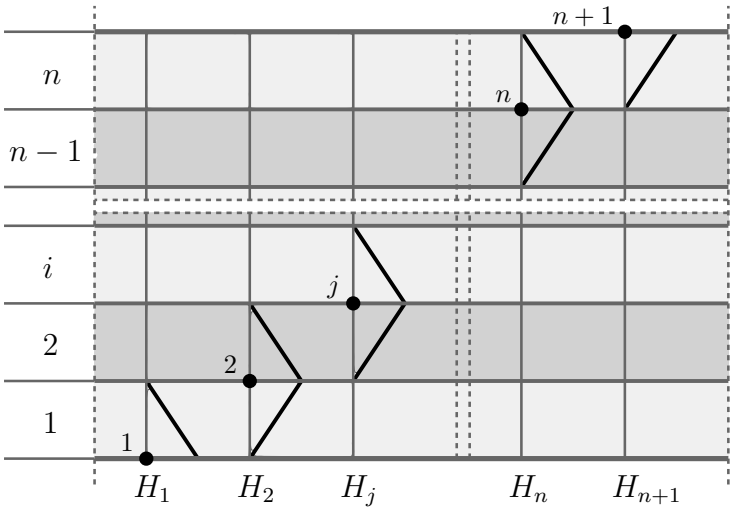

Figure 4.2: Linear shape functions H_j

The vectors $\mathbf{H}_u$, $\mathbf{H}_v$, and $\mathbf{H}_w$ in (4.5) contain one-dimensional linear shape functions, so that

$$\begin{aligned} \mathbf{H}_u &= \left[H_{u(1)},\ H_{u(j)},\ \ldots\ H_{u(n+1)}\right] \quad , \\ \mathbf{H}_v &= \left[H_{v(1)},\ H_{v(j)},\ \ldots\ H_{v(n+1)}\right] \quad , \\ \mathbf{H}_w &= \left[H_{w(1)},\ H_{w(j)},\ \ldots\ H_{w(n+1)}\right] \quad , \end{aligned} \tag{4.6}$$

where the index variable j runs from 1 to $n+1$, n being the number of layers. The entries of the vector $\mathbf{H}_u$ in (4.6) are defined by

$$H_{u(j)} = \begin{cases} \dfrac{1}{2}(1-\zeta_1) & \text{if } j = 1 \\ \left[\dfrac{1}{2}(1+\zeta_{j-1}) \;\middle|\; \dfrac{1}{2}(1-\zeta_j)\right] & \text{if } j > 1 \text{ and } j < (n+1) \\ \dfrac{1}{2}(1+\zeta_n) & \text{if } j = (n+1) \end{cases} \tag{4.7}$$

and are illustrated in figure 4.2. The entries in the vectors $\mathbf{H}_v$ and $\mathbf{H}_w$ are identical. The vectors $\mathbf{I}_u$, $\mathbf{I}_v$, and $\mathbf{I}_w$ contain quadratic hierarchic shape functions, so that

$$\begin{aligned} \mathbf{I}_u &= \left[I_{u(1)},\ I_{u(i)},\ \ldots\ I_{u(n)}\right] \quad , \\ \mathbf{I}_v &= \left[I_{v(1)},\ I_{v(i)},\ \ldots\ I_{v(n)}\right] \quad , \\ \mathbf{I}_w &= \left[I_{w(1)},\ I_{w(i)},\ \ldots\ I_{w(n)}\right] \quad . \end{aligned} \tag{4.8}$$

The entries of the vector $\mathbf{I}_u$ in (4.8) are defined by

$$I_{u(i)} = 1 - \zeta_i^2 \tag{4.9}$$

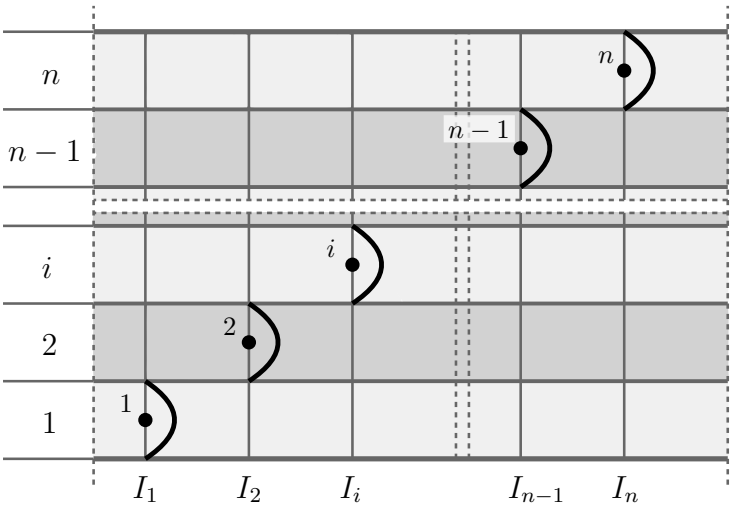

Figure 4.3: Hierarchic quadratic shape functions I_i

and are illustrated in figure 4.3. The entries in the vectors $\mathbf{I}_v$ and $\mathbf{I}_w$ are identical. The vectors $\mathbf{J}_u$, $\mathbf{J}_v$, and $\mathbf{J}_w$ contain cubic hierarchic shape functions, and thus

$$\begin{aligned} \mathbf{J}_u &= \left[J_{u(1)},\ J_{u(i)},\ \dots\ J_{u(n)}\right] \quad , \\ \mathbf{J}_v &= \left[J_{v(1)},\ J_{v(i)},\ \dots\ J_{v(n)}\right] \quad , \\ \mathbf{J}_w &= \left[J_{w(1)},\ J_{w(i)},\ \dots\ J_{w(n)}\right] \quad . \end{aligned} \tag{4.10}$$

The entries of the vector $\mathbf{J}_u$ in (4.10) are defined by

$$J_{u(i)} = \frac{8}{3}\zeta_i\left(1-\zeta_i^2\right) \tag{4.11}$$

and are illustrated in figure 4.4. The entries in the vectors $\mathbf{J}_v$ and $\mathbf{J}_w$ are identical.

For the sake of clarity, the dependent variables have sometimes been dropped in the following equations. It is pointed out that even though the shape functions are identical for all three coordinates, due to an orthogonalization procedure defined later they are altered and then can differ. Therefore, and for the sake of clarity, they are labeled with a sub-index corresponding to the associated displacement.

For later reference, considering $\mathrm{d}\zeta_i = 2/t_i\,\mathrm{d}\xi^3$, the derivatives of the linear shape functions defined in (4.7) are specified by

$$H_{u(j),3} = \begin{cases} -\dfrac{1}{t_1} & \text{if } j = 1 \\ \left[\dfrac{1}{t_{j-1}} \;\middle|\; -\dfrac{1}{t_j}\right] & \text{if } j > 1 \text{ and } j < (n+1) \\ \dfrac{1}{t_n} & \text{if } j = (n+1) \quad , \end{cases} \tag{4.12}$$

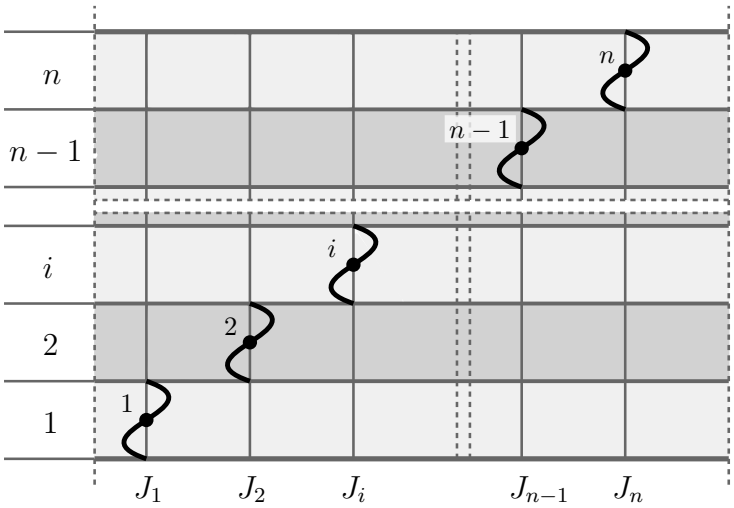

Figure 4.4: Hierarchic cubic shape functions J_i

and the hierarchic quadratic and cubic shape functions defined in (4.9) and (4.11) can be given with

$$I_{u(i),3} = -\frac{4}{t_i}\zeta_i \qquad \text{and} \qquad J_{u(i),3} = \frac{16}{3t_i}\left(1 - 3\zeta_i^2\right) \quad . \tag{4.13}$$

In order to derive the interface to the conventional shell formulation with its standard degrees of freedom the extended product ansatz (4.3) is redefined and resorted, so that

$$\begin{aligned} \tilde{\mathbf{u}}(\xi^1,\xi^2,\xi^3) &= \mathbf{u}_G(\xi^1,\xi^2,\xi^3) + \mathbf{u}_L(\xi^1,\xi^2,\xi^3) \\ &= \mathbf{M}_G(\xi^3)\,\mathbf{m}_G(\xi^1,\xi^2) + \mathbf{M}_L(\xi^3)\,\mathbf{m}_L(\xi^1,\xi^2) \quad , \end{aligned} \tag{4.14}$$

where the matrices $\mathbf{M}_G$ and $\mathbf{M}_L$ and the vectors $\mathbf{m}_G$ and $\mathbf{m}_L$ in (4.14) are specified by

$$\begin{bmatrix} \tilde{u} \\ \tilde{v} \\ \tilde{w} \end{bmatrix} = \begin{bmatrix} 1 & 0 & 0 & \xi^3 & 0 \\ 0 & 1 & 0 & 0 & \xi^3 \\ 0 & 0 & 1 & 0 & 0 \end{bmatrix} \begin{bmatrix} \bar{u} \\ \bar{v} \\ \bar{w} \\ \bar{\beta}_1 \\ \bar{\beta}_2 \end{bmatrix} + \begin{bmatrix} \tilde{\mathbf{M}}_u & \mathbf{0} & \mathbf{0} \\ \mathbf{0} & \tilde{\mathbf{M}}_v & \mathbf{0} \\ \mathbf{0} & \mathbf{0} & \tilde{\mathbf{M}}_w \end{bmatrix} \begin{bmatrix} \tilde{\mathbf{m}}_u \\ \tilde{\mathbf{m}}_v \\ \tilde{\mathbf{m}}_w \end{bmatrix} \quad . \tag{4.15}$$

Through the changes to the extended product ansatz (4.3) performed in (4.14) and specified in (4.15), a transition is made from a generic product ansatz to an ansatz with an additive split consisting of two parts. The first part belongs to the global model and is denoted with a subscript G. This global part of the model is able to reproduce the kinematics of the standard shell formulation. The second part is called the local model and its purpose

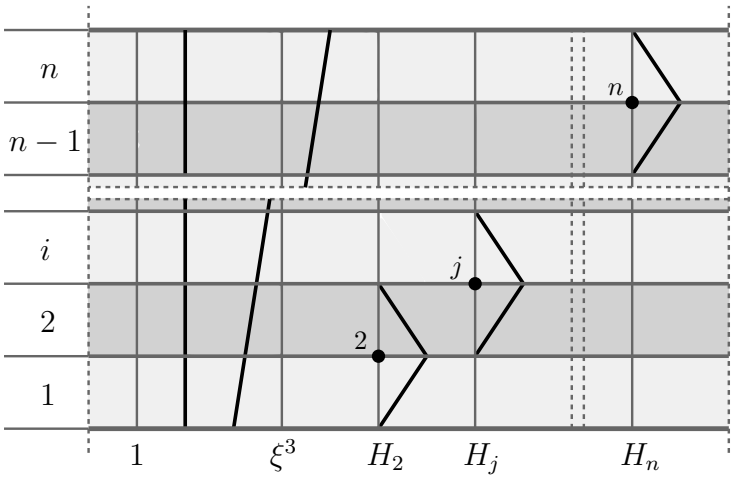

Figure 4.5: Modified shape functions

is to describe local warping and thickness changes. It is denoted with a subscript L. It will be shown later how the complete three-dimensional strain state can be derived from these modifications.

In (4.15), the three displacements $\bar{u}$, $\bar{v}$, and $\bar{w}$ associated with the ξ^1-, ξ^2-, and ξ^3-directions and two rotations $\bar{\beta}_1$ and $\bar{\beta}_2$ around the ξ^1- and ξ^2-axis, that are common in conventional shell theory, are summarized in the vector $\mathbf{m}_G$, which thus corresponds to the vector $\tilde{\mathbf{v}}$ as used in chapter 3. The equations of the shell formulation derived in chapter 3 therefore apply to the global part of the model. The derivation of the interface between the global and local model is presented for smooth shell surfaces with two drilling degrees of freedom. The transfer to the case of three drilling degrees of freedom for shells with intersections is straightforward. The entries in $\mathbf{m}_G$ are global quantities that describe displacements and rotations of the shell reference surface.

The global part of the model can be derived from the generic product ansatz by applying the following procedure and comparing (4.4) and (4.15). As illustrated in figure 4.5, the linear shape functions in the extended product ansatz defined in (4.7) are combined to obtain the terms 1 and ξ^3 through the thickness of the shell. For every additional term introduced a corresponding number of entries in $\mathbf{M}$ and appendant variables in $\mathbf{m}$ need to be eliminated from the extended product ansatz. This means that two entries have to be removed from $\mathbf{M}_u$ to obtain $\tilde{\mathbf{M}}_u$, two entries have to be removed from $\mathbf{M}_v$ to obtain $\tilde{\mathbf{M}}_v$ and one entry has to be removed from $\mathbf{M}_w$ to obtain $\tilde{\mathbf{M}}_w$. The entries in question, which are removed from $\mathbf{H}_u$, $\mathbf{H}_v$ and $\mathbf{H}_w$, are evident from the definitions of the reduced vectors, provided by

$$
\begin{aligned}
\tilde{\mathbf{M}}_u &= \left[\tilde{\mathbf{H}}_u, \quad \mathbf{I}_u, \quad \mathbf{J}_u\right] \quad , & \tilde{\mathbf{H}}_u &= \left[H_{u2},\ H_{u(j)},\ \ldots\ H_{u(n)}\right] \quad , \\
\tilde{\mathbf{M}}_v &= \left[\tilde{\mathbf{H}}_v, \quad \mathbf{I}_v, \quad \mathbf{J}_v\right] \quad , & \tilde{\mathbf{H}}_v &= \left[H_{v2},\ H_{v(j)},\ \ldots\ H_{v(n)}\right] \quad , \\
\tilde{\mathbf{M}}_w &= \left[\tilde{\mathbf{H}}_w, \quad \mathbf{I}_w, \quad \mathbf{J}_w\right] \quad , & \tilde{\mathbf{H}}_w &= \left[H_{w2},\ H_{w(j)},\ \ldots\ H_{w(n+1)}\right] \quad .
\end{aligned}
\tag{4.16}
$$

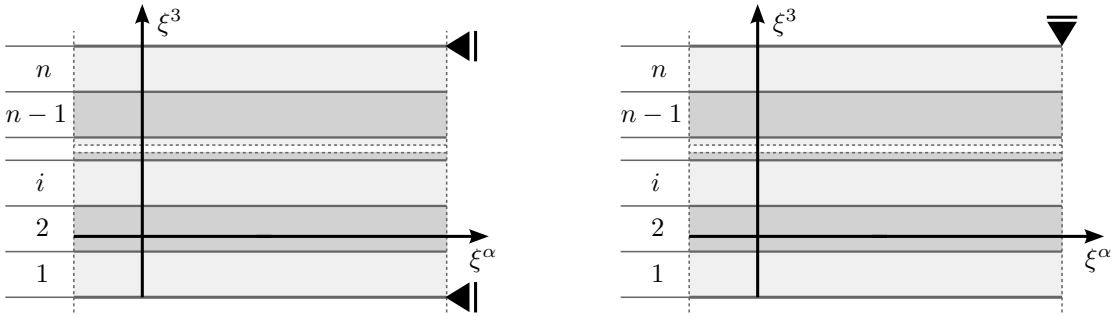

(a) u and v (b) w

Figure 4.6: Boundary conditions of the local model

The other vectors in (4.16) remain unchanged. The local part of the model can effectively be interpreted as an interpolation of the local displacements with some boundary conditions as depicted in figure 4.6. It is noted that this does not mean that the values of the warping functions are zero at the top and the bottom of the composite and the value of the displacement in thickness direction is set to zero at the top of the composite. Through the local model a number of unknowns is introduced into the model. The exact number is derived in chapter 5 in the context of the finite element formulation.

By means of the described procedure, which separates the extended product ansatz (4.3) into two parts (4.14), a clearly defined interface has therefore been derived for the kinematics of the shell model presented in chapter 3 called the global model to the local model derived in this chapter.

4.1.2 Derived strain field

At this point, the Green-Lagrange strains of the coupled global-local model are derived. Similar to the additive split of the ansatz for the displacements, the Green-Lagrange strains are separated into a global and a local part, so that

$$\tilde{\mathbf{E}} = \bar{\mathbf{E}}_G + \bar{\mathbf{E}}_L \quad . \tag{4.17}$$

The vector of global Green-Lagrange strains $\mathbf{E}_G$ was introduced in (3.20) and related to the vector of shell strains $\boldsymbol{\varepsilon}_G$ (3.21) by means of assembly matrix $\mathbf{A}_G$ (3.22)[10], so that

$$\bar{\mathbf{E}}_G = \mathbf{A}_G \boldsymbol{\varepsilon}_G \quad . \tag{4.18}$$

As further motivation for the proposed procedure, the strains resulting from the global model are derived in a linear way, which is applicable for small strains and was published in [105]. It is noted that the following procedure does not replace the procedure to derive

[10] It was already mentioned that the nonlinear shell model of chapter 3 is referred to as the global model in this work. Here and in the following, quantities derived in chapter 3 associated with this model are marked with a subscript G without being explicitly mentioned.

the Green-Lagrange strains introduced in chapter (3.1.2). The linearized Green-Lagrange strains are specified by

$$\mathbf{E}_G^{\text{lin}} = \frac{1}{2}\left(\mathbf{H}_G^T + \mathbf{H}_G\right) = \text{Grad}^s \mathbf{u}_G \quad . \tag{4.19}$$

They are collected in a vector denoted $\bar{\mathbf{E}}_G^{\text{lin}}$ and can be derived from the derivatives of the global displacements, so that

$$\bar{\mathbf{E}}_G^{\text{lin}} = \begin{bmatrix} E_{11}^G \\ E_{22}^G \\ E_{33}^G \\ 2E_{12}^G \\ 2E_{13}^G \\ 2E_{23}^G \end{bmatrix} = \begin{bmatrix} u_{,1} \\ v_{,2} \\ w_{,3} \\ u_{,2} + v_{,1} \\ u_{,3} + w_{,1} \\ v_{,3} + w_{,2} \end{bmatrix} \quad , \tag{4.20}$$

Applying (4.20) to the product ansatz for the global displacements (4.14) leads to

$$\begin{bmatrix} E_{11}^G \\ E_{22}^G \\ E_{33}^G \\ 2E_{12}^G \\ 2E_{13}^G \\ 2E_{23}^G \end{bmatrix} = \begin{bmatrix} 0 & 0 & 1 & 0 & 0 & \xi^3 & 0 & 0 & 0 & 0 & 0 & 0 \\ 0 & 0 & 0 & 0 & 0 & 0 & 0 & 0 & 1 & 0 & 0 & \xi^3 \\ 0 & 0 & 0 & 0 & 0 & 0 & 0 & 0 & 0 & 0 & 0 & 0 \\ 0 & 0 & 0 & 1 & 0 & 0 & \xi^3 & 1 & 0 & 0 & \xi^3 & 0 \\ 1 & 0 & 0 & 0 & 1 & 0 & 0 & 0 & 0 & 0 & 0 & 0 \\ 0 & 1 & 0 & 0 & 0 & 0 & 0 & 0 & 0 & 1 & 0 & 0 \end{bmatrix} \begin{bmatrix} \bar{\beta}_1 \\ \bar{\beta}_2 \\ \bar{u}_{,1} \\ \bar{v}_{,1} \\ \bar{w}_{,1} \\ \bar{\beta}_{1,1} \\ \bar{\beta}_{2,1} \\ \bar{u}_{,2} \\ \bar{v}_{,2} \\ \bar{w}_{,2} \\ \bar{\beta}_{1,2} \\ \bar{\beta}_{2,2} \end{bmatrix} \quad . \tag{4.21}$$

When examining the assembly matrix in (4.21), it becomes apparent that a number of columns are linearly dependent. In order to eliminate the linear dependencies, a number of definitions are made,

$$\begin{aligned} \bar{\gamma}_1 &:= \bar{\beta}_1 + \bar{w}_{,1} \quad , & \bar{\gamma}_2 &:= \bar{\beta}_2 + \bar{w}_{,2} \quad , \\ 2\,\bar{\varepsilon}_{12} &:= \bar{v}_{,1} + \bar{u}_{,2} \quad , & 2\,\bar{\kappa}_{12} &:= \bar{\beta}_{2,1} + \bar{\beta}_{1,2} \quad . \end{aligned} \tag{4.22}$$

In (4.22), additionally to the assumptions some definitions are made which correspond to the common notation in conventional shell theory and were introduced with the vector $\boldsymbol{\varepsilon}$ in (3.21). The remaining components in $\boldsymbol{\varepsilon}$ are obtained by making some further definitions given by

$$\begin{aligned} \bar{\varepsilon}_1 &:= \bar{u}_{,1} \quad , & \bar{\varepsilon}_2 &:= \bar{v}_{,2} \quad , \\ \bar{\kappa}_{11} &:= \bar{\beta}_{1,1} \quad , & \bar{\kappa}_{22} &:= \bar{\beta}_{2,2} \quad . \end{aligned} \tag{4.23}$$

Applying the assumptions and definitions and resorting (4.21) leads to

$$\begin{bmatrix} E_{11}^G \\ E_{22}^G \\ E_{33}^G \\ 2E_{12}^G \\ 2E_{13}^G \\ 2E_{23}^G \end{bmatrix} = \begin{bmatrix} 1 & 0 & 0 & \xi^3 & 0 & 0 & 0 & 0 \\ 0 & 1 & 0 & 0 & \xi^3 & 0 & 0 & 0 \\ 0 & 0 & 0 & 0 & 0 & 0 & 0 & 0 \\ 0 & 0 & 1 & 0 & 0 & \xi^3 & 0 & 0 \\ 0 & 0 & 0 & 0 & 0 & 0 & 1 & 0 \\ 0 & 0 & 0 & 0 & 0 & 0 & 0 & 1 \end{bmatrix} \begin{bmatrix} \varepsilon_{11} \\ \varepsilon_{22} \\ 2\varepsilon_{12} \\ \kappa_{11} \\ \kappa_{22} \\ 2\kappa_{12} \\ \gamma_1 \\ \gamma_2 \end{bmatrix} , \tag{4.24}$$

which corresponds to (4.18) and (3.22). Even though the assembly matrix $\mathbf{A}_G$ is the same in (3.22) and (4.24), in chapter 3, the shell strains were derived in a geometrically nonlinear framework, whereas in this procedure they result from a linear theory. Nevertheless, this procedure serves as motivation for the separation of the extended product ansatz into a global and a local part.

The global part of the model corresponds to the Reissner-Mindlin kinematic, which leads to constant or linear paths of the shell strains through the thickness. For composite laminates, it can only predict jumps in the paths of the shell stresses, but not in the paths of the shell strains. In composite laminates with arbitrary stacking sequences that are transversely isotropic, though, there are jumps in the interlaminar strains. By means of the local part of the model, these jumps in the shell strains can be computed, leading to continuous interlaminar stresses.

At this point, the Green-Lagrange strains that emanate from the local part of the model (4.17) need to be derived from the local part of the extended product ansatz for the displacements (4.14). In principle, the local Green-Lagrange strains could be derived in a nonlinear way, just as the global Green-Lagrange strains were derived. However, because the problems to be investigated are subject to small strains, as a first approach, they are derived in a linear theory in this work. Thus, the linearized local Green-Lagrange strains are defined by

$$\mathbf{E}_L = \frac{1}{2}\left(\mathbf{H}_L^T + \mathbf{H}_L\right) = \mathrm{Grad}^s \mathbf{u}_L \quad . \tag{4.25}$$

Similar to (4.21) for the global Green-Lagrange strains, for the local Green-Lagrange strains this leads to

$$\begin{bmatrix} E_{11}^L \\ E_{22}^L \\ E_{33}^L \\ 2E_{12}^L \\ 2E_{13}^L \\ 2E_{23}^L \end{bmatrix} = \begin{bmatrix} \mathbf{0} & \mathbf{0} & \mathbf{0} & \tilde{\mathbf{M}}_u & \mathbf{0} & \mathbf{0} & \mathbf{0} & \mathbf{0} & \mathbf{0} \\ \mathbf{0} & \mathbf{0} & \mathbf{0} & \mathbf{0} & \mathbf{0} & \mathbf{0} & \mathbf{0} & \tilde{\mathbf{M}}_v & \mathbf{0} \\ \mathbf{0} & \mathbf{0} & \tilde{\mathbf{M}}_{w,3} & \mathbf{0} & \mathbf{0} & \mathbf{0} & \mathbf{0} & \mathbf{0} & \mathbf{0} \\ \mathbf{0} & \mathbf{0} & \mathbf{0} & \mathbf{0} & \tilde{\mathbf{M}}_v & \mathbf{0} & \tilde{\mathbf{M}}_u & \mathbf{0} & \mathbf{0} \\ \tilde{\mathbf{M}}_{u,3} & \mathbf{0} & \mathbf{0} & \mathbf{0} & \mathbf{0} & \tilde{\mathbf{M}}_w & \mathbf{0} & \mathbf{0} & \mathbf{0} \\ \mathbf{0} & \tilde{\mathbf{M}}_{v,3} & \mathbf{0} & \mathbf{0} & \mathbf{0} & \mathbf{0} & \mathbf{0} & \mathbf{0} & \tilde{\mathbf{M}}_w \end{bmatrix} \begin{bmatrix} \tilde{\mathbf{m}}_u \\ \tilde{\mathbf{m}}_v \\ \tilde{\mathbf{m}}_w \\ \tilde{\mathbf{m}}_{u,1} \\ \tilde{\mathbf{m}}_{v,1} \\ \tilde{\mathbf{m}}_{w,1} \\ \tilde{\mathbf{m}}_{u,2} \\ \tilde{\mathbf{m}}_{v,2} \\ \tilde{\mathbf{m}}_{w,2} \end{bmatrix} . \tag{4.26}$$

Thereby the matrix and vector on the right-hand side of the equation are denoted with symbols that conform to the global part of the concept, so that

$$\bar{\mathbf{E}}_L = \mathbf{A}_L \boldsymbol{\varepsilon}_L \quad . \tag{4.27}$$

The linear dependencies in the fourth line of $\mathbf{A}_L$ between $\tilde{\mathbf{M}}_v$ and $\tilde{\mathbf{M}}_u$ are eliminated through the interpolations in the domain for $\boldsymbol{\varepsilon}_L$ in the context of the finite element method. It is noted that even though the symbol $\boldsymbol{\varepsilon}_L$ is employed in order to use a notation that conforms to the global model, this vector contains the local displacements and their derivatives.

Inserting (4.18) and (4.27) into (4.17) and combining the assembly matrices $\mathbf{A}_G$ and $\mathbf{A}_L$ and the vectors $\boldsymbol{\varepsilon}_G$ and $\boldsymbol{\varepsilon}_L$ the Green-Lagrange strains of the global-local model can thus be expressed by

$$\tilde{\mathbf{E}} = \tilde{\mathbf{A}} \tilde{\boldsymbol{\varepsilon}} \qquad \text{with} \qquad \tilde{\boldsymbol{\varepsilon}} = \begin{bmatrix} \boldsymbol{\varepsilon}_G \\ \boldsymbol{\varepsilon}_L \end{bmatrix} \qquad \text{and} \qquad \tilde{\mathbf{A}} = [\mathbf{A}_G, \mathbf{A}_L] \quad . \tag{4.28}$$

The assembly matrix and the vector of global shell strains and local displacements associated with the global-local shell model are denoted by $\tilde{\mathbf{A}}$ and $\tilde{\boldsymbol{\varepsilon}}$ respectively.

By means of the introduced procedure, the kinematics of the shell model presented in chapter 3 is expanded with a local model. A clearly defined interface is provided in order to separate the global and the local part.

4.1.3 Stress resultants

In order to form a work-conjugated pair with $\tilde{\boldsymbol{\varepsilon}}$ the vector $\tilde{\boldsymbol{\sigma}}$ containing the stress resultants of the global-local model is introduced and defined by

$$\tilde{\boldsymbol{\sigma}} = \begin{bmatrix} \boldsymbol{\sigma}_G \\ \boldsymbol{\sigma}_L \end{bmatrix} \quad , \tag{4.29}$$

where $\boldsymbol{\sigma}_G$ is the vector of effective shell stress resultants defined in (3.33) and $\boldsymbol{\sigma}_L$ denotes the vector of higher-order stress resultants, which is set to zero in the variational formulation described later in this chapter. The length of $\boldsymbol{\sigma}_L$ corresponds to the length of $\boldsymbol{\varepsilon}_L$.

The addition of the local model influences the internal virtual work done by the composite shell. In chapter 3.3.2, the internal virtual work was introduced as the integration over the body of the variation of the strain-energy function (3.45). The relation between the strain-energy function Ψ in terms of the right Cauchy-Green tensor (3.45) and the strain-energy $\hat{\Psi}$ as a function of the global shell strains and the local quantities $\tilde{\boldsymbol{\varepsilon}}$, similar to (3.34), can be specified by

$$\delta W_{\text{int}} = \int_{\mathcal{B}_0} \delta \Psi \left(\mathbf{C} \right) \, \mathrm{d}V = \int_{\Omega_0} \delta \tilde{\boldsymbol{\varepsilon}}^T \frac{\partial \hat{\Psi}(\tilde{\boldsymbol{\varepsilon}})}{\partial \tilde{\boldsymbol{\varepsilon}}} \, \mathrm{d}A \quad , \tag{4.30}$$

for the global-local model. The contribution of the local model can be incorporated into the mixed variational formulation via the strain-energy function. Thus, arbitrary three-dimensional constitutive laws can be incorporated without further modifications. This is essential, in order to compute the interlaminar stresses in laminated composites. In a similar way, a procedure of how to incorporate nonlinear three-dimensional constitutive equations by including independent thickness strains is proposed in [71].

The transversely isotropic constitutive law for small strains in terms of the shell stress resultants for the global-local model is defined analogously to (3.76) and (3.77), so that

$$\tilde{\boldsymbol{\sigma}} = \frac{\partial \hat{\Psi}(\tilde{\boldsymbol{\varepsilon}})}{\partial \tilde{\boldsymbol{\varepsilon}}} = \int_{h^-}^{h^+} \tilde{\mathbf{A}}^T \bar{\mathbf{C}}_G \tilde{\mathbf{A}} \bar{\mu} \, \mathrm{d}\xi^3 \tilde{\boldsymbol{\varepsilon}} = \tilde{\mathbf{D}} \tilde{\boldsymbol{\varepsilon}} \quad , \tag{4.31}$$

and, analogous to (3.78), the corresponding strain-energy function can be specified by

$$\hat{\Psi}(\tilde{\boldsymbol{\varepsilon}}) = \frac{1}{2} \tilde{\boldsymbol{\varepsilon}}^T \tilde{\mathbf{D}} \tilde{\boldsymbol{\varepsilon}} \quad . \tag{4.32}$$

The contribution of the local part to the strain-energy function can be clarified by analyzing the material tangent matrix $\tilde{\mathbf{D}}$ for the global-local model, which can be written as

$$\tilde{\mathbf{D}} = \int_{h^-}^{h^+} \begin{bmatrix} \mathbf{A}_G^T \\ \mathbf{A}_L^T \end{bmatrix} \bar{\mathbf{C}}_G \left[\mathbf{A}_G, \, \mathbf{A}_L \right] \bar{\mu} \, \mathrm{d}\xi^3 = \begin{bmatrix} \mathbf{D}_G & \mathbf{D}_{GL} \\ \mathbf{D}_{GL}^T & \mathbf{D}_L \end{bmatrix} \quad . \tag{4.33}$$

The submatrices of the material tangent matrix $\tilde{\mathbf{D}}$ in (4.33) are thus defined by

$$\begin{aligned} \mathbf{D}_G &= \int_{h^-}^{h^+} \mathbf{A}_G^T \bar{\mathbf{C}}_G \mathbf{A}_G \bar{\mu} \, \mathrm{d}\xi^3 \quad , & \mathbf{D}_L &= \int_{h^-}^{h^+} \mathbf{A}_L^T \bar{\mathbf{C}}_G \mathbf{A}_L \bar{\mu} \, \mathrm{d}\xi^3 \quad , \\ \mathbf{D}_{GL} &= \int_{h^-}^{h^+} \mathbf{A}_G^T \bar{\mathbf{C}}_G \mathbf{A}_L \bar{\mu} \, \mathrm{d}\xi^3 \quad , & \mathbf{D}_{GL}^T &= \int_{h^-}^{h^+} \mathbf{A}_L^T \bar{\mathbf{C}}_G \mathbf{A}_G \bar{\mu} \, \mathrm{d}\xi^3 = \mathbf{D}_{LG} \quad . \end{aligned} \tag{4.34}$$

On examining (4.32) to (4.34), it becomes evident that in the strain-energy function the global and the local part of the model are not independent of each other. This makes this concept different from the concept derived in [71]. To elucidate this, the strain-energy function $\hat{\Psi}(\tilde{\boldsymbol{\varepsilon}})$ is divided into four terms with

$$\hat{\Psi}(\tilde{\boldsymbol{\varepsilon}}) = \frac{1}{2} \boldsymbol{\varepsilon}_G^T \mathbf{D}_G \boldsymbol{\varepsilon}_G + \frac{1}{2} \boldsymbol{\varepsilon}_G^T \mathbf{D}_{GL} \boldsymbol{\varepsilon}_L + \frac{1}{2} \boldsymbol{\varepsilon}_L^T \mathbf{D}_{GL}^T \boldsymbol{\varepsilon}_G + \frac{1}{2} \boldsymbol{\varepsilon}_L^T \mathbf{D}_L \boldsymbol{\varepsilon}_L \quad . \tag{4.35}$$

With (4.29) and (4.31) the vector of effective shell stress resultants $\boldsymbol{\sigma}_G$ and higher-order stress resultants $\boldsymbol{\sigma}_L$ can be derived from the strain-energy function by means of

$$\begin{bmatrix} \boldsymbol{\sigma}_G \\ \boldsymbol{\sigma}_L \end{bmatrix} = \frac{\partial \hat{\Psi}(\tilde{\boldsymbol{\varepsilon}})}{\partial \tilde{\boldsymbol{\varepsilon}}} = \begin{bmatrix} \dfrac{\partial \hat{\Psi}}{\partial \boldsymbol{\varepsilon}_G} \\ \dfrac{\partial \hat{\Psi}}{\partial \boldsymbol{\varepsilon}_L} \end{bmatrix} = \int_{h^-}^{h^+} \begin{bmatrix} \mathbf{A}_G^T \\ \mathbf{A}_L^T \end{bmatrix} \bar{\mathbf{S}} \, \bar{\mu} \, \mathrm{d}\xi^3 \quad . \tag{4.36}$$

Considering (4.35) the vector of effective stress resultants $\boldsymbol{\sigma}_G$ can thus be written as

$$\boldsymbol{\sigma}_G = \frac{\partial \hat{\Psi}}{\partial \boldsymbol{\varepsilon}_G} = \mathbf{D}_G \boldsymbol{\varepsilon}_G + \mathbf{D}_{GL} \boldsymbol{\varepsilon}_L \quad , \tag{4.37}$$

and the vector of higher-order stress resultants $\boldsymbol{\sigma}_L$ can be expressed by means of

$$\boldsymbol{\sigma}_L = \frac{\partial \hat{\Psi}}{\partial \boldsymbol{\varepsilon}_L} = \mathbf{D}_{GL}^T \boldsymbol{\varepsilon}_G + \mathbf{D}_L \boldsymbol{\varepsilon}_L = \mathbf{0} \quad . \tag{4.38}$$

As already mentioned, the higher-order stress resultants are set to zero in the variational formulation. When examining (4.37) it becomes obvious that the additional quantities pertaining to the local part of the concept introduce additional terms to the effective stress resultants of the shell model, leading to changed results. This is not desirable, since it has been established that the effective stress resultants derived from the global model accurately describe the real distribution of the effective shell stress resultants. In the following section, a remedy will be presented in the form of an orthogonalization procedure for the local part of the model.

4.2 Orthogonalization procedure

The additional effective stress resultants introduced through the local concept are a result of the coupling of the global and the local model. The local model is to be able to compute the correct path of the interlaminar stresses. Yet, because of the second coupling term in (4.37), all stress resultants are manipulated. Therefore, an orthogonality condition is introduced, which requires that the local part of the model does not modify the effective membrane stress resultants $\tilde{n}^{11}$, $\tilde{n}^{22}$ and $\tilde{n}^{12}$ and effective stress couple resultants $\tilde{m}^{11}$, $\tilde{m}^{22}$ and $\tilde{m}^{12}$. On the other hand, numerical studies have revealed that small changes of the effective shear stress resultants $\tilde{q}^1$ and $\tilde{q}^2$ have to be permitted. In the following, the orthogonality condition will be considered separately for the local in-plane displacements represented by u and v. In order to impose the aforementioned conditions, the requirement

$$\boldsymbol{\sigma}_{GLm} = \int_{h^-}^{h^+} \mathbf{A}_{Gm}^T \bar{\mathbf{S}}_{Lm} \bar{\mu} \, \mathrm{d}\xi^3 = \int_{h^-}^{h^+} \mathbf{A}_{Gm}^T \mathbf{C}_m \mathbf{A}_{Lm} \bar{\mu} \, \mathrm{d}\xi^3 \boldsymbol{\varepsilon}_{Lm} = \mathbf{0} \tag{4.39}$$

necessitates fulfillment. In (4.39), $\mathbf{C}_m$ was defined in (3.75), $\boldsymbol{\sigma}_{GLm}$ is defined by $\boldsymbol{\sigma}_{GLm} = [\tilde{n}_{GL}^{11}, \tilde{n}_{GL}^{22}, \tilde{n}_{GL}^{12}, \tilde{m}_{GL}^{11}, \tilde{m}_{GL}^{22}, \tilde{m}_{GL}^{12}]^T$, $\bar{\mathbf{S}}_{Lm}$ is defined by $\bar{\mathbf{S}}_{Lm} = [S_{Lm}^{11}, S_{Lm}^{22}, S_{Lm}^{12}]^T$, $\boldsymbol{\varepsilon}_{Lm}$ is defined by $\boldsymbol{\varepsilon}_{Lm} = [\tilde{\mathbf{m}}_{u,1}, \tilde{\mathbf{m}}_{v,1}, \tilde{\mathbf{m}}_{u,2}, \tilde{\mathbf{m}}_{v,2}]^T$ and $\mathbf{A}_{Gm}$ and, with (4.16), $\mathbf{A}_{Lm}$ are defined by

$$\mathbf{A}_{Gm} = \begin{bmatrix} 1 & 0 & 0 & \xi^3 & 0 & 0 \\ 0 & 1 & 0 & 0 & \xi^3 & 0 \\ 0 & 0 & 1 & 0 & 0 & \xi^3 \end{bmatrix} \quad \text{and} \quad \mathbf{A}_{Lm} = \begin{bmatrix} \tilde{\mathbf{M}}_u & \mathbf{0} & \mathbf{0} & \mathbf{0} \\ \mathbf{0} & \mathbf{0} & \mathbf{0} & \tilde{\mathbf{M}}_v \\ \mathbf{0} & \tilde{\mathbf{M}}_v & \tilde{\mathbf{M}}_u & \mathbf{0} \end{bmatrix} \quad . \tag{4.40}$$

Requirement (4.39) enforces that the local model does not introduce additional effective membrane stress resultants or effective stress couple resultants by setting the appropriate part of the second coupling term in (4.37) to zero. The orthogonality condition (4.39) is trivially met if

$$\int_{h^-}^{h^+} \mathbf{A}_{Gm}^T \mathbf{C}_m \mathbf{A}_{Lm} \bar{\mu} \, \mathrm{d}\xi^3 = \mathbf{0} \tag{4.41}$$

holds. Exploiting (4.41) leads to the following condition that needs to be fulfilled,

$$\int_{h^-}^{h^+} \begin{bmatrix} C_{11}\tilde{\mathbf{M}}_u & C_{14}\tilde{\mathbf{M}}_u & C_{12}\tilde{\mathbf{M}}_v & C_{14}\tilde{\mathbf{M}}_v \\ C_{21}\tilde{\mathbf{M}}_u & C_{24}\tilde{\mathbf{M}}_u & C_{22}\tilde{\mathbf{M}}_v & C_{24}\tilde{\mathbf{M}}_v \\ C_{41}\tilde{\mathbf{M}}_u & C_{44}\tilde{\mathbf{M}}_u & C_{42}\tilde{\mathbf{M}}_v & C_{44}\tilde{\mathbf{M}}_v \\ \xi^3 C_{11}\tilde{\mathbf{M}}_u & \xi^3 C_{14}\tilde{\mathbf{M}}_u & \xi^3 C_{12}\tilde{\mathbf{M}}_v & \xi^3 C_{14}\tilde{\mathbf{M}}_v \\ \xi^3 C_{21}\tilde{\mathbf{M}}_u & \xi^3 C_{24}\tilde{\mathbf{M}}_u & \xi^3 C_{22}\tilde{\mathbf{M}}_v & \xi^3 C_{24}\tilde{\mathbf{M}}_v \\ \xi^3 C_{41}\tilde{\mathbf{M}}_u & \xi^3 C_{44}\tilde{\mathbf{M}}_u & \xi^3 C_{42}\tilde{\mathbf{M}}_v & \xi^3 C_{44}\tilde{\mathbf{M}}_v \end{bmatrix} \bar{\mu} \, \mathrm{d}\xi^3 = \mathbf{0} \quad . \tag{4.42}$$

The two columns on the left side of the matrix in (4.42) need to be fulfilled for the ξ^1-direction, while the two columns on the right side need to be fulfilled for the ξ^2-direction. In laminated shells made up of arbitrary stacking sequences the stiffness parameters vary through the thickness with each different layer, so that in (4.42), aside from the matrices $\tilde{\mathbf{M}}_u$ and $\tilde{\mathbf{M}}_v$, the stiffness parameters C_{ij} depend on ξ^3. Alternatively to (4.42), the orthogonality condition can be expressed by a sum of integrations in sections for each layer, so that

$$\sum_{i=1}^{n} \int_{t_i^-}^{t_i^+} \begin{bmatrix} C_{11}^i\tilde{\mathbf{M}}_u & C_{14}^i\tilde{\mathbf{M}}_u & C_{12}^i\tilde{\mathbf{M}}_v & C_{14}^i\tilde{\mathbf{M}}_v \\ C_{21}^i\tilde{\mathbf{M}}_u & C_{24}^i\tilde{\mathbf{M}}_u & C_{22}^i\tilde{\mathbf{M}}_v & C_{24}^i\tilde{\mathbf{M}}_v \\ C_{41}^i\tilde{\mathbf{M}}_u & C_{44}^i\tilde{\mathbf{M}}_u & C_{42}^i\tilde{\mathbf{M}}_v & C_{44}^i\tilde{\mathbf{M}}_v \\ \xi^3 C_{11}^i\tilde{\mathbf{M}}_u & \xi^3 C_{14}^i\tilde{\mathbf{M}}_u & \xi^3 C_{12}^i\tilde{\mathbf{M}}_v & \xi^3 C_{14}^i\tilde{\mathbf{M}}_v \\ \xi^3 C_{21}^i\tilde{\mathbf{M}}_u & \xi^3 C_{24}^i\tilde{\mathbf{M}}_u & \xi^3 C_{22}^i\tilde{\mathbf{M}}_v & \xi^3 C_{24}^i\tilde{\mathbf{M}}_v \\ \xi^3 C_{41}^i\tilde{\mathbf{M}}_u & \xi^3 C_{44}^i\tilde{\mathbf{M}}_u & \xi^3 C_{42}^i\tilde{\mathbf{M}}_v & \xi^3 C_{44}^i\tilde{\mathbf{M}}_v \end{bmatrix} \bar{\mu} \, \mathrm{d}\xi^3 = \mathbf{0} \quad . \tag{4.43}$$

Since there are a total of 24 entries in the matrices in (4.42) and considering (4.16), there are $24\,(3n-1)$ equations that need to be fulfilled, $12\,(3n-1)$ associated with the ξ^1-direction and the same number associated with the ξ^2-direction. It is obvious that in general, condition (4.42) is not met. Each shape function is present a total of twelve times, so that without further considerations, each shape function would need to be modified by introducing twelve parameters, so that the requirement is met. A number of different schemes are presented in the following sections, where the number of parameters is reduced by some considerations.

4.2.1 Homogeneous setup in thickness direction

If the material under consideration has a homogeneous setup in thickness direction, the stiffness parameters in (4.42) are constant through the thickness. This is the case, for example, in an isotropic material or when the composite consists of only one unidirectional layer with the same fiber angle φ. Many of the entries in the matrix then are linearly dependent and the requirement (4.42) can therefore be reduced to

$$\int_{h^-}^{h^+} \begin{bmatrix} \tilde{\mathbf{M}}_u \\ \xi^3 \tilde{\mathbf{M}}_u \end{bmatrix} \bar{\mu} \, \mathrm{d}\xi^3 = \mathbf{0} \qquad \text{and} \qquad \int_{h^-}^{h^+} \begin{bmatrix} \tilde{\mathbf{M}}_v \\ \xi^3 \tilde{\mathbf{M}}_v \end{bmatrix} \bar{\mu} \, \mathrm{d}\xi^3 = \mathbf{0} \quad , \tag{4.44}$$

where the requirement has been separated into one part for the ξ^1-direction and one part for the ξ^2-direction. Requirement (4.44) could also be expressed as the sum of integrations over the thickness of the layers in the sequence, similar to (4.43). The number of equations that need to be fulfilled in (4.44) is $4(3n-1)$. In (4.44), each shape function appears twice, so that a corresponding number of parameters must be introduced for each shape function in order to meet requirement (4.44). The shape functions $H_{u(j)}$, $I_{u(i)}$, and $J_{u(i)}$ defined in (4.7), (4.9), and (4.11) are thus modified to become $\hat{H}_{u(j)}$, $\hat{I}_{u(i)}$, and $\hat{J}_{u(i)}$ for the ξ^1-direction, defined by

$$\hat{H}_{u(j)} = \begin{cases} \dfrac{1}{2}(1-\zeta_1) + \alpha^H_{u1} + \beta^H_{u1}\xi^3 & \text{if } j = 1 \\ \left[\dfrac{1}{2}(1+\zeta_{j-1}) + \alpha^H_{u(j-1)} + \beta^H_{u(j-1)}\xi^3\right] & \\ \qquad \left[\dfrac{1}{2}(1-\zeta_j) + \alpha^H_{uj} + \beta^H_{uj}\xi^3\right] & \text{if } j > 1 \text{ and } j < (n+1) \\ \dfrac{1}{2}(1+\zeta_n) + \alpha^H_{un} + \beta^H_{un}\xi^3 & \text{if } j = (n+1) \quad , \end{cases} \tag{4.45}$$

$$\hat{I}_{u(i)} = 1 - \zeta_i^2 + \alpha^I_{ui} + \beta^I_{ui}\xi^3 \quad ,$$

$$\hat{J}_{u(i)} = \frac{8}{3}\zeta_i\left(1-\zeta_i^2\right) + \alpha^J_{ui} + \beta^J_{ui}\xi^3 \quad .$$

The definitions are analogous for the ξ^2-direction. The notation $\hat{(\bullet)}$ has been introduced to denote that two parameters have been added to the shape functions. It is pointed out that even though the shape functions associated with the ξ^1-direction and the ξ^2-direction are identical, the parameters introduced can differ.

The derivatives of the modified shape functions defined in (4.45) are specified by

$$\hat{H}_{u(j),3} = \begin{cases} -\dfrac{1}{t_1} + \beta^H_{u1} & \text{if } j = 1 \\ \left[\dfrac{1}{t_{j-1}} + \beta^H_{u(j-1)} \;\middle|\; -\dfrac{1}{t_j} + \beta^H_{uj} \right] & \text{if } j > 1 \text{ and } j < (n+1) \\ \dfrac{1}{t_n} + \beta^H_{un} & \text{if } j = (n+1) \quad , \end{cases} \tag{4.46}$$

$$\hat{I}_{u(i),3} = -\frac{4}{t_i}\zeta_i + \beta^I_{ui} \quad ,$$

$$\hat{J}_{u(i),3} = \frac{16}{3t_i}\left(1 - 3\zeta_i^2\right) + \beta^J_{ui} \quad .$$

It is noted that the shape functions $\hat{H}_{u1}$ and $\hat{H}_{u(n+1)}$ in (4.45) and their respective derivatives in (4.46) are specified for the sake of completeness, even though they are eliminated when modifying the extended product ansatz to accommodate for the global model.

A system of equations is now set up to derive the unknown parameters added to the shape functions. Inserting the modified shape functions (4.45) with the added parameters, requirement (4.44) is rewritten as

$$\int_{h^-}^{h^+} \begin{bmatrix} \hat{\mathbf{M}}_u \\ \xi^3 \hat{\mathbf{M}}_u \end{bmatrix} \bar{\mu}\, \mathrm{d}\xi^3 = \mathbf{0} \qquad \text{and} \qquad \int_{h^-}^{h^+} \begin{bmatrix} \hat{\mathbf{M}}_v \\ \xi^3 \hat{\mathbf{M}}_v \end{bmatrix} \bar{\mu}\, \mathrm{d}\xi^3 = \mathbf{0} \quad , \tag{4.47}$$

where the matrices $\hat{\mathbf{M}}_u$ and $\hat{\mathbf{M}}_v$ contain the modified shape functions and are defined by

$$\hat{\mathbf{M}}_u = \tilde{\mathbf{M}}_u + \tilde{\boldsymbol{\alpha}}_u + \xi^3 \tilde{\boldsymbol{\beta}}_u \qquad \text{and} \qquad \hat{\mathbf{M}}_v = \tilde{\mathbf{M}}_v + \tilde{\boldsymbol{\alpha}}_v + \xi^3 \tilde{\boldsymbol{\beta}}_v \quad . \tag{4.48}$$

In analogy to (4.16), in (4.48) the vectors $\tilde{\boldsymbol{\alpha}}_u$, $\tilde{\boldsymbol{\beta}}_u$, $\tilde{\boldsymbol{\alpha}}_v$, and $\tilde{\boldsymbol{\beta}}_v$ are introduced with

$$\begin{aligned} \tilde{\boldsymbol{\alpha}}_u &= \left[\tilde{\boldsymbol{\alpha}}^H_u, \boldsymbol{\alpha}^I_u, \boldsymbol{\alpha}^J_u\right] \quad , & \tilde{\boldsymbol{\beta}}_u &= \left[\tilde{\boldsymbol{\beta}}^H_u, \boldsymbol{\beta}^I_u, \boldsymbol{\beta}^J_u\right] \quad , \\ \tilde{\boldsymbol{\alpha}}_v &= \left[\tilde{\boldsymbol{\alpha}}^H_v, \boldsymbol{\alpha}^I_v, \boldsymbol{\alpha}^J_u\right] \quad , & \tilde{\boldsymbol{\beta}}_v &= \left[\tilde{\boldsymbol{\beta}}^H_v, \boldsymbol{\beta}^I_v, \boldsymbol{\beta}^J_u\right] \quad , \end{aligned} \tag{4.49}$$

which contain the parameters added to the shape functions, so that

$$\begin{aligned} \tilde{\boldsymbol{\alpha}}^H_u &= \left[\alpha^H_{u2},\ \alpha^H_{uj},\ \ldots\ \alpha^H_{un}\right] \quad , & \boldsymbol{\alpha}^I_u &= \left[\alpha^I_{u1},\ \alpha^I_{ui},\ \ldots\ \alpha^I_{un}\right] \quad , \\ \tilde{\boldsymbol{\beta}}^H_u &= \left[\beta^H_{u2},\ \beta^H_{uj},\ \ldots\ \beta^H_{un}\right] \quad , & \boldsymbol{\beta}^I_u &= \left[\beta^I_{u1},\ \beta^I_{ui},\ \ldots\ \beta^I_{un}\right] \quad , \\ \tilde{\boldsymbol{\alpha}}^H_v &= \left[\alpha^H_{v2},\ \alpha^H_{vj},\ \ldots\ \alpha^H_{vn}\right] \quad , & \boldsymbol{\alpha}^I_v &= \left[\alpha^I_{v1},\ \alpha^I_{vi},\ \ldots\ \alpha^I_{vn}\right] \quad , \\ \tilde{\boldsymbol{\beta}}^H_v &= \left[\beta^H_{v2},\ \beta^H_{vj},\ \ldots\ \beta^H_{vn}\right] \quad , & \boldsymbol{\beta}^I_v &= \left[\beta^I_{v1},\ \beta^I_{vi},\ \ldots\ \beta^I_{vn}\right] \quad , \end{aligned}$$

$$\begin{aligned}
\boldsymbol{\alpha}_u^J &= \left[\alpha_{u1}^J,\ \alpha_{ui}^J,\ \dots\ \alpha_{un}^J\right] \quad , \\
\boldsymbol{\beta}_u^J &= \left[\beta_{u1}^J,\ \beta_{ui}^J,\ \dots\ \beta_{un}^J\right] \quad , \\
\boldsymbol{\alpha}_v^J &= \left[\alpha_{v1}^J,\ \alpha_{vi}^J,\ \dots\ \alpha_{vn}^J\right] \quad , \\
\boldsymbol{\beta}_v^J &= \left[\beta_{v1}^J,\ \beta_{vi}^J,\ \dots\ \beta_{vn}^J\right] \quad .
\end{aligned} \tag{4.50}$$

Considering (4.50), $2\,(n-1)$ unknown parameters are introduced in (4.47) with $\tilde{\boldsymbol{\alpha}}_u^H$ and $\tilde{\boldsymbol{\beta}}_u^H$, and $4n$ parameters are introduced with $\boldsymbol{\alpha}_u^I$, $\boldsymbol{\beta}_u^I$, $\boldsymbol{\alpha}_u^J$, and $\boldsymbol{\beta}_u^J$. This leads to $2\,(3n-1)$ parameters associated with the ξ^1-direction. The same number of parameters is introduced for the ξ^2-direction and thus the total number of parameters is $4\,(3n-1)$, corresponding to the number of equations that need to be fulfilled in (4.44).

Considering (4.48), the system of equations (4.47) can be rearranged and rewritten as

$$\begin{bmatrix} s_0 & s_1 \\ s_1 & s_2 \end{bmatrix} \begin{bmatrix} \tilde{\boldsymbol{\alpha}}_u \\ \tilde{\boldsymbol{\beta}}_u \end{bmatrix} = \int_{h^-}^{h^+} \begin{bmatrix} \tilde{\mathbf{M}}_u \\ \xi^3 \tilde{\mathbf{M}}_u \end{bmatrix} \bar{\mu}\, \mathrm{d}\xi^3 \tag{4.51}$$

for the ξ^1-direction and

$$\begin{bmatrix} s_0 & s_1 \\ s_1 & s_2 \end{bmatrix} \begin{bmatrix} \tilde{\boldsymbol{\alpha}}_v \\ \tilde{\boldsymbol{\beta}}_v \end{bmatrix} = \int_{h^-}^{h^+} \begin{bmatrix} \tilde{\mathbf{M}}_v \\ \xi^3 \tilde{\mathbf{M}}_v \end{bmatrix} \bar{\mu}\, \mathrm{d}\xi^3 \tag{4.52}$$

for the ξ^2-direction, where in (4.51) and (4.52) the results of integrations over the thickness with s_0, s_1, and s_2 are defined, so that

$$\begin{aligned}
s_0 &= \int_{h^-}^{h^+} 1 \bar{\mu}\, \mathrm{d}\xi^3 = \sum_{i=1}^{n} t_i \quad , \\
s_1 &= \int_{h^-}^{h^+} \xi^3 \bar{\mu}\, \mathrm{d}\xi^3 = \sum_{i=1}^{n} t_i \xi_s^{3i} \quad , \\
s_2 &= \int_{h^-}^{h^+} (\xi^3)^2 \bar{\mu}\, \mathrm{d}\xi^3 = \sum_{i=1}^{n} \left(\frac{(t_i)^3}{12} + t_i (\xi_{si}^3)^2 \right) \quad ,
\end{aligned} \tag{4.53}$$

where t_i denotes the thickness of layer i and ξ_{si}^3 denotes the distance of the middle of the layer i to the reference surface, as they were introduced in figure 3.6. The orthogonalization procedure for a material with a homogeneous setup in thickness direction thus leads to the same system of equations for the ξ^1- and the ξ^2-direction and thus also to the same parameters that are added to the shape functions. With (4.51), a total of $2(3n-1)$

equations have been established to derive the $2(3n-1)$ parameters collected in the vectors $\tilde{\boldsymbol{\alpha}}_u$ and $\tilde{\boldsymbol{\beta}}_u$. In the same way, with (4.52) a total of $2(3n-1)$ equations have been established to derive the $2(3n-1)$ parameters collected in the vectors $\tilde{\boldsymbol{\alpha}}_v$ and $\tilde{\boldsymbol{\beta}}_v$.

If the reference plane is in the middle of the shell, the orthogonalization procedure can be simplified. In this case the components s_1 in (4.51) and in (4.52) are zero and the systems of equations are decoupled, so that (4.51) reduces to

$$\tilde{\boldsymbol{\alpha}}_u = \frac{1}{s_0} \int_{h^-}^{h^+} \tilde{\mathbf{M}}_u \bar{\mu} \, \mathrm{d}\xi^3 \qquad \text{and} \qquad \tilde{\boldsymbol{\beta}}_u = \frac{1}{s_2} \int_{h^-}^{h^+} \xi^3 \tilde{\mathbf{M}}_u \bar{\mu} \, \mathrm{d}\xi^3 \quad , \tag{4.54}$$

and in an analogous way, (4.52) reduces to

$$\tilde{\boldsymbol{\alpha}}_v = \frac{1}{s_0} \int_{h^-}^{h^+} \tilde{\mathbf{M}}_v \bar{\mu} \, \mathrm{d}\xi^3 \qquad \text{and} \qquad \tilde{\boldsymbol{\beta}}_v = \frac{1}{s_2} \int_{h^-}^{h^+} \xi^3 \tilde{\mathbf{M}}_v \bar{\mu} \, \mathrm{d}\xi^3 \quad . \tag{4.55}$$

The systems of equations thus are reduced to simple equations by which the required parameters can be easily derived.

It is important to note that for a specific geometry of the laminate equations (4.51) and (4.52), or, if the reference surface lies in the middle of the shell, (4.54) and (4.55), have to be solved only once before the commencement of the finite element simulation. Thus, in this case the orthogonalization procedure does not lead to a significant increase in computation time.

The proposed orthogonalization procedure leads to good results for a composite shell with a homogeneous setup in thickness direction, as will be shown for a simply-supported plate in chapter 8.1.1. It can also be applied to inhomogeneous composite shells with multiple layers and arbitrary stacking sequences. Since requirement (4.42) is not met then, it only yields results that are correct on an average. It does constitute an improvement over the global model, though, as the path of the interlaminar shear stresses is approximated with a quadratic parable, rather than with piecewise constant results. In this way, the boundary conditions at the top and the bottom of the composite are met and the values are continuous at layer boundaries. The higher the number of layers in the composite shell is, the better the results can be approximated by a quadratic parable, as can be seen from the example with 15 layers in chapter 8.1.1. Thus, in this case, the orthogonalization procedure is capable to yield satisfactory predictions of peaks in the interlaminar shear stresses. In the next section, different orthogonalization procedures for composite shells with an inhomogeneous setup in thickness direction are derived.

4.2.2 Inhomogeneous setup in thickness direction

In this section, two orthogonalization procedures for composite shells with arbitrary stacking sequences are derived, for which requirement (4.42) must be met, since using an orthogonalization procedure as derived in the preceding section leads to results that are only correct on an average.

Summation procedure

In the first procedure, the twelve equations in the first two columns in the orthogonalization requirement (4.42) for the ξ^1-direction and the twelve equations in the other two columns for the ξ^2-direction are united to two equations respectively by a summation of several equations. In composite shells with multiple layers and arbitrary stacking sequences the values of the stiffness parameters jump at the layer boundaries, thus depending on the thickness coordinate ξ^3. The orthogonalization requirement is expressed as a summation over integration over the thickness of each layer similar to (4.43), so that it becomes

$$\sum_{i=1}^{n} \int_{t_i^-}^{t_i^+} \begin{bmatrix} C_u^i \tilde{\mathbf{M}}_u \\ C_u^i \xi^3 \tilde{\mathbf{M}}_u \end{bmatrix} \bar{\mu}\, \mathrm{d}\xi^3 = \mathbf{0} \qquad \text{and} \qquad \sum_{i=1}^{n} \int_{t_i^-}^{t_i^+} \begin{bmatrix} C_v^i \tilde{\mathbf{M}}_v \\ C_v^i \xi^3 \tilde{\mathbf{M}}_v \end{bmatrix} \bar{\mu}\, \mathrm{d}\xi^3 = \mathbf{0} \quad , \tag{4.56}$$

where C_u^i and C_v^i are defined as summations over the stiffness parameters in layer i, so that

$$\begin{aligned} C_u^i &= C_{11}^i + C_{21}^i + C_{41}^i + C_{14}^i + C_{24}^i + C_{44}^i \quad , \\ C_v^i &= C_{12}^i + C_{22}^i + C_{42}^i + C_{14}^i + C_{24}^i + C_{44}^i \quad . \end{aligned} \tag{4.57}$$

Analogous to the orthogonalization procedure in the preceding section two parameters are introduced for every shape function and a system of equations is set up to derive the unknown parameters by rewriting (4.56) as

$$\sum_{i=1}^{n} \int_{t_i^-}^{t_i^+} \begin{bmatrix} C_u^i \hat{\mathbf{M}}_u \\ C_u^i \xi^3 \hat{\mathbf{M}}_u \end{bmatrix} \bar{\mu}\, \mathrm{d}\xi^3 = \mathbf{0} \qquad \text{and} \qquad \sum_{i=1}^{n} \int_{t_i^-}^{t_i^+} \begin{bmatrix} C_v^i \hat{\mathbf{M}}_v \\ C_v^i \xi^3 \hat{\mathbf{M}}_v \end{bmatrix} \bar{\mu}\, \mathrm{d}\xi^3 = \mathbf{0} \quad , \tag{4.58}$$

where $\hat{\mathbf{M}}_u$ and $\hat{\mathbf{M}}_v$ are defined in (4.48), and thus, rearranging (4.58), the system of equations can be rewritten as

$$\begin{bmatrix} s_{u0} & s_{u1} \\ s_{u1} & s_{u2} \end{bmatrix} \begin{bmatrix} \tilde{\boldsymbol{\alpha}}_u \\ \tilde{\boldsymbol{\beta}}_u \end{bmatrix} = \sum_{i=1}^{n} \int_{t_i^-}^{t_i^+} \begin{bmatrix} C_u^i \tilde{\mathbf{M}}_u \\ C_u^i \xi^3 \tilde{\mathbf{M}}_u \end{bmatrix} \bar{\mu}\, \mathrm{d}\xi^3 \tag{4.59}$$

for the ξ^1-direction and

$$\begin{bmatrix} s_{v0} & s_{v1} \\ s_{v1} & s_{v2} \end{bmatrix} \begin{bmatrix} \tilde{\boldsymbol{\alpha}}_v \\ \tilde{\boldsymbol{\beta}}_v \end{bmatrix} = \sum_{i=1}^{n} \int_{t_i^-}^{t_i^+} \begin{bmatrix} C_v^i \tilde{\mathbf{M}}_v \\ C_v^i \xi^3 \tilde{\mathbf{M}}_v \end{bmatrix} \bar{\mu}\, \mathrm{d}\xi^3 \tag{4.60}$$

for the ξ^2-direction. In (4.59) and (4.60), the results of integrations over the thickness with s_{u0}^C, s_{u1}^C, s_{u2}^C, s_{v0}^C, s_{v1}^C and s_{v2}^C are defined, so that

$$
\begin{aligned}
s_{u0} &= \sum_{i=1}^{n} \int_{t_i^-}^{t_i^+} C_u^i \bar{\mu} \, \mathrm{d}\xi^3 = \sum_{i=1}^{n} C_u^i t_i \quad , \\
s_{u1} &= \sum_{i=1}^{n} \int_{t_i^-}^{t_i^+} C_u^i \xi^3 \bar{\mu} \, \mathrm{d}\xi^3 = \sum_{i=1}^{n} C_u^i t_i \xi_s^{3i} \quad , \\
s_{u2} &= \sum_{i=1}^{n} \int_{t_i^-}^{t_i^+} C_u^i (\xi^3)^2 \bar{\mu} \, \mathrm{d}\xi^3 = \sum_{i=1}^{n} C_u^i \left(\frac{(t_i)^3}{12} + t_i (\xi_{si}^3)^2 \right) \quad ,
\end{aligned}
\tag{4.61}
$$

and the factors s_v can be derived in an analogous way by replacing the u in (4.61) with v. Similar to the preceding section, with (4.59) and (4.60) a total of $4\,(3n-1)$ equations have been established to derive the $4(3n-1)$ parameters collected in the vectors $\tilde{\boldsymbol{\alpha}}_u$, $\tilde{\boldsymbol{\beta}}_u$, $\tilde{\boldsymbol{\alpha}}_v$ and $\tilde{\boldsymbol{\beta}}_v$. Unlike the orthogonalization procedure for homogeneous composite shells, in this procedure the derived parameters in $\tilde{\boldsymbol{\alpha}}_u$ and $\tilde{\boldsymbol{\alpha}}_v$ and the parameters in $\tilde{\boldsymbol{\beta}}_u$ and $\boldsymbol{\beta}_v$ differ, because of the varying stiffness parameters.

If the reference plane is in the middle of the shell and the stacking sequence is symmetric, then the orthogonalization procedure can be simplified. In this case the components s_{u1} in (4.59) and s_{v1} in (4.60) are zero and the systems of equations are decoupled, so that (4.59) reduces to

$$
\tilde{\boldsymbol{\alpha}}_u = \frac{1}{s_{u0}} \sum_{i=1}^{n} \int_{t_i^-}^{t_i^+} C_u^i \tilde{\mathbf{M}}_u \bar{\mu} \, \mathrm{d}\xi^3 \qquad \text{and} \qquad \tilde{\boldsymbol{\beta}}_u = \frac{1}{s_{u2}} \sum_{i=1}^{n} \int_{t_i^-}^{t_i^+} \xi^3 C_u^i \tilde{\mathbf{M}}_u \bar{\mu} \, \mathrm{d}\xi^3 \quad , \tag{4.62}
$$

after some rearrangement. In an analogous way, (4.60) reduces to

$$
\tilde{\boldsymbol{\alpha}}_v = \frac{1}{s_{v0}} \sum_{i=1}^{n} \int_{t_i^-}^{t_i^+} C_v^i \tilde{\mathbf{M}}_v \bar{\mu} \, \mathrm{d}\xi^3 \qquad \text{and} \qquad \tilde{\boldsymbol{\beta}}_v = \frac{1}{s_{v2}} \sum_{i=1}^{n} \int_{t_i^-}^{t_i^+} \xi^3 C_v^i \tilde{\mathbf{M}}_v \bar{\mu} \, \mathrm{d}\xi^3 \quad . \tag{4.63}
$$

The systems of equations thus reduce to simple equations by which the required parameters can be easily derived. The proposed summation procedure seeks to approximate the path of the interlaminar shear stresses, but is incapable of computing the exact path, since the equations in the orthogonality requirement are not fulfilled exactly, but only on an average.

Method of least squares

In the second procedure, the method of least squares is used to derive an approximate solution of the overdetermined system of equations in (4.42). Introducing two parameters for every shape function and setting up a system of equations to derive the unknown parameters the orthogonalization requirement expressed as a summation over integration over the thickness of each layer in (4.43) is rewritten as

$$\sum_{i=1}^{n} \int_{t_i^-}^{t_i^+} \begin{bmatrix} C_{11}^i \hat{\mathbf{M}}_u & C_{14}^i \hat{\mathbf{M}}_u & C_{12}^i \hat{\mathbf{M}}_v & C_{14}^i \hat{\mathbf{M}}_v \\ C_{21}^i \hat{\mathbf{M}}_u & C_{24}^i \hat{\mathbf{M}}_u & C_{22}^i \hat{\mathbf{M}}_v & C_{24}^i \hat{\mathbf{M}}_v \\ C_{41}^i \hat{\mathbf{M}}_u & C_{44}^i \hat{\mathbf{M}}_u & C_{42}^i \hat{\mathbf{M}}_v & C_{44}^i \hat{\mathbf{M}}_v \\ \xi^3 C_{11}^i \hat{\mathbf{M}}_u & \xi^3 C_{14}^i \hat{\mathbf{M}}_u & \xi^3 C_{12}^i \hat{\mathbf{M}}_v & \xi^3 C_{14}^i \hat{\mathbf{M}}_v \\ \xi^3 C_{21}^i \hat{\mathbf{M}}_u & \xi^3 C_{24}^i \hat{\mathbf{M}}_u & \xi^3 C_{22}^i \hat{\mathbf{M}}_v & \xi^3 C_{24}^i \hat{\mathbf{M}}_v \\ \xi^3 C_{41}^i \hat{\mathbf{M}}_u & \xi^3 C_{44}^i \hat{\mathbf{M}}_u & \xi^3 C_{42}^i \hat{\mathbf{M}}_v & \xi^3 C_{44}^i \hat{\mathbf{M}}_v \end{bmatrix} \bar{\mu} \, \mathrm{d}\xi^3 = \mathbf{0} \quad , \tag{4.64}$$

where $\hat{\mathbf{M}}_u$ and $\hat{\mathbf{M}}_v$ are defined in (4.48). The first two columns of the matrix in (4.64) need to be fulfilled for the ξ^1-direction, while the other two columns need to be fulfilled for the ξ^2-direction. Rearranging (4.64) and separating for the two directions, the system of equations can be rewritten as

$$\begin{bmatrix} \mathbf{s}_{u0} & \mathbf{s}_{u1} \\ \mathbf{s}_{u1} & \mathbf{s}_{u2} \end{bmatrix} \begin{bmatrix} \tilde{\boldsymbol{\alpha}}_u \\ \tilde{\boldsymbol{\beta}}_u \end{bmatrix} = \sum_{i=1}^{n} \int_{t_i^-}^{t_i^+} \begin{bmatrix} \tilde{\mathbf{M}}_u^C \\ \xi^3 \tilde{\mathbf{M}}_u^C \end{bmatrix} \bar{\mu} \, \mathrm{d}\xi^3 \tag{4.65}$$

for the ξ^1-direction and

$$\begin{bmatrix} \mathbf{s}_{v0} & \mathbf{s}_{v1} \\ \mathbf{s}_{v1} & \mathbf{s}_{v2} \end{bmatrix} \begin{bmatrix} \tilde{\boldsymbol{\alpha}}_v \\ \tilde{\boldsymbol{\beta}}_v \end{bmatrix} = \sum_{i=1}^{n} \int_{t_i^-}^{t_i^+} \begin{bmatrix} \tilde{\mathbf{M}}_v^C \\ \xi^3 \tilde{\mathbf{M}}_v^C \end{bmatrix} \bar{\mu} \, \mathrm{d}\xi^3 \tag{4.66}$$

for the ξ^2-direction. In (4.65), the definitions

$$\mathbf{s}_{u0} = \begin{bmatrix} s_0^{C_{11}} \\ s_0^{C_{21}} \\ s_0^{C_{41}} \\ s_0^{C_{14}} \\ s_0^{C_{24}} \\ s_0^{C_{44}} \end{bmatrix} , \quad \mathbf{s}_{u1} = \begin{bmatrix} s_1^{C_{11}} \\ s_1^{C_{21}} \\ s_1^{C_{41}} \\ s_1^{C_{14}} \\ s_1^{C_{24}} \\ s_1^{C_{44}} \end{bmatrix} , \quad \mathbf{s}_{u2} = \begin{bmatrix} s_2^{C_{11}} \\ s_2^{C_{21}} \\ s_2^{C_{41}} \\ s_2^{C_{14}} \\ s_2^{C_{24}} \\ s_2^{C_{44}} \end{bmatrix} , \quad \tilde{\mathbf{M}}_u^C = \begin{bmatrix} C_{11}^i \tilde{\mathbf{M}}_u \\ C_{21}^i \tilde{\mathbf{M}}_u \\ C_{41}^i \tilde{\mathbf{M}}_u \\ C_{14}^i \tilde{\mathbf{M}}_u \\ C_{24}^i \tilde{\mathbf{M}}_u \\ C_{44}^i \tilde{\mathbf{M}}_u \end{bmatrix} , \tag{4.67}$$

have been made for the ξ^1-direction and in (4.66), the definitions

$$\mathbf{s}_{v0} = \begin{bmatrix} s_0^{C_{12}} \\ s_0^{C_{22}} \\ s_0^{C_{42}} \\ s_0^{C_{14}} \\ s_0^{C_{24}} \\ s_0^{C_{44}} \end{bmatrix}, \quad \mathbf{s}_{v1} = \begin{bmatrix} s_1^{C_{12}} \\ s_1^{C_{22}} \\ s_1^{C_{42}} \\ s_1^{C_{14}} \\ s_1^{C_{24}} \\ s_1^{C_{44}} \end{bmatrix}, \quad \mathbf{s}_{v2} = \begin{bmatrix} s_2^{C_{12}} \\ s_2^{C_{22}} \\ s_2^{C_{42}} \\ s_2^{C_{14}} \\ s_2^{C_{24}} \\ s_2^{C_{44}} \end{bmatrix}, \quad \tilde{\mathbf{M}}_v^C = \begin{bmatrix} C_{12}^i \tilde{\mathbf{M}}_v \\ C_{22}^i \tilde{\mathbf{M}}_v \\ C_{42}^i \tilde{\mathbf{M}}_v \\ C_{14}^i \tilde{\mathbf{M}}_v \\ C_{24}^i \tilde{\mathbf{M}}_v \\ C_{44}^i \tilde{\mathbf{M}}_v \end{bmatrix}, \tag{4.68}$$

have been made for the ξ^2-direction. In (4.67) and (4.68), the results of integrations over the thickness with $s_0^{C_{ab}}$, $s_1^{C_{ab}}$ and $s_2^{C_{ab}}$ are defined, so that

$$\begin{aligned} s_0^{C_{ab}} &= \sum_{i=1}^{n} \int_{t_i^-}^{t_i^+} C_{ab}^i \bar{\mu} \, \mathrm{d}\xi^3 = \sum_{i=1}^{n} C_{ab}^i t_i \quad , \\ s_1^{C_{ab}} &= \sum_{i=1}^{n} \int_{t_i^-}^{t_i^+} C_{ab}^i \xi^3 \bar{\mu} \, \mathrm{d}\xi^3 = \sum_{i=1}^{n} C_{ab}^i t_i \xi_{si}^3 \quad , \\ s_2^{C_{ab}} &= \sum_{i=1}^{n} \int_{t_i^-}^{t_i^+} C_{ab}^i (\xi^3)^2 \bar{\mu} \, \mathrm{d}\xi^3 = \sum_{i=1}^{n} C_{ab}^i \left(\frac{(t_i)^3}{12} + t_i (\xi_{si}^3)^2 \right) \quad . \end{aligned} \tag{4.69}$$

Applying the method of linear least squares to the overdetermined systems of equations (4.65) and (4.66), the orthogonalization parameters can be determined by evaluating

$$\begin{bmatrix} \mathbf{s}_{u0}^T & \mathbf{s}_{u1}^T \\ \mathbf{s}_{u1}^T & \mathbf{s}_{u2}^T \end{bmatrix} \begin{bmatrix} \mathbf{s}_{u0} & \mathbf{s}_{u1} \\ \mathbf{s}_{u1} & \mathbf{s}_{u2} \end{bmatrix} \begin{bmatrix} \tilde{\boldsymbol{\alpha}}_u \\ \tilde{\boldsymbol{\beta}}_u \end{bmatrix} = \begin{bmatrix} \mathbf{s}_{u0}^T & \mathbf{s}_{u1}^T \\ \mathbf{s}_{u1}^T & \mathbf{s}_{u2}^T \end{bmatrix} \sum_{i=1}^{n} \int_{t_i^-}^{t_i^+} \begin{bmatrix} \tilde{\mathbf{M}}_u^C \\ \xi^3 \tilde{\mathbf{M}}_u^C \end{bmatrix} \bar{\mu} \, \mathrm{d}\xi^3 \tag{4.70}$$

for the ξ^1-direction and

$$\begin{bmatrix} \mathbf{s}_{v0}^T & \mathbf{s}_{v1}^T \\ \mathbf{s}_{v1}^T & \mathbf{s}_{v2}^T \end{bmatrix} \begin{bmatrix} \mathbf{s}_{v0} & \mathbf{s}_{v1} \\ \mathbf{s}_{v1} & \mathbf{s}_{v2} \end{bmatrix} \begin{bmatrix} \tilde{\boldsymbol{\alpha}}_v \\ \tilde{\boldsymbol{\beta}}_v \end{bmatrix} = \begin{bmatrix} \mathbf{s}_{v0}^T & \mathbf{s}_{v1}^T \\ \mathbf{s}_{v1}^T & \mathbf{s}_{v2}^T \end{bmatrix} \sum_{i=1}^{n} \int_{t_i^-}^{t_i^+} \begin{bmatrix} \tilde{\mathbf{M}}_v^C \\ \xi^3 \tilde{\mathbf{M}}_v^C \end{bmatrix} \bar{\mu} \, \mathrm{d}\xi^3 \tag{4.71}$$

for the ξ^2-direction. Thus by applying the method of least squares, with (4.70) and (4.71) a total of $4\,(3n-1)$ equations have been established to derive the $4(3n-1)$ parameters collected in the vectors $\boldsymbol{\alpha}_u$, $\boldsymbol{\beta}_u$, $\boldsymbol{\alpha}_v$, and $\boldsymbol{\beta}_v$.

Analogous to the summation procedure, when the reference plane is in the middle of the shell and the stacking sequence is symmetric, then the orthogonalization procedure can

be simplified. In this case, the components summarized in vector $\mathbf{s}_{u1}$ in (4.67) and $\mathbf{s}_{v1}$ in (4.68) are zero and the systems of equations are decoupled, so that (4.70) reduces to

$$\mathbf{s}_{u0}^T\,\mathbf{s}_{u0}\,\tilde{\boldsymbol{\alpha}}_u = \mathbf{s}_{u0}^T \sum_{i=1}^{n} \int_{t_i^-}^{t_i^+} C_u^i \tilde{\mathbf{M}}_u \bar{\mu}\,\mathrm{d}\xi^3 \quad \text{and} \quad \mathbf{s}_{u2}^T\,\mathbf{s}_{u2}\,\tilde{\boldsymbol{\beta}}_u = \mathbf{s}_{u2}^T \sum_{i=1}^{n} \int_{t_i^-}^{t_i^+} \xi^3 C_u^i \tilde{\mathbf{M}}_u \bar{\mu}\,\mathrm{d}\xi^3 \tag{4.72}$$

for the ξ^1-direction and (4.71) reduces to

$$\mathbf{s}_{v0}^T\,\mathbf{s}_{v0}\,\tilde{\boldsymbol{\alpha}}_v = \mathbf{s}_{v0}^T \sum_{i=1}^{n} \int_{t_i^-}^{t_i^+} C_v^i \tilde{\mathbf{M}}_v \bar{\mu}\,\mathrm{d}\xi^3 \quad \text{and} \quad \mathbf{s}_{v2}^T\,\mathbf{s}_{v2}\,\tilde{\boldsymbol{\beta}}_v = \mathbf{s}_{v2}^T \sum_{i=1}^{n} \int_{t_i^-}^{t_i^+} \xi^3 C_v^i \tilde{\mathbf{M}}_v \bar{\mu}\,\mathrm{d}\xi^3 \tag{4.73}$$

for the ξ^2-direction. The systems of equations thus reduce to decoupled equations, where the orthogonalization parameters can be more readily determined. The observations regarding the accuracy of the summation procedure presented in the preceding section also apply to the method of least squares.

Procedure for some special stacking sequences

In the following, the unique characteristics of some special stacking sequences often used in real structures are used to adapt the proposed procedure. The first example is a cross-ply laminate, which consists of an arbitrary number of layers with alternating orientations of $\varphi = 0°$ and $\varphi = 90°$. In the orthogonalization condition (4.42) only the components of the matrix $\mathbf{C}_m$ defined in (3.75) appear. It was already noted in chapter 3.4 that for the fiber orientations of $\varphi = 0°$ and $\varphi = 90°$ the components C_{14}^G, C_{24}^G, C_{41}^G, and C_{42}^G in $\mathbf{C}_m$ are zero. The other components of the matrix $\mathbf{C}_m^0$ for a fiber orientation of $\varphi = 0°$ and the matrix $\mathbf{C}_m^{90}$ for a fiber orientation of $\varphi = 90°$ can be computed with the help of (3.73), so that

$$\mathbf{C}_m^0 = \begin{bmatrix} C_{11}^F & C_{12}^F & 0 \\ C_{21}^F & C_{22}^F & 0 \\ 0 & 0 & C_{44}^F \end{bmatrix} \quad \text{and} \quad \mathbf{C}_m^{90} = \begin{bmatrix} C_{22}^F & C_{12}^F & 0 \\ C_{21}^F & C_{11}^F & 0 \\ 0 & 0 & C_{44}^F \end{bmatrix} . \tag{4.74}$$

Since, for a fiber orientation of $\varphi = 0°$, the fiber-oriented base system and the fixed base system are identical, applying (3.73) leads to $C_{ij}^G = C_{ij}^F$, whereas for $\mathbf{C}_m^{90}$ the components C_{11}^F and C_{22}^F are exchanged.

Taking (4.74) into account while examining the orthogonality condition (4.42) manifests that many of the equations either do not provide a contribution or are linearly dependent. Neglecting the equations with components of $\mathbf{C}_m^0$ and $\mathbf{C}_m^{90}$, which are zero, the twelve equations for the ξ^1-direction and the ξ^2-direction respectively reduce to six equations respectively. Additionally, the components C_{12}^L, C_{21}^L and C_{44}^L remain unchanged through the thickness of a cross-ply laminate, so that their contribution to the orthogonality conditions

are linearly dependent. Thus, for a cross-ply laminate the orthogonality condition expressed as a summation over integration over the thickness of each layer (4.43) reduces to

$$\sum_{i=1}^{n} \int_{t_i^-}^{t_i^+} \begin{bmatrix} C_{11}^i \tilde{\mathbf{M}}_u \\ C_{44}^i \tilde{\mathbf{M}}_u \\ \xi^3 C_{11}^i \tilde{\mathbf{M}}_u \\ \xi^3 C_{44}^i \tilde{\mathbf{M}}_u \end{bmatrix} \bar{\mu} \, \mathrm{d}\xi^3 = \mathbf{0} \qquad \text{and} \qquad \sum_{i=1}^{n} \int_{t_i^-}^{t_i^+} \begin{bmatrix} C_{22}^i \tilde{\mathbf{M}}_v \\ C_{44}^i \tilde{\mathbf{M}}_v \\ \xi^3 C_{22}^i \tilde{\mathbf{M}}_v \\ \xi^3 C_{44}^i \tilde{\mathbf{M}}_v \end{bmatrix} \bar{\mu} \, \mathrm{d}\xi^3 = \mathbf{0} \quad , \tag{4.75}$$

where C_{44}^i could be interchanged with C_{12}^i for the ξ^1-direction and C_{44}^i could be interchanged with C_{21}^i for the ξ^2-direction. The number of equations that need to be fulfilled is thus reduced from $12\,(3n-1)$ in (4.43) for the ξ^1-direction and the ξ^2-direction respectively to $4\,(3n-1)$ in (4.75). It was already established that if two parameters are added to the shape functions (4.48), this introduces $2\,(3n-1)$ parameters in both directions. To derive an approximate solution, the summation procedure or the method of least squares applied to (4.43) in the preceding sections could be adopted for (4.75).

An alternative is the addition of four parameters to the shape functions. Thus, four parameters are added to the shape functions $H_{u(j)}$, $I_{u(i)}$, and $J_{u(i)}$ defined in (4.7), (4.9), and (4.11), so that two additional parameters are added to the modified shape functions specified in (4.45). The additional parameters for the ξ^1-direction are denoted with γ_{uj}^H, δ_{uj}^H, γ_{ui}^I, δ_{ui}^I, γ_{ui}^J, and δ_{ui}^J and the additional parameters for the ξ^2-direction are denoted with γ_{vj}^H, δ_{vj}^H, γ_{vi}^I, δ_{vi}^I, γ_{vi}^J, and δ_{vi}^J and are multiplied with Chebyshev polynomials $\xi_2^{CH}(\xi^3) = 2(\xi^3)^2 - 1$ and $\xi_3^{CH}(\xi^3) = 4(\xi^3)^3 - 3\xi^3$ in order to ensure that the polynomials are orthogonal to each other.

With these additions, a system of equations can now be set up to derive the unknown parameters added to the shape functions. Inserting the modified shape functions with four additional parameters each, requirement (4.75) is rewritten as

$$\sum_{i=1}^{n} \int_{t_i^-}^{t_i^+} \begin{bmatrix} C_{11}^i \hat{\mathbf{M}}_u \\ C_{44}^i \hat{\mathbf{M}}_u \\ \xi^3 C_{11}^i \hat{\mathbf{M}}_u \\ \xi^3 C_{44}^i \hat{\mathbf{M}}_u \end{bmatrix} \bar{\mu} \, \mathrm{d}\xi^3 = \mathbf{0} \qquad \text{and} \qquad \sum_{i=1}^{n} \int_{t_i^-}^{t_i^+} \begin{bmatrix} C_{22}^i \hat{\mathbf{M}}_v \\ C_{44}^i \hat{\mathbf{M}}_v \\ \xi^3 C_{22}^i \hat{\mathbf{M}}_v \\ \xi^3 C_{44}^i \hat{\mathbf{M}}_v \end{bmatrix} \bar{\mu} \, \mathrm{d}\xi^3 = \mathbf{0} \quad , \tag{4.76}$$

where the matrices $\hat{\mathbf{M}}_u$ and $\hat{\mathbf{M}}_v$ contain the modified shape functions and are defined by

$$\begin{aligned} \hat{\mathbf{M}}_u &= \tilde{\mathbf{M}}_u + \tilde{\boldsymbol{\alpha}}_u + \xi^3 \tilde{\boldsymbol{\beta}}_u + \xi_2^{CH} \tilde{\boldsymbol{\gamma}}_u + \xi_3^{CH} \tilde{\boldsymbol{\delta}}_u \quad , \\ \hat{\mathbf{M}}_v &= \tilde{\mathbf{M}}_v + \tilde{\boldsymbol{\alpha}}_v + \xi^3 \tilde{\boldsymbol{\beta}}_v + \xi_2^{CH} \tilde{\boldsymbol{\gamma}}_v + \xi_3^{CH} \tilde{\boldsymbol{\delta}}_v \quad . \end{aligned} \tag{4.77}$$

By adding the additional terms to the ansatz functions, zero-eigenvalues are introduced, which necessitates that a corresponding number of degrees of freedom needs to be removed from the model. By doing so, the number of equations that have to be fulfilled in the orthogonality condition is reduced from $4\,(3n-1)$ in (4.75) to $12\,(n-1)$ in (4.76) for both

the ξ^1- and the ξ^2-direction. Thus, the matrices $\tilde{\mathbf{M}}_u$ and $\tilde{\mathbf{M}}_v$ are defined by

$$\begin{aligned} \tilde{\mathbf{M}}_u &= \begin{bmatrix} \tilde{\mathbf{H}}_u, & \tilde{\mathbf{I}}_u, & \tilde{\mathbf{J}}_u \end{bmatrix} \quad , \\ \tilde{\mathbf{M}}_v &= \begin{bmatrix} \tilde{\mathbf{H}}_v, & \tilde{\mathbf{I}}_v, & \tilde{\mathbf{J}}_v \end{bmatrix} \quad , \end{aligned} \tag{4.78}$$

where $\tilde{\mathbf{H}}_u$ and $\tilde{\mathbf{H}}_v$ correspond to the definitions made in (4.16) and further definitions

$$\begin{aligned} \tilde{\mathbf{I}}_u &= \begin{bmatrix} I_{u1}, & I_{u(i)}, & \dots & I_{u(n-1)} \end{bmatrix} & \tilde{\mathbf{J}}_u &= \begin{bmatrix} J_{u1}, & J_{u(i)}, & \dots & J_{u(n-1)} \end{bmatrix} \\ \tilde{\mathbf{I}}_v &= \begin{bmatrix} I_{v1}, & I_{v(i)}, & \dots & I_{v(n-1)} \end{bmatrix} & \tilde{\mathbf{J}}_v &= \begin{bmatrix} J_{v1}, & J_{v(i)}, & \dots & J_{v(n-1)} \end{bmatrix} \\ \tilde{\mathbf{I}}_w &= \begin{bmatrix} I_{w1}, & I_{w(i)}, & \dots & I_{w(n-1)} \end{bmatrix} & \tilde{\mathbf{J}}_w &= \begin{bmatrix} J_{w1}, & J_{w(i)}, & \dots & J_{w(n-1)} \end{bmatrix} \end{aligned} \tag{4.79}$$

are made. Furthermore, in (4.76), the vectors $\tilde{\boldsymbol{\alpha}}_u$, $\tilde{\boldsymbol{\beta}}_u$, $\tilde{\boldsymbol{\alpha}}_v$, and $\tilde{\boldsymbol{\beta}}_v$ are introduced with

$$\begin{aligned} \tilde{\boldsymbol{\alpha}}_u &= \begin{bmatrix} \tilde{\boldsymbol{\alpha}}_u^H, \tilde{\boldsymbol{\alpha}}_u^I, \tilde{\boldsymbol{\alpha}}_u^J \end{bmatrix} \quad , & \tilde{\boldsymbol{\beta}}_u &= \begin{bmatrix} \tilde{\boldsymbol{\beta}}_u^H, \tilde{\boldsymbol{\beta}}_u^I, \tilde{\boldsymbol{\beta}}_u^J \end{bmatrix} \quad , \\ \tilde{\boldsymbol{\alpha}}_v &= \begin{bmatrix} \tilde{\boldsymbol{\alpha}}_v^H, \tilde{\boldsymbol{\alpha}}_v^I, \tilde{\boldsymbol{\alpha}}_u^J \end{bmatrix} \quad , & \tilde{\boldsymbol{\beta}}_v &= \begin{bmatrix} \tilde{\boldsymbol{\beta}}_v^H, \tilde{\boldsymbol{\beta}}_v^I, \tilde{\boldsymbol{\beta}}_u^J \end{bmatrix} \quad , \end{aligned} \tag{4.80}$$

where the definitions of the vectors $\tilde{\boldsymbol{\alpha}}_u^H$, $\tilde{\boldsymbol{\beta}}_u^H$, $\tilde{\boldsymbol{\alpha}}_v^H$, and $\tilde{\boldsymbol{\beta}}_v^H$ correspond to the definitions made in (4.50) and further definitions

$$\begin{aligned} \tilde{\boldsymbol{\alpha}}_u^I &= \begin{bmatrix} \alpha_{u1}^I, & \alpha_{ui}^I, & \dots & \alpha_{u(n-1)}^I \end{bmatrix} \quad , & \tilde{\boldsymbol{\alpha}}_u^J &= \begin{bmatrix} \alpha_{u1}^J, & \alpha_{ui}^J, & \dots & \alpha_{u(n-1)}^J \end{bmatrix} \quad , \\ \tilde{\boldsymbol{\beta}}_u^I &= \begin{bmatrix} \beta_{u1}^I, & \beta_{ui}^I, & \dots & \beta_{u(n-1)}^I \end{bmatrix} \quad , & \tilde{\boldsymbol{\beta}}_u^J &= \begin{bmatrix} \beta_{u1}^J, & \beta_{ui}^J, & \dots & \beta_{u(n-1)}^J \end{bmatrix} \quad , \\ \tilde{\boldsymbol{\alpha}}_v^I &= \begin{bmatrix} \alpha_{v1}^I, & \alpha_{vi}^I, & \dots & \alpha_{v(n-1)}^I \end{bmatrix} \quad , & \tilde{\boldsymbol{\alpha}}_v^J &= \begin{bmatrix} \alpha_{v1}^J, & \alpha_{vi}^J, & \dots & \alpha_{v(n-1)}^J \end{bmatrix} \quad , \\ \tilde{\boldsymbol{\beta}}_v^I &= \begin{bmatrix} \beta_{v1}^I, & \beta_{vi}^I, & \dots & \beta_{v(n-1)}^I \end{bmatrix} \quad , & \tilde{\boldsymbol{\beta}}_v^J &= \begin{bmatrix} \beta_{v1}^J, & \beta_{vi}^J, & \dots & \beta_{v(n-1)}^J \end{bmatrix} \quad , \end{aligned} \tag{4.81}$$

are made. Considering (4.50 a) and (4.81), $6\,(n-1)$ unknown parameters are introduced in (4.77) with $\tilde{\boldsymbol{\alpha}}_u^H$, $\tilde{\boldsymbol{\beta}}_u^H$, $\tilde{\boldsymbol{\alpha}}_u^I$, $\tilde{\boldsymbol{\beta}}_u^I$, $\tilde{\boldsymbol{\alpha}}_u^J$, and $\tilde{\boldsymbol{\beta}}_u^J$ for the ξ^1-direction and the same number of parameters is introduced for the ξ^2-direction. Also, the vectors $\tilde{\boldsymbol{\gamma}}_u$, $\tilde{\boldsymbol{\delta}}_u$, $\tilde{\boldsymbol{\gamma}}_v$, and $\tilde{\boldsymbol{\delta}}_v$ are introduced in (4.77) with

$$\begin{aligned} \tilde{\boldsymbol{\gamma}}_u &= \begin{bmatrix} \tilde{\boldsymbol{\gamma}}_u^H, \tilde{\boldsymbol{\gamma}}_u^I, \tilde{\boldsymbol{\gamma}}_u^J \end{bmatrix} \quad , & \tilde{\boldsymbol{\delta}}_u &= \begin{bmatrix} \tilde{\boldsymbol{\delta}}_u^H, \tilde{\boldsymbol{\delta}}_u^I, \tilde{\boldsymbol{\delta}}_u^J \end{bmatrix} \quad , \\ \tilde{\boldsymbol{\gamma}}_v &= \begin{bmatrix} \tilde{\boldsymbol{\gamma}}_v^H, \tilde{\boldsymbol{\gamma}}_v^I, \tilde{\boldsymbol{\gamma}}_u^J \end{bmatrix} \quad , & \tilde{\boldsymbol{\delta}}_v &= \begin{bmatrix} \tilde{\boldsymbol{\delta}}_v^H, \tilde{\boldsymbol{\delta}}_v^I, \tilde{\boldsymbol{\delta}}_u^J \end{bmatrix} \quad , \end{aligned} \tag{4.82}$$

which contain the additional parameters added to the shape functions, so that

$$\begin{aligned}
\tilde{\boldsymbol{\gamma}}_u^H &= \left[\gamma_{u2}^H,\ \gamma_{uj}^H,\ \dots\ \gamma_{un}^H\right] \quad , & \tilde{\boldsymbol{\gamma}}_u^I &= \left[\gamma_{u1}^I,\ \gamma_{ui}^I,\ \dots\ \gamma_{u(n-1)}^I\right] \quad , \\
\tilde{\boldsymbol{\delta}}_u^H &= \left[\delta_{u2}^H,\ \delta_{uj}^H,\ \dots\ \delta_{un}^H\right] \quad , & \tilde{\boldsymbol{\delta}}_u^I &= \left[\delta_{u1}^I,\ \delta_{ui}^I,\ \dots\ \delta_{u(n-1)}^I\right] \quad , \\
\tilde{\boldsymbol{\gamma}}_v^H &= \left[\gamma_{v2}^H,\ \gamma_{vj}^H,\ \dots\ \gamma_{vn}^H\right] \quad , & \tilde{\boldsymbol{\gamma}}_v^I &= \left[\gamma_{v1}^I,\ \gamma_{vi}^I,\ \dots\ \gamma_{v(n-1)}^I\right] \quad , \\
\tilde{\boldsymbol{\delta}}_v^H &= \left[\delta_{v2}^H,\ \delta_{vj}^H,\ \dots\ \delta_{vn}^H\right] \quad , & \tilde{\boldsymbol{\delta}}_v^I &= \left[\delta_{v1}^I,\ \delta_{vi}^I,\ \dots\ \delta_{v(n-1)}^I\right] \quad ,
\end{aligned}$$

$$\begin{aligned}
\tilde{\boldsymbol{\gamma}}_u^J &= \left[\gamma_{u1}^J,\ \gamma_{ui}^J,\ \dots\ \gamma_{u(n-1)}^J\right] \quad , \\
\tilde{\boldsymbol{\delta}}_u^J &= \left[\delta_{u1}^J,\ \delta_{ui}^J,\ \dots\ \delta_{u(n-1)}^J\right] \quad , \\
\tilde{\boldsymbol{\gamma}}_v^J &= \left[\gamma_{v1}^J,\ \gamma_{vi}^J,\ \dots\ \gamma_{v(n-1)}^J\right] \quad , \\
\tilde{\boldsymbol{\delta}}_v^J &= \left[\delta_{v1}^J,\ \delta_{vi}^J,\ \dots\ \delta_{v(n-1)}^J\right] \quad .
\end{aligned} \tag{4.83}$$

A total of $6\,(n-1)$ unknown parameters are therefore introduced in (4.77) with $\tilde{\boldsymbol{\gamma}}_u^H$, $\tilde{\boldsymbol{\delta}}_u^H$, $\tilde{\boldsymbol{\gamma}}_u^I$, $\tilde{\boldsymbol{\delta}}_u^I$, $\tilde{\boldsymbol{\gamma}}_u^J$, and $\tilde{\boldsymbol{\delta}}_u^J$ for the ξ^1-direction and the same number of parameters is introduced for the ξ^2-direction. The total number of parameters introduced thus is $24\,(n-1)$.

Rearranging (4.76) and considering (4.77) leads to

$$\begin{bmatrix} s_0^{C11} & s_1^{C11} & t_2^{C11} & t_{3a}^{C11} \\ s_0^{C44} & s_1^{C44} & t_2^{C44} & t_{3a}^{C44} \\ s_1^{C11} & s_2^{C11} & t_{3b}^{C11} & t_4^{C11} \\ s_1^{C44} & s_2^{C44} & t_{3b}^{C44} & t_4^{C44} \end{bmatrix} \begin{bmatrix} \tilde{\boldsymbol{\alpha}}_u \\ \tilde{\boldsymbol{\beta}}_u \\ \tilde{\boldsymbol{\gamma}}_u \\ \tilde{\boldsymbol{\delta}}_u \end{bmatrix} = \sum_{i=1}^{n} \int_{t_i^-}^{t_i^+} \begin{bmatrix} C_{11}^i \hat{\mathbf{M}}_u \\ C_{44}^i \hat{\mathbf{M}}_u \\ \xi^3 C_{11}^i \hat{\mathbf{M}}_u \\ \xi^3 C_{44}^i \hat{\mathbf{M}}_u \end{bmatrix} \bar{\mu}\, \mathrm{d}\xi^3 \tag{4.84}$$

for the ξ^1-direction and

$$\begin{bmatrix} s_0^{C22} & s_1^{C22} & t_2^{C22} & t_{3a}^{C22} \\ s_0^{C44} & s_1^{C44} & t_2^{C44} & t_{3a}^{C44} \\ s_1^{C22} & s_2^{C22} & t_{3b}^{C22} & t_4^{C22} \\ s_1^{C44} & s_2^{C44} & t_{3b}^{C44} & t_4^{C44} \end{bmatrix} \begin{bmatrix} \tilde{\boldsymbol{\alpha}}_v \\ \tilde{\boldsymbol{\beta}}_v \\ \tilde{\boldsymbol{\gamma}}_v \\ \tilde{\boldsymbol{\delta}}_v \end{bmatrix} = \sum_{i=1}^{n} \int_{t_i^-}^{t_i^+} \begin{bmatrix} C_{22}^i \hat{\mathbf{M}}_v \\ C_{44}^i \hat{\mathbf{M}}_v \\ \xi^3 C_{22}^i \hat{\mathbf{M}}_v \\ \xi^3 C_{44}^i \hat{\mathbf{M}}_v \end{bmatrix} \bar{\mu}\, \mathrm{d}\xi^3 \tag{4.85}$$

for the ξ^2-direction, where $s_0^{C_{ab}}$, $s_1^{C_{ab}}$, and $s_2^{C_{ab}}$ are defined in (4.69) and the factors $t_2^{C_{ab}}$, $t_{3a}^{C_{ab}}$, $t_{3b}^{C_{ab}}$, and $t_4^{C_{ab}}$ denote integrations over the Chebyshev polynomials, which can be

specified with

$$
\begin{aligned}
t_2^{C_{ab}} &= \sum_{i=1}^{n} \int_{t_i^-}^{t_i^+} C_{ab}^i \xi_2^{CH} \bar{\mu} \, \mathrm{d}\xi^3 = \sum_{i=1}^{n} C_{ab}^i \left(\frac{(t_i)^3}{6} + t_i \left[2(\xi_{si}^3)^2 - 1 \right] \right) \quad , \\
t_{3a}^{C_{ab}} &= \sum_{i=1}^{n} \int_{t_i^-}^{t_i^+} C_{ab}^i \xi_3^{CH} \bar{\mu} \, \mathrm{d}\xi^3 = \sum_{i=1}^{n} C_{ab}^i \left((t_i)^3 \xi_{si}^3 + t_i (\xi_{si}^3) \left[4(\xi_{si}^3)^2 - 3 \right] \right) \quad , \\
t_{3b}^{C_{ab}} &= \sum_{i=1}^{n} \int_{t_i^-}^{t_i^+} C_{ab}^i \xi^3 \xi_2^{CH} \bar{\mu} \, \mathrm{d}\xi^3 = \sum_{i=1}^{n} C_{ab}^i \left(\frac{(t_i)^3}{2} \xi_{si}^3 + t_i (\xi_{si}^3) \left[2(\xi_{si}^3)^2 - 1 \right] \right) \quad , \\
t_4^{C_{ab}} &= \sum_{i=1}^{n} \int_{t_i^-}^{t_i^+} C_{ab}^i \xi^3 \xi_3^{CH} \bar{\mu} \, \mathrm{d}\xi^3 \\
&= \sum_{i=1}^{n} C_{ab}^i \left(\frac{(t_i)^5}{20} + (t_i)^3 \left[2(\xi_{si}^3)^2 - \frac{1}{4} \right] + t_i (\xi_{si}^3)^2 \left[4(\xi_{si}^3)^2 - 3 \right] \right) \quad .
\end{aligned}
\tag{4.86}
$$

With (4.84), a total of $12\,(n-1)$ equations have been established to derive the $12\,(n-1)$ parameters collected in the vectors $\tilde{\boldsymbol{\alpha}}_u$, $\tilde{\boldsymbol{\beta}}_u$, $\tilde{\boldsymbol{\gamma}}_u$, and $\tilde{\boldsymbol{\delta}}_u$. In the same way, with (4.85) a total of $12\,(n-1)$ equations have been established to derive the $12\,(n-1)$ parameters collected in the vectors $\tilde{\boldsymbol{\alpha}}_v$, $\tilde{\boldsymbol{\beta}}_v$, $\tilde{\boldsymbol{\gamma}}_v$, and $\tilde{\boldsymbol{\delta}}_v$.

Analogous to the preceding orthogonalization procedures, when the reference plane is in the middle of the shell and the stacking sequence is symmetric, then the orthogonalization procedure can be simplified. In this case the components $s_1^{C_{ab}}$, $t_{3a}^{C_{ab}}$, and $t_{3b}^{C_{ab}}$ in (4.84) and (4.85) are zero and the systems of equations can be decoupled into two smaller systems of equations for both directions.

In order to apply the procedure outlined in this section, two quadratic parables of the form $(\alpha - \beta(\xi^3)^2)$ have to be introduced for the two entries of 1 in the fifth and sixth lines of $\mathbf{A}_G$ (4.24). The parameters have to be determined for a particular stacking sequence and geometry of the composite shell. A generalization of how to determine the parameters cannot be specified and is a subject for further research.

The equations presented in this section hold for cross-ply laminates. Similar considerations yield similar equations for an angle-ply laminate with fiber angles of $\pm\varphi = 45°$. Assembling the matrices $\mathbf{C}_m^{45}$ and $\mathbf{C}_m^{-45}$ with the help of (3.73) and $\sin(45°) = \cos(45°) = \cos(-45°) = -(\sin(-45°))$ leads to an orthogonality condition for this angle-ply laminate, which can be written as

$$
\sum_{i=1}^{n} \int_{t_i^-}^{t_i^+} \begin{bmatrix} C_{11}^i \tilde{\mathbf{M}}_u \\ C_{41}^i \tilde{\mathbf{M}}_u \\ \xi^3 C_{11}^i \tilde{\mathbf{M}}_u \\ \xi^3 C_{41}^i \tilde{\mathbf{M}}_u \end{bmatrix} \bar{\mu} \, \mathrm{d}\xi^3 = \mathbf{0} \qquad \text{and} \qquad \sum_{i=1}^{n} \int_{t_i^-}^{t_i^+} \begin{bmatrix} C_{22}^i \tilde{\mathbf{M}}_v \\ C_{42}^i \tilde{\mathbf{M}}_v \\ \xi^3 C_{22}^i \tilde{\mathbf{M}}_v \\ \xi^3 C_{42}^i \tilde{\mathbf{M}}_v \end{bmatrix} \bar{\mu} \, \mathrm{d}\xi^3 = \mathbf{0} \tag{4.87}
$$

for the ξ^1- and the ξ^2-direction, respectively, which is similar to the orthogonality condition for the cross-ply laminate (4.75), but differs in the stiffness parameters. It is noted that unlike $\mathbf{C}_m^0$ and $\mathbf{C}_m^{90}$ the matrices $\mathbf{C}_m^{45}$ and $\mathbf{C}_m^{-45}$ are dense. Analogous to the procedure presented for cross-ply laminates, all other equations from the orthogonality requirement (4.42) vanish due to linear dependencies. Thus, in (4.87) the coefficient C_{11}^i can be replaced with C_{21}^i or C_{44}^i and the coefficient C_{41}^i can be replaced with C_{14}^i or C_{24}^i for the ξ^1-direction, and C_{22}^i can be replaced with C_{12}^i or C_{44}^i and C_{42}^i can be replaced with C_{14}^i or C_{24}^i for the ξ^2-direction, without changing the results for the parameters when applying the orthogonalization procedure. The orthogonalization parameters for an angle-ply laminate with fiber orientations of $\varphi = \pm 45°$ can thus be derived by the procedure that was presented for cross-ply laminates.

Similar to the orthogonalization procedure for composites with a homogeneous setup in thickness direction, in all the orthogonalization procedures introduced for composites with an inhomogeneous setup in thickness direction, the established orthogonality conditions have to be solved only once before the commencement of the finite element simulation for a specific geometry, thus not leading to a significant increase in computation time.

4.3 Global-local mixed variational principle

In this section the mixed variational formulation of the global model introduced in chapter 3.5 is modified to incorporate the local model. The three-field Hu-Washizu functional for the global-local shell model is given in the form

$$\Pi(\tilde{\mathbf{v}}, \tilde{\boldsymbol{\sigma}}, \tilde{\boldsymbol{\varepsilon}}) = \int_{\Omega_0} [\hat{\Psi}(\tilde{\boldsymbol{\varepsilon}}) + \boldsymbol{\sigma}_G^T(\boldsymbol{\varepsilon}_g(\tilde{\mathbf{v}}) - \boldsymbol{\varepsilon}_G)] \, \mathrm{d}A - \int_{\Omega_0} \mathbf{u}^T \bar{\mathbf{p}} \, \mathrm{d}A - \int_{\Gamma_{\sigma 0}} \mathbf{u}^T \, \bar{\mathbf{t}} \, \mathrm{d}s \quad , \tag{4.88}$$

with the independent displacement field $\tilde{\mathbf{v}} = [\mathbf{u}, \boldsymbol{\omega}]^T$ made up of the displacement vector $\mathbf{u}$ and the vector of rotational parameters of the shell middle surface $\boldsymbol{\omega}$, the independent field $\tilde{\boldsymbol{\varepsilon}}$ containing the global shell strains and local displacements and their derivatives, and the independent field $\tilde{\boldsymbol{\sigma}}$, which contains the global effective stress resultants $\boldsymbol{\sigma}_G$ and the higher-order stress resultants $\boldsymbol{\sigma}_L$.

Similar to (3.84), the stationary condition of (4.88) can then be given by invoking the directional derivative (2.71) with respect to the three independent fields $\tilde{\mathbf{v}}$, $\tilde{\boldsymbol{\varepsilon}}$, and $\tilde{\boldsymbol{\sigma}}$, so that

$$\begin{aligned} \delta\Pi = g(\tilde{\boldsymbol{\theta}}, \delta\tilde{\boldsymbol{\theta}}) = \int_{\Omega_0} \left[\delta\tilde{\boldsymbol{\varepsilon}}^T \frac{\partial \hat{\Psi}}{\partial \tilde{\boldsymbol{\varepsilon}}} - \delta\boldsymbol{\varepsilon}_G^T \boldsymbol{\sigma}_G + \delta\boldsymbol{\sigma}_G^T (\boldsymbol{\varepsilon}_g - \boldsymbol{\varepsilon}_G) + \delta\boldsymbol{\varepsilon}_g^T \boldsymbol{\sigma}_G \right] \mathrm{d}A \\ - \int_{\Omega_0} \delta\mathbf{u}_G^T \bar{\mathbf{p}} \, \mathrm{d}A - \int_{\Gamma_{\sigma 0}} \delta\mathbf{u}_G^T \, \bar{\mathbf{t}} \, \mathrm{d}s = 0 \quad , \end{aligned} \tag{4.89}$$

with $\tilde{\boldsymbol{\theta}} = [\tilde{\mathbf{v}}, \tilde{\boldsymbol{\sigma}}, \tilde{\boldsymbol{\varepsilon}}]^T$ and $\delta\tilde{\boldsymbol{\theta}} = [\delta\tilde{\mathbf{v}}, \delta\tilde{\boldsymbol{\sigma}}, \delta\tilde{\boldsymbol{\varepsilon}}]^T$. In (4.89), the variation of $\tilde{\boldsymbol{\varepsilon}}$ and the variation

of $\tilde{\boldsymbol{\sigma}}$ have been introduced by

$$\delta\tilde{\boldsymbol{\varepsilon}} = [\delta\boldsymbol{\varepsilon}_G, \delta\boldsymbol{\varepsilon}_L]^T \qquad \text{and} \qquad \delta\tilde{\boldsymbol{\sigma}} = [\delta\boldsymbol{\sigma}_G, \mathbf{0}]^T \quad . \tag{4.90}$$

The entries in the vector $\delta\boldsymbol{\varepsilon}_g$ in (4.90) can be gathered from (3.35), while $\delta\boldsymbol{\varepsilon}_G$ and $\delta\boldsymbol{\varepsilon}_L$ represent the variation of the independent shell strains and the independent local quantities. The variation of the independent effective shell stress resultants is represented by $\delta\boldsymbol{\sigma}_G$. As already mentioned, the higher-order stress resultants $\boldsymbol{\sigma}_L$ are set to zero in the variational formulation ($\delta\boldsymbol{\sigma}_L = \mathbf{0}$). All aforementioned quantities are approximated by interpolation functions in the scope of the finite element formulation introduced in the following chapter.

When comparing (4.90) with (3.84), it becomes evident that the local part of the model is introduced via the strain-energy function $\Psi(\tilde{\boldsymbol{\varepsilon}})$. Separating the strain-energy function into the global and the local part, the first term in (4.89) can be rewritten as

$$\delta\tilde{\boldsymbol{\varepsilon}}^T \frac{\partial\hat{\Psi}}{\partial\tilde{\boldsymbol{\varepsilon}}} = \delta\boldsymbol{\varepsilon}_G{}^T \frac{\partial\hat{\Psi}}{\partial\boldsymbol{\varepsilon}_G} + \delta\boldsymbol{\varepsilon}_L^T \frac{\partial\hat{\Psi}}{\partial\boldsymbol{\varepsilon}_L} \quad . \tag{4.91}$$

Thus, the contributions of the global model and the local model are identified, and with (4.91), the stationary condition (4.89) can be rewritten as

$$\begin{aligned} g(\tilde{\boldsymbol{\theta}}, \delta\tilde{\boldsymbol{\theta}}) = &\int_{\Omega_0} \left[\delta\boldsymbol{\varepsilon}_G{}^T \left(\frac{\partial\hat{\Psi}}{\partial\boldsymbol{\varepsilon}_G} - \boldsymbol{\sigma}_G \right) + \delta\boldsymbol{\varepsilon}_L^T \frac{\partial\hat{\Psi}}{\partial\boldsymbol{\varepsilon}_L} + \delta\boldsymbol{\sigma}_G^T (\boldsymbol{\varepsilon}_g - \boldsymbol{\varepsilon}_G) + \delta\boldsymbol{\varepsilon}_g^T \boldsymbol{\sigma}_G \right] \mathrm{d}A \\ &- \int_{\Omega_0} \delta\mathbf{u}_G^T \bar{\mathbf{p}} \, \mathrm{d}A - \int_{\Gamma_{\sigma 0}} \delta\mathbf{u}_G^T \bar{\mathbf{t}} \, \mathrm{d}s = 0 \quad , \end{aligned} \tag{4.92}$$

which is different from (3.84) only in the contribution of the local model in the form of the strain-energy function. It is noted that in (4.92), the subscript g in $\boldsymbol{\varepsilon}_g$ indicates that these are geometric strains as a function of the displacement field while the subscript G in $\boldsymbol{\varepsilon}_G$ refers to the independent global shell strains as part of the variational formulation. The geometric boundary conditions $\mathbf{u} = \bar{\mathbf{u}}$ are fulfilled as constraints. The variational formulation (4.92) is the basis of the finite element formulation of the global-local shell model, which will be discussed in the next chapter.

The static field equation associated with the contribution of the local model in (4.92) can be derived by means of integrations by parts, so that

$$\int_{\Omega_0} \delta\boldsymbol{\varepsilon}_L^T \frac{\partial\hat{\Psi}}{\partial\boldsymbol{\varepsilon}_L} \, \mathrm{d}A = \int_{\Omega_0} \int_{h^-}^{h^+} \mathbf{S} : \mathrm{Grad}^s \delta\mathbf{u}_L \, \mathrm{d}\xi^3 \, \mathrm{d}A = - \int_{\Omega_0} \int_{h^-}^{h^+} \mathrm{Div}\, \mathbf{S} \cdot \delta\mathbf{u}_L \, \mathrm{d}\xi^3 \, \mathrm{d}A \quad , \tag{4.93}$$

where the boundary conditions have been set to zero and are therefore neglected. The local term in (4.92) thus requires that the local equilibrium equations are fulfilled ($\mathrm{Div}\, \mathbf{S} = \mathbf{0}$).

Similar to (3.85), the stationary condition can thus be rewritten as

$$
\begin{aligned}
g(\tilde{\boldsymbol{\theta}}, \delta\tilde{\boldsymbol{\theta}}) = & \int_{\Omega_0} \left[\delta\boldsymbol{\varepsilon}_G{}^T \left(\frac{\partial \hat{\Psi}}{\partial \boldsymbol{\varepsilon}_G} - \boldsymbol{\sigma}_G \right) - \operatorname{Div} \mathbf{S} \cdot \delta\mathbf{u}_L + \delta\boldsymbol{\sigma}_G^T \left(\boldsymbol{\varepsilon}_g - \boldsymbol{\varepsilon}_G \right) \right] \mathrm{d}A \\
& - \int_{\Omega_0} \left[\left(\frac{1}{j} \left(j\mathbf{n}^\alpha \right)_{,\alpha} + \bar{\mathbf{p}} \right) \cdot \delta\mathbf{u}_G + \left(\frac{1}{j} \left(j\mathbf{m}^\alpha \right)_{,\alpha} + \mathbf{x}_{,\alpha} \times \mathbf{n}^\alpha \right) \cdot \delta\mathbf{w}_G \right] \mathrm{d}A \\
& - \int_{\Gamma_{\sigma 0}} \left[\left(j\mathbf{n}^\alpha \nu_\alpha - \bar{\mathbf{t}} \right) \cdot \delta\mathbf{u}_G + \left(j\mathbf{m}^\alpha \nu_\alpha \right) \cdot \delta\mathbf{w}_G \right] \mathrm{d}s \quad .
\end{aligned}
\tag{4.94}
$$

By applying the fundamental lemma of variational calculus, the Euler-Lagrange equations can be derived from (4.94) and are summarized at this point for the global-local model. Exploiting the second and third line in (4.94), the resultant form of the balance of linear and angular momentum and the static boundary conditions can be derived analogous to (3.56), yielding

$$
\left.
\begin{aligned}
\frac{1}{j} \left(j\mathbf{n}^\alpha \right)_{,\alpha} + \bar{\mathbf{p}} &= \mathbf{0} \\
\frac{1}{j} \left(j\mathbf{m}^\alpha \right)_{,\alpha} + \mathbf{x}_{,\alpha} \times \mathbf{n}^\alpha &= \mathbf{0}
\end{aligned}
\right\} \text{in } \Omega_0 \qquad \text{and} \qquad
\left.
\begin{aligned}
j\mathbf{n}^\alpha \nu_\alpha - \bar{\mathbf{t}} &= \mathbf{0} \\
j\mathbf{m}^\alpha \nu_\alpha &= \mathbf{0}
\end{aligned}
\right\} \text{on } \Gamma_{\sigma 0} \quad .
\tag{4.95}
$$

Exploiting the first line in (4.94) analogous to (3.86), a field equation that contains the strain-energy function, a local equilibrium equation and a geometric field equation can be derived. They are specified by

$$
\left.
\begin{aligned}
\frac{\partial \hat{\Psi}}{\partial \boldsymbol{\varepsilon}_G} - \boldsymbol{\sigma}_G &= \mathbf{0} \\
\boldsymbol{\varepsilon}_g - \boldsymbol{\varepsilon}_G &= \mathbf{0}
\end{aligned}
\right\} \text{in } \Omega_0 \qquad \text{and} \qquad \operatorname{Div} \mathbf{S} = \mathbf{0} \text{ in } \mathcal{B}_0 \quad .
\tag{4.96}
$$

With (4.95) and (4.96) the field equations for the global-local shell model developed in this work are summarized.

4.4 Linearization of the global-local mixed variational principle

As the variational formulation (4.92) is a nonlinear function in $\tilde{\boldsymbol{\theta}}$, a consistent linearization of the quantities in the nonlinear problem must be derived in order to utilize solution techniques of Newton's type. The linearization of the global-local variational formulation largely corresponds to the linearization of the global variational formulation (3.87), so that

$$
L \left[g(\tilde{\boldsymbol{\theta}}, \delta\tilde{\boldsymbol{\theta}}), \Delta\tilde{\boldsymbol{\theta}} \right] = g(\tilde{\boldsymbol{\theta}}, \delta\tilde{\boldsymbol{\theta}}) + D \left[g(\tilde{\boldsymbol{\theta}}, \delta\tilde{\boldsymbol{\theta}}) \right] \cdot \Delta\tilde{\boldsymbol{\theta}} \quad ,
\tag{4.97}
$$

and analogous to (3.89), with conservative loads $\bar{\mathbf{p}}$ and $\bar{\mathbf{t}}$, the directional derivative of the variational formulation is

$$D\left[g(\tilde{\boldsymbol{\theta}}, \delta\tilde{\boldsymbol{\theta}})\right] \cdot \Delta\tilde{\boldsymbol{\theta}} = \int_{\Omega_0} \Big[\delta\tilde{\boldsymbol{\varepsilon}}^T \frac{\partial^2 \hat{\Psi}}{\partial\tilde{\boldsymbol{\varepsilon}}\partial\tilde{\boldsymbol{\varepsilon}}} \Delta\tilde{\boldsymbol{\varepsilon}} - \delta\boldsymbol{\varepsilon}_G^T \Delta\boldsymbol{\sigma}_G + \delta\boldsymbol{\sigma}_G^T \left(\Delta\boldsymbol{\varepsilon}_g - \Delta\boldsymbol{\varepsilon}_G\right) + \delta\boldsymbol{\varepsilon}_g^T \Delta\boldsymbol{\sigma}_G + \Delta\delta\boldsymbol{\varepsilon}_g^T \boldsymbol{\sigma}_G \Big] \, \mathrm{d}A \quad , \tag{4.98}$$

which is needed in the finite element formulation of the global-local shell model discussed in the next chapter. In (4.98), the material tangent matrix $\tilde{\mathbf{D}}$ defined in (4.31) enters as the second derivative of the strain-energy function, so that

$$\frac{\partial^2 \hat{\Psi}(\tilde{\boldsymbol{\varepsilon}})}{\partial\tilde{\boldsymbol{\varepsilon}}\partial\tilde{\boldsymbol{\varepsilon}}} = \frac{\partial\tilde{\boldsymbol{\sigma}}}{\partial\tilde{\boldsymbol{\varepsilon}}} = \tilde{\mathbf{D}} \quad . \tag{4.99}$$

In (4.98), the linearization of $\tilde{\boldsymbol{\varepsilon}}$ and the linearization of $\tilde{\boldsymbol{\sigma}}$ have been introduced with

$$\Delta\tilde{\boldsymbol{\varepsilon}} = \left[\Delta\boldsymbol{\varepsilon}_G, \Delta\boldsymbol{\varepsilon}_L\right]^T \qquad \text{and} \qquad \Delta\tilde{\boldsymbol{\sigma}} = \left[\Delta\boldsymbol{\sigma}_G, \mathbf{0}\right]^T \quad . \tag{4.100}$$

The vectors $\Delta\boldsymbol{\varepsilon}_G$ and $\Delta\boldsymbol{\varepsilon}_L$ represent the linearization of the independent shell strains and the independent local quantities. The linearization of the independent effective shell stress resultants is represented by $\Delta\boldsymbol{\sigma}_G$. All of the aforementioned quantities are approximated by interpolation functions in the scope of the finite element formulation introduced later. The entries in the vectors $\Delta\boldsymbol{\varepsilon}_g$ and $\Delta\delta\boldsymbol{\varepsilon}_g$ are defined in (3.91) and (3.92), respectively.

In order to derive the contribution of the local part of the model, the first term in the linearized variational formulation (4.98) is separated and, with (4.37) and (4.38), is rewritten as

$$\delta\tilde{\boldsymbol{\varepsilon}}^T \tilde{\mathbf{D}} \, \Delta\tilde{\boldsymbol{\varepsilon}} = \delta{\boldsymbol{\varepsilon}_G}^T \left(\mathbf{D}_G \Delta\boldsymbol{\varepsilon}_G + \mathbf{D}_{GL} \Delta\boldsymbol{\varepsilon}_L\right) + \delta\boldsymbol{\varepsilon}_L^T \left(\mathbf{D}_{GL}^T \Delta\boldsymbol{\varepsilon}_G + \mathbf{D}_L \Delta\boldsymbol{\varepsilon}_L\right) \quad . \tag{4.101}$$

Examining (4.101), the coupling between the global and the local part of the model stands out. In the next chapter, the implementation of an appropriate finite element formulation will be discussed.

Chapter 5

Finite element formulation

The global-local variational formulation $g(\tilde{\boldsymbol{\theta}}, \delta\tilde{\boldsymbol{\theta}})$ given in (4.92) is the basis of the finite shell element implementation. The Newton-Raphson method is used to find a solution for this nonlinear function. Thus, the linearization of (4.92) based on a first-order Taylor expansion is the starting point for nonlinear numerical simulations. Analogous to (4.97), it can be specified by

$$L\left[g(\tilde{\boldsymbol{\theta}}^h, \delta\tilde{\boldsymbol{\theta}}^h), \Delta\tilde{\boldsymbol{\theta}}^h\right] = g(\tilde{\boldsymbol{\theta}}^h, \delta\tilde{\boldsymbol{\theta}}^h) + D\left[g(\tilde{\boldsymbol{\theta}}^h, \delta\tilde{\boldsymbol{\theta}}^h\right] \cdot \Delta\tilde{\boldsymbol{\theta}}^h \quad , \tag{5.1}$$

where the term $g(\tilde{\boldsymbol{\theta}}^h, \delta\tilde{\boldsymbol{\theta}}^h)$ is the residuum and the incremental values $\Delta\tilde{\boldsymbol{\theta}}^h$ are calculated in every iteration, so that $L\left[g(\tilde{\boldsymbol{\theta}}^h, \delta\tilde{\boldsymbol{\theta}}^h), \Delta\tilde{\boldsymbol{\theta}}^h\right] = 0$ is fulfilled. The values are then updated and the procedure is repeated until the residuum vanishes, meaning that a solution for $\tilde{\boldsymbol{\theta}}^h$ has been found. The superscript h indicates that the respective quantity is approximated in the scope of the finite element formulation and that the independent fields in both terms in (5.1) are approximated with appropriate interpolation functions. Considering (4.92), the first term can thus be written with the approximated fields, and thus

$$\begin{aligned} g(\tilde{\boldsymbol{\theta}}^h, \delta\tilde{\boldsymbol{\theta}}^h) = \int_{\Omega_0} \Bigg[& \delta\boldsymbol{\varepsilon}_G^{hT} \left(\frac{\partial \Psi}{\partial \boldsymbol{\varepsilon}_G^h} - \boldsymbol{\sigma}_G^h \right) + \delta\boldsymbol{\varepsilon}_L^{hT} \frac{\partial \hat{\Psi}}{\partial \boldsymbol{\varepsilon}_L^h} \\ & + \delta\boldsymbol{\sigma}_G^{hT} \left(\boldsymbol{\varepsilon}_g^h - \boldsymbol{\varepsilon}_G^h \right) + \delta\boldsymbol{\varepsilon}_g^{hT} \boldsymbol{\sigma}_G^h \Bigg] \, \mathrm{d}A \\ & - \int_{\Omega_0} \delta\mathbf{u}^{hT} \bar{\mathbf{p}} \, \mathrm{d}A - \int_{\Gamma_{\sigma 0}} \delta\mathbf{u}^{hT} \, \bar{\mathbf{t}} \, \mathrm{d}s = 0 \quad . \end{aligned} \tag{5.2}$$

Considering (4.98), the second term in (5.1) can be specified with the approximated fields by means of

$$\begin{aligned} D\left[g\right] \cdot \Delta\boldsymbol{\theta}^h = \int_{\Omega_0} \Big[& \delta\tilde{\boldsymbol{\varepsilon}}^{hT} \tilde{\mathbf{D}} \, \Delta\tilde{\boldsymbol{\varepsilon}}^h - \delta\boldsymbol{\varepsilon}_G^{hT} \Delta\boldsymbol{\sigma}_G^h + \delta\boldsymbol{\sigma}_G^{hT} \left(\Delta\boldsymbol{\varepsilon}_g^h - \Delta\boldsymbol{\varepsilon}_G^h \right) \\ & + \delta\boldsymbol{\varepsilon}_g^{hT} \Delta\boldsymbol{\sigma}_G^h + \Delta\delta\boldsymbol{\varepsilon}_g^{hT} \boldsymbol{\sigma}_G^h \Big] \, \mathrm{d}A \quad . \end{aligned} \tag{5.3}$$

The interpolation functions of the independent fields that appear in (5.2) and (5.3) are now introduced.

5.1 Interpolation of the independent fields

As the global-local finite shell element is based on a three-field variational formulation, interpolation functions need to be established for the field $\tilde{\mathbf{v}}$ containing the displacement vector $\mathbf{u}$ and the vector of rotational parameters $\boldsymbol{\omega}$, for the independent effective stress resultant field $\boldsymbol{\sigma}_G$, and for the independent field $\tilde{\boldsymbol{\varepsilon}}$, containing the global shell strains and local quantities, and their respective variations and linearizations. The interpolation of $\tilde{\mathbf{v}}$ corresponds to the procedure presented in [131], while the interpolation of $\boldsymbol{\sigma}_G$ is based on [46, 111]. The interpolation of $\boldsymbol{\varepsilon}_G$ is discussed in [47]. As the interpolation functions for $\boldsymbol{\varepsilon}_L$ need to be incorporated into the existing model, the complete global-local finite element shell implementation is discussed in this chapter.

5.1.1 Initial and current reference surfaces

The interpolation functions for $\tilde{\mathbf{v}}$ can be derived from the interpolations of the initial and current reference surfaces. As was already pointed out, for reasons of numerical robustness 4-node elements are chosen for the interpolation of the displacement field. The element has five degrees of freedom at each node that does not lie on an intersection in the shell structure and six degrees of freedom on each node that does. The isoparametric concept is employed for quadrilaterals when defining the 4-node elements. The local numbering of the nodes is illustrated in figure 5.1. The initial geometry is approximated by the same bilinear interpolation functions for the position vector $\mathbf{X}$ and the director vector $\mathbf{D}$ on the reference surface of the element, so that

$$\mathbf{X}^h = \sum_{I=1}^{4} N_I \, \mathbf{X}_I \qquad \text{and} \qquad \mathbf{D}^h = \sum_{I=1}^{4} N_I \, \mathbf{D}_I \quad . \tag{5.4}$$

The index I in (5.4) represents the number of the node, so that I runs from one to four in each element. The shape functions are defined by

$$N_I = \frac{1}{4}(1 + \xi_I \xi)(1 + \eta_I \eta) \quad , \tag{5.5}$$

with $\xi_I \in \{-1, \quad 1, \quad 1, -1\}$ and $\eta_I \in \{-1, -1, \quad 1, \quad 1\}$. By means of the bilinear shape functions (5.5) a map is applied of the coordinates $\{\xi, \eta\} \in [-1, \quad 1]$ from the unit square to the reference surface in the reference configuration [131].

During the finite element simulation, when the nodal position vectors $\mathbf{X}_I$ are set up the local base vectors denoted $\mathbf{A}_{\alpha I}$ and the director vector $\mathbf{D}_I = \mathbf{A}_{3I}$ are also set up in every node of the finite element mesh.

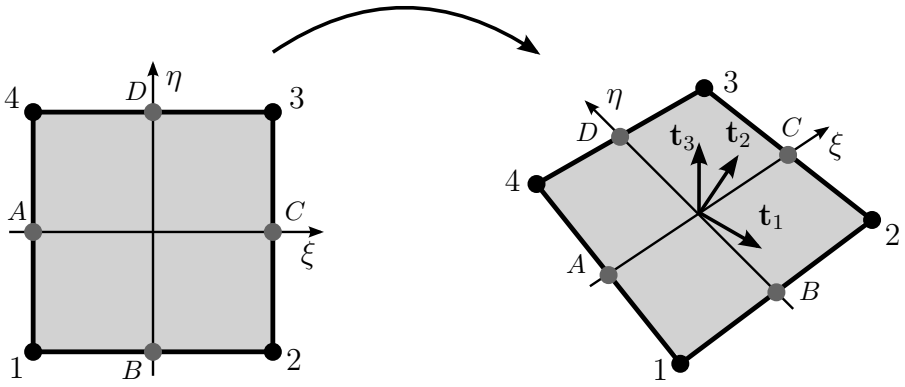

Figure 5.1: 4-node shell element

For computational reasons, an additional orthogonal base system is set up with the help of the position vectors $\mathbf{X}_I$ at the center of each element. It is illustrated in figure 5.1 and defined by

$$\mathbf{t}_1 = \frac{\left(\widehat{\mathbf{d}}_\mathbf{1} + \widehat{\mathbf{d}}_\mathbf{2}\right)}{\left|\widehat{\mathbf{d}}_\mathbf{1} + \widehat{\mathbf{d}}_\mathbf{2}\right|} \quad , \qquad \mathbf{t}_2 = \frac{\left(\widehat{\mathbf{d}}_\mathbf{1} - \widehat{\mathbf{d}}_\mathbf{2}\right)}{\left|\widehat{\mathbf{d}}_\mathbf{1} - \widehat{\mathbf{d}}_\mathbf{2}\right|} \qquad \text{and} \qquad \mathbf{t}_3 = \mathbf{t}_1 \times \mathbf{t}_2 \quad , \tag{5.6}$$

where the vectors $\widehat{\mathbf{d}}_\mathbf{1}$ and $\widehat{\mathbf{d}}_\mathbf{2}$ are specified with

$$\widehat{\mathbf{d}}_\mathbf{1} = \frac{\bar{\mathbf{d}}_1}{\left|\bar{\mathbf{d}}_1\right|} \qquad \text{and} \qquad \widehat{\mathbf{d}}_\mathbf{2} = \frac{\bar{\mathbf{d}}_2}{\left|\bar{\mathbf{d}}_2\right|} \quad . \tag{5.7}$$

In (5.7), further vectors $\bar{\mathbf{d}}_1$ and $\bar{\mathbf{d}}_2$ are defined by

$$\bar{\mathbf{d}}_1 = \mathbf{X}_3 - \mathbf{X}_1 \qquad \text{and} \qquad \bar{\mathbf{d}}_2 = \mathbf{X}_2 - \mathbf{X}_4 \quad . \tag{5.8}$$

An alternative to the base system in (5.6) is given in [54]. The in-plane base vectors $\mathbf{t}_1$ and $\mathbf{t}_2$ span a tangent plane at the center of the element. The coordinates associated with the in-plane base vectors $\mathbf{t}_1$ and $\mathbf{t}_2$ are denoted by ξ_1 and ξ_2, and should not be confused with the coordinates ξ and η that are associated with the bilinear shape functions (5.5).

Since the derivatives of the interpolated position vector $\mathbf{X}^h_{,\alpha}$ and the interpolated director vector $\mathbf{D}^h_{,\alpha}$ to the coordinates ξ_1 and ξ_2 are needed and both vectors are approximated by the shape functions, the derivatives of the shape functions (5.5) to the coordinates ξ_1 and ξ_2 need to be specified. They can be written as

$$\begin{bmatrix} N_{I,1} \\ N_{I,2} \end{bmatrix} = \mathbf{J}^{-1} \begin{bmatrix} N_{I,\xi} \\ N_{I,\eta} \end{bmatrix} \quad , \tag{5.9}$$

where $\mathbf{J}^{-1}$ denotes the inverse of the Jacobian matrix $\mathbf{J}$, which is defined by

$$\mathbf{J} = \begin{bmatrix} \dfrac{\partial \xi_1}{\partial \xi} & \dfrac{\partial \xi_2}{\partial \xi} \\ \dfrac{\partial \xi_1}{\partial \eta} & \dfrac{\partial \xi_2}{\partial \eta} \end{bmatrix} = \begin{bmatrix} \mathbf{X}^h_{,\xi} \cdot \mathbf{t}_1 & \mathbf{X}^h_{,\xi} \cdot \mathbf{t}_2 \\ \mathbf{X}^h_{,\eta} \cdot \mathbf{t}_1 & \mathbf{X}^h_{,\eta} \cdot \mathbf{t}_2 \end{bmatrix} \quad , \tag{5.10}$$

and $(\bullet)_{,\alpha}$ denotes derivatives to the coordinates ξ_α. The derivatives of the interpolated position vectors $\mathbf{X}^h_{,\xi}$ and $\mathbf{X}^h_{,\eta}$ can be determined with the help of the shape functions, so that

$$\mathbf{X}^h_{,\xi} = \mathbf{G}^0_\xi + \eta\,\mathbf{G}^1 \qquad \text{and} \qquad \mathbf{X}^h_{,\eta} = \mathbf{G}^0_\eta + \xi\,\mathbf{G}^1 \tag{5.11}$$

hold, with the definitions

$$\mathbf{G}^0_\xi = \frac{1}{4}\sum_{I=1}^{4} \xi_I\,\mathbf{X}_I \quad , \qquad \mathbf{G}^0_\eta = \frac{1}{4}\sum_{I=1}^{4} \eta_I\,\mathbf{X}_I \quad , \qquad \mathbf{G}^1 = \frac{1}{4}\sum_{I=1}^{4} \xi_I\,\eta_I\,\mathbf{X}_I \quad . \tag{5.12}$$

Thus, the inverse of the Jacobian matrix can be written as

$$\mathbf{J}^{-1} = \frac{1}{\det \mathbf{J}} \begin{bmatrix} J_{22} & -J_{12} \\ -J_{12} & J_{11} \end{bmatrix} \quad . \tag{5.13}$$

The derivatives of the interpolated position vector $\mathbf{X}^h_{,\alpha}$ and the interpolated director vector $\mathbf{D}^h_{,\alpha}$ with respect to the coordinates ξ_α can thus be determined with the help of (5.9), so that

$$\mathbf{X}^h_{,\alpha} = \sum_{I=1}^{4} N_{I,\alpha}\;\mathbf{X}_I \qquad \text{and} \qquad \mathbf{D}^h_{,\alpha} = \sum_{I=1}^{4} N_{I,\alpha}\;\mathbf{D}_I \quad . \tag{5.14}$$

The position vector $\mathbf{x}$ and the director vector $\mathbf{d}$ on the reference surface of the element in the current configuration are interpolated with the same shape functions (5.5) as the corresponding vectors in reference configuration (5.4), so that

$$\mathbf{x}^h = \sum_{I=1}^{4} N_I\,\mathbf{x}_I \qquad \text{and} \qquad \mathbf{d}^h = \sum_{I=1}^{4} N_I\,\mathbf{d}_I \quad . \tag{5.15}$$

In (5.15), $\mathbf{x}_I$ is the current nodal position vector $\mathbf{x}_I = \mathbf{X}_I + \mathbf{u}_I$ (3.3). The nodal director vector in the current configuration $\mathbf{d}_I = \mathbf{R}_I\mathbf{D}_I$ (3.10) is updated with the help of the Euler-Rodrigues formula introduced in (3.11). As was already mentioned in chapter 3.1.1, the procedure using the Euler-Rodrigues representation is singularity-free for $\omega < 2\pi$. For larger angles a multiplicative update of the total rotation tensor after a certain number of load steps must be applied.

Analogous to (5.14), the derivatives of the interpolated position vector $\mathbf{x}^h_{,\alpha}$ and the interpolated director vector $\mathbf{d}^h_{,\alpha}$ to the coordinates ξ_α can be derived with the help of (5.9), and thus

$$\mathbf{x}^h_{,\alpha} = \sum_{I=1}^{4} N_{I,\alpha}\;\mathbf{x}_I \qquad \text{and} \qquad \mathbf{d}^h_{,\alpha} = \sum_{I=1}^{4} N_{I,\alpha}\;\mathbf{d}_I \quad . \tag{5.16}$$

A finite element approximation of the shell membrane strains $\varepsilon^h_{\alpha\beta}$, curvatures $\kappa^h_{\alpha\beta}$, and shear strains γ^h_α can now be specified with the help of (5.4), (5.14), (5.15), and (5.16).

However, a finite shell element which implements the approximation of the transverse shear strains emanating from the Reissner-Mindlin kinematics does not pass the bending patch test introduced in [121] due to shear locking effects [45]. One remedy for this is reduced integration. The quality of the results of the reduced integration procedure, however, is highly problem-dependent and is usually more suitable for beam elements. For shell elements, often rank deficient stiffness matrices are obtained. A more suitable scheme is the application of an assumed shear strain interpolation presented in [33]. In this procedure the edge midpoints denoted by A, B, C and D as illustrated in figure 5.1 are the evaluation points, so that the transverse shear strains related to the element coordinates ξ and η can be specified with

$$\begin{bmatrix} \gamma_\xi^h \\ \gamma_\eta^h \end{bmatrix} = \begin{bmatrix} \frac{1}{2}\left[(1-\eta)\,\gamma_\xi^B + (1+\eta)\,\gamma_\xi^D\right] \\ \frac{1}{2}\left[(1-\xi)\,\gamma_\eta^A + (1+\xi)\,\gamma_\eta^C\right] \end{bmatrix} . \tag{5.17}$$

The interpolated transverse shear strains at the midpoints can be derived by evaluating

$$\begin{aligned} \gamma_\xi^M &= \left[\mathbf{x}_{,\xi}\cdot\mathbf{d} - \mathbf{X}_{,\xi}\cdot\mathbf{D}\right]^M \qquad \text{with} \qquad M = B, D \quad , \\ \gamma_\eta^L &= \left[\mathbf{x}_{,\eta}\cdot\mathbf{d} - \mathbf{X}_{,\eta}\cdot\mathbf{D}\right]^L \qquad \text{with} \qquad L = A, C \quad , \end{aligned} \tag{5.18}$$

where the director vectors are specified by

$$\begin{aligned} \mathbf{d}^A &= \frac{1}{2}\left(\mathbf{d}_4 + \mathbf{d}_1\right) \quad , & \mathbf{d}^B &= \frac{1}{2}\left(\mathbf{d}_1 + \mathbf{d}_2\right) \quad , \\ \mathbf{d}^C &= \frac{1}{2}\left(\mathbf{d}_2 + \mathbf{d}_3\right) \quad , & \mathbf{d}^D &= \frac{1}{2}\left(\mathbf{d}_3 + \mathbf{d}_4\right) \quad , \\ \mathbf{D}^A &= \frac{1}{2}\left(\mathbf{D}_4 + \mathbf{D}_1\right) \quad , & \mathbf{D}^B &= \frac{1}{2}\left(\mathbf{D}_1 + \mathbf{D}_2\right) \quad , \\ \mathbf{D}^C &= \frac{1}{2}\left(\mathbf{D}_2 + \mathbf{D}_3\right) \quad , & \mathbf{D}^D &= \frac{1}{2}\left(\mathbf{D}_3 + \mathbf{D}_4\right) \quad , \end{aligned} \tag{5.19}$$

and the derivatives of the interpolated position vectors in (5.18) are written as

$$\begin{aligned} \mathbf{x}_{,\eta}^A &= \frac{1}{2}\left(\mathbf{x}_4 - \mathbf{x}_1\right) \quad , & \mathbf{x}_{,\xi}^B &= \frac{1}{2}\left(\mathbf{x}_2 - \mathbf{x}_1\right) \quad , \\ \mathbf{x}_{,\eta}^C &= \frac{1}{2}\left(\mathbf{x}_3 - \mathbf{x}_2\right) \quad , & \mathbf{x}_{,\xi}^D &= \frac{1}{2}\left(\mathbf{x}_3 - \mathbf{x}_4\right) \quad , \\ \mathbf{X}_{,\eta}^A &= \frac{1}{2}\left(\mathbf{X}_4 - \mathbf{X}_1\right) \quad , & \mathbf{X}_{,\xi}^B &= \frac{1}{2}\left(\mathbf{X}_2 - \mathbf{X}_1\right) \quad , \\ \mathbf{X}_{,\eta}^C &= \frac{1}{2}\left(\mathbf{X}_3 - \mathbf{X}_2\right) \quad , & \mathbf{X}_{,\xi}^D &= \frac{1}{2}\left(\mathbf{X}_3 - \mathbf{X}_4\right) \quad . \end{aligned} \tag{5.20}$$

The interpolated transverse shear strains γ_1^h and γ_2^h can then be derived with the help of (5.13) by evaluating

$$\begin{bmatrix} \gamma_1^h \\ \gamma_2^h \end{bmatrix} = \mathbf{J}^{-1} \begin{bmatrix} \gamma_\xi^h \\ \gamma_\eta^h \end{bmatrix} \quad . \tag{5.21}$$

It is pointed out that even though the aforementioned procedure to derive the transverse shear strains in the finite element equation is not compatible with the variational formulation, it circumvents the problem of shear locking and is preferable to the method of reduced integration.

With the help of (3.19), the interpolated shell strains can be collected in a vector denoted $\boldsymbol{\varepsilon}_g^h$ (5.22), similar to (3.20), where the subscript g indicates that these are geometric strains as a function of the displacement field in the variational formulation.

$$\boldsymbol{\varepsilon}_g^h = \begin{bmatrix} \varepsilon_{11}^h \\ \varepsilon_{22}^h \\ 2\varepsilon_{12}^h \\ \kappa_{11}^h \\ \kappa_{22}^h \\ 2\kappa_{12}^h \\ \gamma_1^h \\ \gamma_2^h \end{bmatrix} = \begin{bmatrix} \frac{1}{2}\left(\mathbf{x}_{,1}^h \cdot \mathbf{x}_{,1}^h - \mathbf{X}_{,1}^h \cdot \mathbf{X}_{,1}^h\right) \\ \frac{1}{2}\left(\mathbf{x}_{,2}^h \cdot \mathbf{x}_{,2}^h - \mathbf{X}_{,2}^h \cdot \mathbf{X}_{,2}^h\right) \\ \mathbf{x}_{,1}^h \cdot \mathbf{x}_{,2}^h - \mathbf{X}_{,1}^h \cdot \mathbf{X}_{,2}^h \\ \mathbf{x}_{,1}^h \cdot \mathbf{d}_{,1}^h - \mathbf{X}_{,1}^h \cdot \mathbf{D}_{,1}^h \\ \mathbf{x}_{,2}^h \cdot \mathbf{d}_{,2}^h - \mathbf{X}_{,2}^h \cdot \mathbf{D}_{,2}^h \\ \mathbf{x}_{,1}^h \cdot \mathbf{d}_{,2}^h + \mathbf{x}_{,2}^h \cdot \mathbf{d}_{,1}^h - \mathbf{X}_{,1}^h \cdot \mathbf{D}_{,2}^h - \mathbf{X}_{,2}^h \cdot \mathbf{D}_{,1}^h \\ \mathbf{J}^{-1} \begin{Bmatrix} \frac{1}{2}\left[(1-\eta)\,\gamma_\xi^B + (1+\eta)\,\gamma_\xi^D\right] \\ \frac{1}{2}\left[(1-\xi)\,\gamma_\eta^A + (1+\xi)\,\gamma_\eta^C\right] \end{Bmatrix} \end{bmatrix} . \tag{5.22}$$

In the same way the variations of the shell strains were derived in (3.35), the variations of the interpolated shell strains can be derived. Analogous to (5.22) they are collected in a vector denoted $\delta\boldsymbol{\varepsilon}_G^h$ and specified by

$$\delta\boldsymbol{\varepsilon}_g^h = \begin{bmatrix} \delta\varepsilon_{11}^h \\ \delta\varepsilon_{22}^h \\ 2\delta\varepsilon_{12}^h \\ \delta\kappa_{11}^h \\ \delta\kappa_{22}^h \\ 2\delta\kappa_{12}^h \\ \delta\gamma_1^h \\ \delta\gamma_2^h \end{bmatrix} = \begin{bmatrix} \delta\mathbf{x}_{,1}^h \cdot \mathbf{x}_{,1}^h \\ \delta\mathbf{x}_{,2}^h \cdot \mathbf{x}_{,2}^h \\ \delta\mathbf{x}_{,1}^h \cdot \mathbf{x}_{,2}^h + \delta\mathbf{x}_{,2}^h \cdot \mathbf{x}_{,1}^h \\ \delta\mathbf{x}_{,1}^h \cdot \mathbf{d}_{,1}^h + \delta\mathbf{d}_{,1}^h \cdot \mathbf{x}_{,1}^h \\ \delta\mathbf{x}_{,2}^h \cdot \mathbf{d}_{,2}^h + \delta\mathbf{d}_{,2}^h \cdot \mathbf{x}_{,2}^h \\ \delta\mathbf{x}_{,1}^h \cdot \mathbf{d}_{,2}^h + \delta\mathbf{x}_{,2}^h \cdot \mathbf{d}_{,1}^h + \delta\mathbf{d}_{,1}^h \cdot \mathbf{x}_{,2}^h + \delta\mathbf{d}_{,2}^h \cdot \mathbf{x}_{,1}^h \\ \mathbf{J}^{-1} \begin{Bmatrix} \frac{1}{2}[(1-\eta)\,\delta\gamma_\xi^B + (1+\eta)\,\delta\gamma_\xi^D \\ \frac{1}{2}[(1-\xi)\,\delta\gamma_\eta^A + (1+\xi)\,\delta\gamma_\eta^C] \end{Bmatrix} \end{bmatrix} . \tag{5.23}$$

The variations of the interpolated transverse shear strains in (5.23) are evaluated at the edge midpoints with the help of (5.18), (5.19), and (5.20), so that

$$\begin{aligned} \delta\gamma_\xi^M &= \left[\delta\mathbf{x}_{,\xi} \cdot \mathbf{d} + \mathbf{x}_{,\xi} \cdot \delta\mathbf{d}\right]^M \qquad \text{with} \qquad M = B, D \quad , \\ \delta\gamma_\eta^L &= \left[\delta\mathbf{x}_{,\eta} \cdot \mathbf{d} + \mathbf{x}_{,\eta} \cdot \delta\mathbf{d}\right]^L \qquad \text{with} \qquad L = A, C \quad , \end{aligned} \tag{5.24}$$

where $\delta\mathbf{x}_{,\alpha}^h$ and $\delta\mathbf{d}_{,\alpha}^h$ are vectors containing interpolations of variations with the help of the shape functions and, with $\delta\mathbf{x}_I = \delta\mathbf{u}_I$, are specified with

$$\delta\mathbf{x}_{,\alpha}^h = \sum_{I=1}^{4} N_{I,\alpha}\ \delta\mathbf{u}_I \qquad \text{and} \qquad \delta\mathbf{d}_{,\alpha}^h = \sum_{I=1}^{4} N_{I,\alpha}\ \delta\mathbf{d}_I \quad . \tag{5.25}$$

The variation of the nodal director vector $\mathbf{d}_I$ can be derived by means of the procedure discussed in chapter 3.3.1. Thus, with (3.44),

$$\delta\mathbf{d}_I = \mathbf{W}_I^T \mathbf{H}_I \bar{\mathbf{T}}_I \delta\boldsymbol{\beta}_I \tag{5.26}$$

holds. Consequently, accounting for (5.25) and (5.26), the vector containing the variations of the shell strains $\delta\boldsymbol{\varepsilon}_G^h$ defined in (5.23) can be expressed by means of the derivatives of the shape functions, so that

$$\delta\boldsymbol{\varepsilon}_g^h = \sum_{I=1}^{4} \begin{bmatrix} N_{I,1}\,\mathbf{x}_{,1}^T & \mathbf{0} \\ N_{I,2}\,\mathbf{x}_{,2}^T & \mathbf{0} \\ N_{I,1}\,\mathbf{x}_{,2}^T + N_{I,2}\,\mathbf{x}_{,1}^T & \mathbf{0} \\ N_{I,1}\,\mathbf{d}_{,1}^T & N_{I,1}\,\mathbf{b}_{I1}^T \\ N_{I,2}\,\mathbf{d}_{,2}^T & N_{I,2}\,\mathbf{b}_{I2}^T \\ N_{I,1}\,\mathbf{d}_{,2}^T + N_{I,2}\,\mathbf{d}_{,1}^T & N_{I,1}\,\mathbf{b}_{I2}^T + N_{I,2}\,\mathbf{b}_{I1}^T \\ \mathbf{J}^{-1} \begin{Bmatrix} N_{I,\xi}\,\mathbf{d}_M^T \\ N_{I,\eta}\,\mathbf{d}_L^T \end{Bmatrix} & \mathbf{J}^{-1} \begin{Bmatrix} N_{I,\xi}\,\xi_I\,\mathbf{b}_M^T \\ N_{I,\eta}\,\eta_I\,\mathbf{b}_L^T \end{Bmatrix} \end{bmatrix} \begin{bmatrix} \delta\mathbf{u}_I \\ \delta\boldsymbol{\beta}_I \end{bmatrix} \quad . \tag{5.27}$$

The index h is omitted in the matrix in (5.27) for clarity. Further definitions

$$\mathbf{b}_{I\alpha} = \mathbf{K}_I^T\,\mathbf{x}_{,\alpha} \quad , \qquad \mathbf{b}_M = \mathbf{K}_I^T\,\mathbf{x}_{,\xi}^M \qquad \text{and} \qquad \mathbf{b}_L = \mathbf{K}_I^T\,\mathbf{x}_{,\eta}^L \tag{5.28}$$

are made with $\mathbf{K}_I = \mathbf{W}_I^T \mathbf{H}_I \bar{\mathbf{T}}_I$, where the allocation of the midside nodes to the corner nodes is given by

$$(I, M, L) \in \{(1, B, A); (2, B, C); (3, D, C); (4, D, A)\} \quad . \tag{5.29}$$

The matrix in (5.27) is denoted by $\mathbf{B}_I$ and the vector is denoted by $\delta\tilde{\mathbf{v}}_I$, so that

$$\delta\boldsymbol{\varepsilon}_g^h = \sum_{I=1}^{4} \mathbf{B}_I\,\delta\tilde{\mathbf{v}}_I = \mathbf{B}\,\delta\tilde{\mathbf{v}} \quad . \tag{5.30}$$

With (5.30), the interpolation functions for the vector $\delta\boldsymbol{\varepsilon}_g^h$ in (5.3), that holds the variations of the shell strains emanating from the field $\tilde{\mathbf{v}}$, have been established.

The linearization vector $\Delta\boldsymbol{\varepsilon}_g^h$ in (5.3) can be approximated in an analogous way to the approximation of the vector $\delta\boldsymbol{\varepsilon}_g^h$. With the derivatives of the approximated linearized vectors $\Delta\mathbf{x}_{,\alpha}^h$ and $\Delta\mathbf{d}_{,\alpha}^h$, given with

$$\Delta\mathbf{x}_{,\alpha}^h = \sum_{I=1}^{4} N_{I,\alpha}\,\Delta\mathbf{u}_I \qquad \text{and} \qquad \Delta\mathbf{d}_{,\alpha}^h = \sum_{I=1}^{4} N_{I,\alpha}\,\Delta\mathbf{d}_I \quad , \tag{5.31}$$

the linearization vector $\Delta\boldsymbol{\varepsilon}_g^h$ can be specified by replacing δ in (5.30) with Δ, so that

$$\Delta\boldsymbol{\varepsilon}_g^h = \sum_{I=1}^{4} \mathbf{B}_I \, \Delta\tilde{\mathbf{v}}_I = \mathbf{B} \, \Delta\tilde{\mathbf{v}} \quad . \tag{5.32}$$

In the same way the linearized variations of the shell strains were derived in (3.92), the linearized variations of the interpolated shell strains can be derived. Analogous to (5.22) they are collected in a vector denoted by $\Delta\delta\boldsymbol{\varepsilon}_G^h$ and defined by

$$\Delta\delta\boldsymbol{\varepsilon}_G^h = \begin{bmatrix} \Delta\delta\varepsilon_{11}^h \\ \Delta\delta\varepsilon_{22}^h \\ 2\Delta\delta\varepsilon_{12}^h \\ \Delta\delta\kappa_{11}^h \\ \Delta\delta\kappa_{22}^h \\ 2\Delta\delta\kappa_{12}^h \\ \\ \Delta\delta\gamma_1^h \\ \Delta\delta\gamma_2^h \end{bmatrix} = \begin{bmatrix} \delta\mathbf{x}_{,1}^h \cdot \Delta\mathbf{x}_{,1}^h \\ \delta\mathbf{x}_{,2}^h \cdot \Delta\mathbf{x}_{,2}^h \\ \delta\mathbf{x}_{,1}^h \cdot \Delta\mathbf{x}_{,2}^h + \delta\mathbf{x}_{,2}^h \cdot \Delta\mathbf{x}_{,1}^h \\ \delta\mathbf{x}_{,1}^h \cdot \Delta\mathbf{d}_{,1}^h + \delta\mathbf{d}_{,1}^h \cdot \Delta\mathbf{x}_{,1}^h + \mathbf{x}_{,1}^h \cdot \Delta\delta\mathbf{d}_{,1}^h \\ \delta\mathbf{x}_{,2}^h \cdot \Delta\mathbf{d}_{,2}^h + \delta\mathbf{d}_{,2}^h \cdot \Delta\mathbf{x}_{,2}^h + \mathbf{x}_{,2}^h \cdot \Delta\delta\mathbf{d}_{,2}^h \\ \delta\mathbf{x}_{,1}^h \cdot \Delta\mathbf{d}_{,2}^h + \delta\mathbf{x}_{,2}^h \cdot \Delta\mathbf{d}_{,1}^h + \delta\mathbf{d}_{,1}^h \cdot \Delta\mathbf{x}_{,2}^h + \delta\mathbf{d}_{,2}^h \cdot \Delta\mathbf{x}_{,1}^h \\ \quad + \mathbf{x}_{,1}^h \cdot \Delta\delta\mathbf{d}_{,2}^h + \mathbf{x}_{,2}^h \cdot \Delta\delta\mathbf{d}_{,1}^h \\ \mathbf{J}^{-1} \begin{Bmatrix} \frac{1}{2}[(1-\eta)\,\Delta\delta\gamma_\xi^B + (1+\eta)\,\Delta\delta\gamma_\xi^D] \\ \frac{1}{2}[(1-\xi)\,\Delta\delta\gamma_\eta^A + (1+\xi)\,\Delta\delta\gamma_\eta^C] \end{Bmatrix} \end{bmatrix} . \tag{5.33}$$

The variations of the interpolated transverse shear strains in (5.33) are evaluated at the edge midpoints with the help of (5.18), (5.19), and (5.20), yielding

$$\begin{aligned} \Delta\delta\gamma_\xi^M &= [\delta\mathbf{x}_{,\xi} \cdot \Delta\mathbf{d} + \Delta\mathbf{x}_{,\xi} \cdot \delta\mathbf{d} + \mathbf{x}_{,\xi} \cdot \Delta\delta\mathbf{d}]^M \qquad \text{with} \qquad M = B, D \quad , \\ \Delta\delta\gamma_\eta^L &= [\delta\mathbf{x}_{,\eta} \cdot \Delta\mathbf{d} + \Delta\mathbf{x}_{,\eta} \cdot \delta\mathbf{d} + \mathbf{x}_{,\eta} \cdot \Delta\delta\mathbf{d}]^L \qquad \text{with} \qquad L = A, C \quad . \end{aligned} \tag{5.34}$$

The derivative of the approximated linearized variational vector $\Delta\delta\mathbf{d}_{,\alpha}^h$ in (5.33) is written as

$$\Delta\delta\mathbf{d}_{,\alpha}^h = \sum_{I=1}^{4} N_{I,\alpha} \; \Delta\delta\mathbf{d}_I \quad . \tag{5.35}$$

In (5.33), there are terms that are dot products of vectors $\mathbf{x}_{,\alpha}^h$ and $\Delta\delta\mathbf{d}_{,\alpha}^h$. Because these vectors are approximated with interpolation functions defined in (5.25) and (5.35) the nodal vectors $\mathbf{x}_I$ are multiplied with the linearized variation of the nodal director vector $\Delta\delta\mathbf{d}_I$. Hence, the procedure discussed in chapter 3.6 can be employed to derive these terms. With (3.93),

$$\mathbf{h}_I \cdot \Delta\delta\mathbf{d}_I = \mathbf{h}_I \cdot \Delta\left(\delta\mathbf{w}_I \times \mathbf{d}_I\right) = \delta\mathbf{w}_I \cdot \mathbf{M}_I \Delta\mathbf{w}_I \tag{5.36}$$

holds, where the vector $\mathbf{h}_I$ can be any vector $\mathbf{h}_I \in R^3$, such as an arbitrary nodal vector $\mathbf{x}_I$. Thus, with the help of (5.25), (5.26), (5.31), (5.35), and (5.36) the term $\Delta\delta\boldsymbol{\varepsilon}_g^{hT}\boldsymbol{\sigma}_G^h$ in (5.3) can be derived by evaluating

$$\Delta\delta\boldsymbol{\varepsilon}_g^{hT}\boldsymbol{\sigma}_G^h = \sum_{I=1}^{4}\sum_{K=1}^{4} \delta\tilde{\mathbf{v}}_I^T \, \mathbf{k}_{\sigma IK} \, \Delta\tilde{\mathbf{v}}_K \quad , \tag{5.37}$$

where the matrix $\mathbf{k}_{\sigma IK}$ can be derived after some algebra and is defined in [131]. The vector $\boldsymbol{\sigma}_G^h$ in (5.37) and therefore also the matrix $\mathbf{k}_{\sigma IK}$ contain interpolation functions for the effective shell stress resultants defined in (3.33), which will be discussed in the next section.

With (5.30), (5.32), and (5.37) the interpolations of $\delta\boldsymbol{\varepsilon}_g^{hT}$, $\Delta\boldsymbol{\varepsilon}_g^{hT}$ and $\Delta\delta\boldsymbol{\varepsilon}_g^{hT}$ have been specified. Thus, the finite element approximations of vectors containing geometric strains as a function of the displacement field can be inserted in (5.3) on the basis of the interpolations of the initial and current reference surfaces. Next, the interpolation of the independent stress resultant field will be derived.

5.1.2 Stress resultant field

For the interpolation of the independent stress resultant field $\boldsymbol{\sigma}_G$ a procedure is chosen which allows the element to pass standard patch tests, for example the tests defined in [80]. A discussion of the patch test in connection with the bending part is given in [45] and a discussion of the complete approximation in [131]. As already mentioned the chosen interpolation is based on [111]. The original procedure for plane stress problems is presented in [90].

The independent stress resultant field $\boldsymbol{\sigma}_G^h$ is interpolated by

$$\boldsymbol{\sigma}_G^h = \mathbf{N}_\sigma \, \hat{\boldsymbol{\sigma}}_G \quad , \tag{5.38}$$

where $\mathbf{N}_\sigma$ is defined by

$$\mathbf{N}_\sigma = \begin{bmatrix} \mathbf{1}_3 & \mathbf{0} & \mathbf{0} & \mathbf{N}_\sigma^m & \mathbf{0} & \mathbf{0} \\ \mathbf{0} & \mathbf{1}_3 & \mathbf{0} & \mathbf{0} & \mathbf{N}_\sigma^b & \mathbf{0} \\ \mathbf{0} & \mathbf{0} & \mathbf{1}_2 & \mathbf{0} & \mathbf{0} & \mathbf{N}_\sigma^s \end{bmatrix} \quad , \tag{5.39}$$

and the components $\mathbf{N}_\sigma^m$, $\mathbf{N}_\sigma^b$ and $\mathbf{N}_\sigma^s$ are matrices defined by

$$\mathbf{N}_\sigma^m = \mathbf{N}_\sigma^b = \mathbf{T}_\sigma^0 \begin{bmatrix} \eta - \bar{\eta} & 0 \\ 0 & \xi - \bar{\xi} \\ 0 & 0 \end{bmatrix} \quad \text{and} \quad \mathbf{N}_\sigma^s = \tilde{\mathbf{T}}_\sigma^0 \begin{bmatrix} \eta - \bar{\eta} & 0 \\ 0 & \xi - \bar{\xi} \end{bmatrix} \quad . \tag{5.40}$$

The matrices $\mathbf{T}_\sigma^0$ and $\tilde{\mathbf{T}}_\sigma^0$ describe a transformation of covariant tensor components to the local Cartesian element coordinate system at the element center. They are defined by

$$\mathbf{T}_\sigma^0 = \begin{bmatrix} J_{11}^0 J_{11}^0 & J_{21}^0 J_{21}^0 & 2 J_{11}^0 J_{21}^0 \\ J_{12}^0 J_{12}^0 & J_{22}^0 J_{22}^0 & 2 J_{12}^0 J_{22}^0 \\ J_{11}^0 J_{12}^0 & J_{21}^0 J_{22}^0 & J_{11}^0 J_{22}^0 + J_{12}^0 J_{21}^0 \end{bmatrix} \quad \text{and} \quad \tilde{\mathbf{T}}_\sigma^0 = \begin{bmatrix} J_{11}^0 & J_{21}^0 \\ J_{12}^0 & J_{22}^0 \end{bmatrix} \quad . \tag{5.41}$$

In (5.41), the coefficients $J^0_{\alpha\beta}$ are the components of the Jacobian matrix $\mathbf{J}$ (5.10) evaluated at the element center and the constants in (5.40) $\bar{\xi}$ and $\bar{\eta}$ are defined by

$$\bar{\xi} = \frac{1}{A_e} \int_{\Omega_{\mathrm{el}}} \xi \, \mathrm{d}A \qquad \text{and} \qquad \bar{\eta} = \frac{1}{A_e} \int_{\Omega_{\mathrm{el}}} \eta \, \mathrm{d}A \qquad \text{with} \qquad A_e = \int_{\Omega_{\mathrm{el}}} \mathrm{d}A \quad . \tag{5.42}$$

The interpolation of the independent stress resultant field in (5.38) thus consists of a constant and a varying part. The vector $\boldsymbol{\sigma}^h_G$ holds a total of 14 parameters, three constant parameters for the membrane and the bending part, respectively, two constant parameters for the shear part, and two parameters for the membrane, bending and shear part, respectively. The constants $\bar{\xi}$ and $\bar{\eta}$ are introduced in order to derive partly decoupled matrices, since the linear functions are orthogonal to the constant functions. The variation and linearization of $\boldsymbol{\sigma}^h_G$ are specified by

$$\delta\boldsymbol{\sigma}^h_G = \mathbf{N}_\sigma \, \delta\hat{\boldsymbol{\sigma}}_G \qquad \text{and} \qquad \Delta\boldsymbol{\sigma}^h_G = \mathbf{N}_\sigma \, \Delta\hat{\boldsymbol{\sigma}}_G \quad . \tag{5.43}$$

The interpolation of $\boldsymbol{\sigma}^h_G$ (5.38) is used to derive the matrix $\mathbf{k}_{\sigma IK}$ in (5.37). With (5.43) the interpolated variation and linearization of $\boldsymbol{\sigma}^h_G$ have been specified and can be inserted into (5.3). In the next section, the interpolation of the independent field containing the shell strains and local quantities will be derived.

5.1.3 Field of global shell strains and local quantities

The interpolation of the independent field containing the shell strains and local quantities $\tilde{\boldsymbol{\varepsilon}}^h$ (5.44) consists of two parts. The first part approximates the global shell strains $\boldsymbol{\varepsilon}^h_G$ and the second part approximates the local displacements and their derivatives $\boldsymbol{\varepsilon}^h_L$, so that

$$\tilde{\boldsymbol{\varepsilon}}^h = \begin{bmatrix} \boldsymbol{\varepsilon}^h_G \\ \boldsymbol{\varepsilon}^h_L \end{bmatrix} = \begin{bmatrix} \mathbf{N}_{\varepsilon G} & \mathbf{0} \\ \mathbf{0} & \mathbf{N}_{\varepsilon L} \end{bmatrix} \begin{bmatrix} \hat{\boldsymbol{\varepsilon}}_G \\ \hat{\boldsymbol{\varepsilon}}_L \end{bmatrix} \quad . \tag{5.44}$$

A similar separation is realized in [71]. However, the second part in [71] concerns only the interlaminar normal strains and only global functions over the whole thickness of the laminate are utilized. Additionally, the local warping of the cross section is not accounted for and therefore the path of the transverse shear strains cannot be accurately predicted.

The interpolation of the global part largely corresponds to the procedure presented in [71]. The global part is divided into two further parts for transversely isotropic materials, and thus

$$\boldsymbol{\varepsilon}^h_G = \mathbf{N}_{\varepsilon G} \hat{\boldsymbol{\varepsilon}}_G = \begin{bmatrix} \mathbf{N}^1_{\varepsilon G}, & \mathbf{N}^2_{\varepsilon G} \end{bmatrix} \begin{bmatrix} \hat{\boldsymbol{\varepsilon}}^1_G \\ \hat{\boldsymbol{\varepsilon}}^2_G \end{bmatrix} \quad . \tag{5.45}$$

The first part is analogous to the interpolation of the independent shell stresses, whereas the second part corresponds to the enhanced strain interpolation in [116]. The reason for this is that for isotropic materials it is sufficient to use the same interpolation functions

for the stresses and the strains. On the other hand, for shells of materials that exhibit transversely isotropic behavior, introducing additional interpolation functions increases the performance of the shell element, as this leads to better convergence behavior for laminated shells with coupled membrane and bending stiffnesses [47]. This is the case for laminated shells with certain stacking sequences. Similar work has been carried out in [63, 64, 91]. In order to avoid conflicts, the functions of the second part are chosen orthogonal to the stress interpolation.

The first part of the global strains is interpolated in the same way the independent stress resultant field $\boldsymbol{\sigma}_G$ (5.38) is interpolated in chapter 5.1.2, so that $\mathbf{N}^1_{\varepsilon G}$ is defined by

$$\mathbf{N}^1_{\varepsilon G} = \begin{bmatrix} \mathbf{1}_3 & \mathbf{0} & \mathbf{0} & \mathbf{N}^{m1}_{\varepsilon} & \mathbf{0} & \mathbf{0} \\ \mathbf{0} & \mathbf{1}_3 & \mathbf{0} & \mathbf{0} & \mathbf{N}^{b1}_{\varepsilon} & \mathbf{0} \\ \mathbf{0} & \mathbf{0} & \mathbf{1}_2 & \mathbf{0} & \mathbf{0} & \mathbf{N}^{s1}_{\varepsilon} \end{bmatrix} \quad , \tag{5.46}$$

and the components $\mathbf{N}^{m1}_{\varepsilon}$, $\mathbf{N}^{b1}_{\varepsilon}$ and $\mathbf{N}^{s1}_{\varepsilon}$ are matrices defined by

$$\mathbf{N}^{m1}_{\varepsilon} = \mathbf{N}^{b1}_{\varepsilon} = \mathbf{T}^0_{\varepsilon} \begin{bmatrix} \eta - \bar{\eta} & 0 \\ 0 & \xi - \bar{\xi} \\ 0 & 0 \end{bmatrix} \qquad \text{and} \qquad \mathbf{N}^{s1}_{\varepsilon} = \mathbf{N}^{s}_{\sigma} \quad , \tag{5.47}$$

with matrix $\mathbf{T}^0_{\varepsilon}$, which describes a transformation of covariant tensor components to the local Cartesian coordinate system at the element center, and is defined by

$$\mathbf{T}^0_{\varepsilon} = \begin{bmatrix} J^0_{11}J^0_{11} & J^0_{21}J^0_{21} & J^0_{11}J^0_{21} \\ J^0_{12}J^0_{12} & J^0_{22}J^0_{22} & J^0_{12}J^0_{22} \\ 2J^0_{11}J^0_{12} & 2J^0_{21}J^0_{22} & J^0_{11}J^0_{22} + J^0_{12}J^0_{21} \end{bmatrix} \quad . \tag{5.48}$$

It is noted that the matrix $\mathbf{T}^0_{\varepsilon}$ in (5.48) is slightly different than the matrix $\mathbf{T}^0_{\sigma}$ in (5.41). Analogous to the interpolation of the independent effective stress resultants in the preceding section the vector $\hat{\boldsymbol{\varepsilon}}^1_G$ in (5.45) holds 14 parameters.

For the second part of the interpolated global strains the matrix $\mathbf{N}^2_{\varepsilon G}$ in (5.45) can be specified by

$$\mathbf{N}^2_{\varepsilon G} = \begin{bmatrix} \mathbf{N}^{m2}_{\varepsilon} & \mathbf{0} \\ \mathbf{0} & \mathbf{N}^{b2}_{\varepsilon} \\ \mathbf{0} & \mathbf{0} \end{bmatrix} \quad , \tag{5.49}$$

where the components $\mathbf{N}^{m2}_{\varepsilon}$ and $\mathbf{N}^{b2}_{\varepsilon}$ are matrices defined by

$$\mathbf{N}^{m2}_{\varepsilon} = \mathbf{N}^{b2}_{\varepsilon} = \frac{j_0}{j} \left(\mathbf{T}^0_{\sigma}\right)^{-T} \mathbf{M}_{\alpha} \quad , \qquad \text{with} \qquad \alpha = 2, 4 \tag{5.50}$$

and $j_0 = j\,(\xi = 0, \eta = 0)$. Depending on the choice of the matrix $\mathbf{M}_\alpha$ in (5.50) the membrane and bending strains can be interpolated with two or four parameters, with $\mathbf{M}_2$ and $\mathbf{M}_4$ defined by

$$\mathbf{M}_2 = \begin{bmatrix} \xi & 0 \\ 0 & \eta \\ 0 & 0 \end{bmatrix} \qquad \text{and} \qquad \mathbf{M}_4 = \begin{bmatrix} \xi & 0 & \xi\eta & 0 \\ 0 & \eta & 0 & \xi\eta \\ 0 & 0 & 0 & 0 \end{bmatrix} \quad . \tag{5.51}$$

Because the membrane and the bending part in (5.49) lead to interpolations with two or four parameters, respectively, the vector $\hat{\boldsymbol{\varepsilon}}_G^2$ in (5.45) holds four, six, or eight parameters.

The approximation of the local field $\boldsymbol{\varepsilon}_L^h$ introduced in (4.26) containing the local displacements and their derivatives takes the form

$$\boldsymbol{\varepsilon}_L^h = \mathbf{N}_{\varepsilon L} \hat{\boldsymbol{\varepsilon}}_L \quad , \tag{5.52}$$

so that the matrix $\mathbf{N}_{\varepsilon L}$ and vector of unknowns $\hat{\boldsymbol{\varepsilon}}_L$ need to be derived. Two different procedures will be presented.

In the first procedure, the local displacements $\mathbf{m}_L$ introduced in (4.14) are interpolated by

$$\mathbf{m}_L^h = \sum_{I=1}^{4} N_I \, \mathbf{n}_I^L \quad , \tag{5.53}$$

where the same bilinear shape functions N_I are used as for the interpolation of the position and director vectors in (5.5). Thus the vector $\boldsymbol{\varepsilon}_L^h$ is approximated by

$$\boldsymbol{\varepsilon}_L^h = \begin{bmatrix} \mathbf{m}_L^h \\ \mathbf{m}_{L,1}^h \\ \mathbf{m}_{L,2}^h \end{bmatrix} = \sum_{I=1}^{4} \begin{bmatrix} N_I \\ N_{I,1} \\ N_{I,2} \end{bmatrix} \mathbf{n}_I^L \quad . \tag{5.54}$$

In order to conform to the notation in (5.44) and (5.52) the matrix $\mathbf{N}_{\varepsilon L}$ is defined by

$$\mathbf{N}_{\varepsilon L} = \begin{bmatrix} \mathbf{N}_1 & \mathbf{N}_2 & \mathbf{N}_3 & \mathbf{N}_4 \\ \mathbf{N}_{1,1} & \mathbf{N}_{2,1} & \mathbf{N}_{3,1} & \mathbf{N}_{4,1} \\ \mathbf{N}_{1,2} & \mathbf{N}_{2,2} & \mathbf{N}_{3,2} & \mathbf{N}_{4,2} \end{bmatrix} \quad , \tag{5.55}$$

where the components of $\mathbf{N}_{\varepsilon L}$ are matrices that contain the shape functions or their derivatives on the diagonal and all other entries are zero. The vector of unknowns therefore becomes

$$\hat{\boldsymbol{\varepsilon}}_L = \begin{bmatrix} \mathbf{n}_1^L \\ \mathbf{n}_2^L \\ \mathbf{n}_3^L \\ \mathbf{n}_4^L \end{bmatrix} \quad . \tag{5.56}$$

Thus, through this procedure $4(3n-1)$ unknowns have been introduced for both the ξ^1-direction and the ξ^2-direction, while $12n$ unknowns have been introduced for the ξ^3-direction. A total of $4(9n-2)$ unknowns are therefore introduced by the local model and are contained in the vector $\hat{\boldsymbol{\varepsilon}}_L$ (5.56). Each matrix $\mathbf{N}_i$ in (5.56) has dimensions of $(9n-2)\times(9n-2)$ and each vector $\mathbf{n}_i^L$ has $9n-2$ entries. This of course leads to high computational costs. In the second procedure, however, the number of unknowns is significantly reduced.

For the second procedure, it is considered that the derivatives to the two coordinates in the plane ξ^1 and ξ^2 are zero and the matrix $\mathbf{A}_L$ and vector $\boldsymbol{\varepsilon}_L$ can be downsized and written as

$$\begin{bmatrix} E_{11}^L \\ E_{22}^L \\ E_{33}^L \\ 2E_{12}^L \\ 2E_{13}^L \\ 2E_{23}^L \end{bmatrix} = \begin{bmatrix} \mathbf{0} & \mathbf{0} & \mathbf{0} \\ \mathbf{0} & \mathbf{0} & \mathbf{0} \\ \mathbf{0} & \mathbf{0} & \tilde{\mathbf{M}}_{w,3} \\ \mathbf{0} & \mathbf{0} & \mathbf{0} \\ \tilde{\mathbf{M}}_{u,3} & \mathbf{0} & \mathbf{0} \\ \mathbf{0} & \tilde{\mathbf{M}}_{v,3} & \mathbf{0} \end{bmatrix} \begin{bmatrix} \tilde{\mathbf{m}}_u \\ \tilde{\mathbf{m}}_v \\ \tilde{\mathbf{m}}_w \end{bmatrix} \quad . \tag{5.57}$$

The reduced form given in (5.57) leads to elementwise constant values. Thus, no interpolation functions in the domain that depend on the in-plane coordinates ξ^1 and ξ^2 are introduced and the quantities in each element are simply interpolated by means of

$$\boldsymbol{\varepsilon}_L^h = \mathbf{1}\,\hat{\boldsymbol{\varepsilon}}_L \qquad \text{with} \qquad \hat{\boldsymbol{\varepsilon}}_L = \begin{bmatrix} \hat{\mathbf{m}}_u \\ \hat{\mathbf{m}}_v \\ \hat{\mathbf{m}}_w \end{bmatrix} \quad , \tag{5.58}$$

where $\mathbf{1}$ is a unit matrix, the length of which corresponds to the length of $\hat{\boldsymbol{\varepsilon}}_L$ and $\boldsymbol{\varepsilon}_L^h$. Thus, in this procedure, $3n-1$ unknowns are introduced for both the ξ^1-direction and the ξ^2-direction and $3n$ unknowns are introduced for the ξ^3-direction, leading to a total of $9n-2$ unknowns.

For the sake of completeness, the variation and linearization of the global field $\boldsymbol{\varepsilon}^h$ are specified with

$$\delta\boldsymbol{\varepsilon}_G^h = \mathbf{N}_{\varepsilon G}\delta\hat{\boldsymbol{\varepsilon}}_G \qquad \text{and} \qquad \Delta\boldsymbol{\varepsilon}_G^h = \mathbf{N}_{\varepsilon G}\Delta\hat{\boldsymbol{\varepsilon}}_G \quad , \tag{5.59}$$

while the variation and linearization of the local field $\boldsymbol{\varepsilon}^h$ are given by

$$\delta\boldsymbol{\varepsilon}_L^h = \mathbf{N}_{\varepsilon L}\delta\hat{\boldsymbol{\varepsilon}}_L \qquad \text{and} \qquad \Delta\boldsymbol{\varepsilon}_L^h = \mathbf{N}_{\varepsilon L}\Delta\hat{\boldsymbol{\varepsilon}}_L \quad . \tag{5.60}$$

Thus, the interpolation functions for all the independent fields that appear in (5.3) have been defined.

5.2 Interpolation of the linearized global-local mixed variational principle

With the interpolations of the independent fields established, they can be inserted into the linearized weak form, (5.1). The first term in (5.1) is approximated by inserting the interpolations (5.30), (5.38), (5.43 a), (5.45), (5.59 a), and (5.60 a) into (5.2), so that

$$g(\tilde{\boldsymbol{\theta}}^h, \delta\tilde{\boldsymbol{\theta}}^h) = \sum_{\text{el}=1}^{\text{numel}} \left[\delta\hat{\boldsymbol{\varepsilon}}_G^T \mathbf{f}_G^e + \delta\hat{\boldsymbol{\varepsilon}}_L^T \mathbf{f}_L^e + \delta\hat{\boldsymbol{\sigma}}_G^T \mathbf{f}^s + \delta\tilde{\mathbf{v}}^T \left(\mathbf{f}^i - \mathbf{f}^a\right)\right]_{\text{el}} \quad , \tag{5.61}$$

where the summation index runs from 1 to the number of elements used to discretize the problem. In (5.61), the definitions

$$\begin{aligned} \mathbf{f}_G^e &= \int_{\Omega_0} \mathbf{N}_{\varepsilon G}^T \frac{\partial \Psi}{\partial \boldsymbol{\varepsilon}_G^h} \,\mathrm{d}A + \hat{\mathbf{F}}\hat{\boldsymbol{\sigma}}_G \quad , & \mathbf{f}_L^e &= \int_{\Omega_0} \mathbf{N}_{\varepsilon L}^T \frac{\partial \Psi}{\partial \boldsymbol{\varepsilon}_L^h} \,\mathrm{d}A \quad , \\ \mathbf{f}^s &= \int_{\Omega_0} \mathbf{N}_\sigma^T \boldsymbol{\varepsilon}_g^h \,\mathrm{d}A + \hat{\mathbf{F}}^T \hat{\boldsymbol{\varepsilon}}_G \quad , & \mathbf{f}^i &= \int_{\Omega_0} \mathbf{G}^T \hat{\boldsymbol{\sigma}}_G \,\mathrm{d}A \quad , \end{aligned} \tag{5.62}$$

have been made and $\mathbf{f}^a$ is the external load vector that corresponds to the standard displacement formulation. Further, the definitions

$$\hat{\mathbf{F}} = -\int_{\Omega_0} \mathbf{N}_{\varepsilon G}^T \mathbf{N}_\sigma \,\mathrm{d}A \qquad \text{and} \qquad \mathbf{G} = \int_{\Omega_0} \mathbf{N}_\sigma^T \mathbf{B} \,\mathrm{d}A \tag{5.63}$$

have been made. The matrix $\hat{\mathbf{F}}$ can be integrated analytically, since only polynomials of the coordinates ξ and η are involved [131]. With the area element of the shell reference surface denoted by A_e defined in (5.42), a decoupled matrix is thus obtained for $\hat{\mathbf{F}}$ and is specified by

$$\hat{\mathbf{F}} = \begin{bmatrix} A_e \, \mathbf{1}_8 & \mathbf{0} \\ \mathbf{0} & \mathbf{f}_{(6\times6)} \end{bmatrix} \qquad \text{with} \qquad \mathbf{f}_{(6\times6)} = \begin{bmatrix} \mathbf{f}^m & \mathbf{0} & \mathbf{0} \\ \mathbf{0} & \mathbf{f}^b & \mathbf{0} \\ \mathbf{0} & \mathbf{0} & \mathbf{f}^s \end{bmatrix} \quad . \tag{5.64}$$

The components of the submatrices $\mathbf{f}^m$, $\mathbf{f}^b$ and $\mathbf{f}^s$ are defined in [131].

The second term in (5.1) is approximated by inserting the interpolations (5.30), (5.32), (5.37), (5.43), (5.59), and (5.60) into (5.3), and thus

$$\begin{aligned} D[g] \cdot \Delta\boldsymbol{\theta}^h = \sum_{\text{el}=1}^{\text{numel}} \big[& \delta\hat{\boldsymbol{\varepsilon}}_G^T \mathbf{H}_G \,\Delta\hat{\boldsymbol{\varepsilon}}_G + \delta\hat{\boldsymbol{\varepsilon}}_G^T \mathbf{H}_{LG}^T \,\Delta\hat{\boldsymbol{\varepsilon}}_L + \delta\hat{\boldsymbol{\varepsilon}}_L^T \mathbf{H}_{LG} \,\Delta\hat{\boldsymbol{\varepsilon}}_G + \delta\hat{\boldsymbol{\varepsilon}}_L^T \mathbf{H}_L \,\Delta\hat{\boldsymbol{\varepsilon}}_L \\ & + \delta\hat{\boldsymbol{\varepsilon}}_G^T \hat{\mathbf{F}} \,\Delta\hat{\boldsymbol{\sigma}}_G + \delta\hat{\boldsymbol{\sigma}}_G^T \mathbf{G} \,\Delta\tilde{\mathbf{v}} + \delta\hat{\boldsymbol{\sigma}}_G^T \hat{\mathbf{F}}^T \,\Delta\hat{\boldsymbol{\varepsilon}}_G + \delta\tilde{\mathbf{v}}^T \mathbf{G}^T \,\Delta\hat{\boldsymbol{\sigma}}_G \\ & + \delta\tilde{\mathbf{v}}^T \mathbf{K}_g \,\Delta\tilde{\mathbf{v}} \big]_{\text{el}} \quad , \end{aligned} \tag{5.65}$$

where the definitions

$$\begin{aligned} \mathbf{H}_G &= \int_{\Omega_0} \mathbf{N}_{\varepsilon G}^T \mathbf{D}_G \mathbf{N}_{\varepsilon G} \, \mathrm{d}A \quad , & \mathbf{H}_{LG} &= \int_{\Omega_0} \mathbf{N}_{\varepsilon L}^T \mathbf{D}_{LG} \mathbf{N}_{\varepsilon G} \, \mathrm{d}A \quad , \\ \mathbf{H}_L &= \int_{\Omega_0} \mathbf{N}_{\varepsilon L}^T \mathbf{D}_L \mathbf{N}_{\varepsilon L} \, \mathrm{d}A \quad , & \mathbf{K}_g &= \int_{\Omega_0} \mathbf{k}_\sigma \, \mathrm{d}A \quad , \end{aligned} \tag{5.66}$$

are made and $\mathbf{k}_\sigma$ can be derived from (5.37). Inserting (5.61) and (5.65) into (5.1) yields

$$L\left[g(\tilde{\boldsymbol{\theta}}^h, \delta\tilde{\boldsymbol{\theta}}^h), \Delta\tilde{\boldsymbol{\theta}}^h\right] = \sum_{\text{el}=1}^{\text{numel}} \begin{bmatrix} \delta\tilde{\mathbf{v}} \\ \delta\hat{\boldsymbol{\sigma}}_G \\ \delta\hat{\boldsymbol{\varepsilon}}_G \\ \delta\hat{\boldsymbol{\varepsilon}}_L \end{bmatrix}_{\text{el}}^T \left\{ \begin{bmatrix} \mathbf{K}_g & \mathbf{G}^T & \mathbf{0} & \mathbf{0} \\ \mathbf{G} & \mathbf{0} & \hat{\mathbf{F}}^T & \mathbf{0} \\ \mathbf{0} & \hat{\mathbf{F}} & \mathbf{H}_G & \mathbf{H}_{LG}^T \\ \mathbf{0} & \mathbf{0} & \mathbf{H}_{LG} & \mathbf{H}_L \end{bmatrix} \begin{bmatrix} \Delta\tilde{\mathbf{v}} \\ \Delta\hat{\boldsymbol{\sigma}}_G \\ \Delta\hat{\boldsymbol{\varepsilon}}_G \\ \Delta\hat{\boldsymbol{\varepsilon}}_L \end{bmatrix} + \begin{bmatrix} \mathbf{f}^i - \mathbf{f}^a \\ \mathbf{f}^s \\ \mathbf{f}_G^e \\ \mathbf{f}_L^e \end{bmatrix} \right\}_{\text{el}} . \tag{5.67}$$

Considering $\delta\tilde{\boldsymbol{\theta}}^h \neq \mathbf{0}$ in (5.67) leads to a set of equations for each element, specified by

$$\begin{aligned} \mathbf{K}_g\Delta\tilde{\mathbf{v}} + \mathbf{G}^T\Delta\hat{\boldsymbol{\sigma}}_G + \mathbf{f}^i - \mathbf{f}^a &= \mathbf{r} \quad , \\ \mathbf{G}\Delta\tilde{\mathbf{v}} + \hat{\mathbf{F}}^T\Delta\hat{\boldsymbol{\varepsilon}}_G + \mathbf{f}^s &= \mathbf{0} \quad , \\ \hat{\mathbf{F}}\Delta\hat{\boldsymbol{\sigma}}_G + \mathbf{H}_G\Delta\hat{\boldsymbol{\varepsilon}}_G + \mathbf{H}_{LG}^T\boldsymbol{\Delta}\hat{\boldsymbol{\varepsilon}}_L + \mathbf{f}_G^e &= \mathbf{0} \quad , \\ \mathbf{H}_{LG}\Delta\hat{\boldsymbol{\varepsilon}}_G + \mathbf{H}_L\Delta\hat{\boldsymbol{\varepsilon}}_L + \mathbf{f}_L^e &= \mathbf{0} \quad . \end{aligned} \tag{5.68}$$

The symbol $\mathbf{r}$ denotes the vector of element nodal forces. The local field $\Delta\hat{\boldsymbol{\varepsilon}}_L$ is eliminated out of the last two equations in (5.68) by means of a Gauss elimination procedure called static condensation [29]. Thus, (5.68 d) is solved for $\Delta\hat{\boldsymbol{\varepsilon}}_L$,

$$\Delta\hat{\boldsymbol{\varepsilon}}_L = \mathbf{H}_L^{-1}\left(-\mathbf{f}_L^e - \mathbf{H}_{LG}\Delta\hat{\boldsymbol{\varepsilon}}_G\right) \quad , \tag{5.69}$$

and inserted into (5.68 c), so that the four equations in (5.68) for each element reduce to three,

$$\begin{aligned} \mathbf{K}_g\Delta\tilde{\mathbf{v}} + \mathbf{G}^T\Delta\hat{\boldsymbol{\sigma}}_G + \mathbf{f}^i - \mathbf{f}^a &= \mathbf{r} \quad , \\ \mathbf{G}\Delta\tilde{\mathbf{v}} + \hat{\mathbf{F}}^T\Delta\hat{\boldsymbol{\varepsilon}}_G + \mathbf{f}^s &= \mathbf{0} \quad , \\ \hat{\mathbf{F}}\Delta\hat{\boldsymbol{\sigma}}_G + \bar{\mathbf{H}}_G\Delta\hat{\boldsymbol{\varepsilon}}_G + \bar{\mathbf{f}}_G^e &= \mathbf{0} \quad , \end{aligned} \tag{5.70}$$

where the definitions

$$\bar{\mathbf{H}}_G = \mathbf{H}_G - \mathbf{H}_{LG}^T\mathbf{H}_L^{-1}\mathbf{H}_{LG} \qquad \text{and} \qquad \bar{\mathbf{f}}_G^e = \mathbf{f}_G^e - \mathbf{H}_{LG}^T\mathbf{H}_L^{-1}\mathbf{f}_L^e \tag{5.71}$$

have been made. The parameters $\Delta\hat{\boldsymbol{\sigma}}_G$ and $\Delta\hat{\boldsymbol{\varepsilon}}_G$ in (5.70) can be eliminated on the element level, because the stresses and strains are interpolated discontinuously across the element boundaries. Solving (5.70 b) for the incremental strain parameters yields

$$\Delta\hat{\boldsymbol{\varepsilon}}_G = \hat{\mathbf{F}}^{-T}\left(-\mathbf{G}\Delta\tilde{\mathbf{v}} - \mathbf{f}^s\right) \quad . \tag{5.72}$$

Solving (5.70 c) for the incremental stress parameters and inserting (5.72) yields

$$\Delta\hat{\boldsymbol{\sigma}}_G = \hat{\mathbf{F}}^{-1}\left(-\bar{\mathbf{H}}_G\hat{\mathbf{F}}^{-T}\left(-\mathbf{G}\Delta\tilde{\mathbf{v}} - \mathbf{f}^s\right) - \bar{\mathbf{f}}^e_G\right) \quad . \tag{5.73}$$

Inserting (5.73) into (5.70 a) yields

$$\mathbf{K}_T\Delta\tilde{\mathbf{v}} + \hat{\mathbf{f}} = \mathbf{r} \quad , \tag{5.74}$$

where, with (5.62), definitions

$$\mathbf{K}_T = \mathbf{G}_T\hat{\mathbf{H}}\mathbf{G} + \mathbf{K}_g \qquad \hat{\mathbf{f}} = \mathbf{G}_T\left(\hat{\boldsymbol{\sigma}}_G - \hat{\mathbf{H}}\mathbf{f}^s - \hat{\mathbf{F}}^{-1}\bar{\mathbf{f}}^e_G\right) - \mathbf{f}^a \quad , \tag{5.75}$$

have been made, with further definition

$$\hat{\mathbf{H}} = \hat{\mathbf{F}}^{-1}\bar{\mathbf{H}}_G\hat{\mathbf{F}}^{-T} \quad . \tag{5.76}$$

The three equations in (5.70) for each element thus reduce to one. The system of equations in (5.67) therefore reduces to

$$L\left[g(\tilde{\boldsymbol{\theta}}^h, \delta\tilde{\boldsymbol{\theta}}^h), \Delta\tilde{\boldsymbol{\theta}}^h\right] = \sum_{\text{el}=1}^{\text{numel}} \delta\tilde{\mathbf{v}}^T\left(\mathbf{K}_T\Delta\tilde{\mathbf{v}} + \hat{\mathbf{f}}\right) = 0 \quad . \tag{5.77}$$

Standard assembly procedures are employed to derive the global matrices. Solving the system of equations yields the increment $\Delta\tilde{\mathbf{v}}$, which is used to update the nodal displacements and rotational parameters on a global level. The strain and stress parameters are updated on the element level with the help of the strain increments $\Delta\hat{\boldsymbol{\varepsilon}}_G$ and the stress increments $\Delta\hat{\boldsymbol{\sigma}}_G$ by evaluating relations (5.72) and (5.73). The local quantities can then be updated by means of the increments $\Delta\hat{\boldsymbol{\varepsilon}}_L$ derived from (5.69).

Chapter 6

Calculation of interlaminar shear stresses - an enhanced FSDT model

In this chapter, a procedure based on an enhanced first-order shear deformation theory (FSDT) for the computation of the interlaminar shear stresses in layered composite plates is presented. It should be viewed separately from the global-local shell model discussed in the preceding chapters, in that it is a post-processing procedure that introduces some warping functions and exploits the equilibrium equations to determine the interlaminar shear stresses. The procedure can be applied to finite plate and shell elements[11]. Two different models based on two different two-dimensional finite elements have been developed with this approach. Model 1 is based on a 4-node element, while model 2 is based on a 9-node element. In both models, the derivatives of curvatures and strains of the reference surface with respect to the in-plane coordinates have to be obtained. Before the different models are described in detail, the basic equations valid for both models are presented.

6.1 Basic equations

For the basic equations some definitions have to be made. Because a finite shell element is the subject of this work, the definitions will be made on the basis of a shell model, as illustrated in figure 6.1. A reference surface with coordinates x, y in the plane of the plate and z perpendicular to the plate is defined. The reference surface can be but does not have to be in the middle of the plate. As shown in figure 6.2, the plate is comprised of n layers and the layer index i runs from 1 to n. In each layer, a normalized coordinate is defined as $0 \leq \zeta \leq 1$. The thickness of the plate is denoted by h. If the middle of the plate is chosen as the reference surface, the top and the bottom of the plate, denoted by h^+ and h^-, can be specified by $h^+ = h/2$ and $h^- = -h/2$.

The kinematics is based on the Reissner-Mindlin theory, so that the layer strains can be expressed by means of

$$\bar{\boldsymbol{\varepsilon}} = \boldsymbol{\varepsilon} + z\,\boldsymbol{\kappa} \quad . \tag{6.1}$$

[11] A paper on this procedure is published in [106].

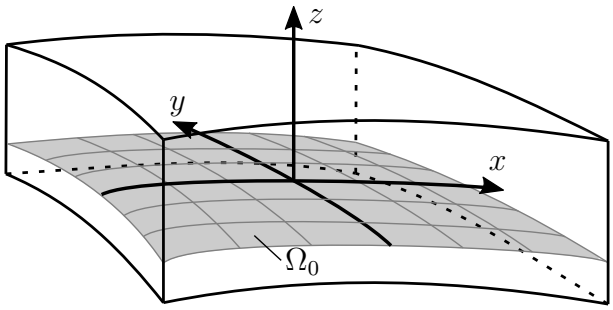

Figure 6.1: Shell with coordinate system

The vector of membrane strains $\boldsymbol{\varepsilon}$ and the vector of curvatures $\boldsymbol{\kappa}$ are defined by

$$\boldsymbol{\varepsilon} = \begin{bmatrix} \varepsilon_x \\ \varepsilon_y \\ \varepsilon_{xy} \end{bmatrix} = \begin{bmatrix} u_{x,x} \\ u_{y,y} \\ u_{x,y} + u_{y,x} \end{bmatrix} \qquad \text{and} \qquad \boldsymbol{\kappa} = \begin{bmatrix} \kappa_x \\ \kappa_y \\ \kappa_{xy} \end{bmatrix} = \begin{bmatrix} \beta_{x,x} \\ \beta_{y,y} \\ \beta_{x,y} + \beta_{y,x} \end{bmatrix} \quad . \tag{6.2}$$

Here, ε_x, ε_y and ε_{xy} are the membrane strains, whereas κ_x, κ_y and κ_{xy} are the curvatures of the shell. The displacements are denoted by u_x and u_y, while β_x and β_y describe the slopes of deformed cross sections. The transverse shear stresses $\bar{\gamma}_{xz}$ and $\bar{\gamma}_{yz}$ are defined as derivatives of the aforementioned warping functions $\varphi_x(z)$ and $\varphi_y(z)$, so that

$$\bar{\gamma}_{xz} = \varphi_{x,z}(z) \qquad \text{and} \qquad \bar{\gamma}_{yz} = \varphi_{y,z}(z) \tag{6.3}$$

hold. For the calculation of the transverse shear stresses the equilibrium equations specified by

$$\sigma_{x,x} + \tau_{xy,y} + \tau_{xz,z} = 0 \qquad \text{and} \qquad \sigma_{y,y} + \tau_{xy,x} + \tau_{yz,z} = 0 \tag{6.4}$$

in the x- and y-direction neglecting the body forces are exploited. In order to do so, a constitutive law assuming transversely isotropic material behavior and reduced to a two-dimensional theory in a standard way is introduced, so that

$$\boldsymbol{\sigma} = \mathbf{C}\, \bar{\boldsymbol{\varepsilon}} \qquad \text{and} \qquad \boldsymbol{\tau} = \mathbf{C}_s\, \bar{\boldsymbol{\gamma}} \quad , \tag{6.5}$$

where the vectors and matrices are defined by

$$\begin{bmatrix} \sigma_x \\ \sigma_y \\ \tau_{xy} \end{bmatrix} = \begin{bmatrix} C_{11} & C_{12} & C_{13} \\ C_{21} & C_{22} & C_{23} \\ C_{31} & C_{32} & C_{33} \end{bmatrix} \begin{bmatrix} \bar{\varepsilon}_x \\ \bar{\varepsilon}_y \\ \bar{\varepsilon}_{xy} \end{bmatrix} \quad \text{and} \quad \begin{bmatrix} \tau_{xz} \\ \tau_{yz} \end{bmatrix} = \begin{bmatrix} C_{44} & C_{45} \\ C_{54} & C_{55} \end{bmatrix} \begin{bmatrix} \bar{\gamma}_{xz} \\ \bar{\gamma}_{yz} \end{bmatrix} . \tag{6.6}$$

The equilibrium equations (6.4) are now rewritten as

$$\boldsymbol{\tau}_{,z} + \mathbf{b} = \mathbf{0} \quad , \qquad \begin{bmatrix} \tau_{xz,z} \\ \tau_{yz,z} \end{bmatrix} + \begin{bmatrix} b_x \\ b_y \end{bmatrix} = \begin{bmatrix} 0 \\ 0 \end{bmatrix} \quad , \qquad \begin{bmatrix} b_x \\ b_y \end{bmatrix} = \begin{bmatrix} \sigma_{x,x} + \tau_{xy,y} \\ \sigma_{y,y} + \tau_{xy,x} \end{bmatrix} . \tag{6.7}$$

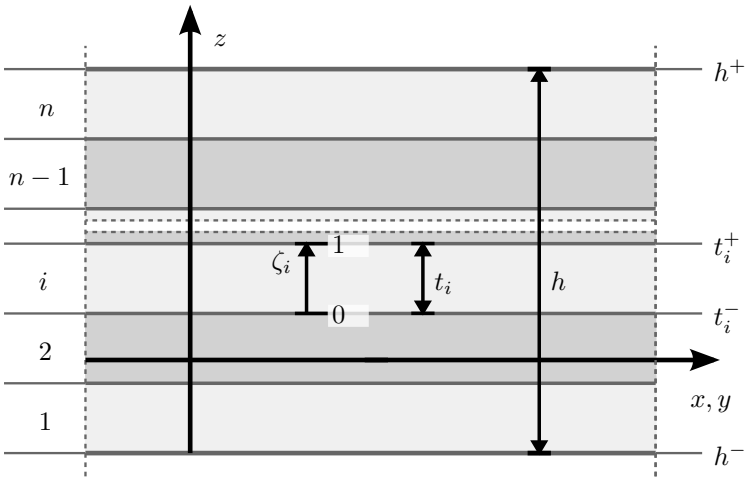

Figure 6.2: Layered composite shell

Inserting the constitutive equations (6.5) into (6.7) yields

$$\mathbf{b} = \mathbf{B}\,\mathbf{x} \quad , \tag{6.8}$$

where the matrix $\mathbf{B}$ and the vector $\mathbf{x}$ are defined by

$$\mathbf{B} = \begin{bmatrix} \mathbf{C}_1 & \mathbf{C}_3 & z\,\mathbf{C}_1 & z\,\mathbf{C}_3 \\ \mathbf{C}_3 & \mathbf{C}_2 & z\,\mathbf{C}_3 & z\,\mathbf{C}_2 \end{bmatrix} \quad , \qquad \mathbf{x} = \begin{bmatrix} \boldsymbol{\varepsilon}_{,x} \\ \boldsymbol{\varepsilon}_{,y} \\ \boldsymbol{\kappa}_{,x} \\ \boldsymbol{\kappa}_{,y} \end{bmatrix} \quad , \tag{6.9}$$

$$\mathbf{C}_1 = [C_{11}, C_{12}, C_{13}] \quad , \qquad \mathbf{C}_2 = [C_{21}, C_{22}, C_{23}] \quad , \qquad \mathbf{C}_3 = [C_{31}, C_{32}, C_{33}] \quad . \tag{6.10}$$

Because the fiber orientation varies in each subsequent layer, the material constants $C_{kl} = C_{lk}$ vary as well. The index i is omitted in order to simplify the notation. It is noted that the number of unknowns contained in $\mathbf{x}$ depends on the number of layers.

6.2 Derivatives of membrane strains and curvatures

In the following, two different procedures, called Model 1 and Model 2, will be described to determine the unknowns contained in the vector $\mathbf{x}$ in (6.9).

6.2.1 Model 1 - 4-node element

The procedure denoted Model 1 uses 4-node elements with bilinear shape functions. Since the second derivatives of the displacement field cannot be computed in this case, a procedure to obtain them is explained in the following.

Regularized minimum problem

In order to obtain the derivatives of the membrane strains and curvatures a system of four equations is set up. The first two conditions describe the boundary conditions of the transverse shear stresses $\tau_{xz}(z = h^+)$ and $\tau_{yz}(z = h^+)$ at the upper surface of the laminate, while the other two describe the definitions of the shear forces q_x and q_y.

The boundary conditions at the top of the composite are determined by integrating (6.4) with respect to z and incorporating (6.7), so that

$$\begin{bmatrix} \tau_{xz}(z = h^+) \\ \tau_{yz}(z = h^+) \end{bmatrix} = \begin{bmatrix} \tau_{xz}(z = h^-) \\ \tau_{yz}(z = h^-) \end{bmatrix} - \int_{h^-}^{h^+} \begin{bmatrix} b_x \\ b_y \end{bmatrix} \mathrm{d}z = \begin{bmatrix} 0 \\ 0 \end{bmatrix} \tag{6.11}$$

holds, which, inserting (6.8), can be rewritten as

$$\boldsymbol{\tau}(z = h^+) = \boldsymbol{\tau}(z = h^-) - \int_{h^-}^{h^+} \mathbf{B}\,\mathrm{d}z\;\mathbf{x} = \mathbf{0} \quad . \tag{6.12}$$

Although the boundary condition $\boldsymbol{\tau}(z = h^-) = \mathbf{0}$ at the lower surface is not fulfilled in the same way, this is done by the displacement method that is described later.

The other two conditions require that integrating the transverse shear stresses through the thickness equals the shear forces q_x and q_y, and thus

$$\int_{h^-}^{h^+} \begin{bmatrix} \tau_{xz} \\ \tau_{yz} \end{bmatrix} \mathrm{d}z = \begin{bmatrix} q_x \\ q_y \end{bmatrix} \quad . \tag{6.13}$$

Considering (6.7) leads to

$$\begin{aligned} \int_{h^-}^{h^+} \begin{bmatrix} \tau_{xz} \\ \tau_{yz} \end{bmatrix} \mathrm{d}z &= \int_{h^-}^{h^+} \begin{bmatrix} \tau_{xz} + z(\sigma_{x,x} + \tau_{xy,y} + \tau_{xz,z}) \\ \tau_{yz} + z(\sigma_{y,y} + \tau_{xy,x} + \tau_{yz,z}) \end{bmatrix} \mathrm{d}z \\ &= \underbrace{\begin{bmatrix} z\,\tau_{xz} \\ z\,\tau_{yz} \end{bmatrix}_{h^-}^{h^+}}_{\mathbf{0}} + \int_{h^-}^{h^+} \begin{bmatrix} b_x \\ b_y \end{bmatrix} z\,\mathrm{d}z \quad , \end{aligned} \tag{6.14}$$

which, with (6.8), can be rewritten as

$$\int_{h^-}^{h^+} \boldsymbol{\tau}\,\mathrm{d}z = \int_{h^-}^{h^+} \mathbf{B}\,z\,\mathrm{d}z\;\mathbf{x} = \mathbf{q} \quad . \tag{6.15}$$

The system of equations to determine the derivatives of strains and curvatures can be written as

$$\mathbf{A}\,\mathbf{x} = \tilde{\mathbf{q}} \quad , \tag{6.16}$$

where the matrix $\mathbf{A}$ and vector $\tilde{\mathbf{q}}$ are defined by

$$\mathbf{A} := \int_{h^-}^{h^+} \begin{bmatrix} \mathbf{B} \\ z\,\mathbf{B} \end{bmatrix} \mathrm{d}z \qquad \text{and} \qquad \tilde{\mathbf{q}} = \begin{bmatrix} \mathbf{0} \\ \mathbf{q} \end{bmatrix} \quad . \tag{6.17}$$

As this system of equations is underdetermined, it is solved by a regularized minimum problem given with

$$\frac{1}{2}\,\mathbf{r}^T\mathbf{r} + \frac{\alpha}{2}\,\mathbf{x}^T\mathbf{x} \quad \rightarrow \quad \min \quad . \tag{6.18}$$

Here, $\mathbf{r} = \mathbf{A}\,\mathbf{x} - \tilde{\mathbf{q}}$ denotes the residual vector and $\alpha > 0$ is a regularization parameter. Minimization yields

$$(\mathbf{A}^T\mathbf{A} + \alpha\,\mathbf{1})\,\mathbf{x} = \mathbf{A}^T\tilde{\mathbf{q}} \quad , \tag{6.19}$$

where $\mathbf{1}$ is a twelfth order unit matrix. The matrix $\mathbf{A}^T\mathbf{A}$ has 4 non-zero eigenvalues and is therefore rank deficient, necessitating the regularization. The parameter $\alpha = Z\,\alpha^*$ is normalized by a factor $Z = [H^2 \sum_{i=1}^{n} 0.5\,(C_{44} + C_{55})h^i]^2$, which is motivated by (6.5), (6.9), (6.17), and (6.19). With a sufficiently large α using floating point arithmetic, the system of equations (6.19) is regular and can be solved for $\mathbf{x}$. As to the choice of the normalized parameter α^*, an investigation of the sensitivity of this parameter is conducted in [106].

6.2.2 A special solution for symmetric laminates

Symmetric laminates possess some special characteristics that can be taken advantage of in proposing a special solution for the calculation of the transverse shear stresses. In such symmetric laminates, membrane and bending behavior are decoupled. For transverse loading, the in-plane stresses vanish identically, thus $\boldsymbol{\varepsilon} \equiv \mathbf{0}$. The derivatives of $\boldsymbol{\varepsilon}$

$$\boldsymbol{\varepsilon}_{,x} = \mathbf{0} \qquad \text{and} \qquad \boldsymbol{\varepsilon}_{,y} = \mathbf{0} \tag{6.20}$$

vanish also. A transformation matrix denoted by $\mathbf{T}$ is introduced that rotates the coordinate system around an angle φ, so that, using the abbreviations $s = \sin\varphi$ and $c = \cos\varphi$,

$$\hat{\mathbf{x}} = \mathbf{T}\,\mathbf{x} \qquad \text{or} \qquad \begin{bmatrix} \hat{x} \\ \hat{y} \end{bmatrix} = \begin{bmatrix} c & s \\ -s & c \end{bmatrix} \begin{bmatrix} x \\ y \end{bmatrix} \quad , \tag{6.21}$$

holds. Analogous to [41] for membrane strains, the curvatures can be transformed with the help of a transformation matrix $\hat{\mathbf{T}}$, defined by

$$\hat{\boldsymbol{\kappa}} = \hat{\mathbf{T}}\,\boldsymbol{\kappa} \qquad \text{or} \qquad \begin{bmatrix} \hat{\kappa}_x \\ \hat{\kappa}_y \\ \hat{\kappa}_{xy} \end{bmatrix} = \begin{bmatrix} c^2 & s^2 & sc \\ s^2 & c^2 & -sc \\ -2sc & 2sc & c^2 - s^2 \end{bmatrix} \begin{bmatrix} \kappa_x \\ \kappa_y \\ \kappa_{xy} \end{bmatrix} \quad . \tag{6.22}$$

The transformation of the stiffness matrices and shear forces,

$$\hat{\mathbf{D}} = \hat{\mathbf{T}}^{-T}\,\mathbf{D}\,\hat{\mathbf{T}}^{-1} \quad , \qquad \hat{\mathbf{C}} = \hat{\mathbf{T}}^{-T}\,\mathbf{C}\,\hat{\mathbf{T}}^{-1} = \begin{bmatrix} \hat{\mathbf{C}}_1 \\ \hat{\mathbf{C}}_2 \\ \hat{\mathbf{C}}_3 \end{bmatrix} \qquad \text{and} \qquad \hat{\mathbf{q}} = \mathbf{T}\,\mathbf{q} \quad , \tag{6.23}$$

where $\mathbf{D}$ and $\hat{\mathbf{q}}$ are defined by

$$\mathbf{D} = \int_{h^-}^{h^+} z^2\,\mathbf{C}\,dz \qquad \text{and} \qquad \hat{\mathbf{q}} = [\hat{q}_x, \hat{q}_y]^T \quad , \tag{6.24}$$

is straightforward. The angle φ is determined to be

$$\varphi = \frac{1}{2}\arctan\left(\frac{\kappa_{xy}}{\kappa_x - \kappa_y}\right) \quad , \tag{6.25}$$

using the condition

$$\hat{\kappa}_{xy} = \hat{\beta}_{x,\hat{y}} + \hat{\beta}_{y,\hat{x}} = -2\,s\,c\,(\kappa_x - \kappa_y) + (c^2 - s^2)\,\kappa_{xy} \equiv 0 \quad . \tag{6.26}$$

If the denominator in (6.25) is zero, a small perturbation is introduced. Each term in (6.26) must vanish, so that

$$\hat{\beta}_{x,\hat{y}} \equiv 0 \qquad \text{and} \qquad \hat{\beta}_{y,\hat{x}} \equiv 0 \quad , \tag{6.27}$$

because $\hat{\beta}_x$ and $\hat{\beta}_y$ are independent functions of $\hat{x}$ and $\hat{y}$ and in general $\hat{\beta}_{x,\hat{y}} \neq -\hat{\beta}_{y,\hat{x}}$ holds. In this case also the derivatives of $\hat{\kappa}_{xy}$ in (6.26) and $\hat{\beta}_{x,\hat{y}}$ and $\hat{\beta}_{y,\hat{x}}$ in (6.27) with respect to the coordinates $\hat{x}$ and $\hat{y}$ vanish, and thus

$$\begin{aligned} \hat{\kappa}_{xy,\hat{x}} &= 0 \quad , & \hat{\kappa}_{x,\hat{y}} &= \hat{\beta}_{x,\hat{y}\hat{x}} = 0 \quad , \\ \hat{\kappa}_{xy,\hat{y}} &= 0 \quad , & \hat{\kappa}_{y,\hat{x}} &= \hat{\beta}_{y,\hat{x}\hat{y}} = 0 \quad . \end{aligned} \tag{6.28}$$

Considering (6.20) and (6.28) the derivatives of the curvatures remain as the parameters that need to be determined, so that

$$\hat{\mathbf{x}} = [0, 0, 0, 0, 0, 0, \hat{\kappa}_{x,\hat{x}}, 0, 0, 0, \hat{\kappa}_{y,\hat{y}}, 0]^T \quad , \tag{6.29}$$

and the system of equations (6.16) reduces to a coupled system of two equations

$$\begin{bmatrix} \hat{D}_{11} & \hat{D}_{23} \\ \hat{D}_{13} & \hat{D}_{22} \end{bmatrix} \begin{bmatrix} \hat{\kappa}_{x,\hat{x}} \\ \hat{\kappa}_{y,\hat{y}} \end{bmatrix} = \begin{bmatrix} \hat{q}_x \\ \hat{q}_y \end{bmatrix} \quad . \tag{6.30}$$

In this way it is possible to compute the vector $\mathbf{b}$ by means of

$$\mathbf{b} = \mathbf{T}\,\hat{\mathbf{b}} \quad , \qquad \hat{\mathbf{b}} = \hat{\mathbf{B}}\,\hat{\mathbf{x}} \quad , \qquad \hat{\mathbf{B}} = \begin{bmatrix} \hat{\mathbf{C}}_1 & \hat{\mathbf{C}}_3 & z\,\hat{\mathbf{C}}_1 & z\,\hat{\mathbf{C}}_3 \\ \hat{\mathbf{C}}_3 & \hat{\mathbf{C}}_2 & z\,\hat{\mathbf{C}}_3 & z\,\hat{\mathbf{C}}_2 \end{bmatrix} \quad , \tag{6.31}$$

and the transverse shear stresses can be calculated as described in section 6.3. In the exceptional case of $\hat{\beta}_{x,\hat{y}} = -\hat{\beta}_{y,\hat{x}}$ at singular points this model cannot be applied.

6.2.3 Model 2 - 9-node element

When using a 9-node element the derivatives of strains and curvatures can be computed as the second derivatives of the displacement field. The required first derivatives of the biquadratic shape functions $N_I(\xi, \eta)$ for 9-node elements, where the index I runs from one to nine, can be derived from

$$\begin{bmatrix} x_{,\xi} & y_{,\xi} \\ x_{,\eta} & y_{,\eta} \end{bmatrix} \begin{bmatrix} N_{I,x} \\ N_{I,y} \end{bmatrix} = \begin{bmatrix} N_{I,\xi} \\ N_{I,\eta} \end{bmatrix} \quad , \tag{6.32}$$

with the help of the Jacobi matrix, which can be written as

$$\begin{bmatrix} x_{,\xi} & y_{,\xi} \\ x_{,\eta} & y_{,\eta} \end{bmatrix} = \begin{bmatrix} J_{11} & J_{12} \\ J_{21} & J_{22} \end{bmatrix} = \sum_{I=1}^{9} \begin{bmatrix} N_{I,\xi}\, x_I & N_{I,\xi}\, y_I \\ N_{I,\eta}\, x_I & N_{I,\eta}\, y_I \end{bmatrix} \quad . \tag{6.33}$$

By applying the product rule and the chain rule of differentiation the second derivatives can be determined from (6.32) using (6.33), so that

$$\begin{bmatrix} J_{11}J_{11} & J_{12}J_{12} & 2J_{11}J_{12} \\ J_{21}J_{21} & J_{22}J_{22} & 2J_{21}J_{22} \\ J_{11}J_{21} & J_{12}J_{22} & J_{11}J_{22} + J_{12}J_{21} \end{bmatrix} \begin{bmatrix} N_{I,xx} \\ N_{I,yy} \\ N_{I,xy} \end{bmatrix} = \begin{bmatrix} N_{I,\xi\xi} - J_{11,\xi}\, N_{I,x} - J_{12,\xi}\, N_{I,y} \\ N_{I,\eta\eta} - J_{21,\eta}\, N_{I,x} - J_{22,\eta}\, N_{I,y} \\ N_{I,\xi\eta} - J_{11,\eta}\, N_{I,x} - J_{22,\xi}\, N_{I,y} \end{bmatrix} \tag{6.34}$$

holds. The derivatives of $J_{\alpha\beta}$ with respect to ξ and η can be directly computed from (6.33).

6.3 Calculation of the transverse shear stresses

Having obtained the derivatives of the strains and curvatures, the vector $\mathbf{b}$ in (6.7) can be computed, and it is now possible to compute the warping functions introduced in (6.3). Accounting for (6.5 b) leads to a coupled system of linear inhomogeneous ordinary differential equations given with

$$\begin{bmatrix} C_{44} & C_{45} \\ C_{54} & C_{55} \end{bmatrix} \begin{bmatrix} \varphi_{x,zz} \\ \varphi_{y,zz} \end{bmatrix} = - \begin{bmatrix} b_x \\ b_y \end{bmatrix} \quad . \tag{6.35}$$

The following equations are specified for a specific layer i. Nevertheless, the index is omitted so as to simplify the notation. With the normalized coordinate ζ running from 0 to 1 in each layer the thickness coordinate z is parameterized by $z = z_1 + \zeta t$. Here, z_1 denotes the coordinate at the bottom of the respective layer and t denotes the thickness of the same layer. The right-hand side in (6.35) is now reformulated in terms of the normalized coordinate ζ, so that

$$\mathbf{b} = (\mathbf{B}_0 + \zeta\, \mathbf{B}_1)\, \mathbf{x} \qquad \text{or} \qquad \begin{bmatrix} b_x \\ b_y \end{bmatrix} = \begin{bmatrix} b_x^0 \\ b_y^0 \end{bmatrix} + \zeta \begin{bmatrix} b_x^1 \\ b_y^1 \end{bmatrix} \quad , \tag{6.36}$$

where the definitions

$$\mathbf{B}_0 = \begin{bmatrix} \mathbf{C}_1 & \mathbf{C}_3 & z_1\,\mathbf{C}_1 & z_1\,\mathbf{C}_3 \\ \mathbf{C}_3 & \mathbf{C}_2 & z_1\,\mathbf{C}_3 & z_1\,\mathbf{C}_2 \end{bmatrix} \quad \text{and} \quad \mathbf{B}_1 = \begin{bmatrix} \mathbf{0} & \mathbf{0} & h\,\mathbf{C}_1 & h\,\mathbf{C}_3 \\ \mathbf{0} & \mathbf{0} & h\,\mathbf{C}_3 & h\,\mathbf{C}_2 \end{bmatrix} \tag{6.37}$$

were made. The system of differential equations (6.35) can be solved with a homogeneous and a particular part, so that

$$\begin{aligned} \varphi_x &= \varphi_x^h + \varphi_x^p \quad , \quad \varphi_x^h = c_{x1} + c_{x2}\zeta \quad , \quad \varphi_x^p = c_{x3}\zeta^2 + c_{x4}\zeta^3 \quad , \\ \varphi_y &= \varphi_y^h + \varphi_y^p \quad , \quad \varphi_y^h = c_{y1} + c_{y2}\zeta \quad , \quad \varphi_y^p = c_{y3}\zeta^2 + c_{y4}\zeta^3 \quad , \end{aligned} \tag{6.38}$$

with coefficients c_{x1} to c_{x4} and c_{y1} to c_{y4}. By inserting the particular solution into the system of differential equations (6.35), the coefficients c_{x3} and c_{x4} are determined to be

$$\begin{bmatrix} C_{44} & C_{45} \\ C_{54} & C_{55} \end{bmatrix} \begin{bmatrix} c_{x3} \\ c_{y3} \end{bmatrix} = - \begin{bmatrix} b_x^0 \\ b_y^0 \end{bmatrix} \frac{h^2}{2} \quad , \tag{6.39}$$

and the coefficients c_{y3} and c_{y4} can be specified by

$$\begin{bmatrix} C_{44} & C_{45} \\ C_{54} & C_{55} \end{bmatrix} \begin{bmatrix} c_{x4} \\ c_{y4} \end{bmatrix} = - \begin{bmatrix} b_x^1 \\ b_y^1 \end{bmatrix} \frac{h^3}{6} \quad . \tag{6.40}$$

The solution for the coefficients can be given with

$$\begin{aligned} c_{x3} &= -(b_x^0 C_{55} - b_y^0 C_{45})\frac{h^2}{2D} \quad , \quad c_{y3} = -(b_y^0 C_{44} - b_x^0 C_{54})\frac{h^2}{2D} \quad , \\ c_{x4} &= -(b_x^1 C_{55} - b_y^1 C_{45})\frac{h^3}{6D} \quad , \quad c_{y4} = -(b_y^1 C_{44} - b_x^1 C_{54})\frac{h^3}{6D} \quad , \end{aligned} \tag{6.41}$$

where $D = C_{44}C_{55} - C_{45}C_{54}$. The remaining coefficients c_{x1}, c_{x2}, c_{y1} and c_{y2} of the homogeneous solution are expressed with the discrete values of φ_x and φ_y at the layer boundaries, so that

$$\begin{aligned} \varphi_{x1} &= \varphi_x(0) \\ \varphi_{x2} &= \varphi_x(1) \\ \varphi_{y1} &= \varphi_y(0) \\ \varphi_{y2} &= \varphi_y(1) \end{aligned} \quad \rightarrow \quad \begin{aligned} c_{x1} &= \varphi_{x1} \\ c_{x2} &= \varphi_{x2} - \varphi_{x1} - c_{x3} - c_{x4} \\ c_{y1} &= \varphi_{y1} \\ c_{y2} &= \varphi_{y2} - \varphi_{y1} - c_{y3} - c_{y4} \quad . \end{aligned} \tag{6.42}$$

Having all the coefficients at hand, the quadratic shape of the transverse shear stresses can be expressed as derivatives of the warping functions incorporating the constitutive equation (6.5 b), so that

$$\begin{aligned} \tau_{xz} &= C_{44}\,\varphi_{x,z} + C_{45}\,\varphi_{y,z} \\ &= \frac{C_{44}}{t}(c_{x2} + 2c_{x3}\zeta + 3c_{x4}\zeta^2) + \frac{C_{45}}{t}(c_{y2} + 2c_{y3}\zeta + 3c_{y4}\zeta^2) \quad , \\ \tau_{yz} &= C_{45}\,\varphi_{x,z} + C_{55}\,\varphi_{y,z} \\ &= \frac{C_{45}}{t}(c_{x2} + 2c_{x3}\zeta + 3c_{x4}\zeta^2) + \frac{C_{55}}{t}(c_{y2} + 2c_{y3}\zeta + 3c_{y4}\zeta^2) \quad . \end{aligned} \tag{6.43}$$

In order to establish a system of equations for each layer, (6.43) is evaluated at the layer boundaries and, considering the definitions in figure 6.3, the values of the transverse shear stresses at the top and the bottom of a layer can be given with

$$\begin{aligned}
\tau_{x1} = -\tau_{xz}(0) &= -\frac{C_{44}}{t}c_{x2} - \frac{C_{45}}{h}c_{y2} \\
&= \frac{C_{44}}{t}(\varphi_{x1} - \varphi_{x2} + c_{x3} + c_{x4}) + \frac{C_{45}}{t}(\varphi_{y1} - \varphi_{y2} + c_{y3} + c_{y4}) \quad , \\
\tau_{x2} = \tau_{xz}(1) &= \frac{C_{44}}{t}(c_{x2} + 2c_{x3} + 3c_{x4}) + \frac{C_{45}}{t}(c_{y2} + 2c_{y3} + 3c_{y4}) \\
&= \frac{C_{44}}{t}(\varphi_{x2} - \varphi_{x1} + c_{x3} + 2c_{x4}) + \frac{C_{45}}{t}(\varphi_{y2} - \varphi_{y1} + c_{y3} + 2c_{y4}) \quad , \\
\tau_{y1} = -\tau_{yz}(0) &= -\frac{C_{54}}{t}c_{x2} - \frac{C_{55}}{h}c_{y2} \\
&= \frac{C_{54}}{t}(\varphi_{x1} - \varphi_{x2} + c_{x3} + c_{x4}) + \frac{C_{55}}{t}(\varphi_{y1} - \varphi_{y2} + c_{y3} + c_{y4}) \quad , \\
\tau_{y2} = \tau_{yz}(1) &= \frac{C_{54}}{t}(c_{x2} + 2c_{x3} + 3c_{x4}) + \frac{C_{55}}{t}(c_{y2} + 2c_{y3} + 3c_{y4}) \\
&= \frac{C_{54}}{t}(\varphi_{x2} - \varphi_{x1} + c_{x3} + 2c_{x4}) + \frac{C_{55}}{t}(\varphi_{y2} - \varphi_{y1} + c_{y3} + c_{y4}) \quad .
\end{aligned} \tag{6.44}$$

For the sake of clarity, the layer index i is no longer omitted and a system of equations can be set up for the four unknown transverse shear stresses, and thus

$$\boldsymbol{\tau}_i = \mathbf{k}_i \, \mathbf{v}_i - \mathbf{f}_i \quad , \tag{6.45}$$

where the vectors $\boldsymbol{\tau}_i$, $\mathbf{v}_i$ and $\mathbf{f}_i$ and the matrix $\mathbf{k}_i$ are given with

$$\begin{bmatrix} \tau_{x1} \\ \tau_{y1} \\ \tau_{x2} \\ \tau_{y2} \end{bmatrix} = \frac{1}{h} \begin{bmatrix} C_{44} & C_{45} & -C_{44} & -C_{45} \\ C_{54} & C_{55} & -C_{54} & -C_{55} \\ -C_{44} & -C_{45} & C_{44} & C_{45} \\ -C_{54} & -C_{55} & C_{54} & C_{55} \end{bmatrix} \begin{bmatrix} \varphi_{x1} \\ \varphi_{y1} \\ \varphi_{x2} \\ \varphi_{y2} \end{bmatrix} - \frac{6}{h} \begin{bmatrix} 3\,b_x^0 + b_x^1 \\ 3\,b_y^0 + b_y^1 \\ 3\,b_x^0 + 2b_x^1 \\ 3\,b_y^0 + 2b_y^1 \end{bmatrix} \quad . \tag{6.46}$$

The matrix $\mathbf{k}_i$ is an element stiffness matrix, the vector $\mathbf{v}_i$ contains the values of the warping functions at the top and the bottom of the layer corresponding to the respective transverse shear stresses and the vector $\mathbf{f}_i$ is written in terms of the constants defined in (6.36). An alternative notation for the vector $\mathbf{f}_i$ is

$$\mathbf{f}_i = -\frac{1}{h} \begin{bmatrix} -C_{44}(c_{x3} + c_{x4}) & -C_{45}(c_{y3} + c_{y4}) \\ -C_{54}(c_{x3} + c_{x4}) & -C_{55}(c_{y3} + c_{y4}) \\ -C_{44}(c_{x3} + 2\,c_{x4}) & -C_{45}(c_{y3} + 2c_{y4}) \\ -C_{54}(c_{x3} + 2\,c_{x4}) & -C_{55}(c_{y3} + 2c_{y4}) \end{bmatrix} \quad . \tag{6.47}$$

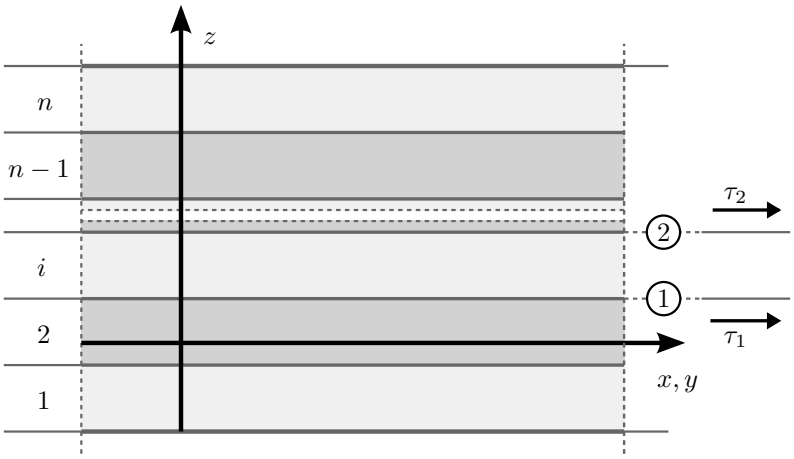

Figure 6.3: Definition of shear stresses at layer boundaries

When assembling the system of equations for each layer to a system of equations for the whole laminate, the continuity of the transverse shear stresses at the layer boundaries can be required by $\sum_{i=1}^{n} \mathbf{T}_i = \mathbf{0}$, where $\mathbf{T}_i$ contains the transverse shear stresses at all layer boundaries. It follows that

$$\sum_{i=1}^{n} \mathbf{T}_i = \sum_{i=1}^{n} \mathbf{a}_i^T \boldsymbol{\tau}_i = \sum_{i=1}^{n} \mathbf{a}_i^T \mathbf{k}_i \mathbf{a}_i \mathbf{V} - \sum_{i=1}^{n} \mathbf{a}_i^T \mathbf{f}_i = \mathbf{0} \quad , \tag{6.48}$$

leading to a linear system of equations written as

$$\mathbf{K}\mathbf{V} = \mathbf{F} \quad . \tag{6.49}$$

The stiffness matrix $\mathbf{K} = \sum_{i=1}^{n} \mathbf{a}_i^T \mathbf{k}_i \mathbf{a}_i$ and the load vector $\mathbf{F} = \sum_{i=1}^{n} \mathbf{a}_i^T \mathbf{f}_i$ for the whole laminate are assembled with the help of the assembly matrix $\mathbf{a}_i$, for which $\mathbf{v}_i = \mathbf{a}_i \mathbf{V}$ holds.

For an arbitrary fixed stacking sequence in a laminate, the sparse stiffness matrix $\mathbf{K}$ has to be set up and factorized only once. Only a back substitution is required to compute the solution of (6.49) and thereby to obtain the discrete warping ordinates at the nodes. As rigid body motions are not permissible, boundary conditions for the warping functions have to be imposed. The choice of the boundary conditions leads to different constants for these functions, but it does not affect the transverse shear stresses. Here, $\varphi_x(z = h^+) = 0$ and $\varphi_y(z = h^+) = 0$ are chosen.

Alternatively to the proposed procedure, since $\mathbf{B}$ is a linear function of ζ, (6.7) could be integrated for each layer with respect to the thickness coordinate z. The drawback of this procedure is that it requires knowledge of the shear stresses of the adjacent lower layer. On the other hand, with the procedure proposed in this chapter, the transverse shear stresses in an arbitrary layer can be calculated without knowing the value of the subjacent layer.

Chapter 7

Parallel programming in a finite element software

Modeling the behavior of physical phenomena with differential equations and then solving them with numerical methods, such as the finite element method, leads to large systems of equations. This is also the case when modeling the behavior of thin-walled structures by discretizing them with the global-local finite shell element that was presented in this work. Specifically through the addition of the local model discussed in chapter 4 a large number of unknowns is introduced on the element level, leading to a considerable increase in computation time when setting up the stiffness matrix. To solve such large systems of equations in a reasonable amount of computation time, high performance computers with ample memory need to be used. On the other hand, it must also be ensured that the software is implemented in a way so as to optimize performance. Thus, for the operations involving multiplications of large matrices and vectors optimized routines should be employed.

Additionally, the software needs to be adapted to modern parallel computer architectures. The solution of such systems of equations with large numbers of unknowns in a sequential way leads to unreasonably long computation times. Taking into account modern computer architectures a parallelization of the computation process should be carried out, in order to efficiently use the resources available.

In this chapter it is shown how the finite element software used in this work was adapted to account for modern computer architectures by parallelizing the implemented code. The modifications carried out thus increase the performance not only of the global-local finite shell element, but also of all the other finite elements implemented in the finite element software. In order to efficiently implement the parallelization of the software, knowledge of the hardware is essential. This includes understanding at least basic concepts of processor technology, computer memory and the way the components of computers or computer systems communicate with each other. A short introduction to the subject of parallel computing including some performance characteristics of parallel systems will be given in the next section, before the implementation of the finite element analysis software used will be discussed.

7.1 Parallel computing

Simulations using the finite element method such as the ones presented in chapter 8 lend themselves well for parallel computing. For this purpose, the problem is separated into a number of smaller problems, which are solved concurrently. In order to describe the steps that were taken to parallelize the algorithms in the developed finite shell element, some definitions with respect to parallel computing and the present situation of computer architectures are briefly discussed.

7.1.1 Overview

As a basis for a computer architecture often the proposal of Von Neumann is used [126]. The Von Neumann computer consists of a processing unit with an arithmetic logic unit and processor registers, a control unit with an instruction register and a program counter, main memory and input and output mechanisms. The control unit executes instructions sequentially and controls the processing unit. Encoded instructions are fetched from the main memory, decoded and executed. The components are connected via a bus. The behavior of a Von Neumann computer is deterministic, meaning that out of one input data stream one result data stream is produced as output.

A common classification of computer architectures is Flynn's taxonomy [37], which defines four different categories that are specified in table 7.1. Of course, computers can be hybrids of these categories and most if not all newly developed computers have to be classified in the MIMD category, but Flynn's taxonomy is easy to understand and gives a good first approximation [89].

	Single Instruction	Multiple Instruction
Single Data	SISD	MISD
Multiple Data	SIMD	MIMD

Table 7.1: Classification of computer architectures according to Flynn

A computer classified as SISD executes instructions sequentially. There is no parallelism in either the instruction or the data streams. An example for such a computer is a uniprocessor machine such as a traditional PC before multiple processors were introduced. SISD computers are hardly produced anymore.

An SIMD computer possesses multiple processors that execute a single instruction on multiple data, essentially meaning that the same operation is repeatedly carried out over a large data set. An example for such a system are modern graphic processing units (GPUs), which are highly effective when processing of large blocks of data needs to be done in parallel.

The MISD architecture is an uncommon architecture, in which the same data stream is manipulated by multiple operations. Computational resources are usually not effectively

used with this scheme. It is however used for fault tolerance as for example in the Space Shuttle flight computers.

Most modern computers belong to the MIMD category, where multiple processors operate independently and execute different instructions on multiple data streams. In order to use the resources of computers that are in the MIMD category, parallelized software programs need to be written. In high-performance computing, parallel concepts have long been used for example in so-called supercomputers, which contain multiple processors that are connected by a local high-speed computer bus. The first supercomputers contained only a few processors, while more recent supercomputers contain tens of thousands of processors. An alternative to supercomputers are computer clusters, which consist of a number of computers that are more loosely connected to each other, for example through local area networks. The computers in the clusters work together, so that in many respects they can be viewed as a single system. If the pool of computers is even more heterogeneous, in that the computers are even more loosely connected, for example because they are geographically dispersed, it is referred to as a grid computing system [62]. The components in a grid computing environment are similar to the processors in a supercomputer. In order to be able to work together the computers must be connected to a network. Most recently the term cloud computing was coined, where computing resources are provided as a service and can be accessed over a web browser. It is therefore similar to the concept of grid computing. In the past, increasing the clock frequency was the primary method of improving processor performance [6]. Due to physical constraints however, the clock frequency of processors has nearly stagnated in the last few years. In order to still increase their performance, producers have resorted to increasing parallelism by assembling off-the-shelf desktop PCs with multi-core processors for several years.

Parallel computers can be further differentiated into categories by how the hardware supports parallelism. At present, three different relevant categories can be specified [108]. Parallel computers significantly differ in the way they use and access memory. In so-called shared memory processing (SMP) systems, the first category, such as multi-core computers, the processing elements are contained within the same machine and they use a common memory. A schematic example of an SMP system is given in figure 7.1a. The bottleneck in SMP systems is the computer bus, which transports data between the components of the system.

A second category of parallel computers are parallel systems with distributed memory. Such a system consists of a number of different autonomous computers, that each possesses its own private memory. As is shown in the schematic example in figure 7.1b, a parallel computer that belongs to the SMP category can be part of such a system with distributed memory. The different computers in such a system are usually referred to as nodes. Since the nodes are autonomous they do not share a common memory. To transfer data they need to communicate with one another via a network by exchanging messages. They are therefore often called message passing systems. Since communication with the help of a network is much slower than via a computer bus, how the nodes of the parallel system are connected, the so-called network topology, has a large bearing on the efficiency of the system.

A third category that needs to be mentioned is parallel computers with intrinsic par-

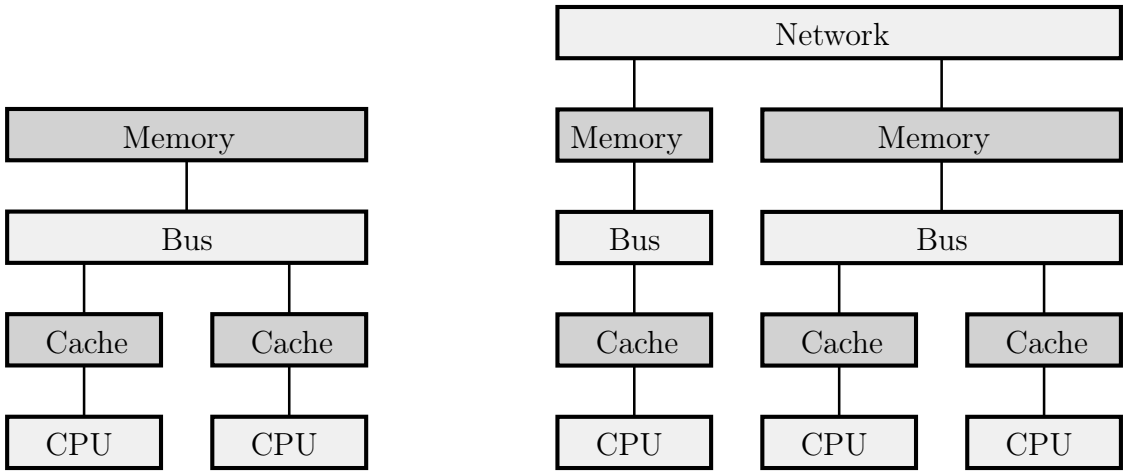

(a) Shared memory (b) Distributed memory

Figure 7.1: Examples for parallel systems with different memory concepts

allelization in accelerator cards, such as GPUs, which were already mentioned. Even though their development was advanced through the computer game industry, they are increasingly used in scientific computer simulations because they provide a high degree of parallelization and are particularly suitable in certain problems, where a large amount of data has to manipulated in parallel.

The increase in parallelism in computing necessitates the development of adequate parallelized software that is able to use the resources at its disposal. For this reason the development of suitable programming models was promoted, some of which will be briefly introduced in the following section.

7.1.2 Programming techniques

In order to program parallel computers a number of different programming techniques have been developed. Different programming techniques have been designed while having different types of parallel computers and especially their underlying memory architecture in mind. They are often divided into classes on that basis.

Data parallelism is a suitable programming technique in parallel systems with multi-core processors. It is based on a sequential control flow and parallel operations on global data structures. The application flow of the distributed operations on the different processors is managed by a single program. The distribution of the workload is carried out by the compiler, which also controls the exchange of messages. Compiler directives are used by the programmer to organize the distribution of the operations. High Performance Fortran (HPF) is a prominent example of a parallel programming technique that employs data parallelism [72]. It has, however, not become widely accepted.

The most popular programming technique on parallel computers using only one physical memory is the shared memory programming model. This technique has been in use for over two decades. In this model, the different parallel threads that execute different tasks can access and manipulate a common memory. Thus, the communication of data is not

necessary, but rather the common address space must be coordinated.

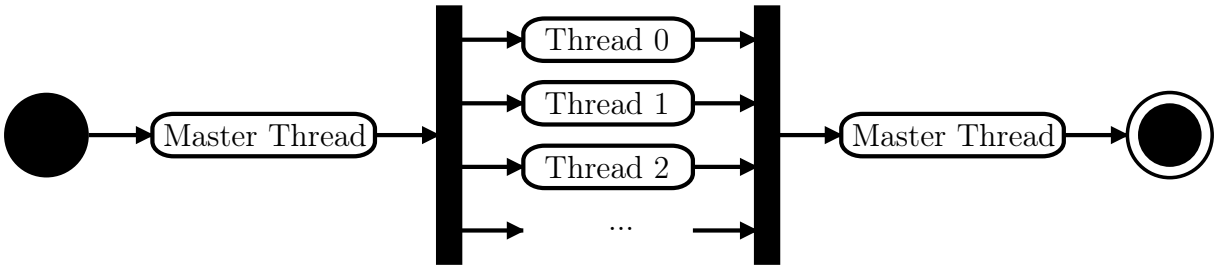

Figure 7.2: Activity diagram of an application flow with a parallel region

A very common shared memory Application Programming Interface (API) in scientific high-performance computing is OpenMP [27]. It is a standardized interface that is managed by a review board and supported by a group of major computer hardware and software vendors. OpenMP is supported for the programming languages `FORTRAN`, `C` and `C++`. It is independent of the hardware and nearly independent of the operating systems. The OpenMP API is made up of a set of compiler directives, library routines and environment variables.

In the OpenMP concept a serial task often referred to as the Master Thread running in a program starts a team of threads, which perform their tasks concurrently. During this time, the Master Thread is idle and only when the threads of the team join does the Master Thread continue to execute. Figure 7.2 shows an activity diagram of how a parallel region is implemented in software by means of the OpenMP model.

The beginning and the end of a parallel region are illustrated by a black bar. At the beginning of the parallel region, a team of threads is created in the serial application flow. Ideally, in a parallel system with p processors a number of p different threads are created, that each perform a task on a different processor. The aim is that the runtime environment allocates the different threads to different processors that are then executed on that processor by means of so-called gang scheduling. In practice this can only approximately be achieved, since where the threads are deployed depends on the processor load. Therefore, some of the threads may be chosen before others or executed consecutively on the same processor.

A major advantage of the OpenMP concept is that it can be conveniently implemented into a serial program. It offers a unified address space for all of the available data, so that data distribution does not need to be considered. When using the OpenMP concept the portion of the serial code that is to be parallelized can be conveyed to the compiler with the help of directives. Data layout and decomposition is thus automatically handled by the compiler, which conducts the parallelization. The directives are treated as comments when the compiler is instructed to compile sequentially.

On the other hand, errors can be inadvertently introduced due to the fact that OpenMP is based on the concept of threads [76]. For instance, it must be avoided that a variable is repeatedly manipulated in parallel, which can lead to unpredictable errors due to race conditions when multiple threads try to manipulate memory at the same time. Thus, protection mechanisms, such as locks, are introduced. On the other hand, locks can lead

to so-called deadlock situations, when two or more threads wait for each other to finish and the program stops executing. Also, debug synchronization can be difficult when trying to find and correct bugs. Care must thus be taken when implementing parallelism with the help of the OpenMP model.

Parallel systems with distributed memory consist of different computer nodes that are connected via a network. Such parallel systems with distributed memory need to use a message-passing system in order to communicate and exchange data. In this programming model different processes that run in parallel communicate with each other by means of messages in order to solve a problem. The messages passed include signals to steer the application flow and data that are exchanged between processors. Not being able to use high-speed computer buses but rather using a network connection means that higher communication times are to be expected, which decreases the efficiency of the implementation. On the other hand, an advantage of this programming technique is that, since data distribution must be considered, race conditions that lead to unpredictable errors are avoided.

The most popular Application Programming Interface in this area is the Message Passing Interface (MPI), which was designed by a group of researchers from academia and industry [38] and is a language-independent communications protocol. It standardizes message passing by defining the syntax and semantics of a core of library routines, thus making different products that use MPI compatible and the software portable. It therefore provides a virtual topology of the machines that are part of the parallel system. MPI programs aim to synchronize different processes, and typically, for maximum performance, each process runs on a different processor in the parallel system. Programs that use the MPI interface usually are written in `C` or `C++`, but implementations in a number of other programming languages are available.

In the scientific field, a number of applications have been developed on other models that involve network communication. Some are based, for example, on the client-server concept, where suitable parameters are sent from a client to a server requesting some form of service. In others, the concept of mobile code is employed in peer-to-peer models, so that a node in the parallel system can dynamically request code which is then automatically executed. The concept of mobile code is taken a step further in the development of autonomously moving code components called mobile agents [85, 97, 103, 104]. Client-server based concepts are widely in use in the non-scientific field, while the concepts of mobile code and mobile agents have not been able to establish themselves [26]. In scientific applications, SMP in combination with OpenMP on shared memory systems and message passing systems with MPI on systems with distributed memory are the most popular.

More recently, APIs have also been developed for programming GPUs. With the introduction of the Compute Unified Device Architecture (CUDA), the use of GPUs became popular in scientific applications. It was originally developed by Nvidia for graphics processing and is therefore limited to Nvidia hardware. With the help of CUDA, software developers can access the virtual instruction set and memory of the elements in GPUs that support CUDA. An API for GPUs that works on more heterogeneous platforms and is not restricted to one particular vendor is OpenCL, which is an open standard maintained by the non-profit technology consortium Khronos Group. Similar to CUDA specifically for Nvidia GPUs, OpenCL gives the software developer access to the GPUs that support the

interface. The key feature of OpenCL is its portability, while CUDA is more optimized, because it runs on a specific hardware.

7.1.3 Performance characteristics

In order to evaluate the performance of parallel systems some performance characteristics need to be defined. On the basis of the performance characteristics a conclusion can be drawn of how much time is gained by performing the computations in parallel and not sequentially. In this work, the cost of implementing the parallelism, the so-called overhead, is included in the assessment. The achieved performance can differ from the theoretical or expected performance dramatically. Reasons for this can be the cost of communication, a small bandwidth of the memory or a small cache.

An obvious performance characteristic is the speedup, denoted by S and defined by

$$S = \frac{T_s}{T_p} \quad . \tag{7.1}$$

It allows an assertion of how much time is gained by solving a problem with a number of processors p opposed to only one processor. In (7.1), T_s is the runtime of the simulation carried out with one processor, while T_p is the runtime with p processors. For T_s, the runtime of the fastest sequential algorithm should be used, but as it is unknown in many cases, the runtime with one processor is often used. The value of the speedup lies in the interval $1 \leq S \leq p$.

A second performance characteristic is the efficiency, denoted by E and defined by

$$E = \frac{S}{p} \quad , \tag{7.2}$$

which relates the Speedup to the number of processors. The efficiency provides information about how well the processors involved in the computation were utilized. It thus allows an assertion of how much time was lost in communication and synchronization. The value of the efficiency lies in the interval $\frac{1}{p} \leq E \leq 1$. It is noted that in a complete analysis of the efficiency of a parallel system, the workload of each processor involved in the computation should be analyzed.

A number of laws have been developed to predict the speedup of a parallel system, but this goes beyond the scope of this thesis[12]. The performance characteristics will be used to evaluate the parallelization of the implemented code, which will be discussed in the next section.

7.2 Implementation in FEAP

The mixed finite shell element introduced was implemented into an extended version of the finite element software FEAP [122], which is a multi-purpose finite element analysis

[12] Such laws are for instance specified in [4, 50].

program for the solution of static and dynamic linear and nonlinear problems.

The develop environment used for the implementation of the global-local finite shell element is Microsoft Visual Studio with Intel Fortran Compiler as part of Intel Fortran Composer XE. In the implementation, many operations involving multiplications of large sparse matrices and vectors are performed on the element level. To date, a large number of libraries exist that offer optimized math routines for such operations. In the implementation of the global-local finite shell element, the routines for multiplications of large sparse matrices and vectors provided by the Math Kernel Library (MKL), which is part of Intel Fortran Composer XE product, are used. In this way, it is assured that the math operations are carried out in an optimized way, reducing computation time. In order to use the routines provided, the matrices and vectors need to be stored in sparse matrix and vector storage formats, which can then be passed to the interfaces to routines provided by the MKL library. The storage formats will not be discussed in this work but are shown in the available documentation of the MKL library.

The software FEAP was originally written for serial computation. A serial stream of instructions was executed one instruction at a time on a central processing unit in one computer in order to solve a problem. Running software in this way on a modern desktop computer with multiple processors is no longer up to date, since only one processor is used, thus leading to very large computation times and a waste of resources. In order to efficiently use the capacity of parallel computers by using several processors simultaneously, computationally expensive parts of the simulation have to be identified, separated into several independent parts and concurrently worked on. A suitable programming technique needs to be chosen to implement the parallelization. In order to do so, the application flow of the software needs to be well-known. For this reason, a short summary of a nonlinear finite element simulation is given at this point.

Figure 7.3 shows an activity diagram of significant activities in a computation with FEAP that are typically carried out in a nonlinear analysis after data relevant to the simulation has been read in from an input file and some operations have been performed in preparation of the simulation. In highly nonlinear problems the load is applied incrementally, so that at first, the load increment must be set and the total number of load steps denoted by l_{max} in figure 7.3 must be determined. A control variable that runs from zero to the number of load steps l_{max} is denoted by l. If the control variable l has not reached the number of load steps l_{max} a loop is entered, where for each applied load an equilibrium state is sought to be reached by solving a system of equations resulting from the finite element implementation. The initial value of the vector of unknowns for the first load step is arbitrary, while the initial value for each following iteration is the displacement vector of the last load step. In order to avoid an infinite loop if the convergence criteria is not met, a maximum number of iterations k_{max} is decided on. A control variable denoted by k runs from zero to the maximum number of iterations k_{max}.

After incrementing the load, the tangential global stiffness matrix and load vector are set up by means of a loop through all finite elements. A control variable that runs from zero to n with n being the number of elements is denoted by i and is set to zero before the loop through all finite elements begins. When the global stiffness matrix and load vector are set up the system of equations can be solved to derive the increment of the vector of unknowns.

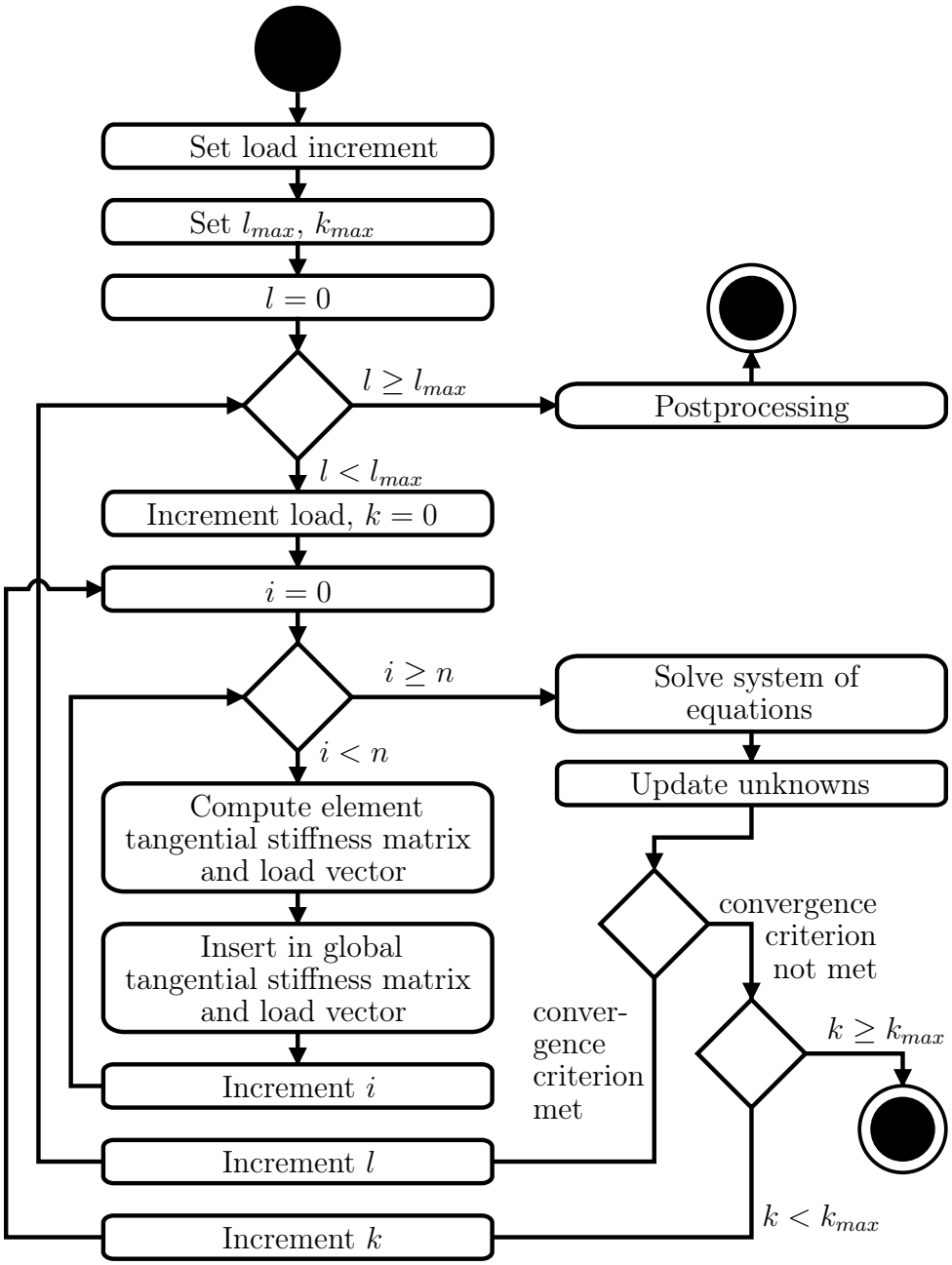

Figure 7.3: Activity diagram of a sequential nonlinear finite element analysis with FEAP

Next, the vector of unknowns is updated by adding the increment of unknowns. At this point, a convergence criterion is evaluated. If it is not met, it is checked if the maximum number of iterations k_{max} has been reached. If this is the case, the simulation is terminated without having reached a solution. Alternatively, a procedure could be implemented, in which the size of the load step is decreased and the procedure is started over. If k_{max} has not been reached, the control variable k is incremented and the global stiffness matrix and load vector have to be set up again with the updated vector of unknowns as the initial value. If the convergence criteria is met, the control variable l is incremented and the simulation either continues with the next load step or, if the maximum number of load steps is reached, terminates after performing some post-processing operations.

With the help of the activity diagram in figure 7.3, the application flow is analyzed, in order to identify the computationally expensive parts of the simulation. The part with the highest computational cost is usually deriving the solution of the system of equations with a numerical solving technique. Also the process of assembling the global stiffness matrix and load vector can inflate the total computation time considerably. This is the case for the global-local finite shell element developed in this work, because a large number of unknowns is introduced on the element level. The solution of the system of equations and the assembling of the global stiffness matrix and load vector are therefore operations that should be carried out concurrently when carrying out nonlinear simulations using computers with parallel architectures.

Figure 7.4 shows an activity diagram where these operations are carried out in parallel. As in figure 7.2, the beginning and the end of the two parallel regions are indicated by black bars. In one parallel region depicted in figure 7.4 the system of equations is solved concurrently. In FEAP, the parallelization is implemented by providing an interface to an external highly efficient parallel solver named PARDISO [99, 100]. The PARDISO package is a software for solving large sparse symmetric and unsymmetric linear systems of equations on shared memory multiprocessors. PARDISO thus is used in computationally intensive simulations to solve the large systems of equations that occur when solving a problem by means of the finite element method.

In the second parallel region the assembling of the global tangential stiffness matrix and the load vector is performed concurrently. To realize the parallelization, a suitable programming technique needs to be chosen and implemented. Since the software is to run on desktop computers with multiple processors and shared memory, using the OpenMP API is an obvious choice to implement the parallelization.

On a parallel system with p processors the work load is separated into p parts. Thus, bearing the OpenMP concept in mind, p threads are created at the beginning of the parallel region. Since the computing time is roughly the same for each cycle of the loop through all the elements the obvious way to implement the parallelization is to split the loop with n cycles into p loops with n/p cycles each. If the division n/p does not yield a whole number, the next best distribution should be chosen. In figure 7.4, this case is not considered, it is assumed that n/p yields a whole number. Each of the threads handles one loop, thus concurrently computing tangential element stiffness matrices and load vectors and inserting them into the global tangential stiffness matrix and global load vector. Ideally, each of the threads executes on a different processor, thus efficiently using the capacity of all the available resources. For the reason mentioned in the previous section, this is only approximately achievable. At the end of the parallel region, the team of threads is joined and the Master Thread continues executing.

When parallelizing the loop, it must be decided which of the variables and fields in the loop must be private to each thread and which variables and fields must be public, so that all of the threads can access them. For example, the fields containing the tangential element stiffness matrix and load vector need to be private to each thread, while the fields containing the global tangential stiffness matrix and global load vector need to be public. Some of the code in the described loop in FEAP had to be altered to ensure that private variables remain private to the thread during the whole loop. While the private

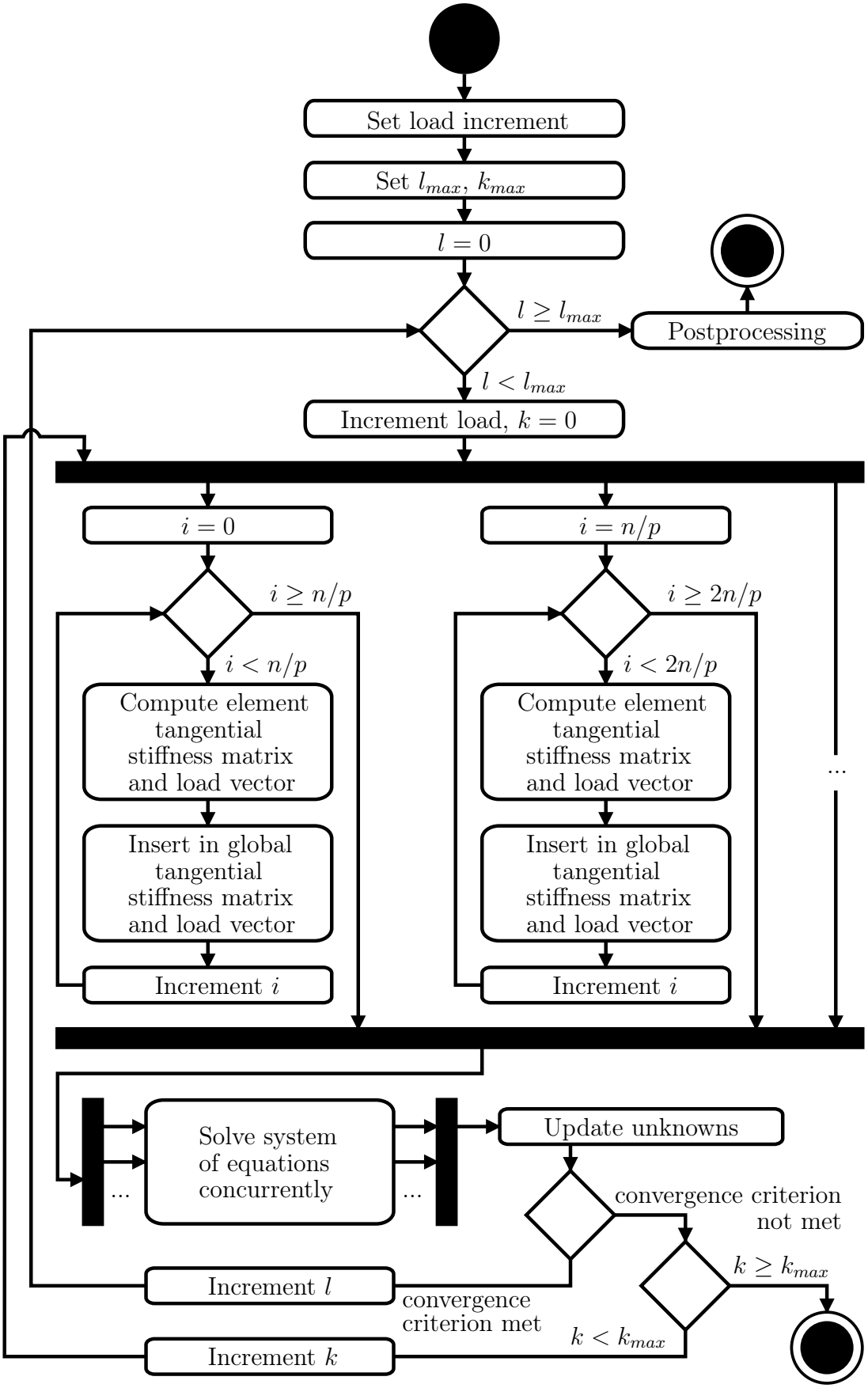

Figure 7.4: Activity diagram of a parallel nonlinear finite element analysis with FEAP

variables and fields are otherwise unproblematic, problems can occur if multiple threads try to access the same address space in public variables and fields, leading to the race conditions already described and therefore to unpredictable errors in the program. This can be circumvented by identifying parts of the code that are vulnerable to race conditions and using compiler directives to ensure that the address space is not manipulated by two or more threads at the same time.

Using the MKL library for sparse matrix-vector operations and using the OpenMP API for the parallelization of the implemented code warrants that the hardware resources are efficiently used, leading to acceptable computation times for nonlinear simulations. In chapter 8.2, the performance gain by means of the parallelization of the code is discussed with the help of performance characteristics such as speedup and efficiency.

Chapter 8

Examples

In this chapter the performance of the implemented finite shell element and the effectiveness of the parallelization are illustrated by some examples. All examples are the result of computations with the finite element software FEAP.

8.1 Numerical examples

To begin with, the capabilities of the global-local finite shell element and the enhanced FSDT model are demonstrated with the example of a simply supported plate. Examples with a different number of layers and different stacking sequences are computed. Next, the results of some simulations with a cylindrical shell are presented. Finally, some geometrically nonlinear examples of box beams and double T-girders are given.

8.1.1 Simply supported plate

The first example, a simply supported square plate subjected to an area load of $p = 1\,\mathrm{N/mm^2}$, is illustrated in figure 8.1. The length of the square plate amounts to $b = 50\,\mathrm{mm}$, while the thickness is $h = 1\,\mathrm{mm}$. A coordinate system is introduced, the origin of which lies in the middle of the plate. The in-plane axes are denoted by ξ^1 and ξ^2 while the axis perpendicular to the plane is denoted by ξ^3. The reference plane is denoted by Ω_0 and separates the plate into two halves with the same thickness, so that the top and the bottom of the plate can be specified by $h^+ = h/2$ and $h^- = -h/2$ respectively.

The material parameters for the transversely isotropic constitutive law (3.64) introduced in chapter 3.4 for a carbon-fiber-reinforced plastic (T300/LY556) are specified by

$$\begin{aligned} E_1 &= 125000\,\mathrm{N/mm^2} \quad , & G_{12} &= 4800\,\mathrm{N/mm^2} \quad , \\ E_2 &= 7400\,\mathrm{N/mm^2} \quad , & \nu_{12} &= 0.34 \quad , \\ \nu_{23} &= 0.37 \quad . \end{aligned} \tag{8.1}$$

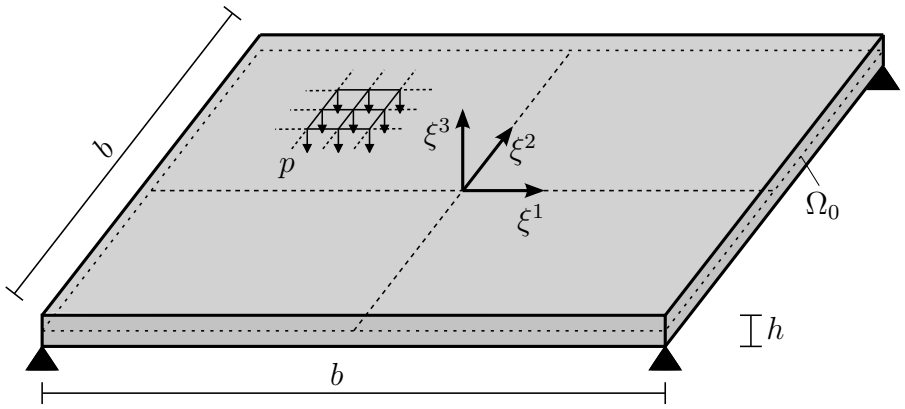

Figure 8.1: Simply supported square plate

In the following, the example is computed with a number of different stacking sequences using different finite elements. For the sake of simplicity, some abbreviations are introduced in table 8.1 for the different finite elements used.

Abbreviation	Model
QB	Brick element with quadratic shape functions
G	Global shell, independent thickness strains
GL1	Global-local shell, elementwise constant
GL2	Global-local shell, full interpolation
PP1	Enhanced FSDT, model 1
PP2	Enhanced FSDT, model 2

Table 8.1: Abbreviations of the different theoretical models

As a reference solution, the results of simulations conducted using brick elements with quadratic ansatz functions are presented. Additionally shown are the results of simulations carried out using the global shell element discussed in chapter 3, including independent thickness strains as proposed in [71], the global-local shell element introduced in chapters 4 and 5 and the enhanced FSDT model presented in chapter 6, which is a post-processing procedure. The two different versions of the global-local shell element and the enhanced FSDT model in table 8.1 were outlined in the respective chapters. The orthogonalization procedure used for the global-local shell element is specified along with the example. The enhanced FSDT model was implemented in a shell element based on a single-field variational principle.

The results of the simulations of the layered composite plate with the different stacking sequences are shown in the following sequence. First, plots are shown of the results for the out-of-plane displacement w, the effective stress couple resultants $\tilde{m}_{11}$, $\tilde{m}_{22}$ and $\tilde{m}_{12}$ and the effective shear stress resultants $\tilde{q}_1$ and $\tilde{q}_2$ using the global-local finite shell element with elementwise constant values. These results correspond to the results using the global finite shell element, showing that the original results for the displacements and effective stress

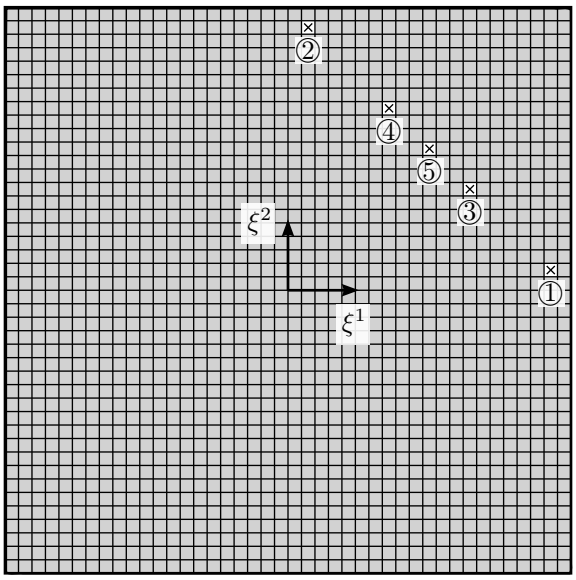

Figure 8.2: Evaluation points for the stresses

resultants are not falsified by the addition of the local part of the model. Thereafter the results of the different finite elements for the stresses S_{ij} are shown through the thickness of the layered composite plate at certain evaluation points. The evaluation points are specified in figure 8.2. For the global-local shell element the results for the warping of the cross section are shown at the evaluation points. Figure 8.2 shows the discretization with two-dimensional elements, so that in this case, the evaluation point is at the element center. For the brick element with quadratic shape functions, the evaluation point is chosen to lie in a node of the mesh. The coordinates of the evaluation points in figure 8.2 are specified in table 8.2.

Point	①	②	③	④	⑤
Coordinate ξ^1	23.21	1.79	16.07	8.93	12.50
Coordinate ξ^2	1.79	23.21	8.93	16.07	12.50

Table 8.2: Coordinates of evaluation points

The discretizations with two-dimensional and three-dimensional finite elements and qualitative representations of the deformed plate are shown in figure 8.3. In simulations with brick elements the plate is discretized with 28x28x12 elements, as illustrated in figure 8.3a. In simulations with shell elements the plate is discretized with 42x42 elements, as illustrated in figure 8.3b. As a large number of brick elements has to be used through the thickness of the plate to receive acceptably accurate results, especially for the stresses, the computation with brick elements takes significantly longer. A qualitative representation of the deformed state of the plate is given in figure 8.3c for the discretization with brick elements and in figure 8.3d for the discretization with shell elements. The maximum displacement in ξ^3-direction is located in the middle of the plate.

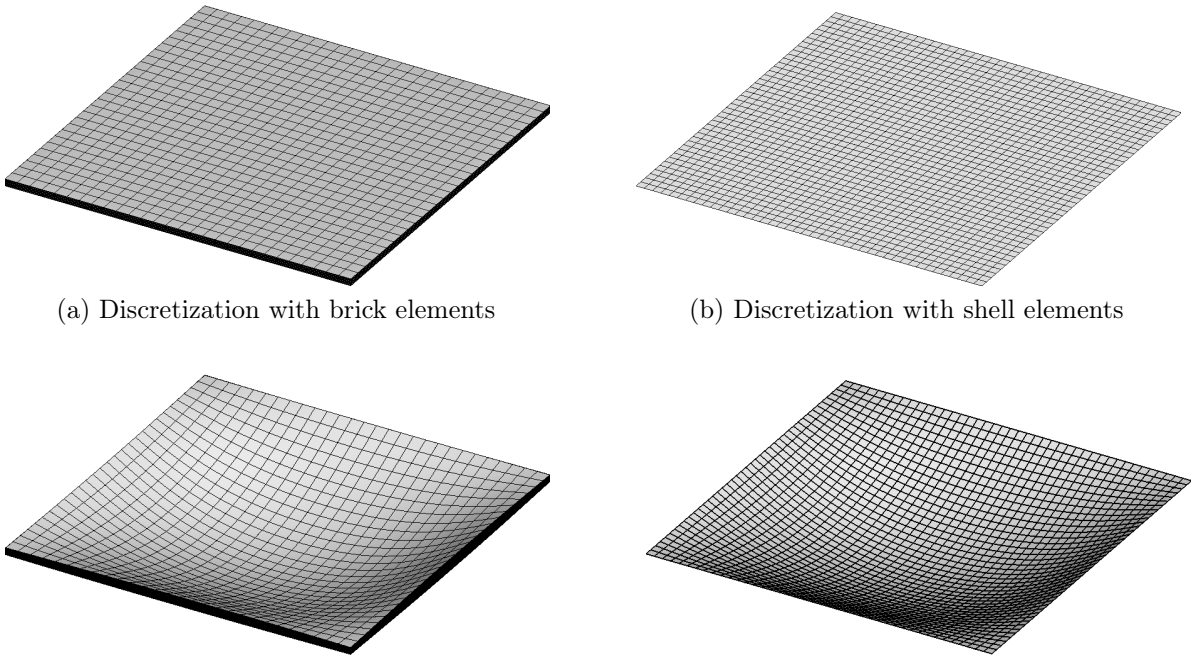

(a) Discretization with brick elements

(b) Discretization with shell elements

(c) Deformed plate with brick elements

(d) Deformed plate with shell elements

Figure 8.3: Discretizations of the plate and qualitative representation of the deformed plate

Homogeneous example

As a first example, the simply supported square plate has only one unidirectional layer with a fiber angle of $\varphi = 0°$. This simple example is given to show the improvements in the results of the out-of-plane stresses achieved by means of the global-local shell and the enhanced FSDT model towards the global model. It is mentioned that for reasons of symmetry the simulation can be performed in a quarter of the plate with appropriate boundary conditions. The orthogonalization procedure with two parameters for homogeneous materials is used in the global-local model. The results for the maximum displacement in ξ^3-direction in the middle of the plate of the different models are specified in table 8.3 using the abbreviations defined in table 8.1.

Model	QB	G	PP1	PP2	GL1	GL2
w_{max} [mm]	7.61	7.58	7.60	7.61	7.60	7.60

Table 8.3: Maximum displacement w_{max}

The results for the displacements using the different finite elements are in good agreement, with the largest discrepancy being less than 0.4 %. The displacements in ξ^3-direction for the plate are shown in figure 8.4a for model GL1. Additionally, the effective stress couple resultants $\tilde{m}_{11}$, $\tilde{m}_{22}$ and $\tilde{m}_{12}$, and the effective shear stress resultants $\tilde{q}_1$ and $\tilde{q}_2$ are shown in figures 8.4b to 8.4f for the same model. The three effective membrane stress resultants $\tilde{n}_{11}$, $\tilde{n}_{22}$ and $\tilde{n}_{12}$ are zero in this problem.

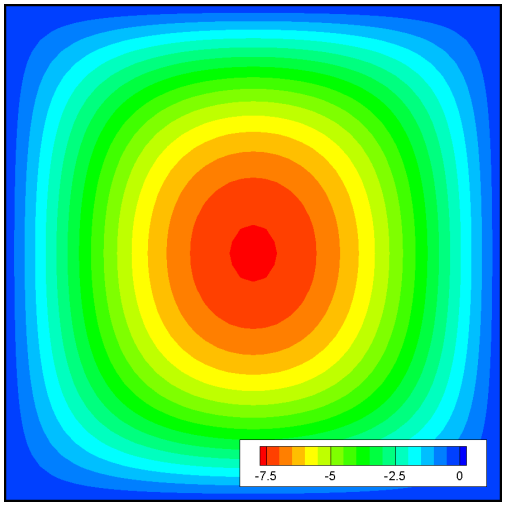

(a) w [mm]

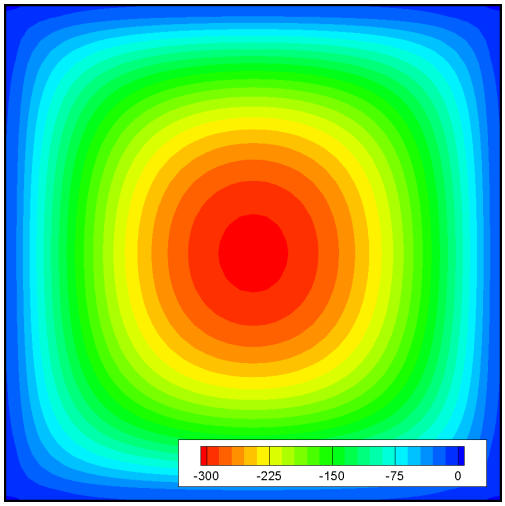

(b) $\tilde{m}_{11}$ [Nmm/mm]

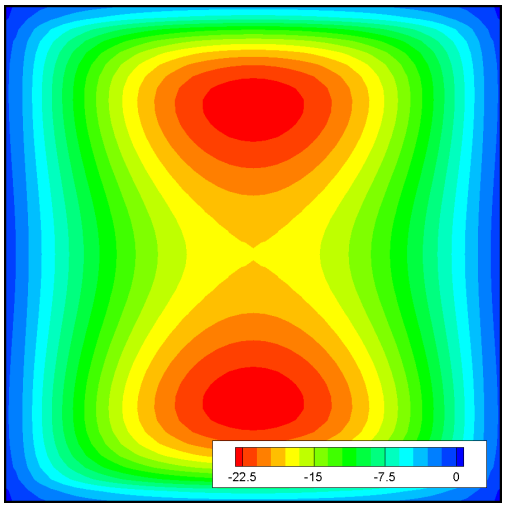

(c) $\tilde{m}_{22}$ [Nmm/mm]

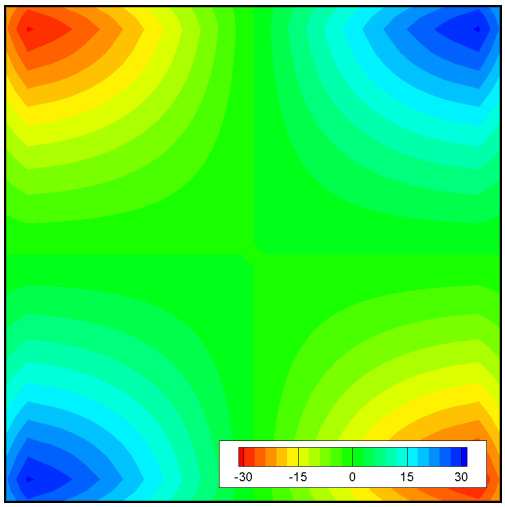

(d) $\tilde{m}_{12}$ [Nmm/mm]

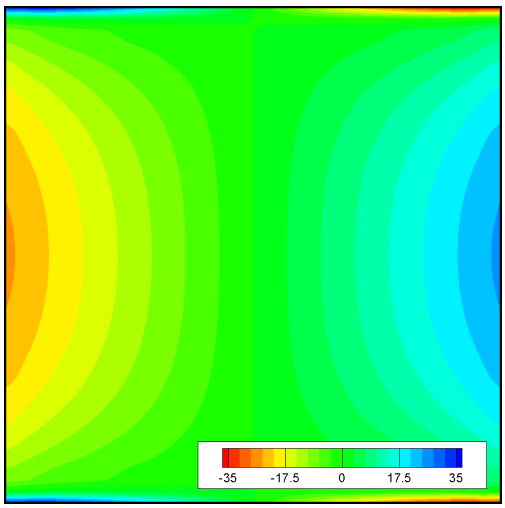

(e) $\tilde{q}_1$ [Nmm/mm]

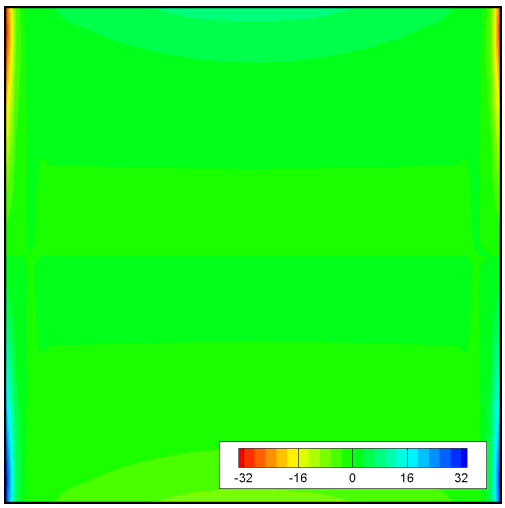

(f) $\tilde{q}_2$ [Nmm/mm]

Figure 8.4: Out-of-plane displacement and effective stress resultants

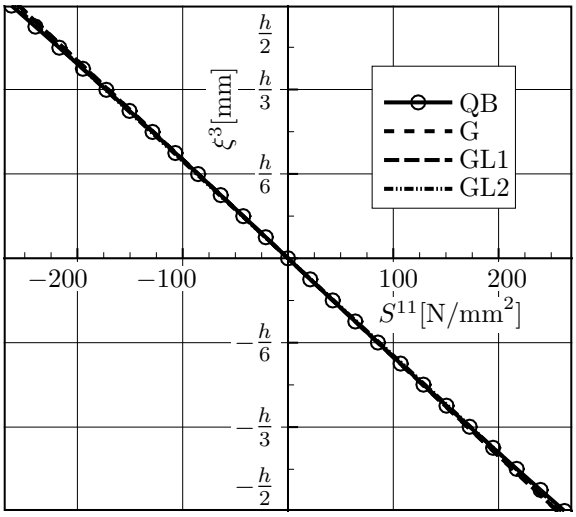

(a) S^{11} [N/mm^2]

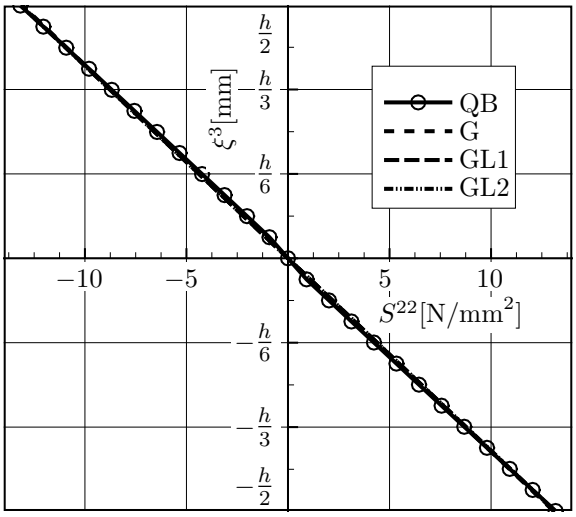

(b) S^{22} [N/mm^2]

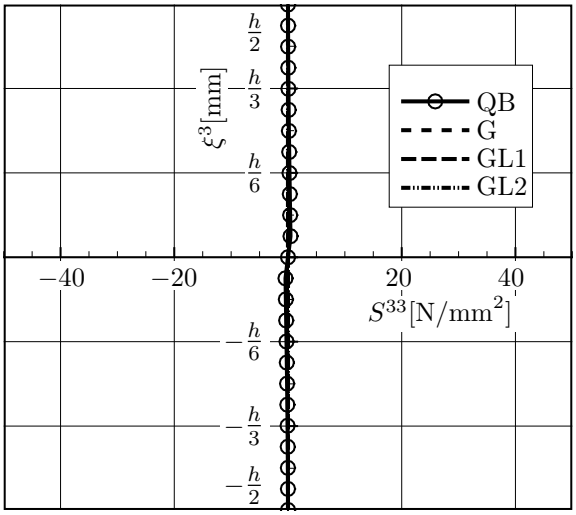

(c) S^{33} [N/mm^2]

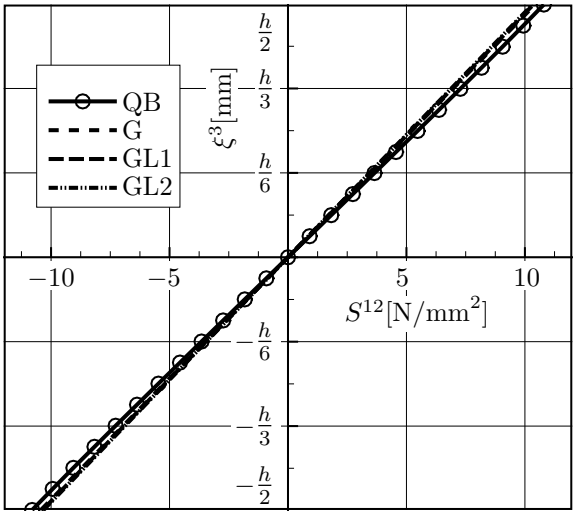

(d) S^{12} [N/mm^2]

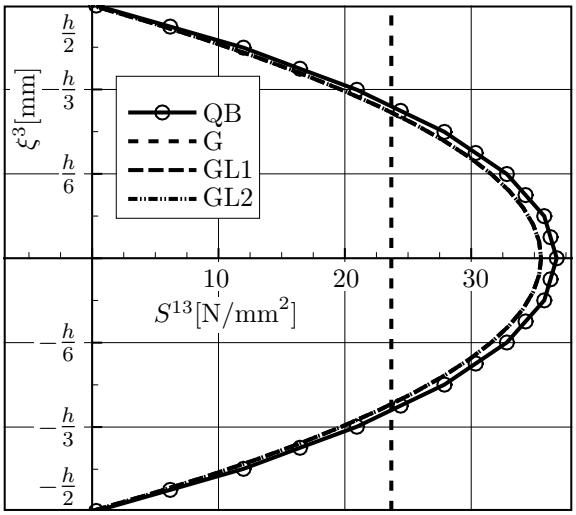

(e) S^{13} [N/mm^2]

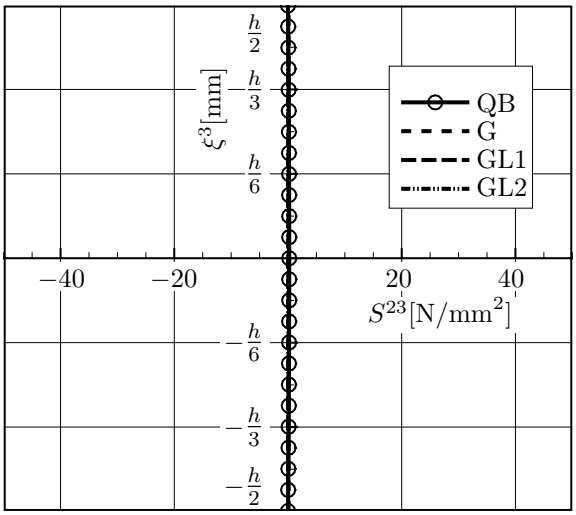

(f) S^{23} [N/mm^2]

Figure 8.5: Stresses through the thickness at evaluation point ①

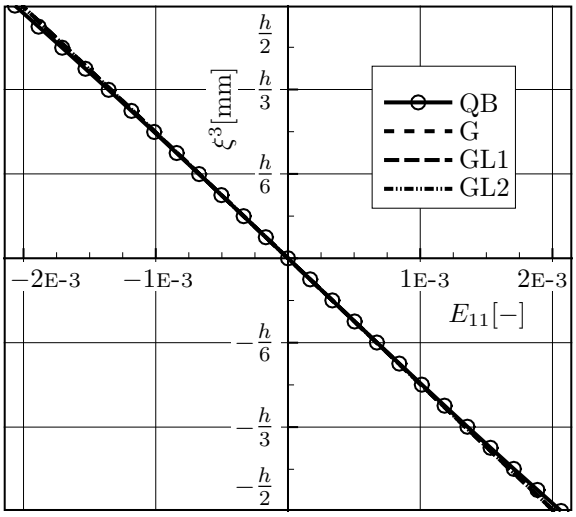

(a) E_{11} [−]

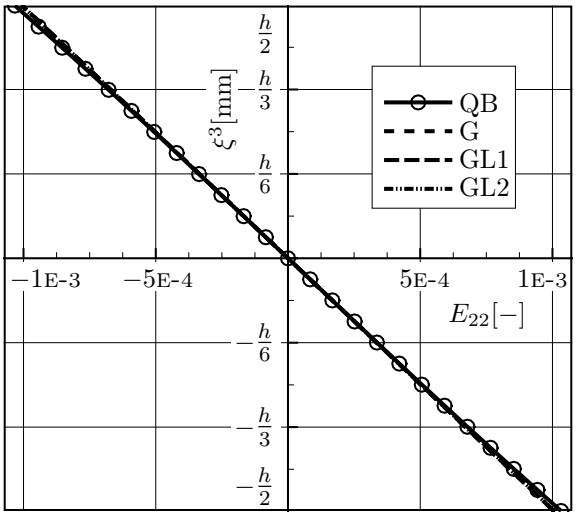

(b) E_{22} [−]

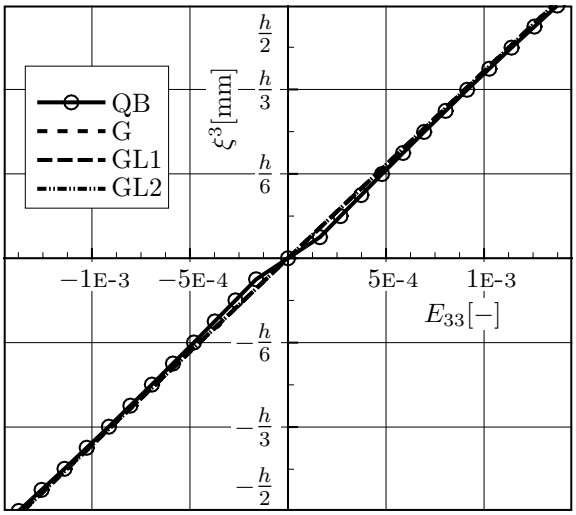

(c) E_{33} [−]

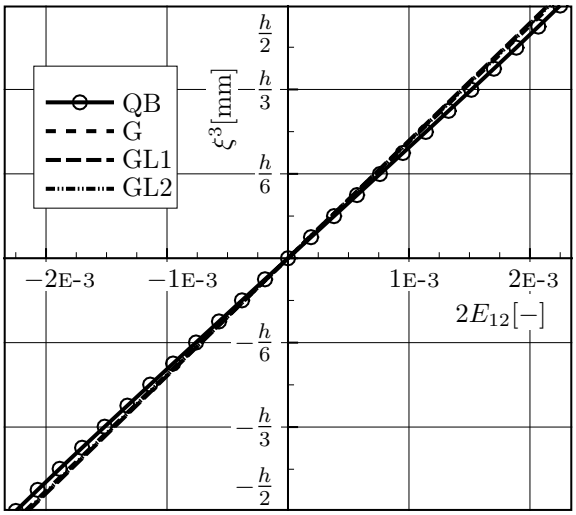

(d) $2E_{12}$ [−]

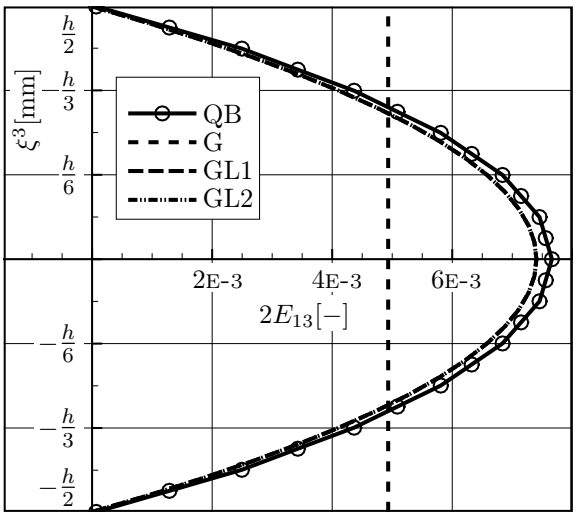

(e) $2E_{13}$ [−]

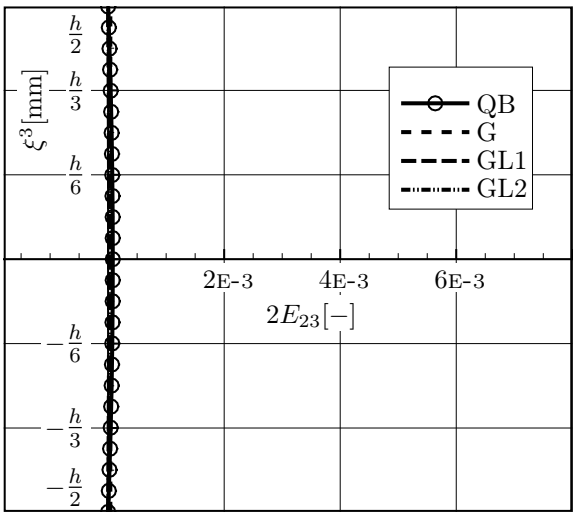

(f) $2E_{23}$ [−]

Figure 8.6: Strains through the thickness at evaluation point ①

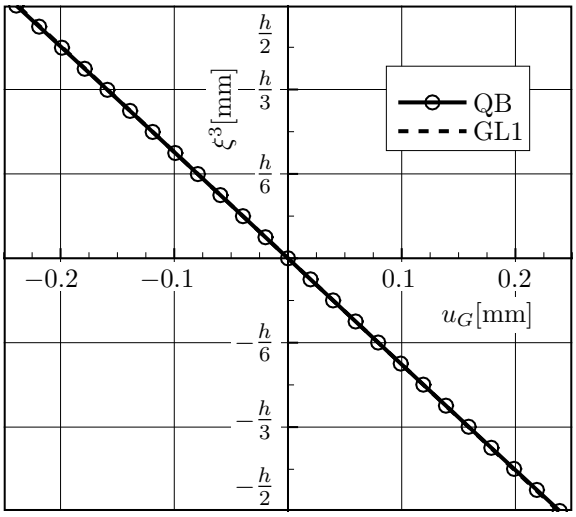

(a) u_G [mm]

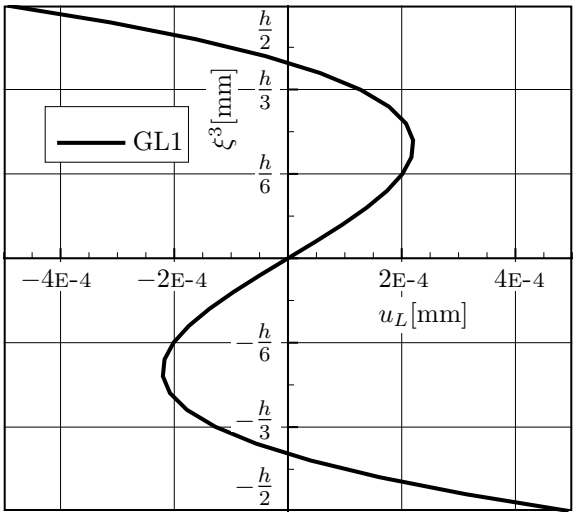

(b) u_L [mm]

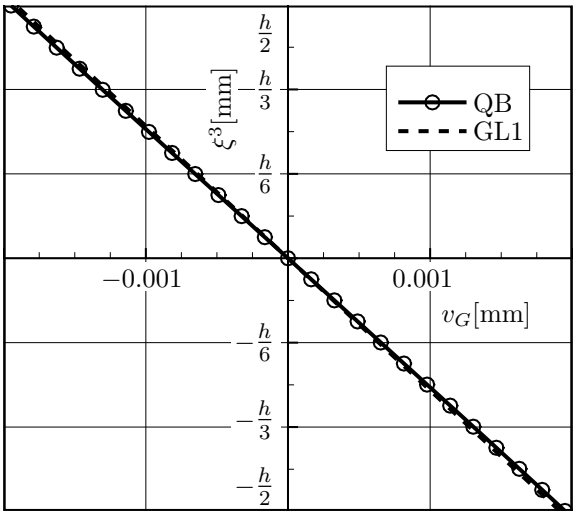

(c) v_G [mm]

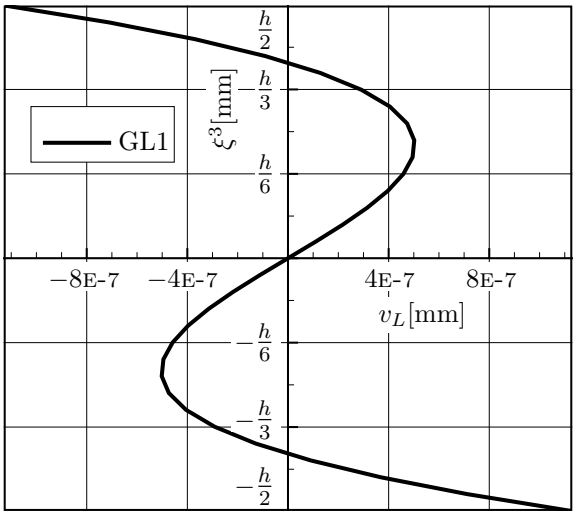

(d) v_L [mm]

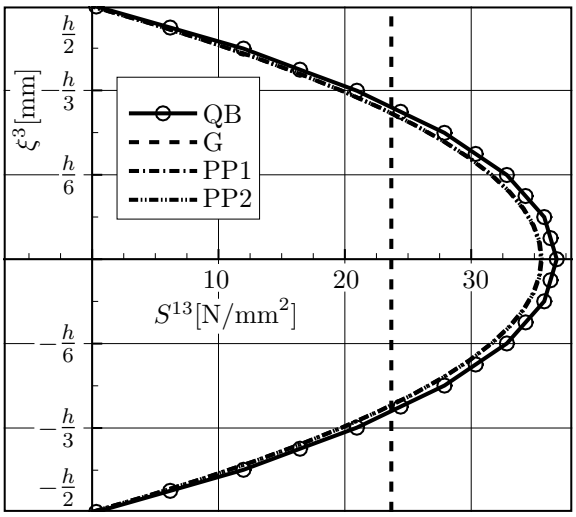

(e) S^{13} [N/mm^2]

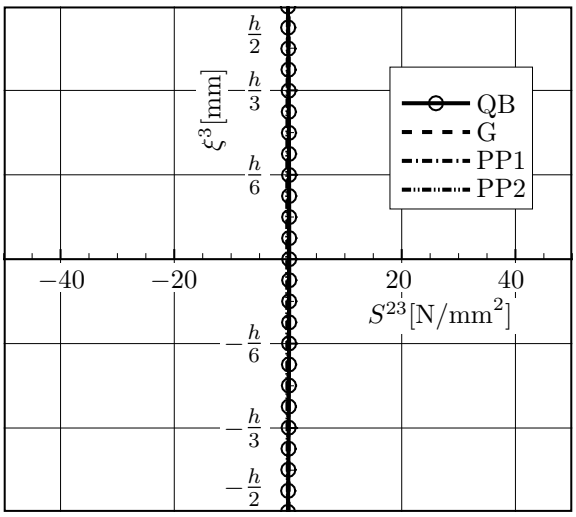

(f) S^{23} [N/mm^2]

Figure 8.7: Displacements and transverse shear stresses (PP1 and PP2) at evaluation point ①

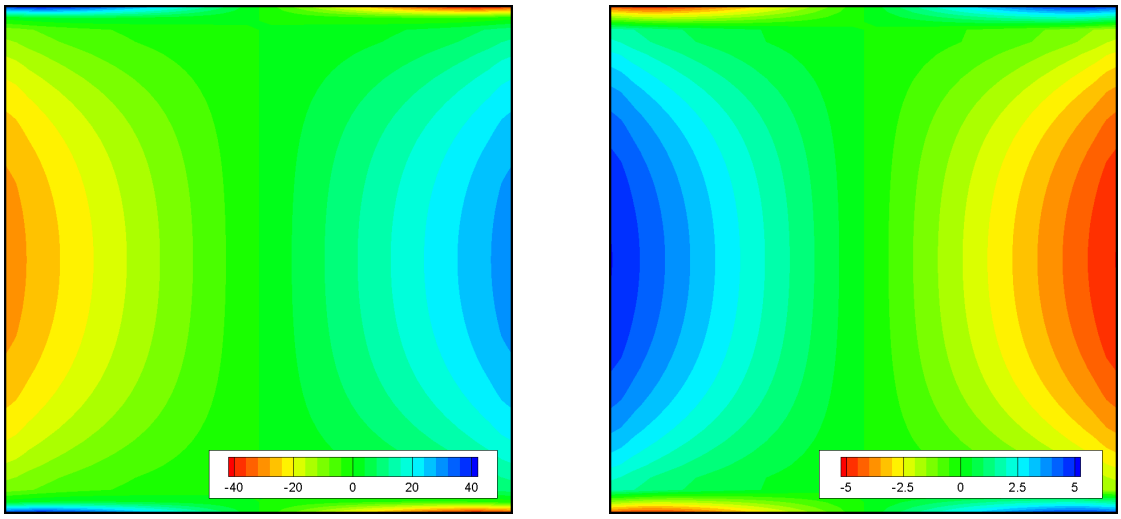

(a) $\tilde{q}_1^G$ [N/mm] (b) $\tilde{q}_1^L$ [N/mm]

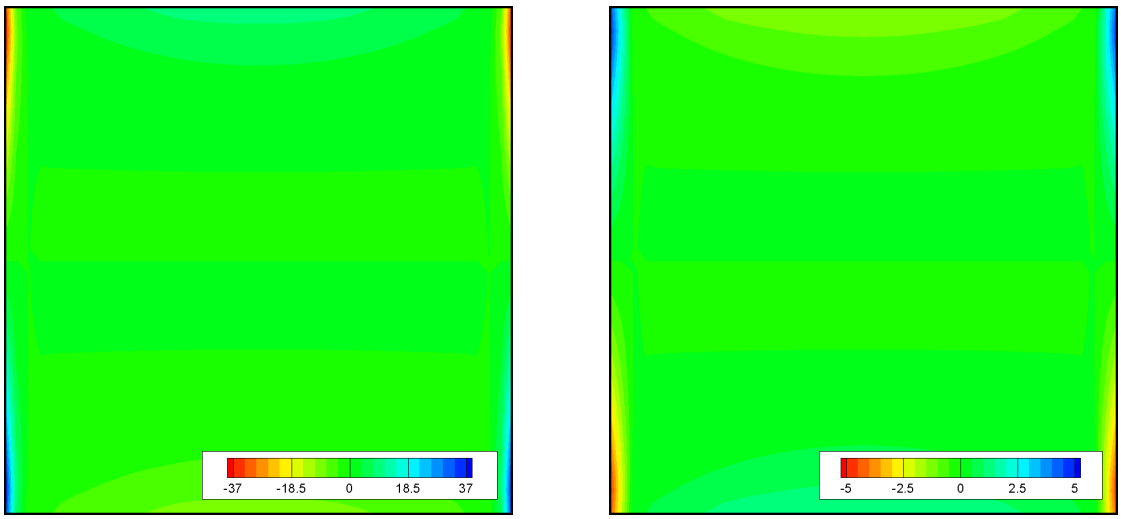

(c) $\tilde{q}_2^G$ [N/mm] (d) $\tilde{q}_2^L$ [N/mm]

Figure 8.8: Separation of shear stress resultants into a global and local part

The results of the effective stress resultants using the coupled global-local model correspond to the results for the global model, which are already sufficiently accurate. For the stress couple resultants and the membrane stress resultants this is a result of the orthogonalization procedure. On the other hand, through the addition of the local model an alteration of the shear stress resultants is permitted. The effective shear stress resultants are separated into a global and a local part. The separated results of the global and the local model are shown in figure 8.8. Adding the results for the global shear stress resultant $\tilde{q}_1^G$ shown in figure 8.8a and the results for the local shear stress resultants $\tilde{q}_1^L$ shown in figure 8.8b yields the shear stress resultant $\tilde{q}_1$ shown in figure 8.4e. It is analogous for $\tilde{q}_2$.

The stresses through the thickness of the plate are shown in figure 8.5 at evaluation point ①. It is apparent that the results for the in-plane stresses S^{11}, S^{22} and S^{12} for the global model and global-local model are in good agreement with the reference solution.

When examining the transverse shear stress S^{13} by means of figure 8.5e at evaluation

point ①, where the shear stress resultant $\tilde{q}_1$ is relatively large, as shown in figure 8.4e, it becomes evident that the result derived by means of the global-local model is in good agreement with the reference solution, whereas the result of the global model yields a constant result through the thickness. This model is only capable of producing a result that is correct on an average. Since the global model only supplies constant paths of the transverse shear strains through the thickness (3.22), the results obtained for the transverse shear stresses by means of the material law are also constant. With the global-local model, the quadratic path of the transverse shear stress S^{13} is accurately reproduced and the results equal zero at the top and bottom of the composite, which needs to be the case considering boundary conditions. Because the other effective shear stress resultant $\tilde{q}_2$ is relatively small, as shown in figure 8.4f, the transverse shear stress S^{23} at evaluation point ① is also small, but it follows a quadratic path. In homogeneous examples with only one unidirectional layer the transverse shear stresses follow a quadratic path without kinks or jumps at every point of the plate. The normal stress S^{33} depicted in figure 8.10c is zero through the thickness of the plate in this example.

In figures 8.7a to 8.7d, plots are shown of the global and local in-plane displacements introduced in (4.14). The global displacements are several orders of magnitude larger than the local in-plane displacements, which describe warping of the cross section. The global in-plane displacements follow a linear path, which is why the global model with its linear strains specified in (4.24) yields good results for the displacements and the stress resultants. It is not able, however, to reproduce the correct path of the out-of-plane stresses. With the introduction of the local model the warping of the cross section and hence also the transverse shear stresses can be derived as part of the variational formulation. The results for the local displacements follow a cubic path through the thickness of the plate, because the highest order terms in the ansatz functions are cubic. The local displacement u_L shown in figure 8.7b corresponds to the transverse shear stress S^{13} depicted in figure 8.5e, while the local displacement v_L shown in figure 8.7d corresponds to the transverse shear stress S^{23} depicted in figure 8.5f. As the local displacement u_L is several orders of magnitude larger than the local displacement v_L, the transverse shear stress S^{13} is larger than the transverse shear stress S^{23}. The results for the transverse shear stresses derived with the enhanced FSDT model discussed in chapter 6 are shown in figures 8.7e and 8.7f. The results correspond largely to the results obtained using the brick element and the global-local shell element.

Inhomogeneous examples

In this section, a number of inhomogeneous examples with different stacking sequences are provided. The first example is a cross-ply laminate with three layers and a stacking sequence of $[0°/90°/0°]$. For reasons of symmetry the simulation can be performed in a quarter of the plate with appropriate boundary conditions. When implementing the orthogonalization of the global-local finite shell element the method of least squares is used considering the special characteristics of cross-ply laminates as discussed in chapter 4.2.2. The summation procedure and the procedure for special stacking sequences applied to cross-ply laminates, with the parameters $\alpha = 1.5$ and $\beta = 10$, outlined in the same chapter, yield very similar results.

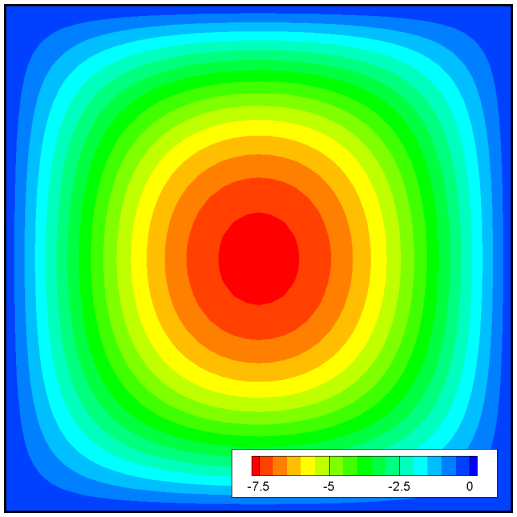

(a) w [mm]

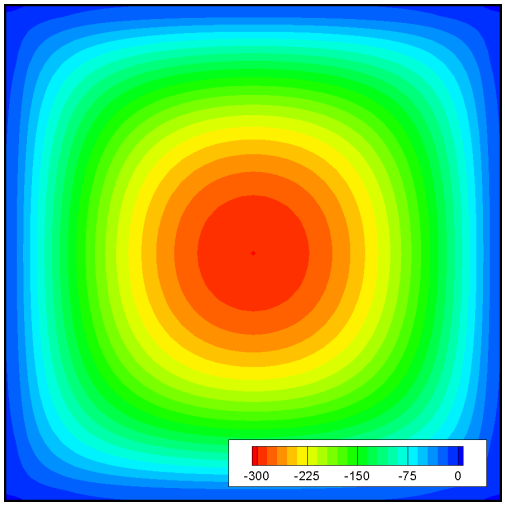

(b) $\tilde{m}_{11}$ [Nmm/mm]

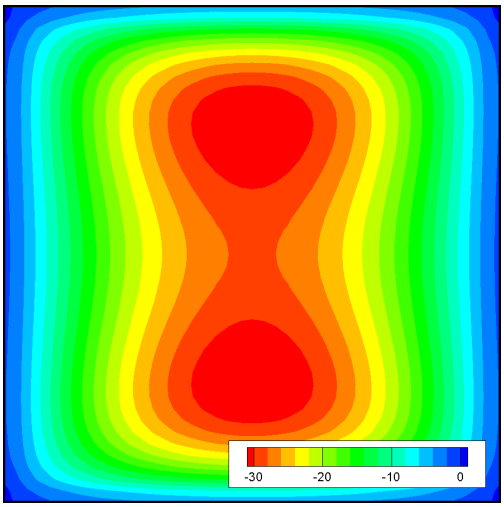

(c) $\tilde{m}_{22}$ [Nmm/mm]

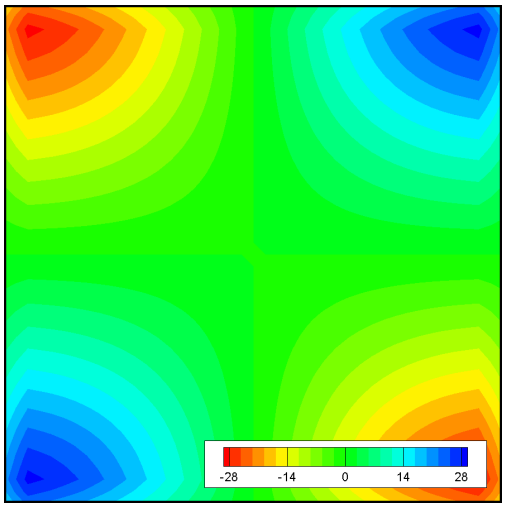

(d) $\tilde{m}_{12}$ [Nmm/mm]

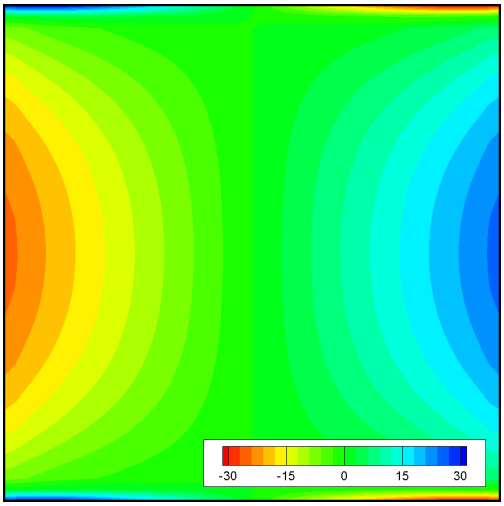

(e) $\tilde{q}_1$ [N/mm]

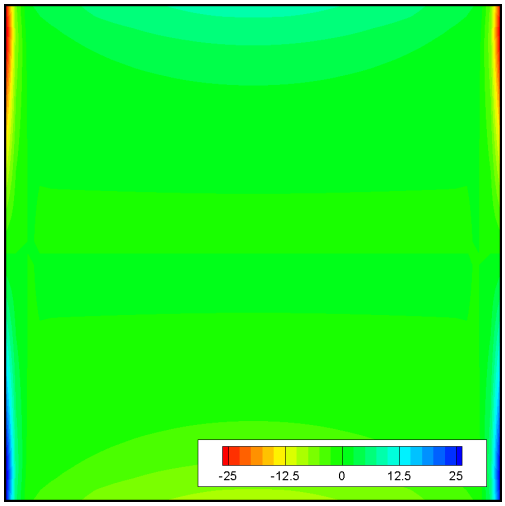

(f) $\tilde{q}_2$ [N/mm]

Figure 8.9: Out-of-plane displacement and effective stress resultants

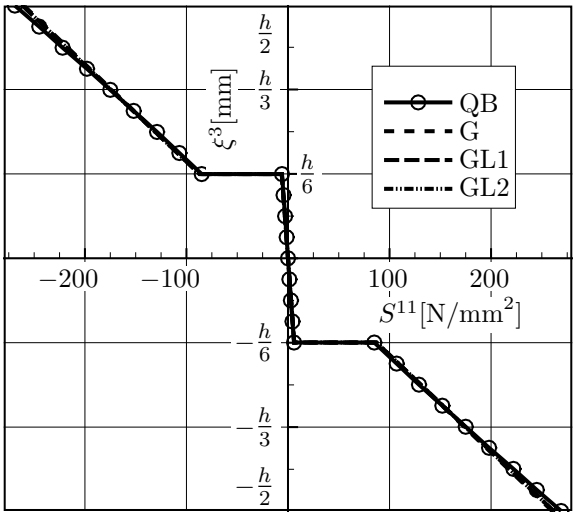

(a) S^{11} [N/mm^2]

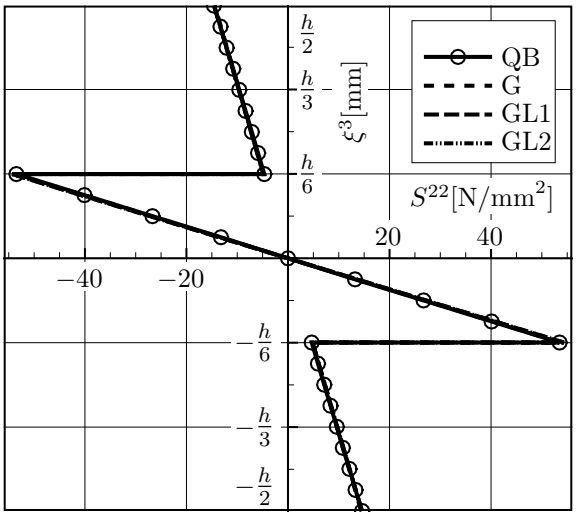

(b) S^{22} [N/mm^2]

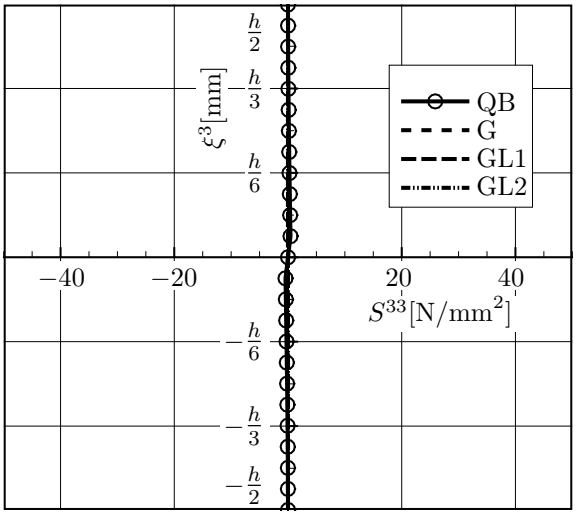

(c) S^{33} [N/mm^2]

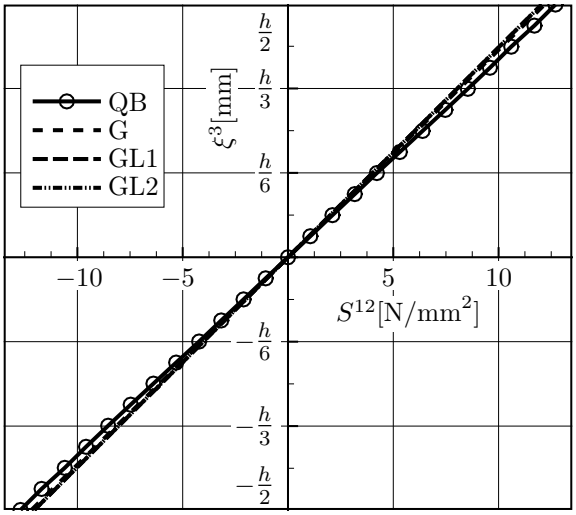

(d) S^{12} [N/mm^2]

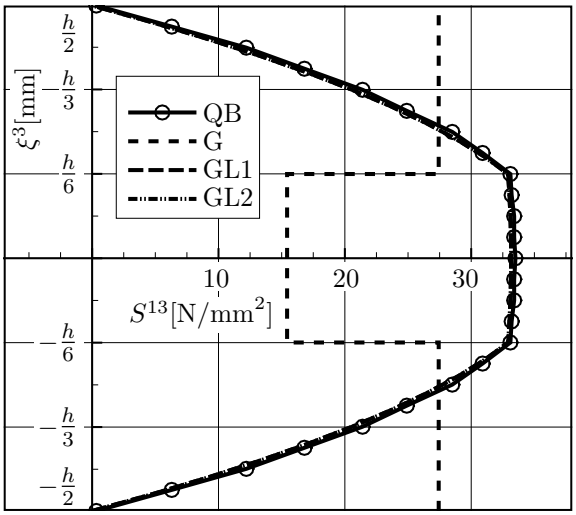

(e) S^{13} [N/mm^2]

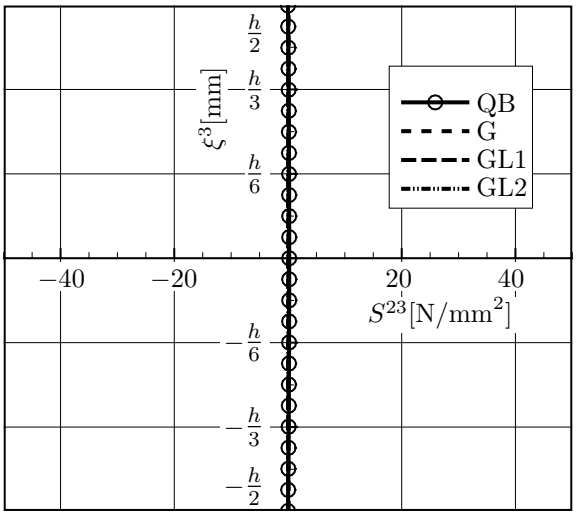

(f) S^{23} [N/mm^2]

Figure 8.10: Stresses through the thickness at evaluation point ①

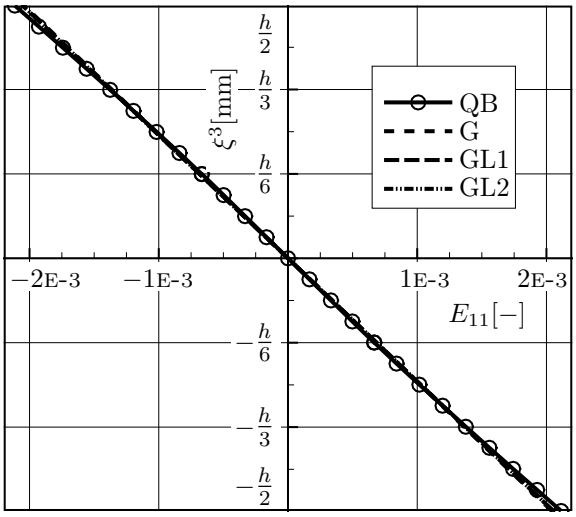

(a) E_{11} [−]

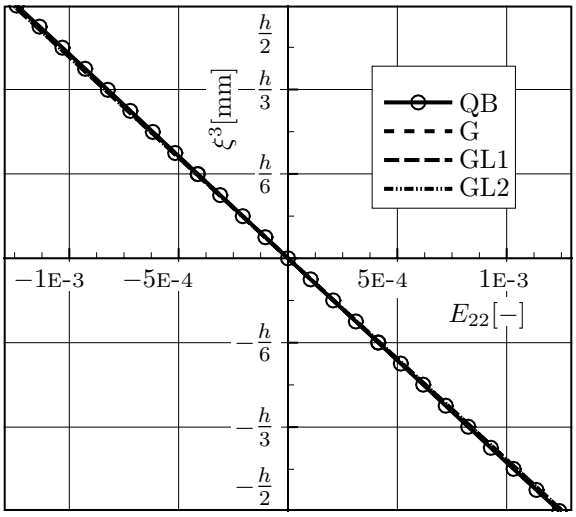

(b) E_{22} [−]

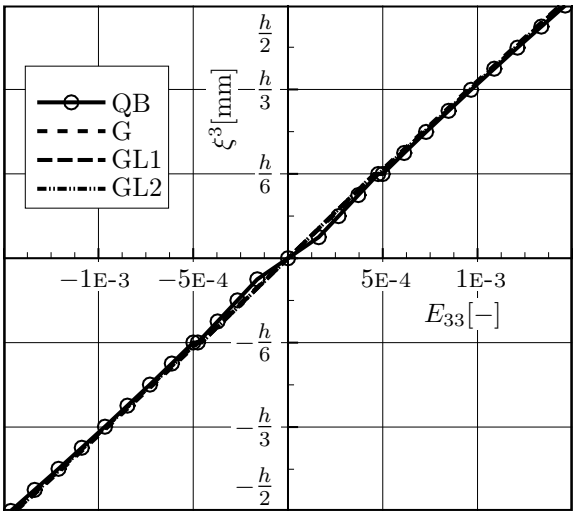

(c) E_{33} [−]

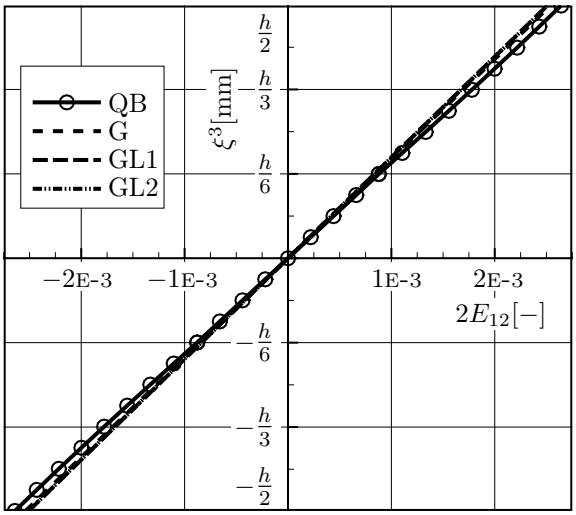

(d) $2E_{12}$ [−]

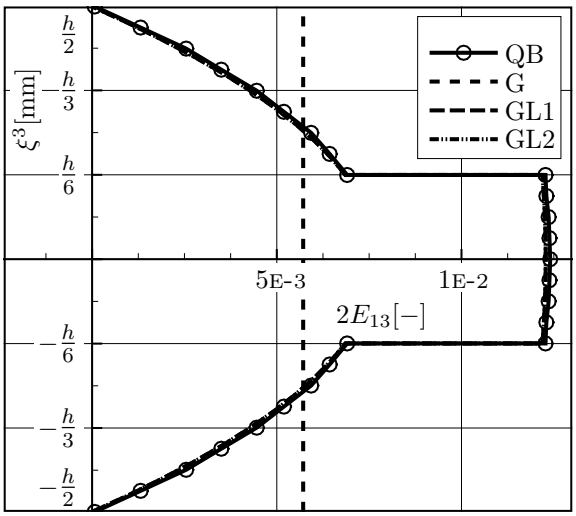

(e) $2E_{13}$ [−]

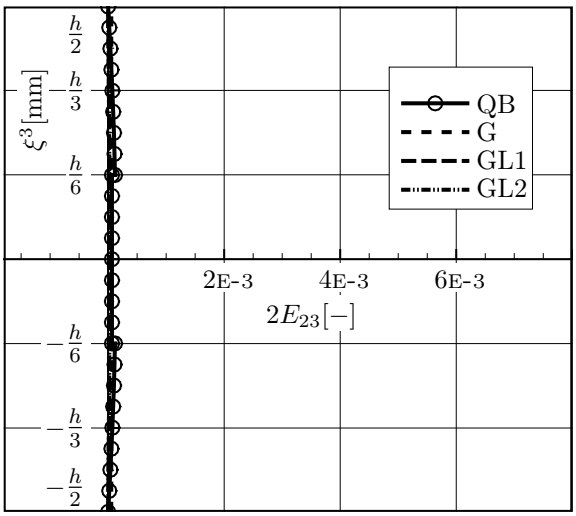

(f) $2E_{23}$ [−]

Figure 8.11: Strains through the thickness at evaluation point ①

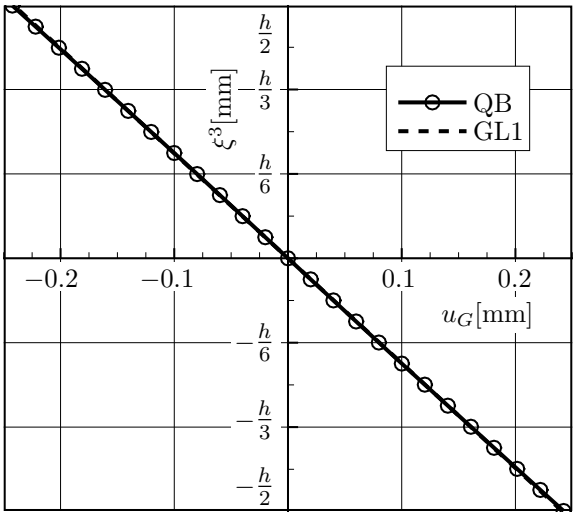

(a) u_G [mm]

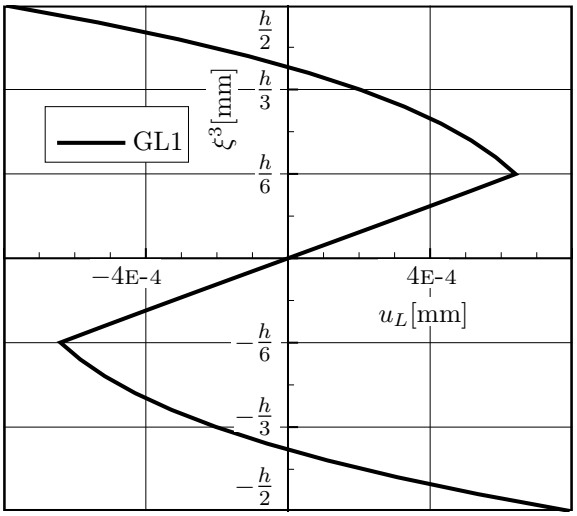

(b) u_L [mm]

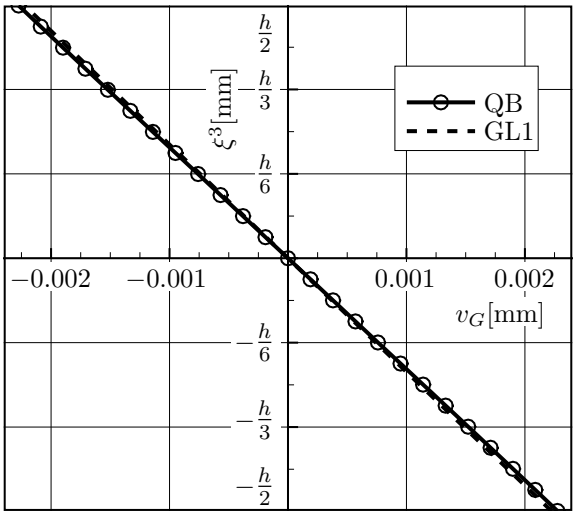

(c) v_G [mm]

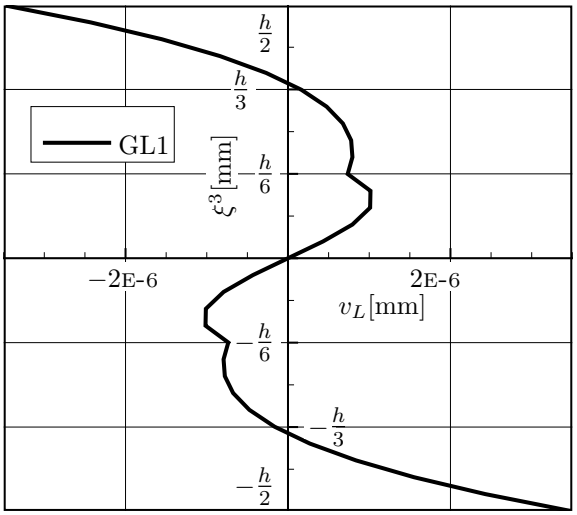

(d) v_L [mm]

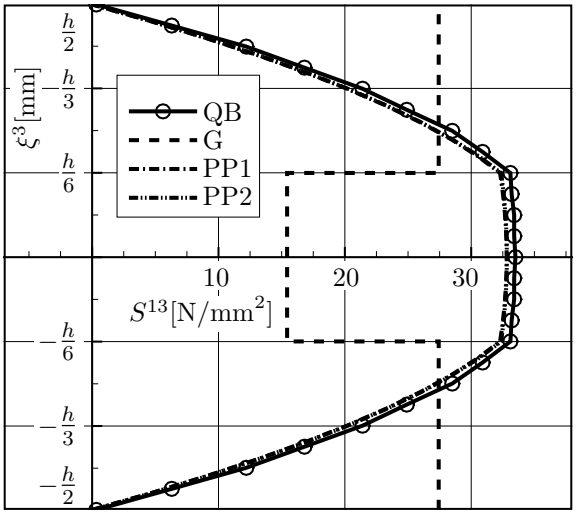

(e) S^{13} [N/mm^2]

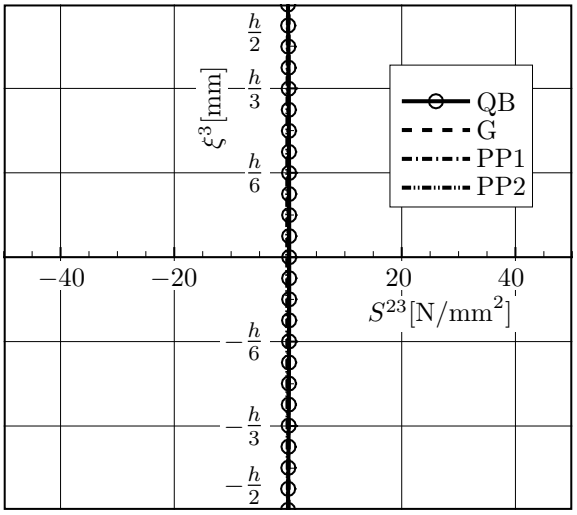

(f) S^{23} [N/mm^2]

Figure 8.12: Displacements and interlaminar shear stresses (PP1 and PP2) at point ①

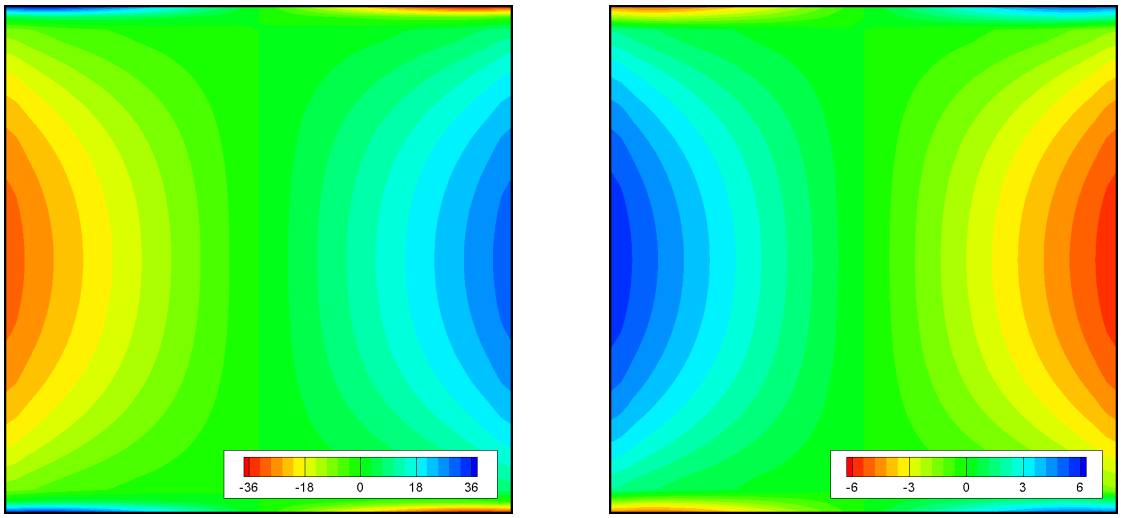

(a) $\tilde{q}_1^G$ [N/mm] (b) $\tilde{q}_1^L$ [N/mm]

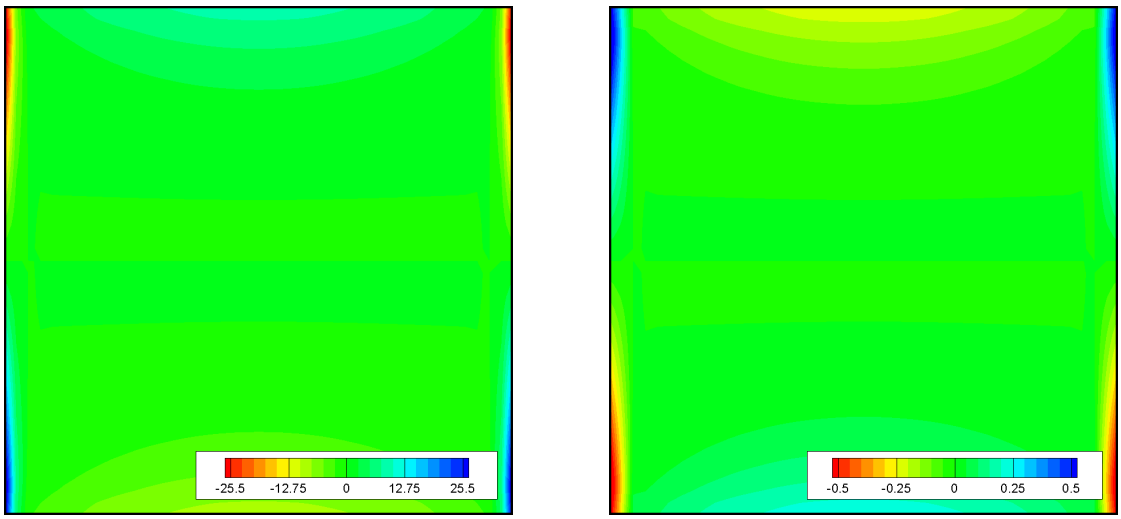

(c) $\tilde{q}_2^G$ [N/mm] (d) $\tilde{q}_2^L$ [N/mm]

Figure 8.13: Separation of shear stress resultants into a global and local part

The results for the maximum displacement of the different models are specified in table 8.4 using the abbreviations defined in table 8.1. The largest discrepancy of the maximum displacement in the middle of the plate is less than 0.65 %. The displacements in ξ^3-direction for the plate are shown in figure 8.9a when using model GL1. Additionally, the effective stress couple resultants $\tilde{m}_{11}$, $\tilde{m}_{22}$ and $\tilde{m}_{12}$, and the effective shear stress resultants $\tilde{q}_1$ and $\tilde{q}_2$ are shown in figures 8.9b to 8.9f for the same model. The three effective membrane stress resultants $\tilde{n}_{11}$, $\tilde{n}_{22}$ and $\tilde{n}_{12}$ are zero.

Model	QB	G	PP1	PP2	GL1	GL2
w_{max} [mm]	7.74	7.69	7.71	7.73	7.74	7.74

Table 8.4: Maximum displacement w_{max}

Analogous to the preceding example, the results for the effective stress resultants using the coupled global-local model correspond to the results for the global model alone, with the shear stress resultants separated into a global and a local part. The separated results of the global and the local model are shown in figure 8.13. Adding the results for the global shear stress resultant $\tilde{q}_1^G$ shown in figure 8.13a and the results for the local shear stress resultants $\tilde{q}_1^L$ shown in figure 8.13b yields the effective shear stress resultant $\tilde{q}_1$ shown in figure 8.9e. It is analogous for $\tilde{q}_2$.

The results for the stresses, strains and displacements through the thickness of the plate are presented for two different evaluation points. Figures 8.10 to 8.12 show the results for evaluation point ①, while figures 8.14 to 8.16 show the results for evaluation point ②. At evaluation point ①, the effective shear stress resultant $\tilde{q}_1$ shown in figure 8.9e is relatively large and the effective shear stress resultant $\tilde{q}_2$ shown in figure 8.9f is relatively small. It is the other way around at evaluation point ②.

The stresses are shown for evaluation point ① in figure 8.10 and for evaluation point ② in figure 8.14, while the strains are shown in figure 8.11 for evaluation point ① and in figure 8.15 for evaluation point ②. Unlike the previous, homogeneous example, there are jumps in the in-plane stresses S^{11} and S^{22}. On the other hand, the in-plane strains E_{11} and E_{22} are continuous throughout the thickness of the laminate. The in-plane stress S^{12} and the in-plane strain $2E_{12}$ both are continuous for cross-ply laminates. The reason for this is that the entries C_{14}^G, C_{24}^G, C_{41}^G, and C_{42}^G are zero and C_{44}^G stays the same through the thickness in cross-ply laminates.

The interlaminar shear stresses S^{13} and S^{23} follow a piecewise quadratic path and are continuous with kinks at the layer boundaries, where the properties of the stiffness matrix change, but there are no jumps. On the other hand, the interlaminar shear strains $2E_{13}$ and $2E_{23}$ exhibit jumps at the layer boundaries. This behavior is characteristic of laminates consisting of transversely isotropic layers. Examining the interlaminar shear stress S^{13} by means of figure 8.10e at evaluation point ①, where the shear stress resultant $\tilde{q}_1$ is relatively large, and the interlaminar shear stress S^{23} by means of figure 8.14f at evaluation point ②, where the shear stress resultant $\tilde{q}_2$ is relatively large, manifests that the results derived by means of the global-local model are in good agreement with the reference solution, whereas the results of the global model yield piecewise constant results with jumps at the layer boundaries. Again, the global model is only capable to reproduce the average result through the thickness.

It is pointed out that with the global-local model, the piecewise quadratic paths of the interlaminar shear stresses S^{13} at evaluation point ① and S^{23} at evaluation point ② are accurately reproduced and the results equal zero at the top and bottom of the composite, which needs to be the case considering boundary conditions. The continuity at the layer boundaries is met. Because the other effective shear stress resultants $\tilde{q}_2$ at evaluation point ① and $\tilde{q}_1$ at evaluation point ② are relatively small the interlaminar shear stresses S^{23} at evaluation point ① and S^{13} at evaluation point ② are also small, but follow a piecewise quadratic path. The qualitative path of the interlaminar shear stress S^{13} depicted in figure 8.10e, with a smaller inclination in the top and bottom layers and a larger inclination in the middle layer, is characteristic of the interlaminar shear stress S^{13} for the stacking sequence in this example.

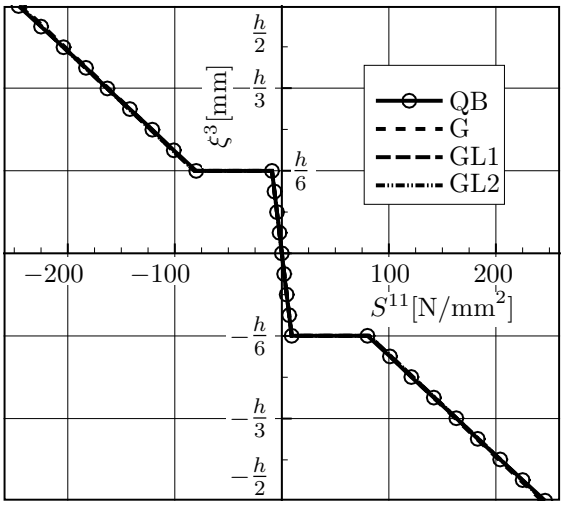

(a) S^{11} [N/mm^2]

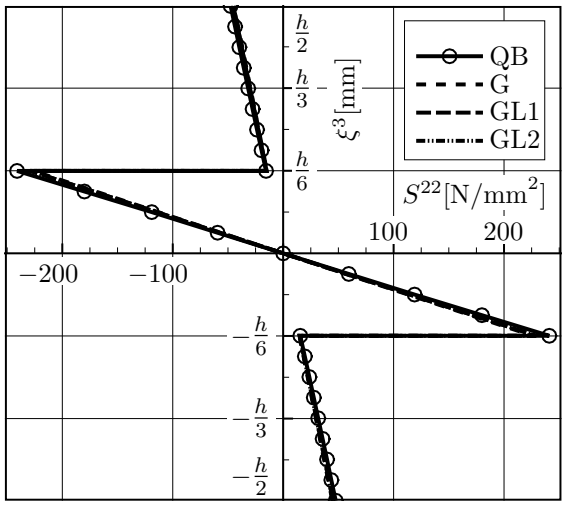

(b) S^{22} [N/mm^2]

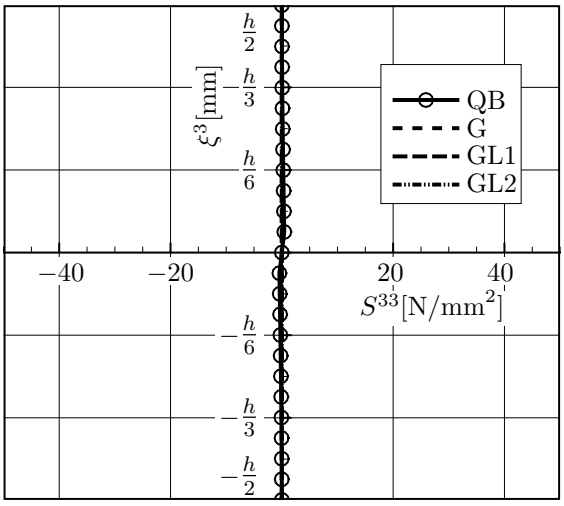

(c) S^{33} [N/mm^2]

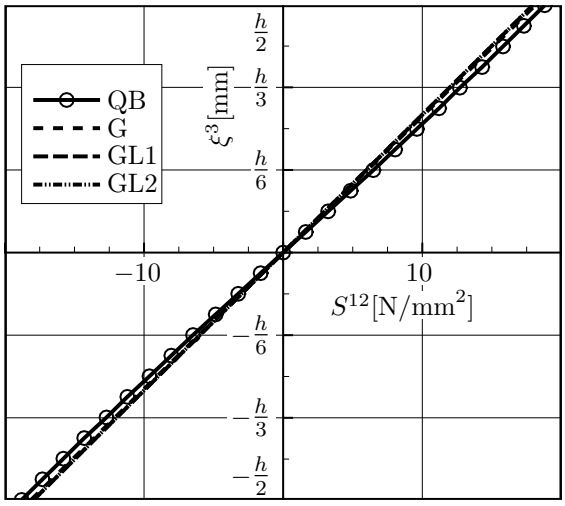

(d) S^{12} [N/mm^2]

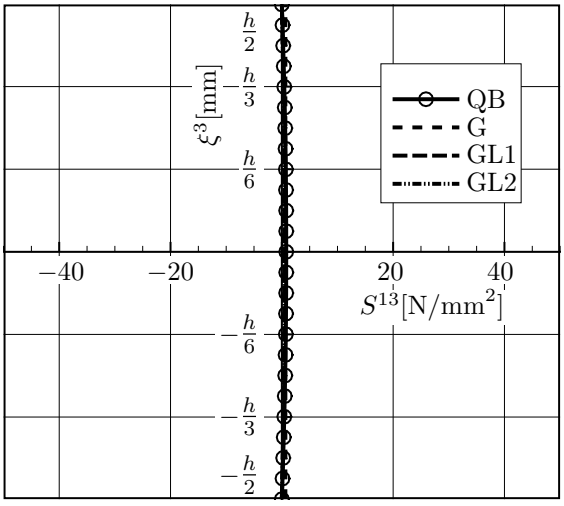

(e) S^{13} [N/mm^2]

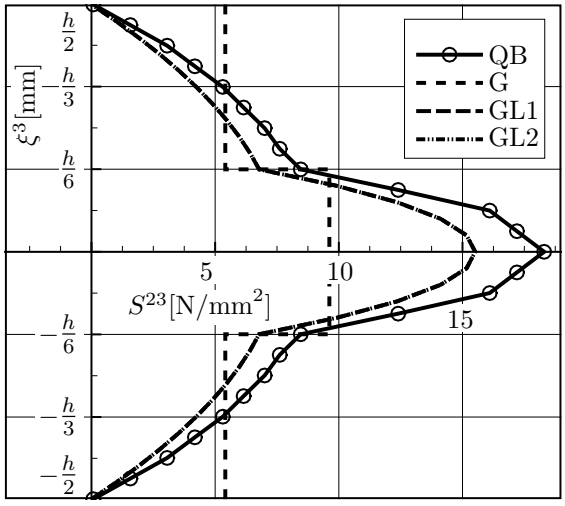

(f) S^{23} [N/mm^2]

Figure 8.14: Stresses at evaluation point ②

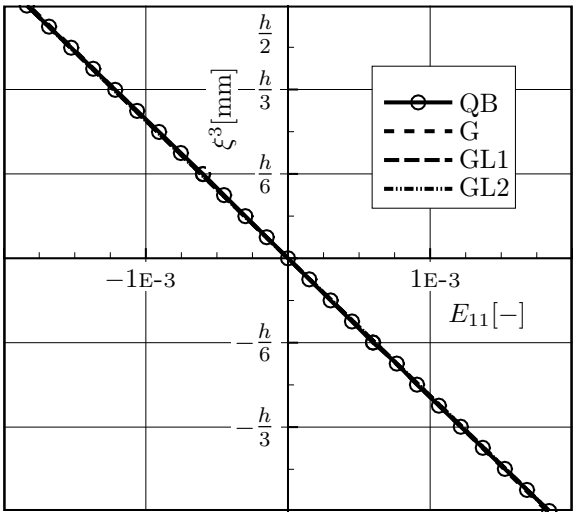

(a) E_{11} [−]

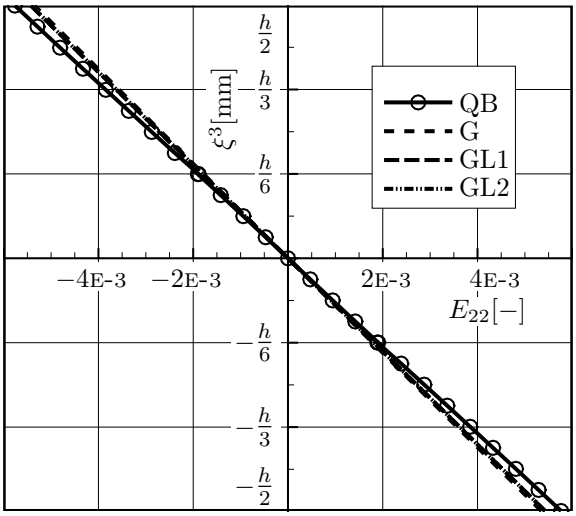

(b) E_{22} [−]

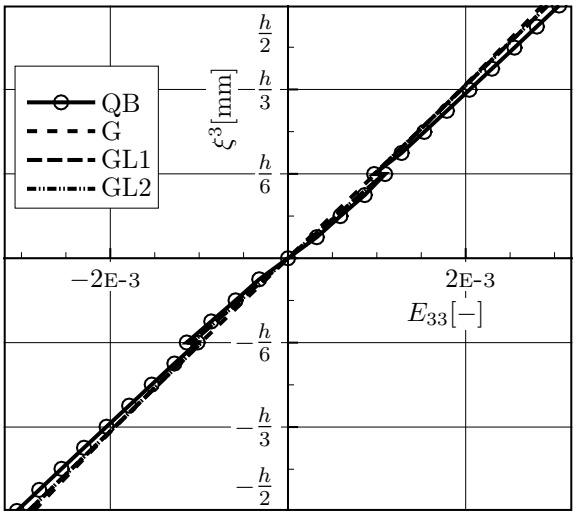

(c) E_{33} [−]

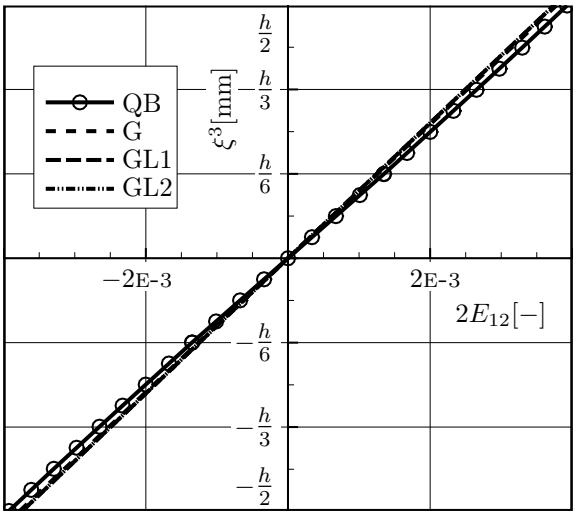

(d) $2E_{12}$ [−]

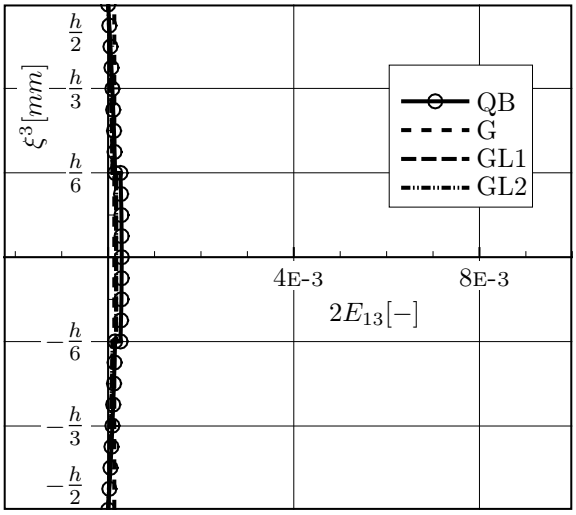

(e) $2E_{13}$ [−]

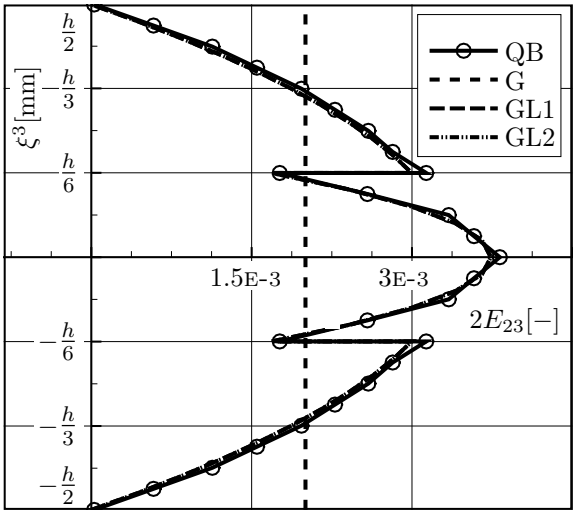

(f) $2E_{23}$ [−]

Figure 8.15: Strains at evaluation point ②

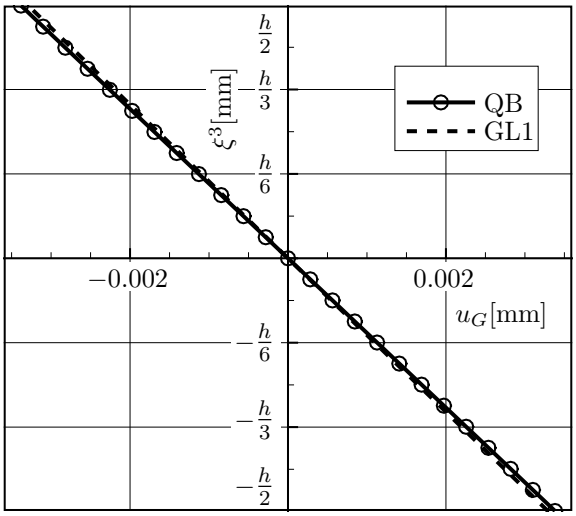

(a) u_G [mm]

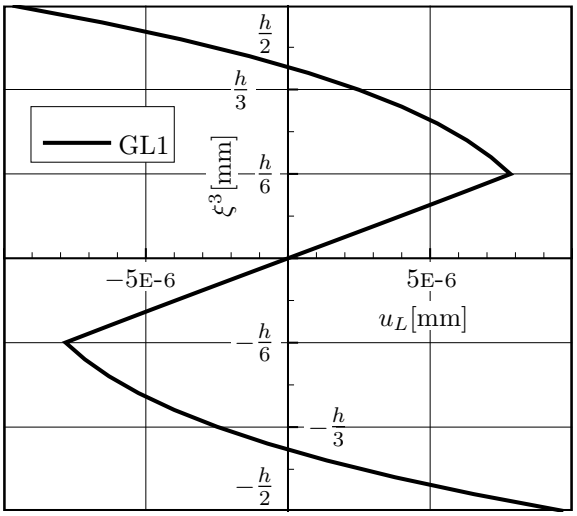

(b) u_L [mm]

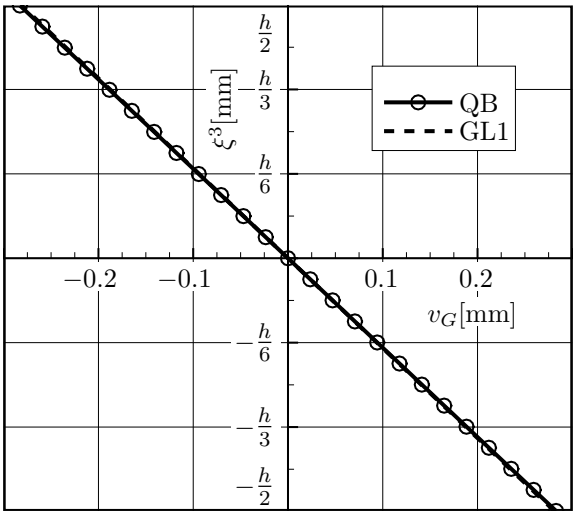

(c) v_G [mm]

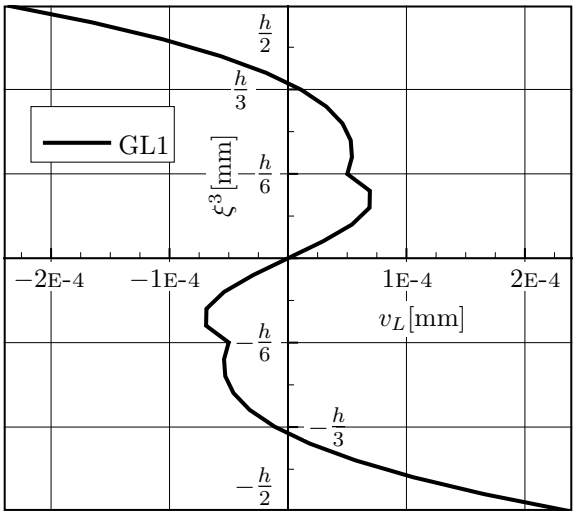

(d) v_L [mm]

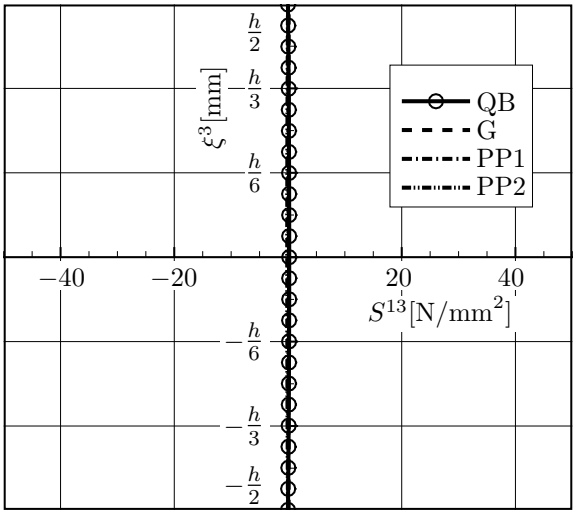

(e) S^{13} [N/mm^2]

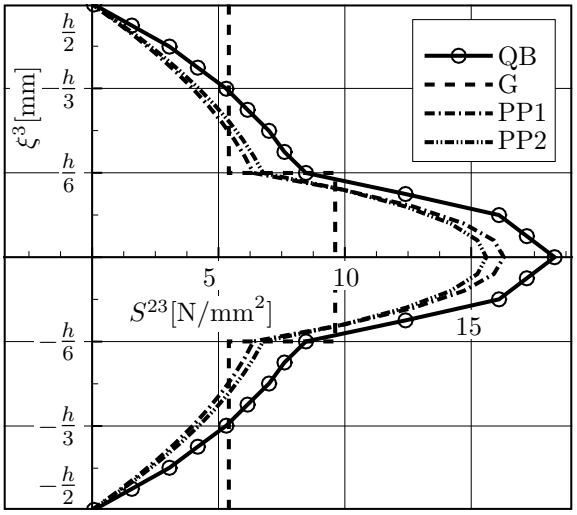

(f) S^{23} [N/mm^2]

Figure 8.16: Displacements and interlaminar shear stresses (PP1 and PP2) at point ②

Similarly, the qualitative path of the interlaminar shear stress S^{23} depicted in figure 8.10f is characteristic of the interlaminar shear stress S^{23} for the stacking sequence in this example. This is the case because the paths of the interlaminar shear stresses are strongly influenced by jumps in the stiffnesses. Cross-ply laminates, which consist of layers that only have fiber orientations of 0° and 90°, display the largest jump in the stiffnesses at the layer boundaries of C^G_{11} and C^G_{22}. These stiffnesses strongly influence the paths of the interlaminar shear stresses in cross-ply laminates.

Because in the simulation with brick elements the area load acts upon the middle of the plate, there is a jump in the path of the interlaminar normal stress S^{33} at this point. When using the global-local shell element with its piecewise functions through the thickness, the results for the interlaminar normal stresses S^{33} depicted in figure 8.10c and figure 8.14c are zero through the thickness of the plate. When using the global shell element the results are only approximately zero, for numerical reasons.

In figures 8.12a to 8.12d and figures 8.16a to 8.16d, plots are shown of the global and local in-plane displacements introduced in (4.14). Similar to the homogeneous example, the global displacements are several orders of magnitude larger than the local displacements. The global in-plane displacements follow a linear path, which is why the global model with its linear strains specified in (4.24) yields good results for the displacements and the stress resultants. It is not able, however, to reproduce the correct path of the interlaminar stresses. With the introduction of the local model the warping of the cross section and hence also the interlaminar shear stresses can be derived.

The results for the local displacements follow a piecewise cubic path through the thickness of the plate with kinks at the layer boundaries, because the highest order terms in the ansatz functions are cubic. The condition of continuity at the layer boundaries is fulfilled. For evaluation point ①, the local displacement u_L shown in figure 8.12b corresponds to the interlaminar shear stress S^{13} depicted in figure 8.10e, while the local displacement v_L shown in figure 8.12d corresponds to the interlaminar shear stress S^{23} depicted in figure 8.10f. As the local displacement u_L at evaluation point ① is several orders of magnitude larger than the local displacement v_L, the interlaminar shear stress S^{13} is larger than the interlaminar shear stress S^{23}. In the same way, for evaluation point ②, the local displacement u_L shown in figure 8.16b corresponds to the interlaminar shear stress S^{13} depicted in figure 8.14e, while the local displacement v_L shown in figure 8.16d corresponds to the interlaminar shear stress S^{23} depicted in figure 8.14f. At evaluation point ② the local displacement v_L is several orders of magnitude larger than the local displacement u_L, and, correspondingly, the interlaminar shear stress S^{23} is larger than the interlaminar shear stress S^{13}.

The results for the interlaminar shear stresses derived with the enhanced FSDT model discussed in chapter 6 are shown in figures 8.12e, 8.12f, 8.16e and 8.16f. The results correspond largely to the results obtained with the quadratic brick element and the global-local shell element.

The second inhomogeneous example is a cross-ply laminate with 15 layers, beginning and ending with a layer that has a fiber orientation of 0°.

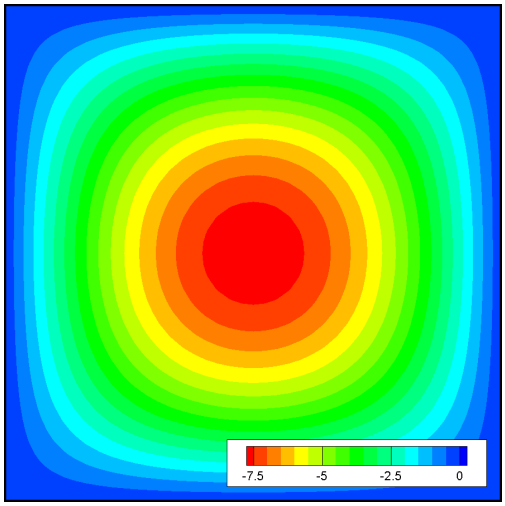

(a) w [mm]

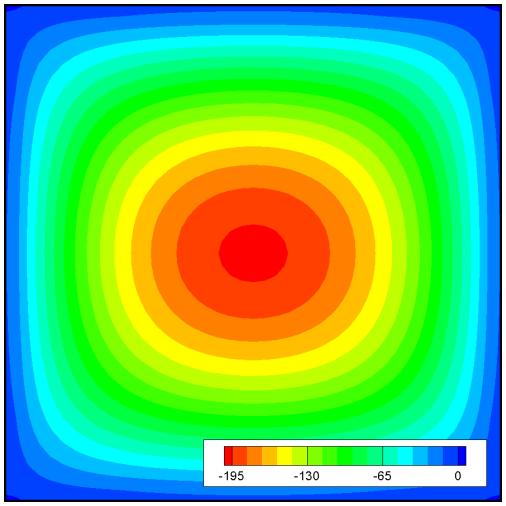

(b) $\tilde{m}_{11}$ [Nmm/mm]

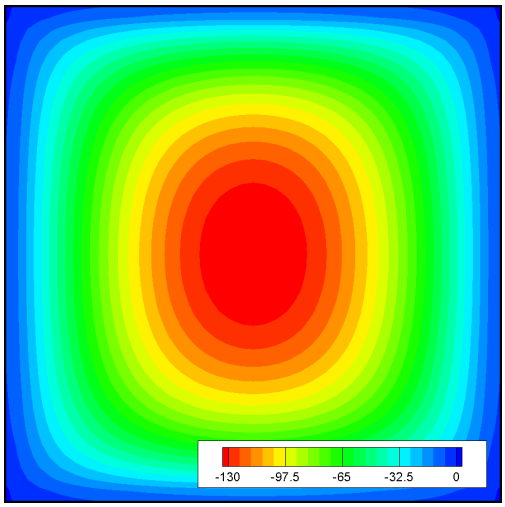

(c) $\tilde{m}_{22}$ [Nmm/mm]

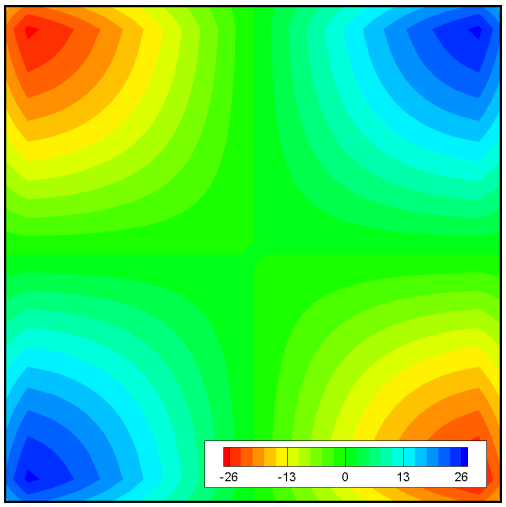

(d) $\tilde{m}_{12}$ [Nmm/mm]

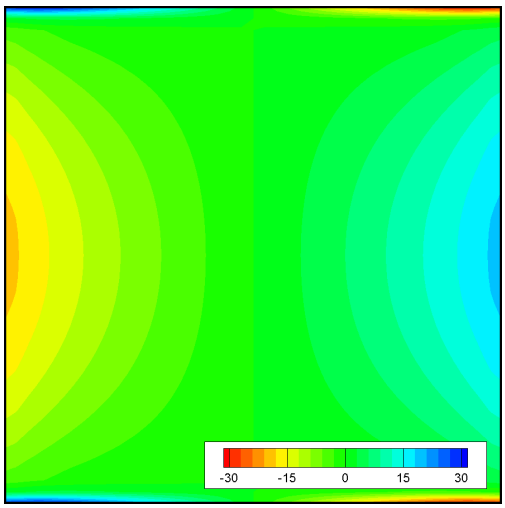

(e) $\tilde{q}_1$ [N/mm]

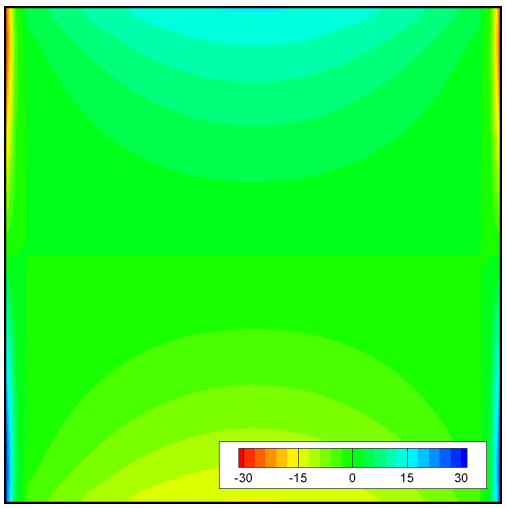

(f) $\tilde{q}_2$ [N/mm]

Figure 8.17: Out-of-plane displacement and effective stress resultants

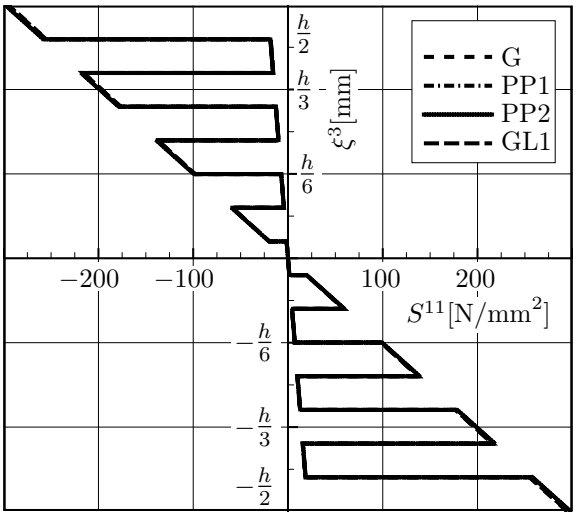

(a) S^{11} [N/mm^2]

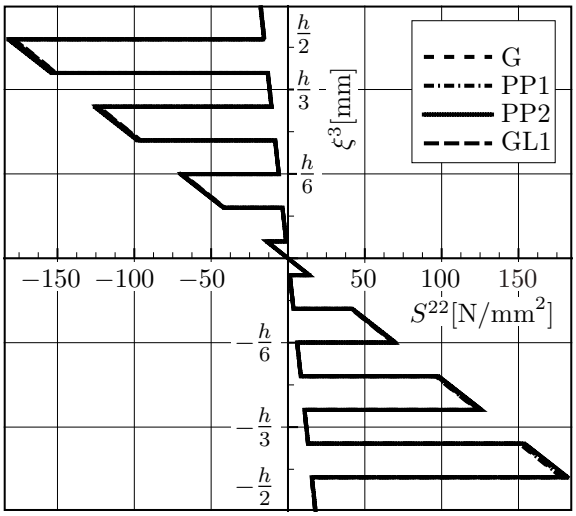

(b) S^{22} [N/mm^2]

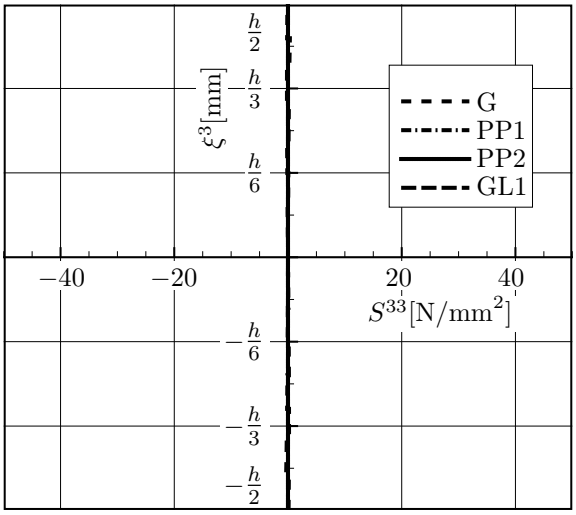

(c) S^{33} [N/mm^2]

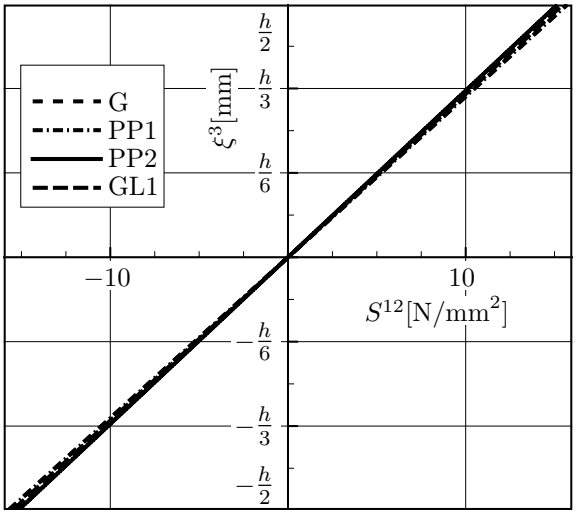

(d) S^{12} [N/mm^2]

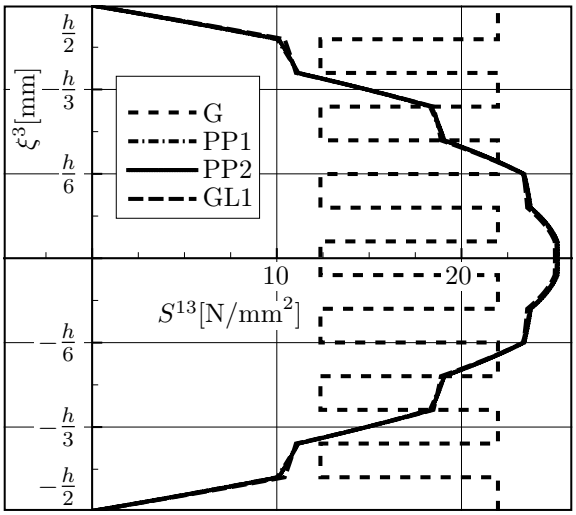

(e) S^{13} [N/mm^2]

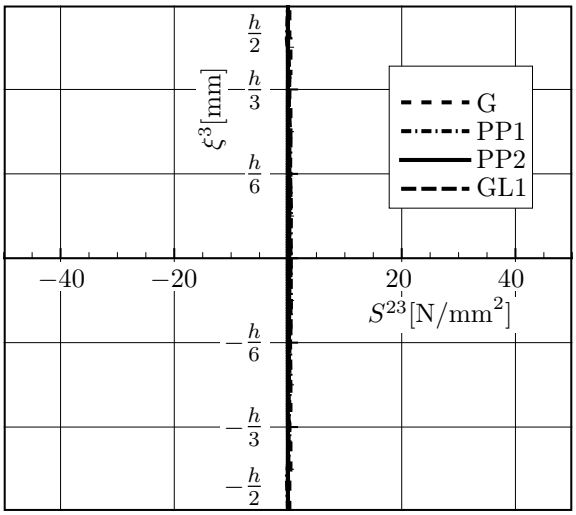

(f) S^{23} [N/mm^2]

Figure 8.18: Stresses at evaluation point ①

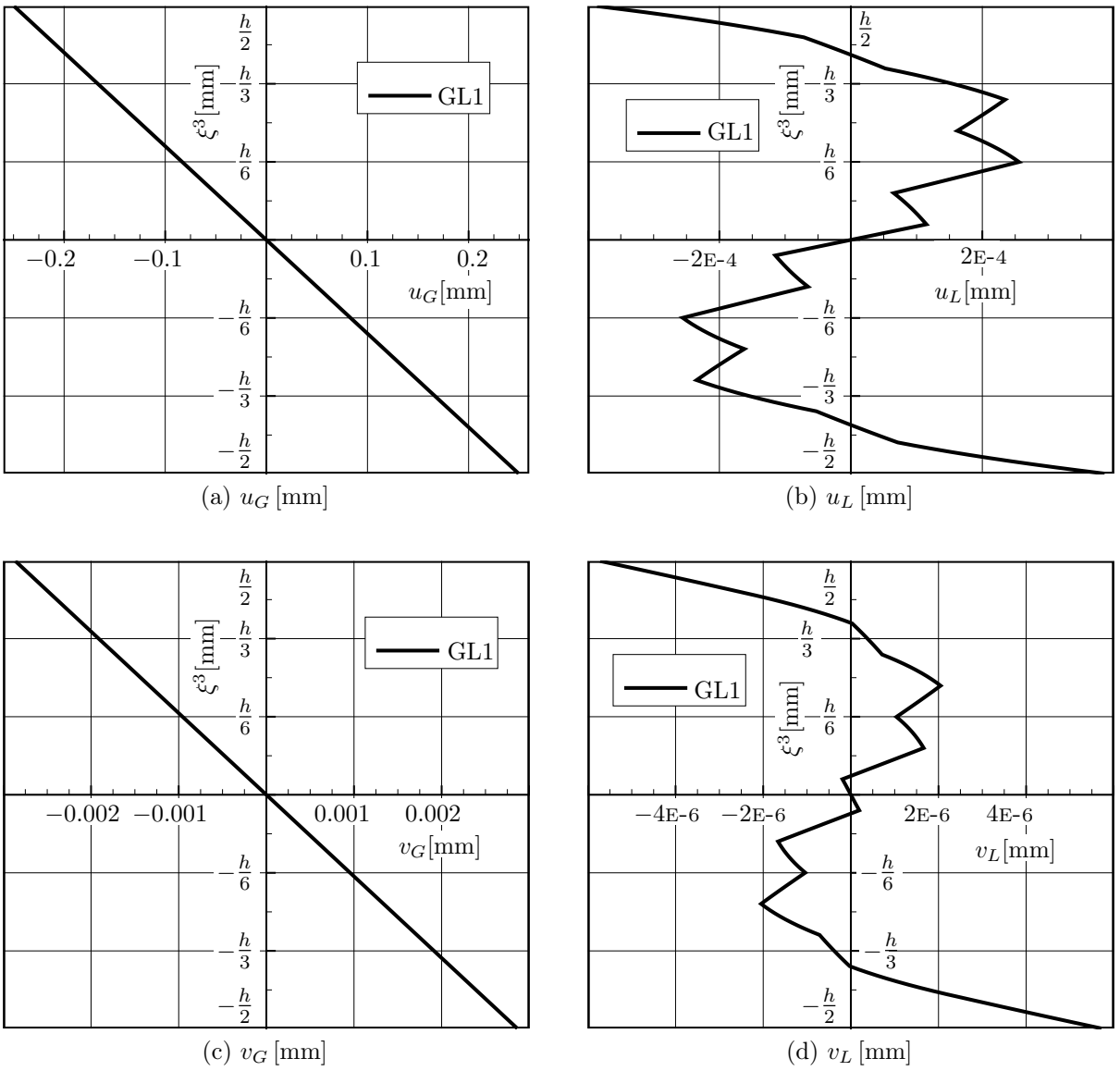

(a) u_G [mm] (b) u_L [mm]

(c) v_G [mm] (d) v_L [mm]

Figure 8.19: Displacements at evaluation point ①

Also in this example, for reasons of symmetry the simulation can be performed in a quarter of the plate with appropriate boundary conditions. When implementing the orthogonalization of the global-local finite shell element the method of least squares is used considering the special characteristics of cross-ply laminates as discussed in chapter 4.2.2. A simulation with quadratic brick elements was not performed, as the large amount of elements in thickness direction needed to derive satisfactory results exceeds the capacity of a standard desktop computer. The results of model GL2 are omitted, as they largely correspond to the results of model GL1.

Model	G	PP1	PP2	GL1
w_{max} [mm]	7.87	7.88	7.90	7.89

Table 8.5: Maximum displacement w_{max}

The results for the maximum displacement of the different models are specified in table 8.5 using the abbreviations defined in table 8.1. The largest discrepancy of the maximum displacement derived by means of the different models is less than 0.3 %. The displacements in ξ^3-direction for the plate are shown in figure 8.17a for model GL1. Additionally, the effective stress couples $\tilde{m}_{11}$, $\tilde{m}_{22}$ and $\tilde{m}_{12}$, and the effective shear stress resultants $\tilde{q}_1$ and $\tilde{q}_2$ are shown in figures 8.17b to 8.17f for the same model. Again, the three effective membrane stress resultants $\tilde{n}_{11}$, $\tilde{n}_{22}$ and $\tilde{n}_{12}$ are zero. The results for the effective stress resultants in this example using the coupled global-local model correspond to the results for the global model alone, with the shear stress resultants separated into a global and a local part. The portrayal of the separated global and local effective shear stress resultants is foregone for this example, as is the portrayal of the strains.

The results for the stresses and displacements through the thickness of the plate are presented for the same two evaluation points as the preceding example. Figures 8.18 and 8.19 show the results for evaluation point ①, while figures 8.20 and 8.21 show the results for evaluation point ②. Similar to the preceding example, at evaluation point ① the effective stress resultant $\tilde{q}_1$ shown in figure 8.17e is relatively large and the effective stress resultant $\tilde{q}_2$ shown in figure 8.17f is relatively small. It is the other way around at evaluation point ②.

The stresses are shown for evaluation point ① in figure 8.18 and for evaluation point ② in figure 8.20. Similar to the preceding example, for the specified stacking sequence there are jumps in the in-plane stresses S^{11} and S^{22} at the layer boundaries. On the other hand, the in-plane strains E_{11} and E_{22}, which are not shown, are continuous throughout the thickness of the laminate. The in-plane stress S^{12} and the in-plane strain $2E_{12}$ are continuous again, for the reason explained in the preceding example.

The interlaminar shear stresses S^{13} and S^{23} follow a piecewise quadratic path and are continuous with kinks at the layer boundaries, where the properties of the stiffness matrix change, but there are no jumps. The paths of the interlaminar shear strains $2E_{13}$ and $2E_{23}$ exhibit jumps at the layer boundaries, much like the preceding example. The results of the simulations using the global-local shell element for the interlaminar shear stresses S^{13} at evaluation point ①, shown in figure 8.18e, where the shear stress resultant $\tilde{q}_1$ is relatively large, and the interlaminar shear stress S^{23} at evaluation point ②, shown in figure 8.20f, where the shear stress resultant $\tilde{q}_2$ is relatively large, are in good agreement with the reference solution, whereas the result of the global model yields piecewise constant results with jumps at the layer boundaries. The global model is only capable of reproducing the average result through the thickness.

The piecewise quadratic paths of the interlaminar shear stresses S^{13} at evaluation point ① and S^{23} at evaluation point ② are accurately reproduced and the results equal zero at the top and bottom of the composite, which needs to be the case considering boundary conditions. The continuity at the layer boundaries is met. The effective shear stress resultants $\tilde{q}_2$ at evaluation point ① and $\tilde{q}_1$ at evaluation point ② are relatively small and, correspondingly, the interlaminar shear stresses S^{23} at evaluation point ① and S^{13} at evaluation point ② are also small, but follow a piecewise quadratic path.

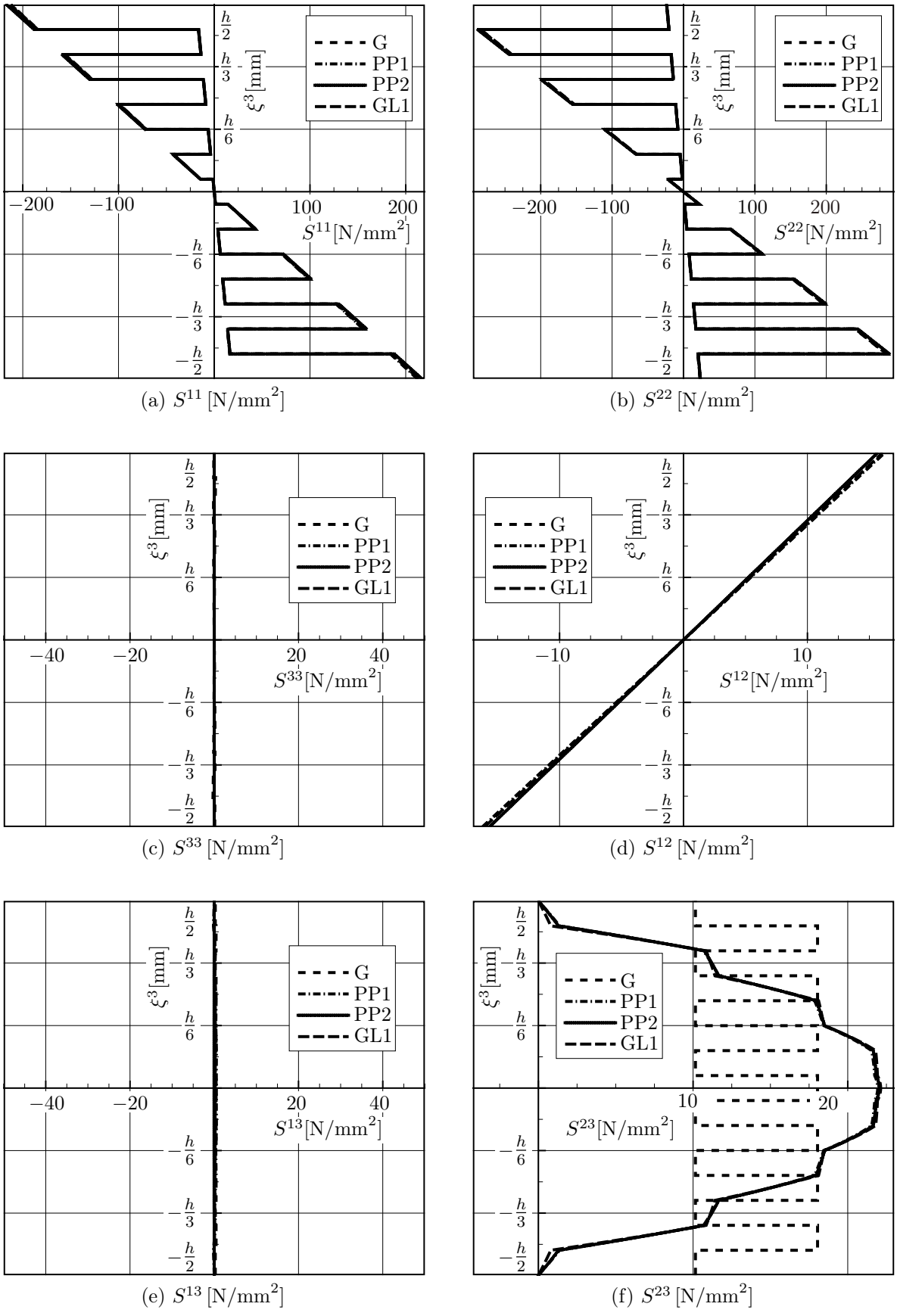

(a) S^{11} [N/mm^2] (b) S^{22} [N/mm^2]

(c) S^{33} [N/mm^2] (d) S^{12} [N/mm^2]

(e) S^{13} [N/mm^2] (f) S^{23} [N/mm^2]

Figure 8.20: Stresses at evaluation point ②

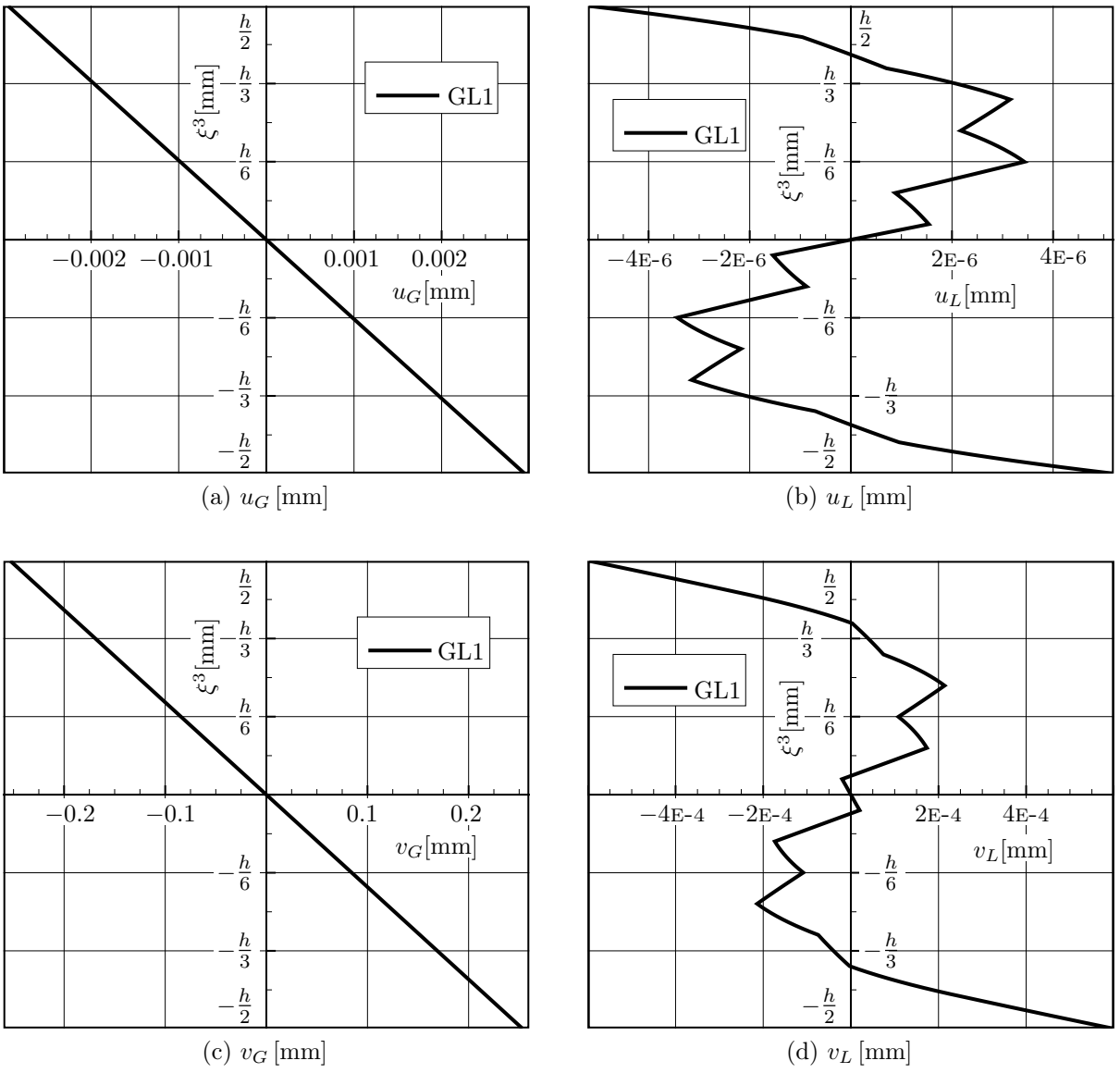

(a) u_G [mm] (b) u_L [mm]

(c) v_G [mm] (d) v_L [mm]

Figure 8.21: Displacements at evaluation point ②

Since in this example also a cross-ply laminate is considered, the qualitative paths of the interlaminar shear stresses S^{13} and S^{23} are mostly influenced by the large jumps in the stiffnesses at the layer boundaries of C^G_{11} and C^G_{22}. The paths of the two interlaminar shear stresses shown in figures 8.18e and 8.20f are characteristic of the paths of the interlaminar shear stresses in the domain of the plate, even though the quantitative values change. The inclination of the path of the interlaminar shear stress S^{13} is smaller in layers with a fiber orientation of 0° than in layers with a fiber orientation of 90°. On the other hand, the inclination of the path of the other interlaminar shear stress S^{23} is larger in layers with a fiber orientation of 0° than in layers with a fiber orientation of 90°. This example shows that the more layers are present in the composite shell, the better the paths of the interlaminar shear stresses can be approximated by quadratic parables. Thus, the orthogonalization procedure with two parameters for a homogeneous shell introduced in chapter 4.2.1 is capable to yield satisfactory predictions of peaks in the interlaminar shear stresses.

The remarks regarding the interlaminar normal stress S^{33} in connection with the previous example also hold for this example. When using the global-local shell element with its piecewise functions through the thickness, the results for the interlaminar normal stress S^{33} depicted in figures 8.18c and 8.20c are zero through the thickness of the plate. When using the global shell element, the results are approximately zero for numerical reasons.

In figures 8.19 and 8.21, plots are shown of the global and local in-plane displacements introduced in (4.14). Similar to the preceding examples, the global displacements are several orders of magnitude larger than the local displacements. The global in-plane displacements follow a linear path. The addition of the local model is needed in order to derive warping of the cross section and hence also the interlaminar shear stresses.

The results for the local displacements follow a piecewise cubic path through the thickness of the plate with kinks at the layer boundaries, because the highest order terms in the ansatz functions are cubic. The paths of the local in-plane displacements thus take a zig-zag form. The condition of continuity at the layer boundaries is fulfilled. For evaluation point ①, the local displacement u_L shown in figure 8.19b corresponds to the interlaminar shear stress S^{13} depicted in figure 8.18e, while the local displacement v_L shown in figure 8.19d corresponds to the interlaminar shear stress S^{23} depicted in figure 8.18f. As the local displacement u_L at evaluation point ① is several orders of magnitude larger than the local displacement v_L, the interlaminar shear stress S^{13} is larger than the interlaminar shear stress S^{23}. In the same way, for evaluation point ②, the local displacement u_L shown in figure 8.21b corresponds to the interlaminar shear stress S^{13} depicted in figure 8.20e, while the local displacement v_L shown in figure 8.21d corresponds to the interlaminar shear stress S^{23} depicted in figure 8.20f. At evaluation point ② the local displacement v_L is several orders of magnitude larger than the local displacement u_L, and therefore the interlaminar shear stress S^{23} is larger than the interlaminar shear stress S^{13}.

The third inhomogeneous example is an angle-ply laminate with three layers and a stacking sequence of $[45°/-45°/45°]$. Unlike the preceding examples, the simulation of this example cannot be performed in a quarter of the plate. The results for the maximum displacement of the different models are specified in table 8.6 using the abbreviations defined in table 8.1. The largest discrepancy of the maximum displacement is less than 1.6 %.

Model	QB	G	PP1	PP2	GL1
w_{max} [mm]	7.25	7.14	7.19	7.23	7.20

Table 8.6: Maximum displacement w_{max}

The procedure for special stacking sequences applied to angle-ply laminates as discussed in chapter 4.2.2 with the parameters $\alpha = 1.5$ and $\beta = 10$ is used in the orthogonalization of the global-local finite shell element. This orthogonalization procedure yields the best results, as the two other procedures, the method of least squares and the summation procedure, both using the special properties of angle-ply laminates, are not able to capture the varying qualitative path of the interlaminar shear stresses.

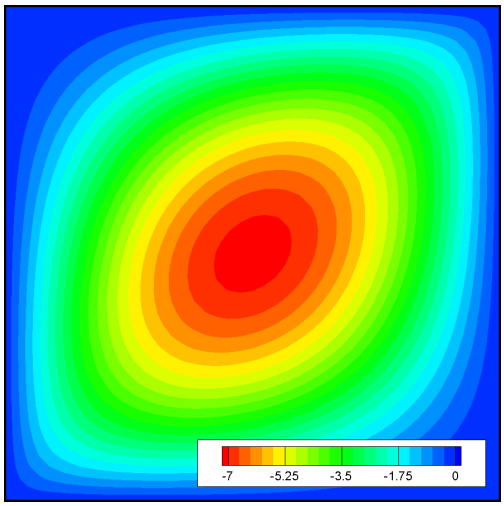

(a) w [mm]

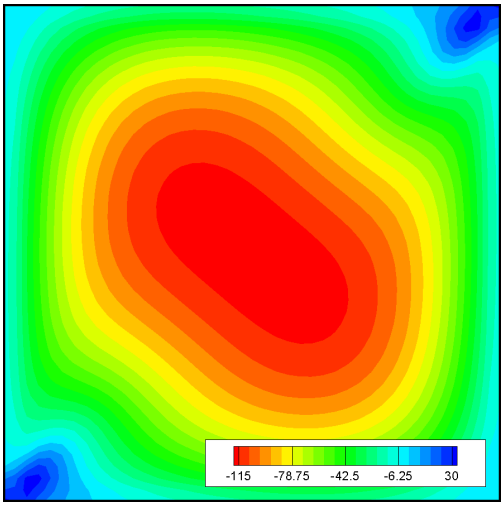

(b) $\tilde{m}_{11}$ [Nmm/mm]

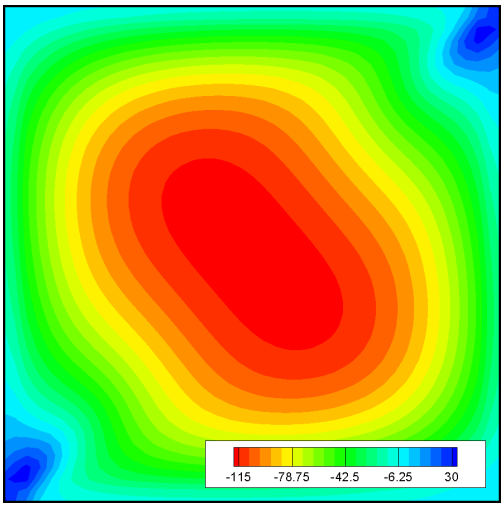

(c) $\tilde{m}_{22}$ [Nmm/mm]

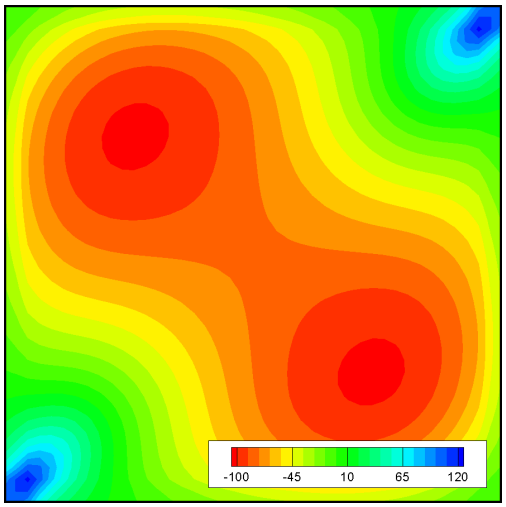

(d) $\tilde{m}_{12}$ [Nmm/mm]

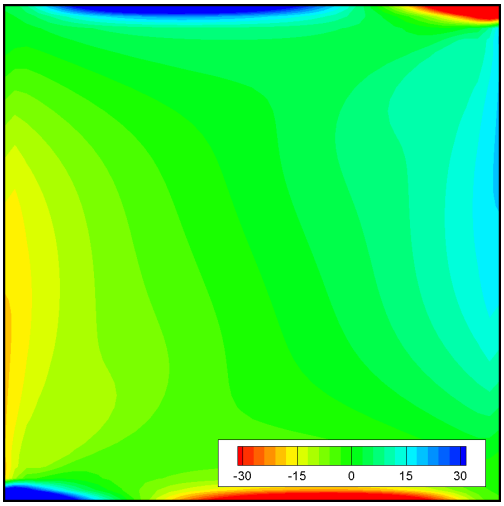

(e) $\tilde{q}_1$ [N/mm]

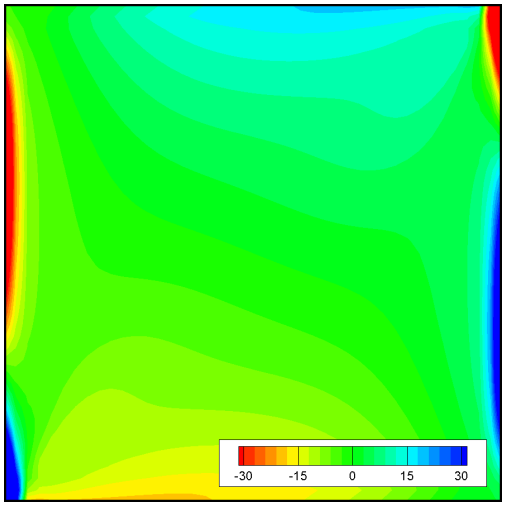

(f) $\tilde{q}_2$ [N/mm]

Figure 8.22: Out-of-plane displacement and effective stress resultants

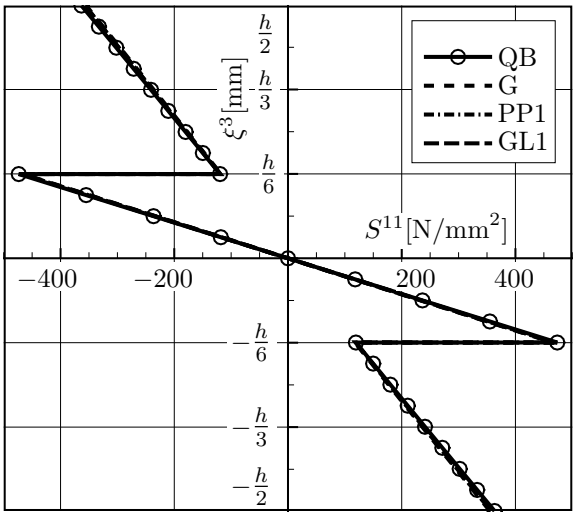

(a) S^{11} [N/mm^2]

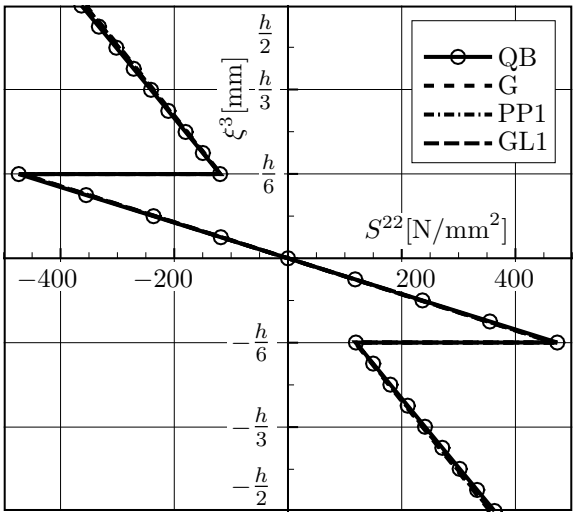

(b) S^{22} [N/mm^2]

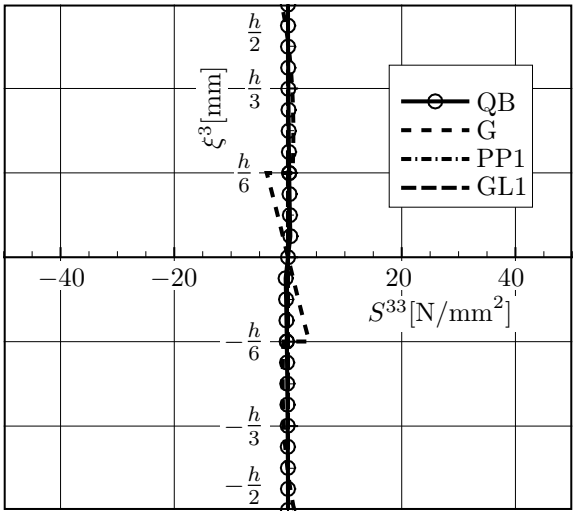

(c) S^{33} [N/mm^2]

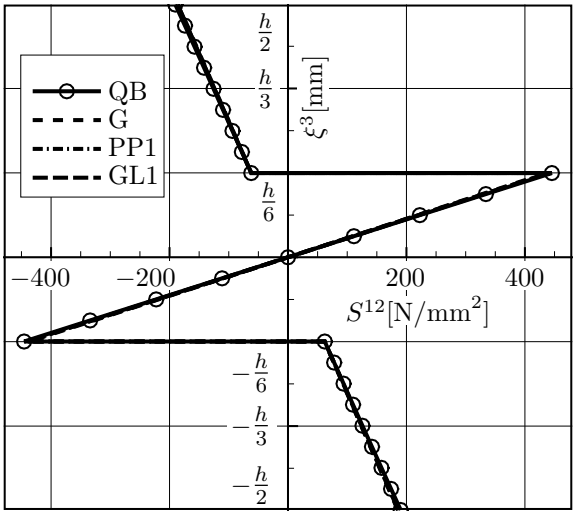

(d) S^{12} [N/mm^2]

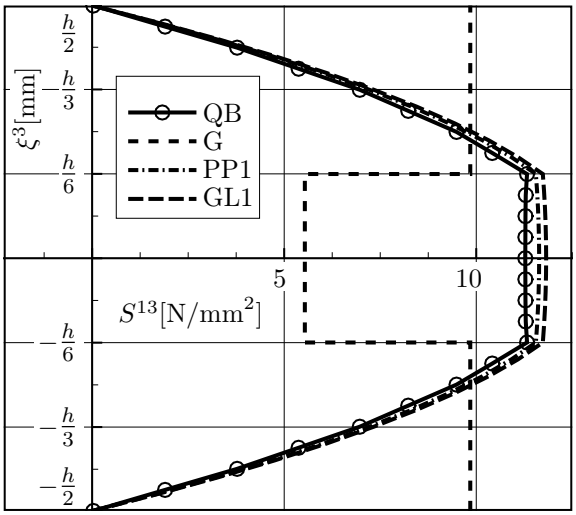

(e) S^{13} [N/mm^2]

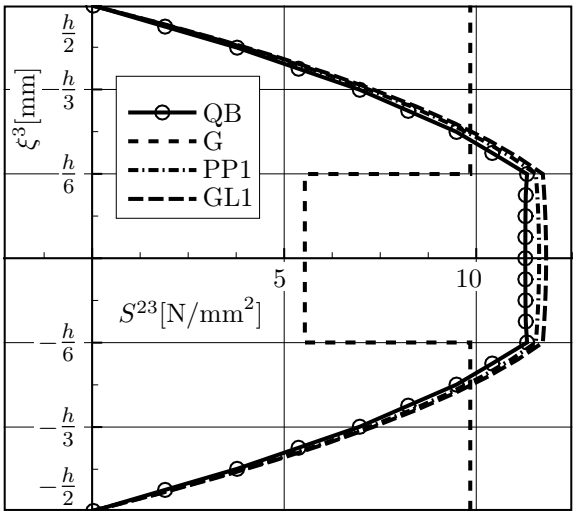

(f) S^{23} [N/mm^2]

Figure 8.23: Stresses at evaluation point ⑤

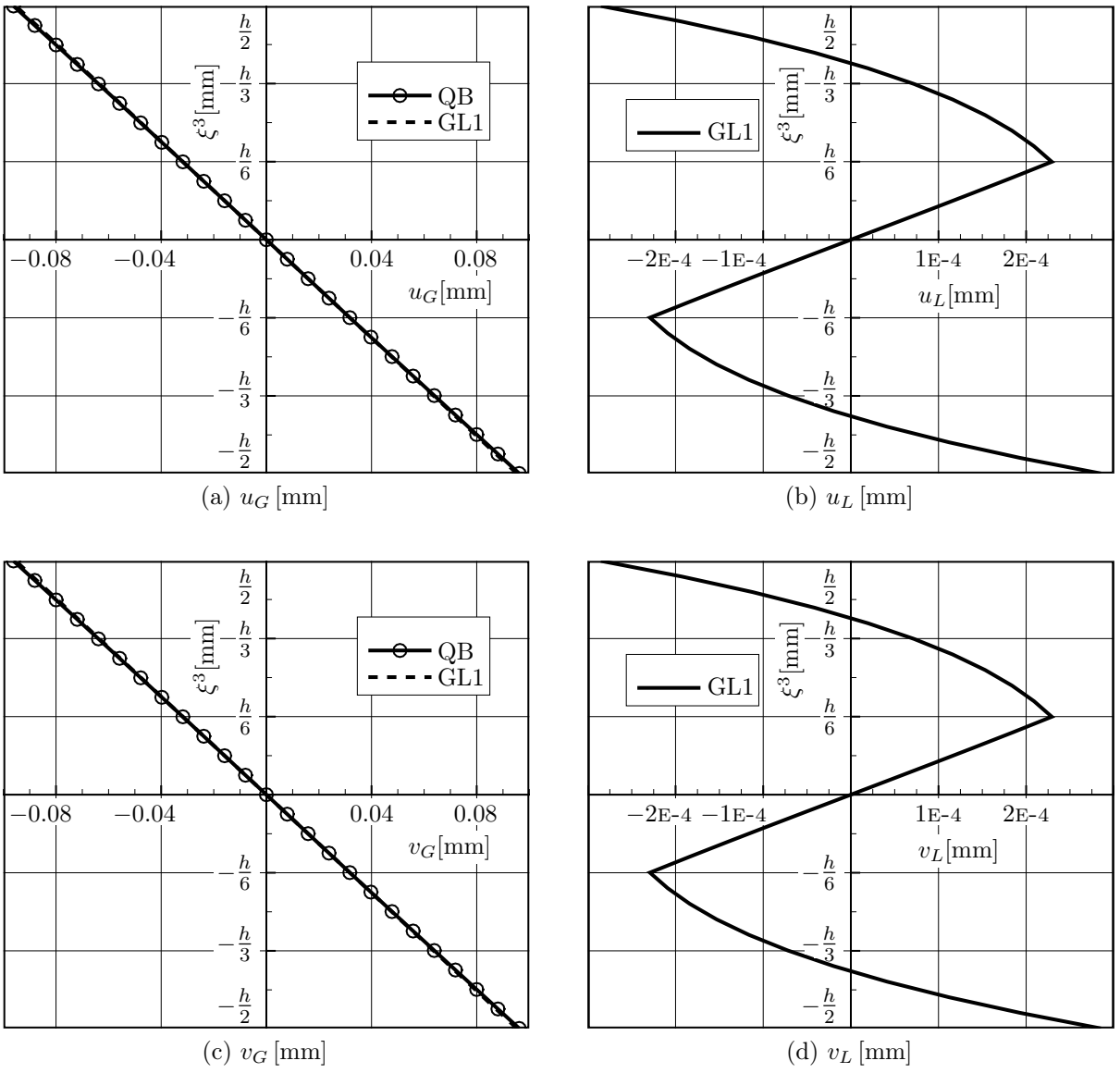

(a) u_G [mm] (b) u_L [mm]

(c) v_G [mm] (d) v_L [mm]

Figure 8.24: Displacements at evaluation point ⑤

Rather, these procedures yield results that are correct on an average and the qualitative path of the results for the interlaminar shear stresses resembles the qualitative path of the results for evaluation point ⑤ in figures 8.23e and 8.23f.

The displacements in the ξ^3-direction for the plate are shown in figure 8.22a for model GL1. Additionally, the effective stress couples $\tilde{m}_{11}$, $\tilde{m}_{22}$ and $\tilde{m}_{12}$, and the effective shear stress resultants $\tilde{q}_1$ and $\tilde{q}_2$ are shown in figures 8.22b to 8.22f for the same model. Again, the three effective membrane stress resultants $\tilde{n}_{11}$, $\tilde{n}_{22}$ and $\tilde{n}_{12}$ are zero.

The results for the effective stress resultants using the coupled global-local model correspond to the results of the global model, with the shear stress resultants separated into a global and a local part. The illustration of the separated global and local effective shear stress resultants is foregone for this example, as is the illustration of the strains.

The results for the stresses through the thickness of the plate are shown for three different evaluation points, while the results for the in-plane displacements are only shown for one

evaluation point. Figures 8.23 and 8.24 show the results of the stresses and displacements for evaluation point ⑤, while figures 8.25 and 8.26 show the results for the stresses at evaluation points ③ and ④. Evaluation point ⑤ lies on the diagonal between the top right and bottom left corners of the plate, while evaluation points ③ and ④ lie in the same distance to evaluation point ⑤ on a line perpendicular to the diagonal.

The paths of the in-plane stresses S^{11}, S^{22}, and S^{12} at all three evaluation points have jumps at the layer boundaries, as shown in figures 8.23, 8.25, and 8.26. On the other hand, the in-plane strains E_{11}, E_{22}, and $2E_{12}$, which are not shown, are continuous throughout the thickness of the laminate. It is noted, that in the previous examples of cross-ply laminates there are no jumps in the in-plane shear stress S^{12}. The reason for the jumps in this example is, that, unlike the previous example, the values of C^G_{14}, C^G_{24}, C^G_{41}, and C^G_{42} are not zero and change from one layer to the next.

The out-of-plane shear stresses S^{13} and S^{23} follow a piecewise quadratic path and are continuous with kinks at the layer boundaries, while the interlaminar shear strains $2E_{13}$ and $2E_{23}$ exhibit jumps at the layer boundaries, much like the preceding examples. The interlaminar shear stress S^{13} depicted in figures 8.23e, 8.25e, and 8.26e and the interlaminar shear stress S^{23} depicted in figures 8.23f, 8.25f, and 8.26f at the specified evaluation points derived by means of the global-local model are in good agreement with the reference solution, whereas the results of the global model yield piecewise constant results with jumps at the layer boundaries. As in the previous examples, the global model is merely capable of reproducing the average result through the thickness. In the global-local model, the piecewise quadratic paths of the interlaminar shear stresses are accurately reproduced and the results equal zero at the top and bottom of the composite due to boundary conditions. The continuity at the layer boundaries is met.

Unlike the previous examples of cross-ply laminates, no characteristic qualitative path of the interlaminar shear stresses can be specified. In this example, the qualitative path of the interlaminar shear stresses strongly varies within the domain. The diagonal on which evaluation point ⑤ lies can be seen as a symmetry axis for the results of the interlaminar shear stresses at evaluation points ③ and ④. The paths of the interlaminar shear stresses S^{13} depicted in figure 8.23e and S^{23} depicted in figure 8.23f at evaluation point ⑤ are exactly the same. On the other hand, the interlaminar shear stress S^{13} at evaluation point ③ shown in figure 8.25e has the same values as S^{23} at evaluation point ④ shown in figure 8.26f, and the interlaminar shear stress S^{23} at evaluation point ③ shown in figure 8.25f has the same values as S^{13} at evaluation point ④ shown in figure 8.26e.

The comments regarding the interlaminar normal stress S^{33} made in the previous examples also hold for this example. The results with the global-local shell element depicted in figures 8.23c, 8.25c, and 8.26c are zero through the thickness of the plate. Just like in the preceding example, this result is achieved exactly by the global-model and its piecewise functions through the thickness, while it is only approximately achieved with the global model.

In figure 8.24 plots are shown of the global and local in-plane displacements introduced in (4.14) for evaluation point ⑤ on the diagonal. The illustrations of the displacements at evaluation points ③ and ④ is foregone here.

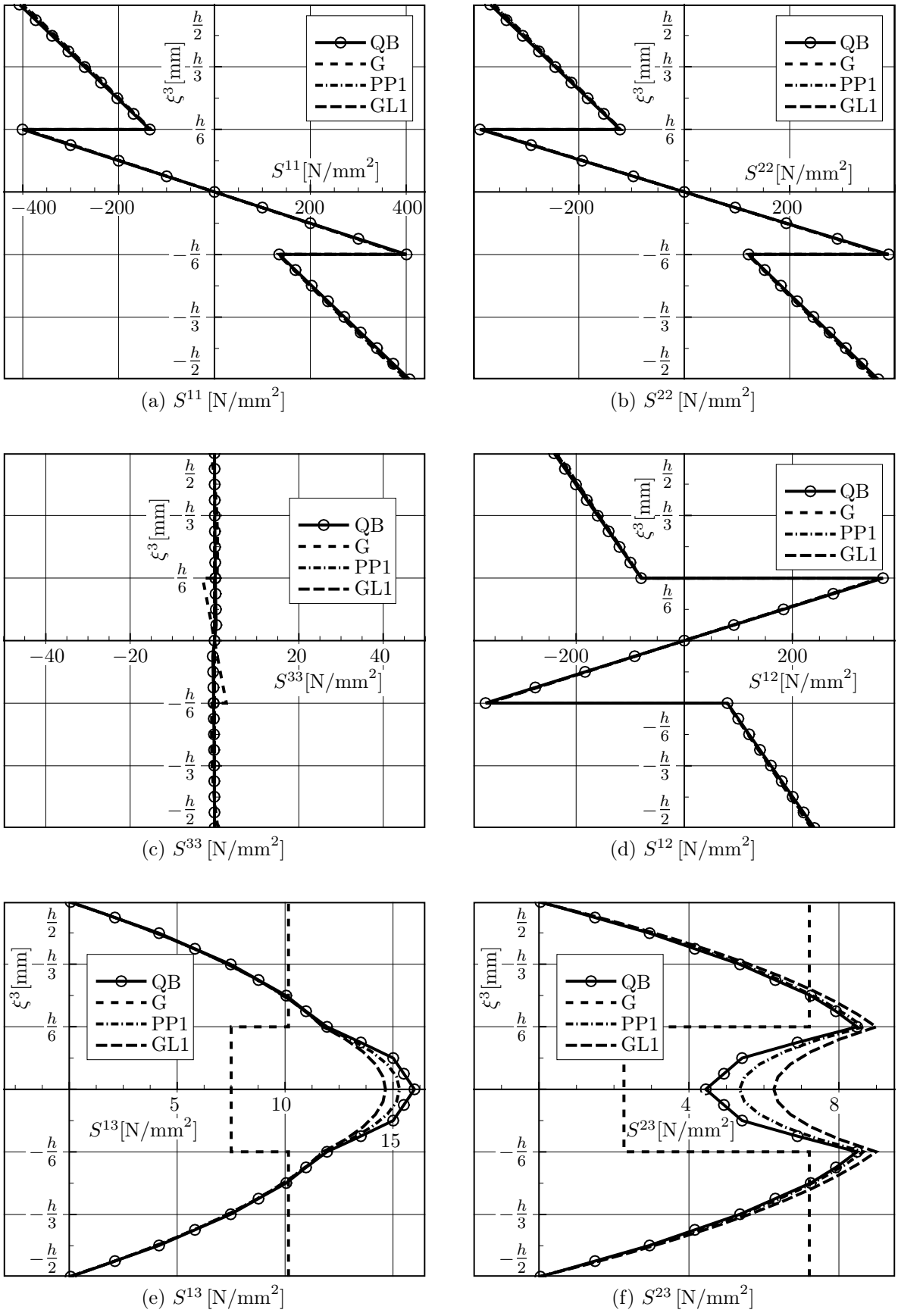

(a) S^{11} [N/mm^2] (b) S^{22} [N/mm^2]

(c) S^{33} [N/mm^2] (d) S^{12} [N/mm^2]

(e) S^{13} [N/mm^2] (f) S^{23} [N/mm^2]

Figure 8.25: Stresses at evaluation point ③

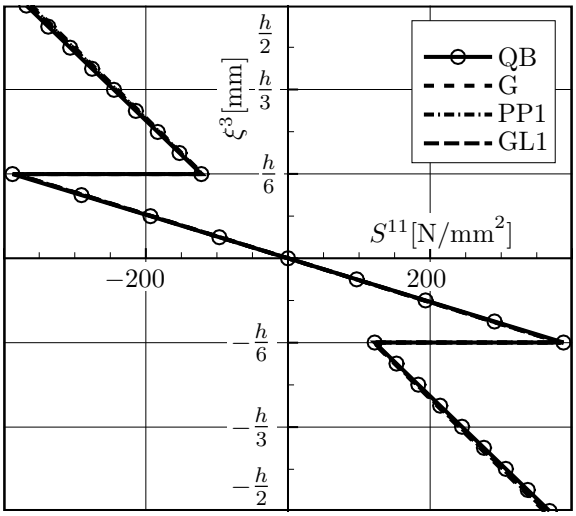

(a) S^{11} [N/mm^2]

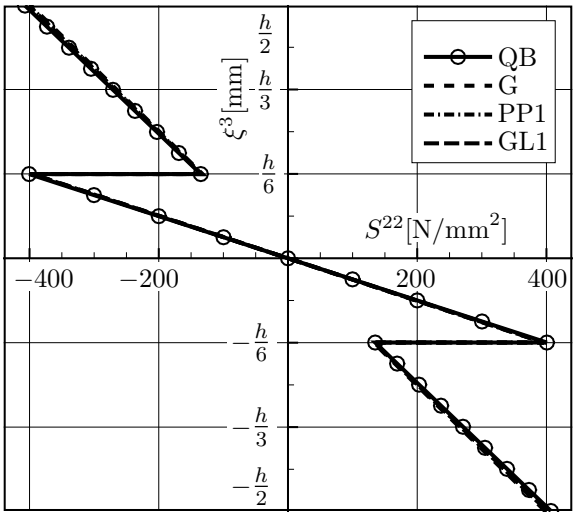

(b) S^{22} [N/mm^2]

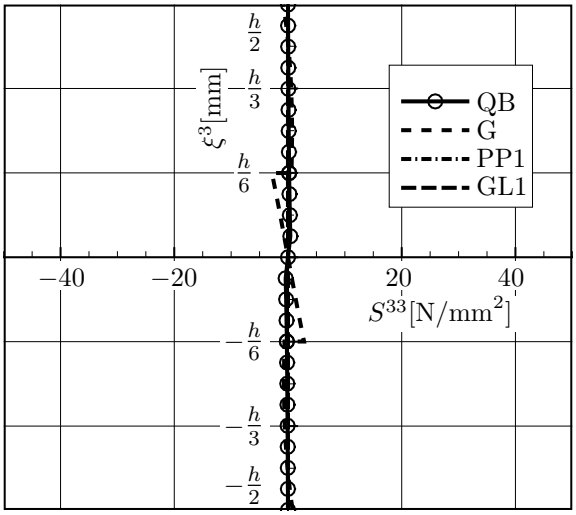

(c) S^{33} [N/mm^2]

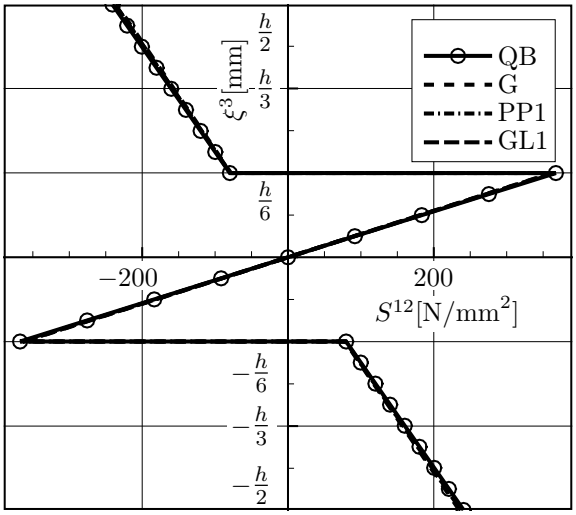

(d) S^{12} [N/mm^2]

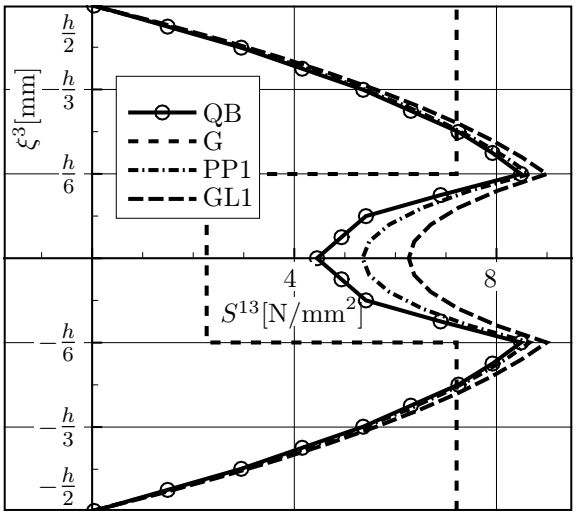

(e) S^{13} [N/mm^2]

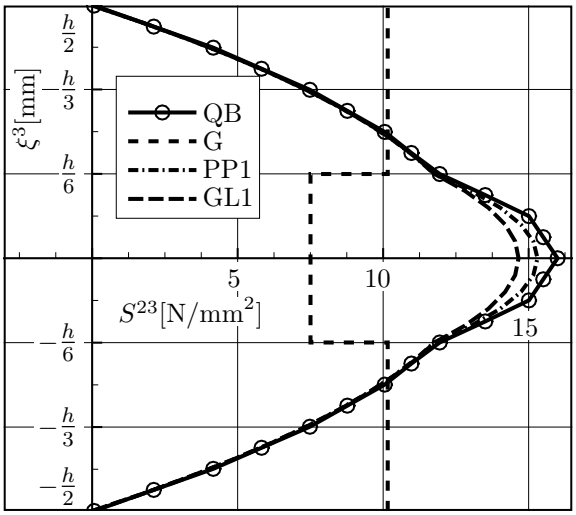

(f) S^{23} [N/mm^2]

Figure 8.26: Stresses at evaluation point ④

Similar to the preceding examples, the global displacements are several orders of magnitude larger than the local displacements. The global in-plane displacements follow a linear path, which is correctly computed with the help of the global model alone. The addition of the local model however is needed in order to derive warping of the cross section and hence also the interlaminar shear stresses. The results for the local displacements follow a piecewise cubic path through the thickness of the plate with kinks at the layer boundaries. The condition of continuity at the layer boundaries is fulfilled. The local displacement u_L shown in figure 8.24b corresponds to the interlaminar shear stress S^{13} depicted in figure 8.23e, while the local displacement v_L shown in figure 8.24d corresponds to the interlaminar shear stress S^{23} depicted in figure 8.23f. As the local displacement u_L at evaluation point ⑤ follows exactly the same path as the local displacement v_L the paths of the interlaminar shear stresses S^{13} and S^{23} are exactly the same.

The presented examples demonstrate the contribution of the local shell model to derive the complete three-dimensional stress state and the capabilities of the enhanced FSDT model to compute the interlaminar shear stresses.

8.1.2 Cylindrical shell

As a further example, a cylindrical fiber-reinforced composite shell is introduced. For symmetry reasons, the computation is conducted on one quarter of the shell, as depicted in figure 8.27, which also shows the coordinate system, boundary conditions and loading. The length of the cylindrical shell is $l = 300\,\text{mm}$ and its radius amounts to $r = 100\,\text{mm}$. Its thickness is $h = 10\,\text{mm}$. The cylindrical shell is subjected to a concentrated load of $F = 10\text{kN}$. The reference plane lies in the middle of the shell and separates it into two halves with the same thickness. An evaluation point ① is chosen to lie close to the point of load application. The coordinates are $x = 15.64$, $y = 10.00$, and $z = 98.75$. The material parameters correspond to those of the preceding example defined in (8.1).

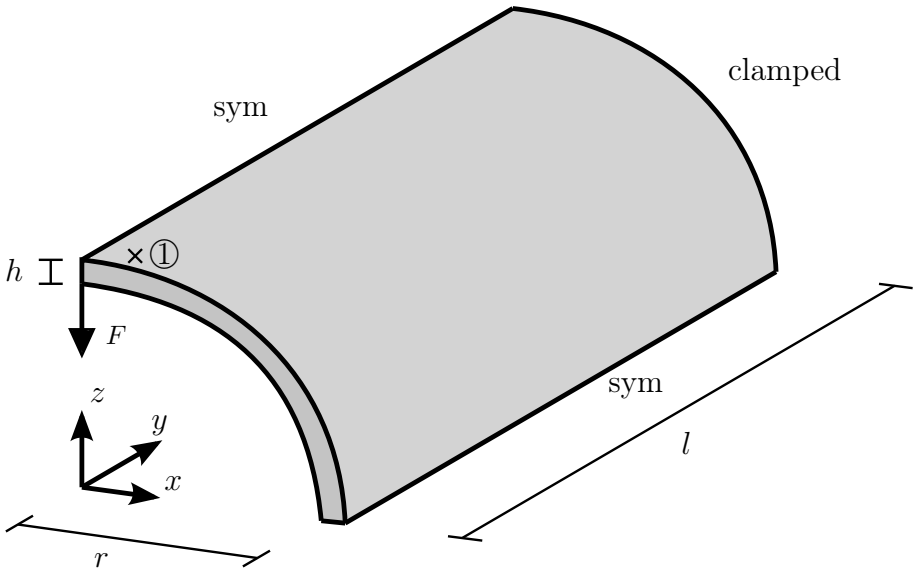

Figure 8.27: Cylindrical shell

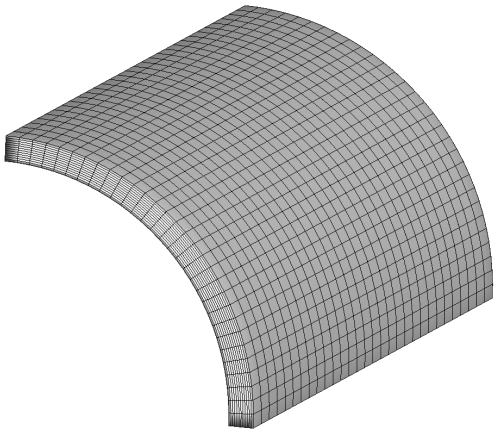

(a) Discretization with solid shell elements

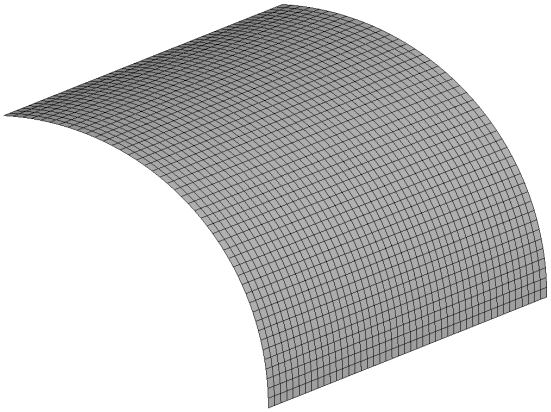

(b) Discretization with shell elements

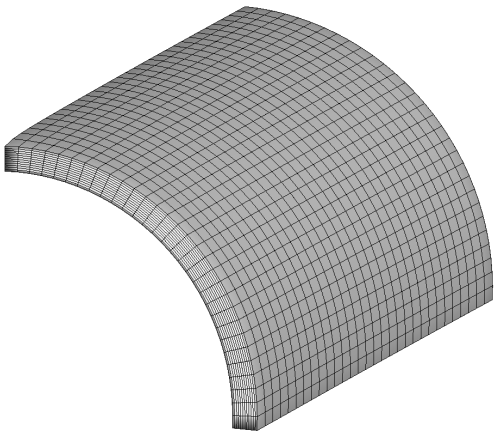

(c) Deformed shell with solid shell elements

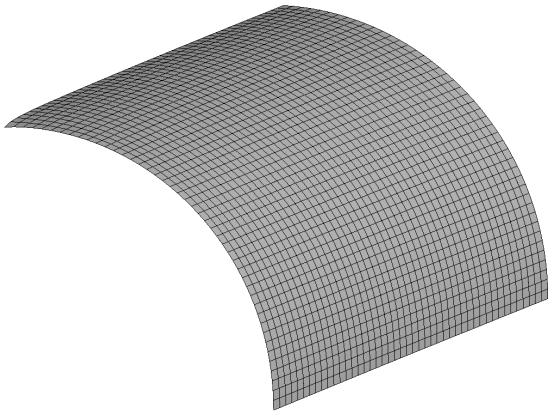

(d) Deformed shell with 2-d shell elements

Figure 8.28: Discretizations of the shell and qualitative representation of the deformed shell

The composite shell consists of three layers and a stacking sequence of $[0°/90°/0°]$. As a reference solution a solid shell element is used [70]. The abbreviations defined in table 8.1 are still valid. Additionally, an abbreviation is introduced for the solid shell element (SS). The reference solution is compared to the results of a simulation carried out using the global shell element discussed in chapter 3, including independent thickness strains as introduced in [71] and the elementwise constant global-local shell element as discussed in chapters 4 and 5. As an orthogonalization procedure the method of least squares is used considering the special characteristics of cross-ply laminates as discussed in chapter 4.2.2.

The discretizations with three-dimensional solid shell elements and two-dimensional elements are shown in figure 8.28. In simulations with three-dimensional elements the shell is discretized with 30x30x12 elements, as illustrated in figure 8.28a. Figure 8.28b shows the discretization of 45x45 with two-dimensional shell elements. The computation with solid shell elements takes much longer, as a large number of elements has to be used in thickness direction in order to receive acceptably accurate results. Evaluation point ① lies on a node of the mesh when the cylindrical shell is discretized with solid shell elements, but it lies in the element center when it is discretized with two-dimensional shell elements. A qualitative representation of the deformed state of the cylindrical shell is given for the solid shell elements in figure 8.28c and for two-dimensional shell elements in 8.28d.

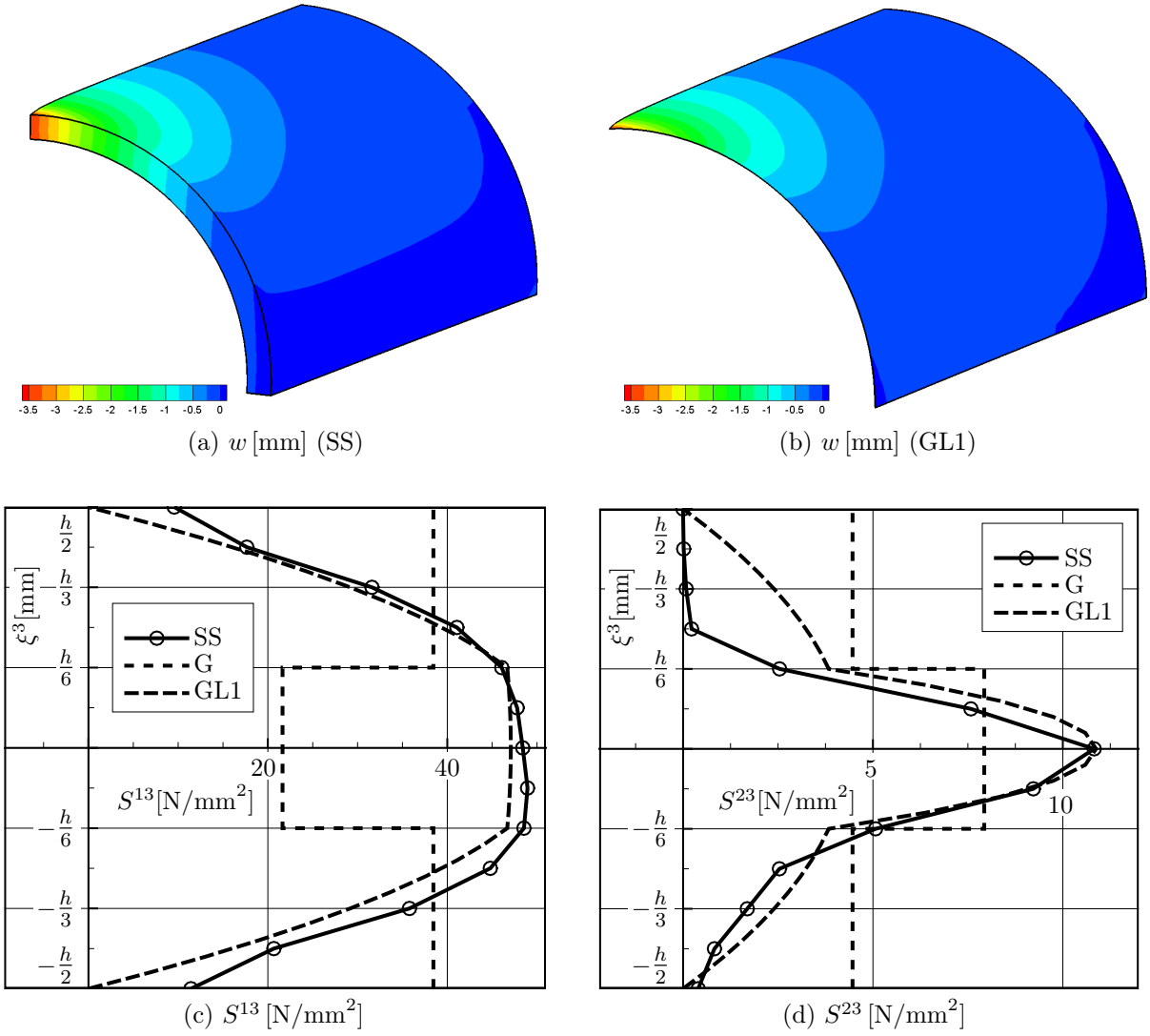

(a) w [mm] (SS) (b) w [mm] (GL1)

(c) S^{13} [N/mm^2] (d) S^{23} [N/mm^2]

Figure 8.29: Displacements and interlaminar shear stresses at evaluation point ①

There is a visible lowering at the point of load application. The results for the maximum displacement in z-direction, denoted by w, at the point of load application of the different models are specified in table 8.7.

Model	SS	G	GL1
w_{max} [mm]	3.51	3.40	3.47

Table 8.7: Maximum displacement w_{max} at point of load application

The results of the different element models show good agreement, with the largest discrepancy being less than 3.3 %. Contour plots of the displacements w are shown in figure 8.29a when using the solid shell element and in 8.29b when using the global-local shell element.

For evaluation point ① defined in figure 8.27, the results of the interlaminar shear stresses are depicted in figures 8.29c and 8.29d. The interlaminar shear stresses S^{13} and S^{23} follow

a piecewise quadratic path and are continuous at the layer boundaries, where the properties of the stiffness matrix changes. This is correctly computed by both the solid shell element and the global-local shell element. The global model yields piecewise constant results with jumps at the layer boundaries. It is able to produce the displacements and stress resultants, but is not able to reproduce the correct path of the interlaminar shear stresses. This example further illustrates the capabilities of the global-local shell model.

8.1.3 Thin-walled structures

In this section, the performance of the shell element is demonstrated by some geometrically nonlinear examples. The simulations were conducted as part of the joint research project dealing with load bearing analysis of thin-walled structures such as box beams and double T-girders.

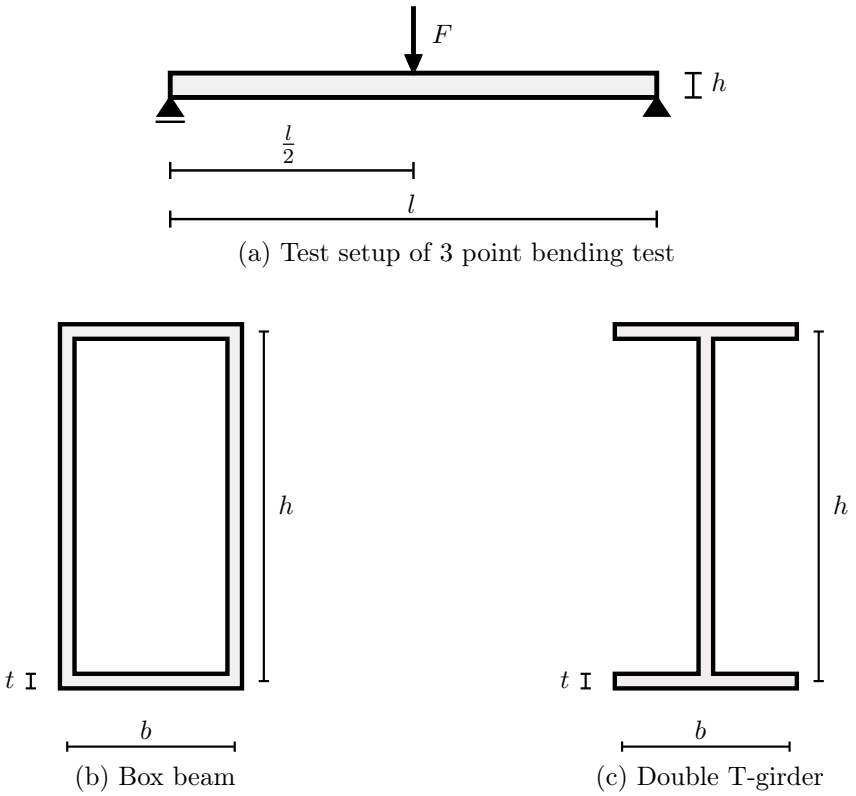

(a) Test setup of 3 point bending test

(b) Box beam

(c) Double T-girder

Figure 8.30: Test setup and cross sections

In the research work a three-point bending system of a beam with a box or a double T cross section was to be investigated. The test setup is illustrated in figure 8.30a, while qualitative representations of the cross sections are given in figures 8.30b and 8.30c. Due to their geometric characteristics, the cross sections of thin-walled structures can be distorted and the structures themselves may buckle. Carrying out stability analysis is therefore indispensable in a complete analysis of the behavior of a thin-walled structure. To carry out the analysis, the box beams or double T-girders are discretized with shell elements and geometrically nonlinear simulations are performed. Different thicknesses of the web

and flange and different stacking sequences are studied. The simulations help to identify critical loads and critical geometries that lead to buckling.

The material parameters are the same as in the preceding examples and are specified in (8.1). The dimensions of the box beam and double T-girder were established in collaboration with the partner projects. For the following simulations with the box beam, the length of the beam is $l = 2000\,\text{mm}$, and a force acts perpendicular to the beam at the middle of the beam. The cross section is $b = 100\,\text{mm}$ wide and $h = 200\,\text{mm}$ high. Different alternatives 1a, 1b, 2a, 2b and 3 are specified in table 8.8. The alternatives differ in the thickness denoted by t of the web and the flange and their stacking sequences.

Alt.	Component	Stacking sequence [°]	t[mm]
1a	Web	$[45/-45/45/-45/45/-45/45/-45/45/-45]_s$	5
	Flange	$[45/-45/45/-45/45/-45/45/-45/45/-45/0]_s$	10
1b	Web	$[45/-45/45/-45/45/-45/45/-45/45/-45]_s$	5
	Flange	$[45/-45/45/-45/45/-45/45/-45/45/-45/0]_s$	15
2a	Web	$[45/-45/45/-45]_s$	5
	Flange	$[45/-45/45/-45/0]_s$	10
2b	Web	$[45/-45/45/-45]_s$	5
	Flange	$[45/-45/45/-45/0]_s$	15
3	Web	$[45/-45/45/-45]_s$	5
	Flange	$[45/-45/45/-45/-45/45/-45/45/0]$	10

Table 8.8: Alternative thicknesses and stacking sequences of the components of the box beam

In the webs, whose function is to absorb the shear forces, layers with a fiber orientation of $[\pm 45°]$ are arranged. A layer with a fiber orientation of $[0°]$ is included in the flange because in it, mainly tension and compressive forces are to be absorbed. In alternatives 1 and 2 this layer is located in the middle of the flange, while in alternative 3 it is placed at the bottom of the flange.

When discretizing the box beam, the symmetry of the system is taken advantage of. The discretization can be gleaned from the illustrations. In the simulation, the support is located at the bottom of the box beam at the short edge of the bottom flange, while the load is applied at the top of the box beam at the opposite short edge of the top flange. Apart from the first example illustrated in figure 8.31, at the supports and at the point of application of the load a stiffener is integrated. The arc-length method[13] is used to solve the systems of equations when conducting the simulations. It is especially suitable to be used in geometrically nonlinear analysis to predict the load-displacement response, because it performs better than ordinary solution techniques near limit and bifurcation points and can handle snap-back and snap-through of the solution curve. A number of different versions of the arc-length method are implemented in FEAP [118, 132]. For the

[13] For theoretical background on the arc-length method, see for example [130, 133].

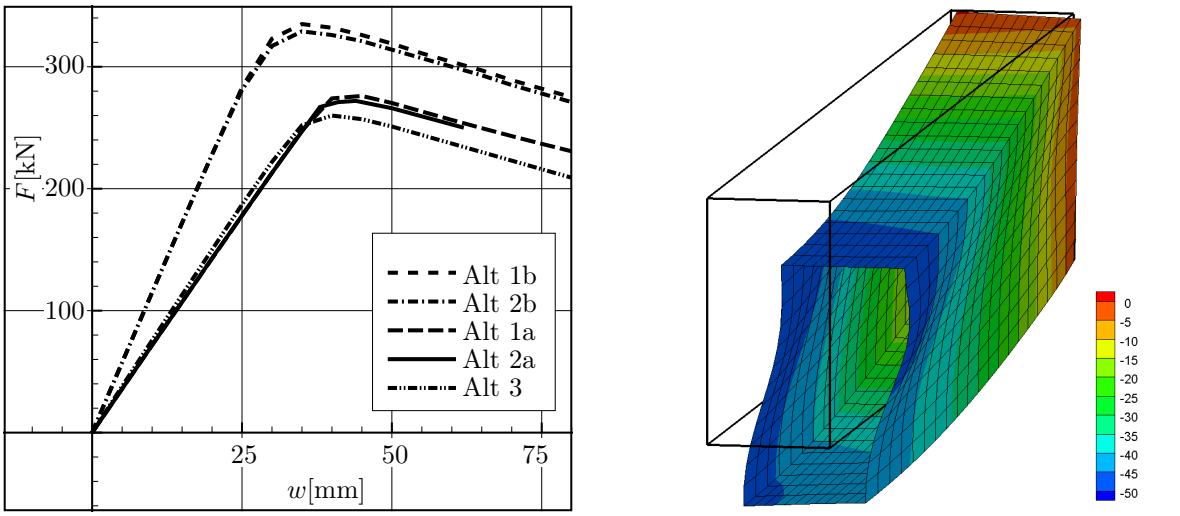

(a) Load deflection curve

(b) Contour plot of w[mm] for alternative 2a

Figure 8.31: Load deflection curve and deformation figure

examples shown in figures 8.31 and 8.32, a displacement controlled version based on a full Newton solution is employed.

The load deflection curve and deformation figure for the box beam are shown in figure 8.31 for simulations without a stiffener. In the load deflection curve shown in figure 8.31a the load is denoted by F and the deflection w is the displacement in the direction of the load. At the beginning of the simulation, the load deflection curve follows a linear path, but when the highest point is reached, it becomes strongly nonlinear. In the beginning larger load steps can be computed, while in the nonlinear part of the simulation, small load steps are required to find a solution and to reach a state of equilibrium. In the cases of the two box beams with the thicker flanges (alternatives 1b and 2b) the ultimate load that can be absorbed is higher than in the cases of the three box beam girders with thinner flanges (alternatives 1a, 2a and 3). A so-called disturbance force is used to reach the sloping curve paths.

The deformation figure with a contour plot of the displacements w in the direction of the applied load in figure 8.31 for alternative 2a shows half of the box beam at the point of highest load. The support is in the back and the point of the load's application is in the front. The black edges without contour show the original position of the box beam. The warping of the cross section, with no stiffener present, can be clearly seen.

In figure 8.32 the load deflection curve and deformation figure for the box beam with stiffeners are shown. The ultimate load reached is significantly higher when stiffeners are present. When the simulations begin, the load deflection curve follows a linear path, but when the ultimate load is reached it becomes strongly nonlinear. In the cases of the two box beams with the thicker flanges (alternatives 1b and 2b), the ultimate load that can be absorbed is higher than in the cases of the three box beam girders with thinner flanges (alternatives 1a, 2a and 3). The deformation figure shown in figure 8.32 for alternative 2a shows half of the box beam at the point of highest load, with the support being in the back and the point of application of the load in the front. The black edges without contour

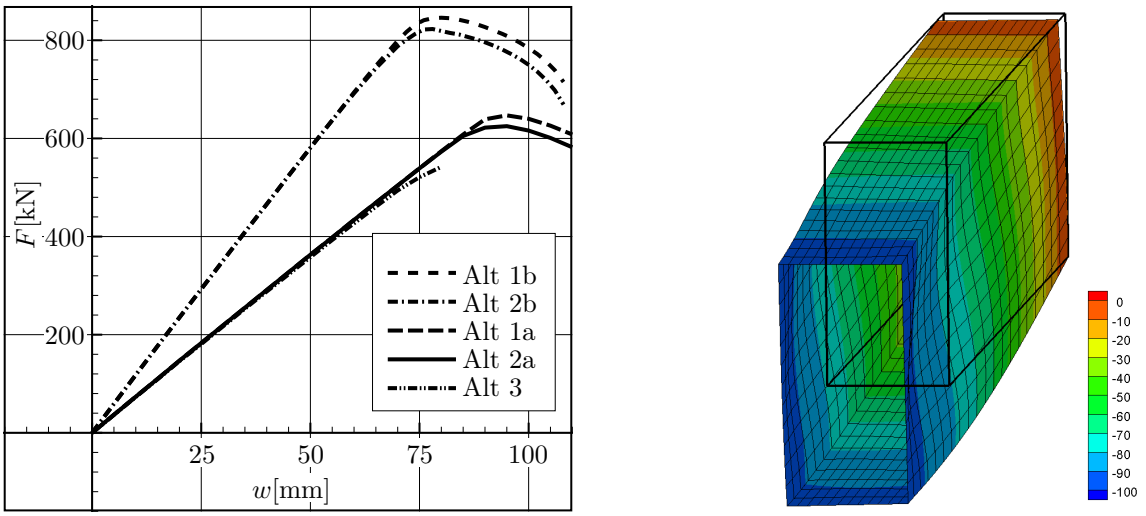

(a) Load deflection curve

(b) Contour plot of w[mm] for alternative 2a

Figure 8.32: Load deflection curve and deformation figure

show the original position of the box beam. The stiffener at the point of load application is removed from the illustration for demonstrative reasons. By comparing figures 8.31b and 8.32b the effect of the stiffener can be seen, because there no longer is any warping of the cross section at the point of the load's application.

For the simulation of the box beam in figure 8.33, a different version of the arc-length method implemented in FEAP is used, which is load controlled and based on a normal plane, full Newton solution. The material parameters and dimensions of the box beam are the same as in the previous examples, while the stacking sequences for the flange and web correspond to alternative 2a in table 8.8. When comparing the load deflection curves in figure 8.32a and figure 8.33a, it becomes obvious that a different path is taken with this solution technique. The load deflection curve of the latter example takes a rather complicated path when the ultimate load is reached, in that it snaps back, leading to smaller deflections in direction of the applied load, before they increase again. In this part of the simulation, extremely small load steps have to be taken in order to reach a solution of the system of equations. The phenomenon of many solution paths in close proximity often appears in stability analysis such as this one.

Analogous to the preceding example, the deformation figure shown in figure 8.33b shows half of the box beam at the point of highest load, with the support being in the back and the point of application of the load being in the front. The black edges without contour show the original position of the box beam. The stiffener at the point of load application is again removed from the illustration for demonstrative reasons. The different paths of the load deflection curves are reflected in the different deformation figures in figures 8.32b and 8.33b. While in the former at the point of application of the load in the middle of the box beam the structure moves to the side leading to drop-off in stiffness of the system, there is no significant buckling noticeable. On the other hand, in the latter case the structure moves to the side and there is also buckling to be seen in the flange of the box beam, which contributes to a further loss in stiffness of the system and thereby also to a lower ultimate load.

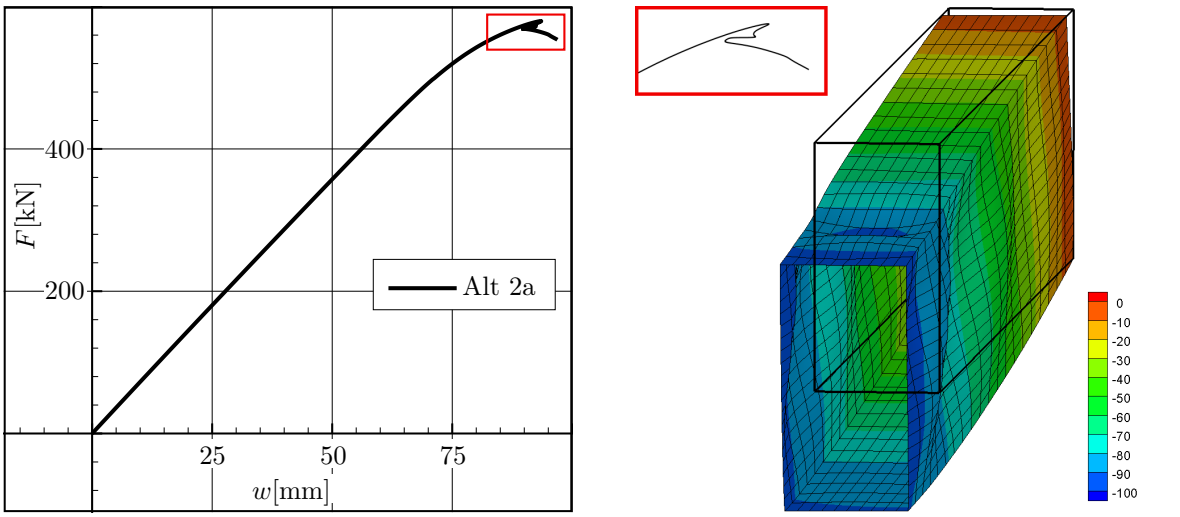

(a) Load deflection curve

(b) Contour plot of w[mm] for alternative 2a

Figure 8.33: Load deflection curve and deformation figure

A 3-point bending test was also carried out for a double T-girder. The length of the beam in this case is $l = 800\,\text{mm}$, and a force acts perpendicular to the beam at the middle of the beam. The cross section is $b = 44\,\text{mm}$ wide and $h = 88\,\text{mm}$ high. The intersections between flange and web are not designed as straight edges, but round components with a radius of 4 mm are placed there. The thicknesses and stacking sequences of the different components of the double T-girder are specified in table 8.9. The subscript number in the stacking sequence of the flange denotes the number of repetitions of layers with this fiber orientation.

Component	Stacking sequence [°]	t[mm]
Web	$[45/-45/45/-45/0]_s$	2.1
Flange	$[0_{17}]$	4.3
Curve	$[45/-45/45/-45]$	1.0

Table 8.9: Thicknesses and stacking sequences of the components of the double T-girder

In the simulation, the symmetry of the system is again taken advantage of. The discretization can be gleaned from the illustration of the deformation figure. Similar to the simulation of the box beam, the support is located at the bottom of the double T-girder at the short edge of the bottom flange, while the load is applied at the top of the double T-girder at the opposite short edge of the top flange. At the supports and at the point of application of the load a stiffener is integrated. In this example, the load controlled version of the arc-length method is used.

The results of the simulation are shown in figure 8.34. The load deflection curve shown in figure 8.34a follows a linear path at the beginning of the simulation, but when the ultimate load is reached it becomes strongly nonlinear. Smaller load steps are required in this part

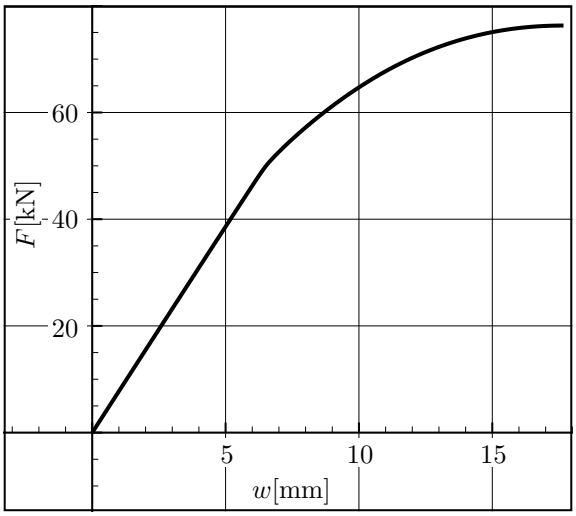

(a) Load deflection curve

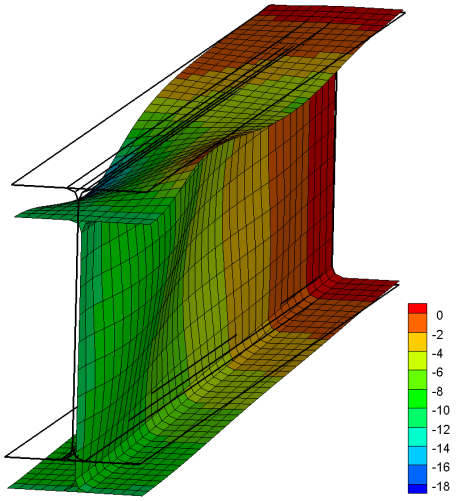

(b) Contour plot of w[mm] for alternative 2a

Figure 8.34: Load deflection curve and deformation figure

of the simulation. The deformation figure with a contour plot of the displacements w in the direction of the applied load shown in figure 8.34b shows half of the double T-girder at the point of highest load, with the support being in the back and the point of application of the load being in the front. The black edges without contour show the original position of the double T-girder. The double T-girder exhibits a large deformation of the top flange and a large buckle in the web. Because of the integrated stiffeners there is no warping of the cross section at the support and at the point load application.

A further example investigates buckling in the web of the box beam. The test setup corresponds to the test setup for the previous examples of the box beam in this section with a stacking sequence corresponding to alternative 1a in table 8.8 with one exception. The thickness of the web is reduced from $t = 5\,\text{mm}$ to $t = 2\,\text{mm}$, which has the effect that the web is more prone to show a buckling behavior.

In figure 8.35, the load deflection curve of the conducted simulation and the deformation figures at five different points are shown. The load steps applied become obvious from the load deflection curve in figure 8.35a, where the round symbol denotes a point where a solution was found. Near point B lies the so-called bifurcation point, where the curve branches into two separate paths. The linear path is called the primary path. The nonlinear path is called the secondary path. Points on the linear path can easily be reached with large load steps, while points on the nonlinear path can only be reached with the help of a disturbance force and small load steps starting from close to the bifurcation point.

Figures 8.35b to 8.35f show contour plots of the displacements perpendicular to the length of the beam denoted by v, in order to make buckling more visible. The original position of the box beam is displayed by the black edges. The figures show half of the box beam. The support is in the back and the point of application of the load is in the front. Point A is reached before the bifurcation point is reached, so that a displacement in the direction of load application in the middle of the box beam can be observed in figure 8.35b, but no significant buckling is apparent.

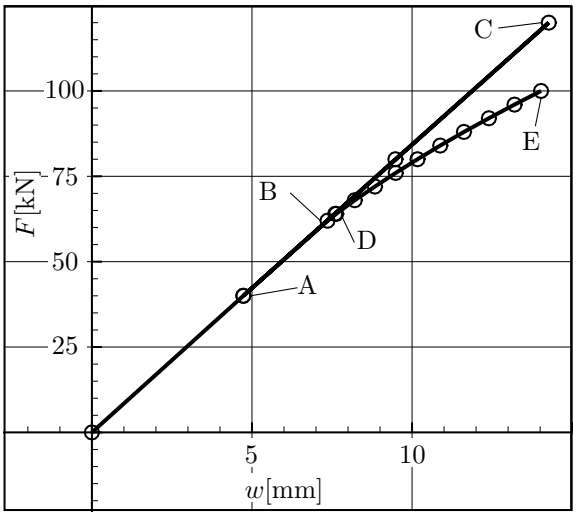

(a) Load deflection curve

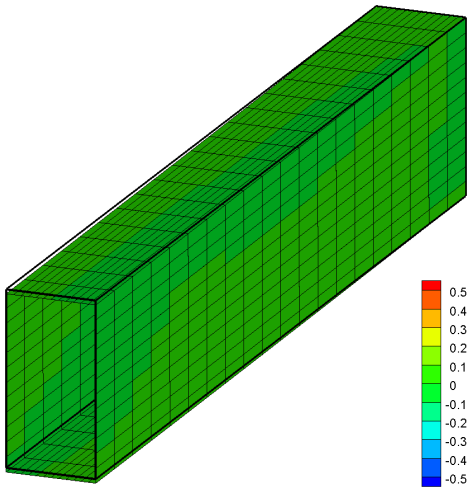

(b) Contour plot of v[mm] at point A

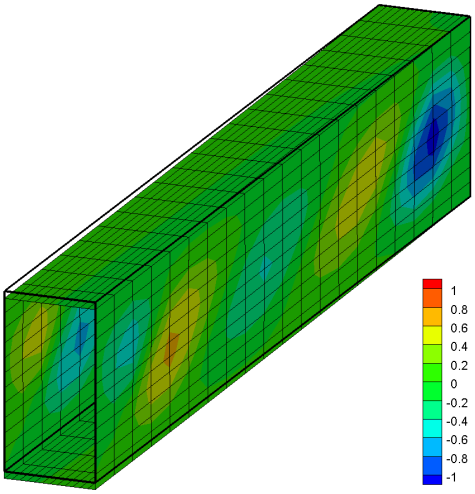

(c) Contour plot of v[mm] at point B

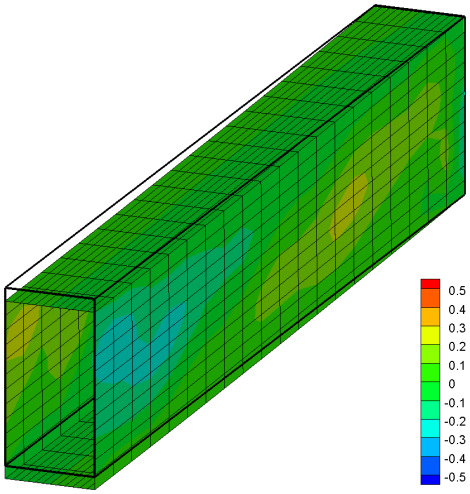

(d) Contour plot of v[mm] at point C

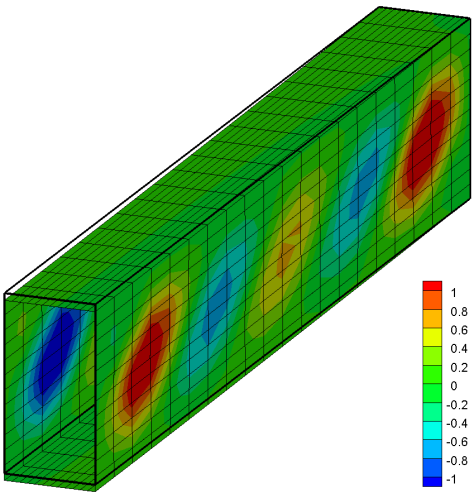

(e) Contour plot of v[mm] at point D

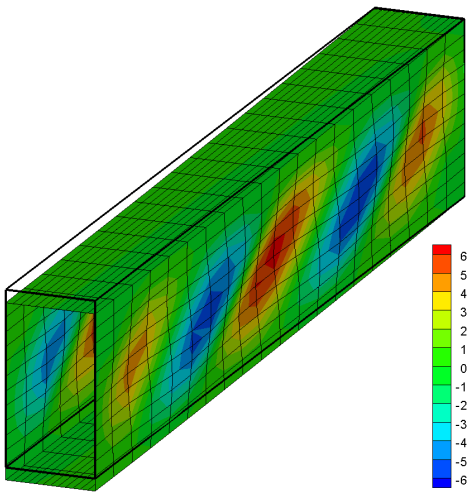

(f) Contour plot of v[mm] at point E

Figure 8.35: Buckling of the box beam

Points B and D lie in close proximity, with point B being on the primary path and point C being on the secondary path. At point B (figure 8.35c), the displacement in the direction of load application has become larger and negative eigenvalues are observed. When passing the bifurcation point the equilibrium is unstable. Continuing the linear computation, at point C (figure 8.35d) the displacement in the direction of load application has become even larger but no significant buckling can be observed. On the secondary path, at point D, where the displacement in the direction of load application has a similar value as at point B, already significant buckling can be observed (figure 8.35e). The buckling becomes more pronounced as the nonlinear simulation continues and the displacement in the direction of load application grows until point E is reached (figure 8.35f).

By means of the presented examples, the performance of the shell element is shown in the geometrically nonlinear framework.

8.2 Parallel programming examples

In chapter 7, it was shown how the process of assembling of the tangential stiffness matrix and the load vector in the finite element software FEAP was parallelized for shared memory processing systems by means of the OpenMP API. This is especially beneficial when performing nonlinear simulations with the global-local finite shell element, where a large number of unknowns is introduced on the element level, leading to a significant increase in computation time. In this section, the performance of the parallel implementation is evaluated by means of the performance characteristics defined in chapter 7.1.3. It is shown how much time is saved in the computation in one iteration. It is noted that a large number of iterations may be carried out in geometrically nonlinear simulations.

As was mentioned in chapter 7.2, for the implementation Microsoft Visual Studio with Intel Fortran Compiler as part of Intel Fortran Composer XE is used. Part of the Intel Fortran Compiler is a parallel optimizing feature called High Performance Parallel Optimizer (HPO), whose function is to analyze, optimize and parallelize loop nests [59]. A number of compiler options can be used to parallelize the software on a multi-processor system. It is shown in the examples, however, that these compiler options do not necessarily lead to faster computation times. Much more effective in this case is the parallelization of the code with the help of the OpenMP API.

The compiler option `\Qparallel` causes the HPO to generate multithreaded code for loops that can be safely executed in parallel [60]. This option works together with the options `\O2` or `\O3`. The goal of the options `\O1`, `\O2` and `\O3` is to optimize for code speed, while `\O3` is the most aggressive option and recommended for applications that have loops that heavily use floating-point calculations and process large data sets. This option usually leads to higher compilation times. A more extensive description is given in [60]. As was also mentioned in chapter 7.2, the Math Kernel Library (MKL) is used for some math operations, particularly those involving multiplications of large matrices and vectors or the solution of large systems of equations. The Intel Math Kernel Library can be used sequentially or in parallel, which needs to be considered when evaluating the parallel performance.

Simulation Number	Optimize for code speed	Use Compiler option to parallelize	Use MKL in parallel	Use OpenMP to parallelize	Time to set up stiffness matrix	Time for solution
1					306.8 s	0.3 s
2	✓				131.2 s	0.3 s
3	✓	✓			181.7 s	0.3 s
4	✓		✓		130.3 s	0.3 s
5				✓	76.6 s	0.3 s
6	✓			✓	53.7 s	0.3 s
7	✓	✓		✓	54.0 s	0.3 s
8	✓		✓	✓	54.6 s	0.3 s

Table 8.10: Computation time for different compiler options and eight virtual cores

As an example, a simulation is carried out of the simply supported square plate subjected to an area load as illustrated in figure 8.1, using the global-local finite shell element with the full interpolation in the domain (GL2). This model leads to a large amount of computation time being spent on the element level, where the additional unknowns are removed from the global computation by means of numerical procedures, as discussed in chapter 5.2. The laminated plate is chosen to be made up of 15 layers, with the fiber angles of the layers being arbitrary, since this does not significantly influence computation time. In a conventional displacement-based finite element, solving the system of equations usually takes much longer than setting up the global stiffness matrix and load vector. For the developed finite shell element it is the other way around, since the large number of unknowns on the element level lead to high computation times spent on the element level, while the global system of equations is solved by a highly efficient parallel solver.

The simulation is carried out on a high-end performance desktop computer manufactured by Intel with a Quad-core processor that is classified by the codename Lynnfield and based on the so-called Nehalem architecture, which in turn is the codename for an Intel processor microarchitecture. The exact model number is Core i7-870. The processor possesses four physical processors, but because of the feature of Hyper-Threading technology (HTT), which is Intel's term for its simultaneous multithreading implementation, the operating system is able to address two virtual cores for every physical core, so that in this case, eight virtual cores can be present. The feature can be turned on and off in the BIOS, and the simulation is carried out for both cases.

The simulations carried out with HTT turned on are illustrated first, so that in this case, the processor possesses eight virtual cores. In table 8.10 the computation times of different

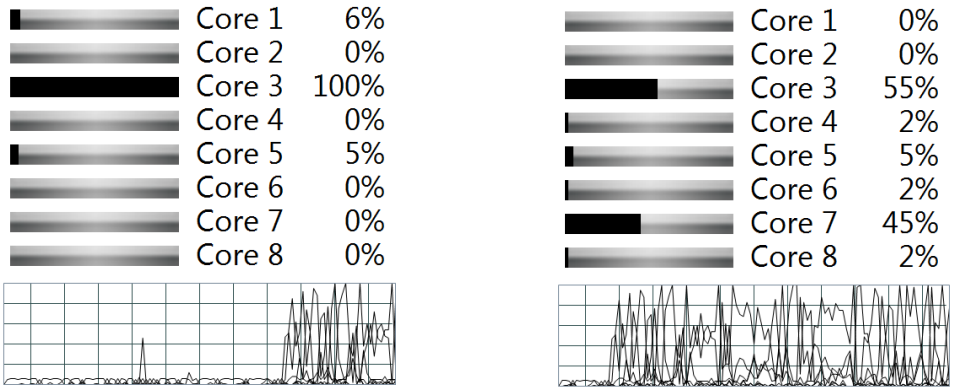

(a) Point in time 1 (b) Point in time 2

Figure 8.36: Degree of capacity utilization at two different points in time for simulation 1

simulations using various compiler directives are specified. Whether the respective compiler option is chosen or not is indicated with a checkmark. Each simulation is carried out a total of five times and the average duration is specified in table 8.10. Since the compiler directives do not influence the process of solving the system of equations on a global level by means of an external solver, the total computation time for this part of the simulation always stays the same. In simulations 1 to 4 the parallelization by means of the OpenMP API is not used. The compiler option to optimize for code speed (simulation 2) strongly decreases the computation time needed to assemble the global stiffness matrix, compared to the case when none of the aforementioned compiler options are chosen (simulation 1). However, additionally using the compiler option to use the parallel optimizing feature (simulation 3) has a detrimental effect, increasing the computation time by almost 40%. Using the parallelized MKL for the math operations (simulation 4) on the element level in addition to the option to optimize for code speed does not significantly decrease computation time compared to simulation 2. Since a large number of operations are performed in quick succession, any gain in computation time is outweighed by overhead.

In figure 8.36, the current degrees of capacity utilization at two different points in time during simulation 1 are shown in the top part of the diagrams. In the lower part the course of the degree of capacity utilization of the different cores is shown, where each different line signifies the degree of capacity utilization of a different core. Since no parallelization is carried out, only a fraction of the available computational power is used. The instruction stream is executed sequentially, and which core of the processor is used is decided by the operating system. This could lead to only one virtual processor executing, while the other seven are idle, or a number of different cores executing at the same time, but only using a part of their capacity. At the first point in time illustrated in figure 8.36a, only Core 3 is running at full capacity while the others are idle, while at the second point in time illustrated in figure 8.36b, two cores, Core 3 and Core 7, are sharing the main workload, while the others are idle. All in all, roughly only one-eighth of the processor's capacity is used.

The OpenMP API is employed in simulations 5 to 8 specified in table 8.10. Using it leads to a significant decrease in computation time (simulation 5), which is further reduced by the compiler option to optimize for code speed (simulation 6). On the other hand,

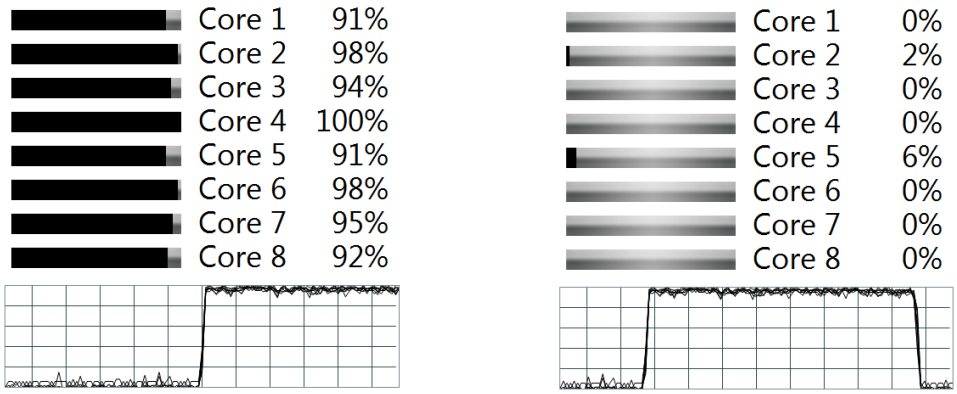

(a) During the simulation (b) After the simulation

Figure 8.37: Degree of capacity utilization during and after simulation 5

choosing the additional options does not have a positive effect (simulations 7 and 8). The current degrees of capacity utilization are shown during simulation 5 in figure 8.37a and after simulation 5 in figure 8.37b in the top part of the diagrams, while the courses of the degree of capacity utilization of the different cores are shown in the lower part of the diagrams. When comparing figures 8.36 and 8.37, it is obvious that using the OpenMP API leads to a much more equally distributed workload for all eight virtual cores.

Comparing simulations one and five by means of table 8.10, it is obvious that, when no other compiler options are specified, using OpenMP leads to a considerably lower computation time. More precisely, the speedup defined as a performance characteristic in chapter 7.1.3 can be derived to be

$$S = \frac{T_s}{T_p} = \frac{306.8\,\mathrm{s}}{76.6\,\mathrm{s}} = 4.0 \quad . \tag{8.2}$$

Since the runtime of the fastest sequential algorithm is not known, the runtime with one processor is used for T_s. The second performance characteristic, the efficiency, is

$$E = \frac{S}{p} = \frac{4.0}{8} = 0.50 \quad . \tag{8.3}$$

Even though the workload of all the cores is high, the capacity of the processor cannot be fully utilized. When evaluating the system's efficiency by means of these two performance characteristics, it must be considered that in this case, there are eight virtual cores, but only four physical cores.

Comparing simulations two and six manifests that, when the compiler option to optimize for code speed is used, additionally using OpenMP decreases computation time. The speedup in this case is

$$S = \frac{T_s}{T_p} = \frac{131.2\,\mathrm{s}}{53.7\,\mathrm{s}} = 2.4 \quad , \tag{8.4}$$

Simulation Number	Optimize for code speed	Use Compiler option to parallelize	Use MKL in parallel	Use OpenMP to parallelize	Time to set up stiffness matrix	Time for solution
1					307.2 s	0.3 s
2	✓				130.7 s	0.3 s
3	✓	✓			143.2 s	0.3 s
4	✓		✓		129.9 s	0.3 s
5				✓	91.0 s	0.3 s
6	✓			✓	53.5 s	0.3 s
7	✓	✓		✓	53.9 s	0.3 s
8	✓		✓	✓	53.5 s	0.3 s

Table 8.11: Computation time for different compiler options and four physical cores

so that the speedup is lower than when not using the compiler option to optimize for code speed. The efficiency can be specified by

$$E = \frac{S}{p} = \frac{2.4}{8} = 0.30 \quad . \tag{8.5}$$

When considering these performance characteristics, it must be accounted for that the parallel system possesses eight virtual cores, but only four physical cores are present.

In summary, it can be determined that the parallelization procedure with OpenMP leads to considerably lower computation times. This is especially the case for geometrically nonlinear simulations, where the stiffness matrix needs to be set up a large number of times. As compiler options with a bearing on the efficiency of the implementation a combination of optimizing for code speed and evaluating OpenMP directives can be recommended, while using the parallel optimizing feature or the parallel version of the MKL does not lead to the desired results in this case.

Next, the simulations are carried out with HTT turned off. In table 8.11, the computation times of different simulations are specified. Analogous to the simulations carried out with Hyper-Threading turned on, when parallelization by means of the OpenMP API is not used (simulations 1 to 4), the compiler option to optimize for code speed (simulation 2) strongly decreases the computation time needed to assemble the global stiffness matrix compared to the case when no compiler options are chosen (simulation 1). In fact, the computation times for simulations 1 and 2 in both cases are roughly the same, so that turning Hyper-Threading on or off obviously does not significantly influence the performance of the sequentially executed code. On the other hand, even though using the compiler option

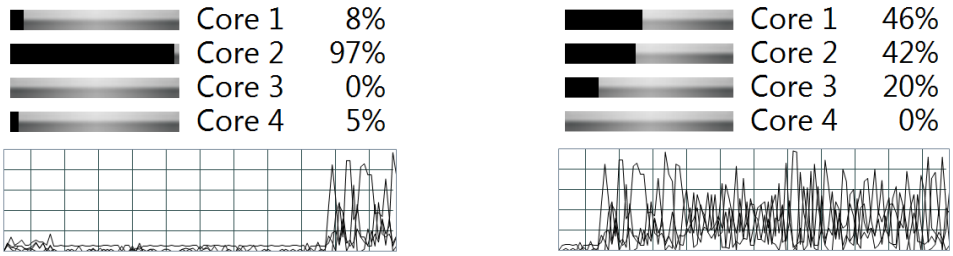

(a) Point in time 1 (b) Point in time 2

Figure 8.38: Degree of capacity utilization at two different points in time during the simulation

instructing the compiler to use the parallel optimizing feature (simulation 3) increases computation time by almost 10%, this is significantly smaller than the increase of 40% with Hyper-Threading turned on. In this case, the HTT feature thus has a negative effect. Using the parallel MKL (simulation 4) with the HTT feature turned off does not lead to a significant decrease of computation time compared with using the sequential MKL, thus yielding a similar result as carrying out the simulations with HTT turned on.

Similar to figure 8.36 for eight virtual cores, figure 8.38 shows the current degree of capacity utilization at two different points in time during simulation 1 in the top part of the diagrams. In the lower part the course of the degree of capacity utilization of the different cores is shown, where each different line signifies the degree of capacity utilization of a different core. Since the instruction stream is carried out sequentially, a large portion of the computational capacity of the processor is left unused. The instruction stream is executed either by one physical processor (Core 2 in figure 8.38a) or is shared by two or more physical cores (Cores 1, 2 and 3 in figure 8.38b), but only roughly one-fourth of the total capacity of the processors is really used.

In simulations 5 to 8 specified in table 8.11 the OpenMP API is used. This leads to a significant decrease in computation time (simulation 5), which is further reduced by the compiler option to optimize for code speed (simulation 6). On the other hand, choosing the additional options does not have a positive effect (simulations 7 and 8). In figure 8.39, the current degrees of capacity utilization are shown during (figure 8.39a) and after (figure 8.39b) simulation 5 in the top part of the diagrams, while the courses of the degree of capacity utilization of the different cores are shown in the lower part of the diagrams. Similar to the conclusion drawn for eight virtual cores, comparing simulation 1 by means of figure 8.38 and simulation 5 by means of figure 8.39 makes it obvious that using the OpenMP API leads to a much more equally distributed workload for all four physical cores.

Comparing the computation times of simulations 1 and 5 by means of table 8.11, the positive effect of using the OpenMP API is manifested, when no other compiler options are chosen. In this case, though, using the Hyper-Threading feature has a more positive effect on processor performance, since the computation time of simulation 5 in table 8.11 is higher than the computation time of simulation 5 in table 8.10. The speedup in this case is

$$S = \frac{T_s}{T_p} = \frac{307.2\,\mathrm{s}}{91.0\,\mathrm{s}} = 3.4 \quad . \tag{8.6}$$

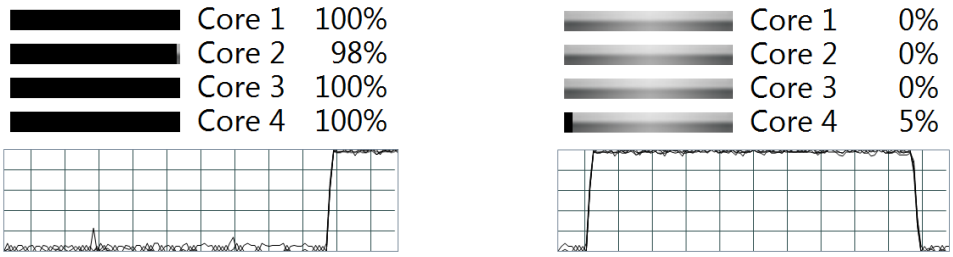

(a) During the simulation (b) After the simulation

Figure 8.39: Degree of capacity utilization during and after simulation 5

Similar to the preceding case, since the runtime of the fastest sequential algorithm is not known, the runtime with one processor is used for T_s. The second performance characteristic, the efficiency, is

$$E = \frac{S}{p} = \frac{3.4}{4} = 0.85 \quad . \tag{8.7}$$

Even though the speedup is lower when Hyper-Threading is turned off (8.6) than when it is turned on (8.2), the efficiency in (8.7) is higher than in (8.3), because it is related to the four physical cores that are actually present, rather than the eight virtual cores.

Comparing simulations 2 and 6 manifests that, when the compiler option to optimize for code speed is used, additionally using OpenMP decreases computation time. The speedup in this case is

$$S = \frac{T_s}{T_p} = \frac{130.7\,\mathrm{s}}{53.5\,\mathrm{s}} = 2.4, \tag{8.8}$$

which is the same speedup that is achieved with the same compiler options and Hyper-Threading turned on (8.4). The efficiency is

$$E = \frac{S}{p} = \frac{2.4}{4} = 0.60, \tag{8.9}$$

which is double the efficiency achieved with Hyper-Threading turned on, because it is related to the four physical cores actually present.

Summarizing, it can thus be stated that the implemented parallelization of the finite element software has a significantly positive effect on the performance of shared memory processing systems. For the described simulations and under the described conditions, the fastest solution is to use the compiler option to optimize for code speed and to use the OpenMP API. Using these options leads to a significant gain in time, which is especially helpful in time-consuming geometrically nonlinear simulations, when the global stiffness matrix needs to be set up a large number of times.

Chapter 9

Conclusion and outlook

This thesis contributes to the theoretical and numerical modeling of fiber-reinforced composites. It further develops a nonlinear composite finite shell element emanating from a variational principle. The underlying shell model is called the global model in this thesis, since the associated field equations have to be fulfilled for the structure as a whole. The variational principle is extended with a local field equation, to be fulfilled at a specific point in the structure. The local field equation is the local equilibrium equation, by which the interlaminar stresses are derived. This part of the model is called the local part. In this global-local variational principle, the higher-order stress resultants are set to zero and the local model enters into the variational principle via the strain-energy function.

A multiplicative decomposition of the displacement field is an essential part of the global-local composite shell model. In the multiplicative decomposition, an ansatz is made for the path of the displacements in the direction of the coordinate perpendicular to the plane of the shell. The ansatz functions chosen are linear shape functions as well as hierarchic and cubic shape functions. The appendant quantities are the displacements at virtual nodes through the thickness of the shell. It is shown that by linearly combining the shape functions, a clearly defined interface can be derived between the global and the local part of the model. Through the local model, the assumptions that cross sections remain straight and are inextensible in thickness direction are given up. Thus, the goal of the local model is to compute warping and thickness changes of the cross sections, and from these results to derive the interlaminar stresses. The local model is introduced based on a geometrically linear theory, since this is admissible for the examples investigated, but it would also be possible to base the local model on a geometrically nonlinear theory, which could be the subject of future research.

The global and local parts of the model are not independent of each other. Rather, coupling terms are introduced into the strain-energy function. Thus, through the addition of the local model, the results of the effective stress resultants are manipulated. In order to circumvent this, an orthogonality condition is introduced, which requires that the addition of the local model to the effective membrane stress resultants and the effective stress couples vanishes. Small changes to the effective shear stress resultants are permitted. For homogeneous materials, the orthogonality conditions can be met by introducing two parameters for every shape function associated with the in-plane displacements. A system of

equations can be set up and solved once for a particular geometry to fulfill the orthogonality condition, thus yielding good results for the in-plane stresses and the interlaminar shear stresses. For inhomogeneous materials, such as fiber-reinforced composites with multiple layers and varying fiber angles, the orthogonality condition cannot be met with two parameters. A number of different orthogonalization procedures were proposed to derive a good approximate solution. However, none of the orthogonalization procedures are able to exactly fulfill the orthogonality condition, thus leading to results for the in-plane displacements and interlaminar shear stresses that are correct on an average. They do lead to an improvement compared to the results of the global shell model alone. An additional orthogonalization procedure introducing four parameters is proposed for laminates with some specific stacking sequences. However, for this procedure to work, the global model has to be manipulated, which cannot be deduced from the theory. Therefore further research in establishing a suitable orthogonalization procedure is needed. It is noted that the higher the number of layers in the composite shell is, the better the results can be approximated by a quadratic parable. Thus, in this case, the orthogonalization procedure for a homogeneous composite with two parameters is capable of yielding satisfactory predictions of peaks in the interlaminar shear stresses. The coupled global-local model leads to vanishing interlaminar normal stresses in the plate example given, whereas in the global model alone, they are approximately zero in inhomogeneous examples for numerical reasons. Further research needs to be carried out to evaluate the performance of the global-local finite shell element for the interlaminar normal stresses and to develop a suitable orthogonalization procedure, if applicable.

As a basis for a nonlinear simulation with the finite element method, the linearization of the three-field global-local variational principle is specified. Suitable interpolation functions of the independent fields, namely the field of global displacements and rotational parameters, the stress resultant field and the field of global shell strains and local quantities are introduced. The interpolation functions are chosen in a way, so as to avoid locking phenomena that frequently occur in shell elements. Two different procedures are proposed for the interpolation of the local field of displacements and their derivatives. In the first procedure, bilinear shape functions are used. In the second procedure, it is considered that the derivatives to the two coordinates in the plane are zero, so that only the local displacements remain. In this procedure, the number of unknowns introduced by the local model is thus significantly reduced. The global-local finite shell element has five or six global degrees of freedom. The local field is eliminated on the element level by means of static condensation. Additionally, the stress resultant field and the strain field are eliminated on the element level by mathematical relations. Standard assembly procedures can be employed to derive the global stiffness matrix and load vector.

An alternative procedure to derive the interlaminar shear stresses based on an FSDT model is proposed, which can be applied in shell and plate elements. In this post-processing procedure, two warping functions are introduced and the equilibrium equations are exploited to set up a system of ordinary differential equations. The method is implemented in a four-node shell element, where the needed derivatives of the membrane strains and the curvatures can be determined by means of a regularized minimum problem, and in a nine-node shell element, where they can be computed from the displacement field.

The performance of the global-local composite finite shell element is illustrated with the

example of a simply supported plate with multiple stacking sequences subjected to a uniform area load. The results are specified with contour plots of the displacements in the direction of the load, and the effective stress resultants. The results for the stresses through the thickness of the plate are presented for a number of evaluation points. As a reference solution, a simulation with quadratic brick elements is used. The results for the stresses of the global-local finite shell element and the results for the interlaminar shear stresses with the post-processing technique are compared with the results of the reference solution and the global finite shell element. Additionally, the warping of the cross section computed with the global-local model is shown at the evaluation points. The improvement due to the addition of the local model is shown. Additionally, the performance of the shell element is demonstrated by some geometrically nonlinear examples, which were conducted in research work dealing with load-bearing analysis of highly-loaded, fiber-reinforced composite box beams and double-T girders.

The addition of the local model leads to a large number of unknowns on the element level and therefore to a significant increase in computation time. In order to decrease the computation time, a parallelization of the finite element software used is undertaken. For this purpose, the sequence of a nonlinear computation with the finite element method is analyzed and tasks are identified that take up a lot of computation time and can be carried out in parallel. Using the OpenMP API, which is suitable for shared memory processing systems, the parallelization is realized for modern computer architectures with multiple cores. A number of examples carried out on a modern desktop computer to illustrate the effectiveness of the implemented parallelization are evaluated by means of the performance characteristics speedup and efficiency. Additional available compiler options for automatic parallelization are included in the analysis.

Some open points regarding the global-local finite shell element presented in this work that require further research were already identified in this chapter. When these issues are resolved the global-local finite shell element can be used in the investigation of interlaminar failure modes such as delamination, because it provides an interface to three-dimensional constitutive laws and is able to provide the peaks of interlaminar stresses. The local part of the model is added by inserting the local equilibrium equation into the variational principle. A similar path can be taken by determining the local stress state as the solution of a boundary value problem in a RVE.

Bibliography

[1] Ahmad, S., Irons, B. M. and Zienkiewicz, O. C. Analysis of thick and thin shell structures by curved finite elements. *International Journal for Numerical Methods in Engineering*, 2(3):419–451, 1970.

[2] Altenbach, H., Altenbach, J. and Kissing, W. *Mechanics of composite structural elements*. Foundations of engineering mechanics. Springer-Verlag, 2004.

[3] Altenbach, J. and Altenbach, H. *Einführung in die Kontinuumsmechanik*. Teubner-Studienbücher. Teubner, 1994.

[4] Amdahl, G. M. Validity of the single processor approach to achieving large scale computing capabilities. In *Proceedings of the April 18-20, 1967, spring joint computer conference*, AFIPS '67 (Spring), pages 483–485. ACM, New York, NY, USA, 1967.

[5] Argyris, J. An excursion into large rotations. *Computer Methods in Applied Mechanics and Engineering*, 32(1-3):85 – 155, 1982.

[6] Asanovic, K., Bodik, R., Catanzaro, B. C., Gebis, J. J., Husbands, P., Keutzer, K., Patterson, D. A., Plishker, W. L., Shalf, J., Williams, S. W. and Yelick, K. A. The landscape of parallel computing research: a view from Berkeley. Technical Report UCB/EECS-2006-183, Electrical Engineering and Computer Sciences, University of California at Berkeley, 2006.

[7] Auricchio, F. and Sacco, E. A mixed-enhanced finite-element for the analysis of laminated composite plates. *International Journal for Numerical Methods in Engineering*, 44(21-22):1481–1504, 1999.

[8] Ball, J. M. Convexity conditions and existence theorems in nonlinear elasticity. *Archive for Rational Mechanics and Analysis*, 63:337–403, 1976.

[9] Ball, J. M. Constitutive inequalities and existence theorems in nonlinear elastostatics. In *Nonlinear analysis and mechanics: Heriot-Watt Symposium (Edinburgh, 1976), Vol. I*. Pitman, London, 1977.

[10] Balzani, C. *Finite Element Modeling of Intra- and Interlaminar Damage Growth in Composite Laminates*. Dissertation, Institut für Baustatik, Universität Karlsruhe, 2009.

[11] Balzani, D., Gruttmann, F. and Schröder, J. Analysis of thin shells using anisotropic polyconvex energy densities. *Computer Methods in Applied Mechanics and Engineering*, 197(9-12):1015 – 1032, 2008.

[12] Bathe, K. *Finite Element Procedures in Engineering Analysis*. Prentice-Hall Civil Engineering and Engineering Mechanics Series. Prentice-Hall, 1982.

[13] Bathe, K.-J., Brezzi, F. and Cho, S. W. The MITC7 and MITC9 plate bending elements. *Computers & Structures*, 32(3-4):797 – 814, 1989.

[14] Bathe, K.-J. and Dvorkin, E. N. A four-node plate bending element based on Mindlin/Reissner plate theory and a mixed interpolation. *International Journal for Numerical Methods in Engineering*, 21(2):367–383, 1985.

[15] Büchter, N., Ramm, E. and Roehl, D. Three-dimensional extension of non-linear shell formulation based on the enhanced assumed strain concept. *International Journal for Numerical Methods in Engineering*, 37(15):2551–2568, 1994.

[16] Belytschko, T. and Leviathan, I. Physical stabilization of the 4-node shell element with one point quadrature. *Computer Methods in Applied Mechanics and Engineering*, 113(3-4):321 – 350, 1994.

[17] Belytschko, T. and Tsay, C.-S. A stabilization procedure for the quadrilateral plate element with one-point quadrature. *International Journal for Numerical Methods in Engineering*, 19(3):405–419, 1983.

[18] Betsch, P., Gruttmann, F. and Stein, E. A 4-node finite shell element for the implementation of general hyperelastic 3d-elasticity at finite strains. *Computer Methods in Applied Mechanics and Engineering*, 130(1-2):57 – 79, 1996.

[19] Bischoff, M. and Ramm, E. On the physical significance of higher order kinematic and static variables in a three-dimensional shell formulation. *International Journal of Solids and Structures*, 37(46-47):6933 – 6960, 2000.

[20] Bletzinger, K.-U., Bischoff, M. and Ramm, E. A unified approach for shear-locking-free triangular and rectangular shell finite elements. *Computers & Structures*, 75(3):321 – 334, 2000.

[21] Brank, B. Nonlinear shell models with seven kinematic parameters. *Computer Methods in Applied Mechanics and Engineering*, 194(21-24):2336 – 2362, 2005.

[22] Brank, B. and Carrera, E. Multilayered shell finite element with interlaminar continuous shear stresses: a refinement of the Reissner-Rindlin formulation. *International Journal for Numerical Methods in Engineering*, 48(6):843–874, 2000.

[23] Buechter, N. and Ramm, E. Shell theory versus degeneration - a comparison in large rotation finite element analysis. *International Journal for Numerical Methods in Engineering*, 34(1):39–59, 1992.

[24] CARRERA, E. C^0 Reissner-Mindlin multilayered plate elements including zig-zag and interlaminar stress continuity. *International Journal for Numerical Methods in Engineering*, 39(11):1797–1820, 1996.

[25] Carrera, E. On the use of the Murakami's zig-zag function in the modeling of layered plates and shells. *Computers & Structures*, 82(7-8):541 – 554, 2004.

[26] Carzaniga, A., Picco, G. and Vigna, G. Is code still moving around? Looking back at a decade of code mobility. In *Software Engineering - Companion, 2007. ICSE 2007 Companion. 29th International Conference on*, pages 9 –20. 2007.

[27] Chandra, R. *Parallel programming in OpenMP*. High performance computing. Morgan Kaufmann Publishers, 2001.

[28] Ciarlet, P. *Mathematical Elasticity. Volume I: Three-Dimensional Elasticity*. Studies in Mathematics and its Applications. North-Hollan, Amsterdam, 1988.

[29] Cook, R. *Concepts and applications of finite element analysis, 4th ed.* Wiley India Pvt. Limited, 2007.

[30] Cosserat, E. and Cosserat, F. *Theorie des Corps Deformables*. Herman et fils, Paris, 1909.

[31] Daniel, I. and Ishai, O. *Engineering mechanics of composite materials*. Oxford University Press, 2005.

[32] De Borst, R. The zero-normal-stress condition in plane-stress and shell elastoplasticity. *Communications in Applied Numerical Methods*, 7(1):29–33, 1991.

[33] Dvorkin, E. N. and Bathe, K.-J. A continuum mechanics based four-node shell element for general non-linear analysis. *Engineering Computations*, 1(1):77–88, 1984.

[34] Dvorkin, E. N., Pantuso, D. and Repetto, E. A. A formulation of the MITC4 shell element for finite strain elasto-plastic analysis. *Computer Methods in Applied Mechanics and Engineering*, 125(1-4):17 – 40, 1995.

[35] Engblom, J. J. and Ochoa, O. O. Through-the-thickness stress distribution for laminated plates of advanced composite materials. *International Journal for Numerical Methods in Engineering*, 21:1759–1776, 1985.

[36] Ericksen, J. L. and Truesdell, C. Exact theory of stress and strain in rods and shells. *Archive for Rational Mechanics and Analysis*, 1:295–323, 1957.

[37] Flynn, M. Very high-speed computing systems. *Proceedings of the IEEE*, 54(12):1901 – 1909, 1966.

[38] Gropp, W., Lusk, E. and Skjellum, A. *Using MPI: portable parallel programming with the message-passing interface*. Scientific and engineering computation. MIT Press, 1999.

[39] Gruttmann, F. *Theorie und Numerik dünnwandiger Faserverbundstrukturen*. Habilitationsschrift, Institut für Baumechank und Numerische Mechanik, Universität Hannover, 1996.

[40] Gruttmann, F., Sauer, R. and Wagner, W. Theory and numerics of three-dimensional beams with elastoplastic material behaviour. *International Journal for Numerical Methods in Engineering*, 48(12):1675–1702, 2000.

[41] Gruttmann, F. and Taylor, R. L. Theory and finite element formulation of rubberlike membrane shells using principal stretches. *International Journal for Numerical Methods in Engineering*, 35(5):1111–1126, 1992.

[42] Gruttmann, F. and Wagner, W. On the numerical analysis of local effects in composite structures. *Composite Structures*, 29(1):1–12, 1994.

[43] Gruttmann, F. and Wagner, W. Coupling of 2d- and 3d-composite shell elements in linear and nonlinear applications. *Computer Methods in Applied Mechanics and Engineering*, 129(1):271–287, 1996.

[44] Gruttmann, F. and Wagner, W. Delamination analysis of thin composite structures using a multi-director formulation. In Topping, B., editor, *Advances in Analysis and Design of Composites*. Civil-Comp Press, Edinburgh, 1996.

[45] Gruttmann, F. and Wagner, W. A stabilized one-point integrated quadrilateral Reissner-Mindlin plate element. *International Journal for Numerical Methods in Engineering*, 61(13):2273–2295, 2004.

[46] Gruttmann, F. and Wagner, W. A linear quadrilateral shell element with fast stiffness computation. *Computer Methods in Applied Mechanics and Engineering*, 194(39-41):4279 – 4300, 2005.

[47] Gruttmann, F. and Wagner, W. Structural analysis of composite laminates using a mixed hybrid shell element. *Computational Mechanics*, 37:479–497, 2006.

[48] Gruttmann, F., Wagner, W., Meyer, L. and Wriggers, P. A nonlinear composite shell element with continuous interlaminar shear stresses. *Computational Mechanics*, 13:175–188, 1993.

[49] Gurtin, M. *An introduction to continuum mechanics*. Mathematics in science and engineering. Academic Press, 1981.

[50] Gustafson, J. L. Reevaluating Amdahl's law. *Communications of the ACM*, 31:532–533, 1988.

[51] Hellinger, E. Die allgemeinen Ansätze der Mechanik der Kontinua. In Klein, F. and Müller, C., editors, *Enzyklopädie der mathematischen Wissenschaften*, volume IV, pages 601–694. Teubner Verlag, Leipzig, 1914.

[52] Herakovich, C. *Mechanics of fibrous composites*. Wiley, 1998.

[53] Holzapfel, G. *Nonlinear solid mechanics: a continuum approach for engineering*. Wiley, 2000.

[54] Hughes, T. *The finite element method: linear static and dynamic finite element analysis*. Dover Civil and Mechanical Engineering Series. Dover Publications, 2000.

[55] Hughes, T. J. and Carnoy, E. Nonlinear finite element shell formulation accounting for large membrane strains. *Computer Methods in Applied Mechanics and Engineering*, 39(1):69 – 82, 1983.

[56] Hughes, T. J. and Pister, K. S. Consistent linearization in mechanics of solids and structures. *Computers & Structures*, 8(3-4):391 – 397, 1978.

[57] Hughes, T. J. R., Taylor, R. L. and Kanoknukulchai, W. A simple and efficient finite element for plate bending. *International Journal for Numerical Methods in Engineering*, 11(10):1529–1543, 1977.

[58] Hughes, T. J. R. and Tezduyar, T. E. Finite elements based upon Mindlin plate theory with particular reference to the four-node bilinear isoparametric element. *Journal of Applied Mechanics*, 48(3):587–596, 1981.

[59] Intel Corporation. Intel Visual Fortran Composer XE 2011 - product brief. 2010.

[60] Intel Corporation. Intel Visual Fortran Compiler XE 12.0 user and reference guides. 2011.

[61] Jones, R. *Mechanics of composite materials*. Materials Science and Engineering Series. Taylor & Francis, 1999.

[62] Kacsuk, P. and Vajda, F. Network-based distributed computing (metacomputing). 1999.

[63] Kasper, E. P. and Taylor, R. L. A mixed-enhanced strain method: Part I: Geometrically linear problems. *Computers & Structures*, 75(3):237 – 250, 2000.

[64] Kasper, E. P. and Taylor, R. L. A mixed-enhanced strain method: Part II: Geometrically nonlinear problems. *Computers & Structures*, 75(3):251 – 260, 2000.

[65] Kienzler, R., Altenbach, H. and Ott, I. *Theories of Plates and Shells: Critical Review and New Applications*. Lecture Notes in Applied and Computational Mechanics. Springer, 2004.

[66] Kim, D.-N. and Bathe, K.-J. A 4-node 3D-shell element to model shell surface tractions and incompressible behavior. *Computers & Structures*, 86(21-22):2027–2041, 2008.

[67] Klinkel, S. *Theorie und Numerik eines Volumen-Schalen-Elementes bei finiten elastischen und plastischen Verzerrungen*. Dissertation, Inst. für Baustatik, Universität Karlsruhe, 2000.

[68] Klinkel, S. and Govindjee, S. Using finite strain 3D-material models in beam and shell elements. *Engineering Computations*, 19(3):254 – 271, 2002.

[69] Klinkel, S., Gruttmann, F. and Wagner, W. A continuum based three-dimensional shell element for laminated structures. *Computers & Structures*, 71(1):43–62, 1999.

[70] Klinkel, S., Gruttmann, F. and Wagner, W. A robust non-linear solid shell element based on a mixed variational formulation. *Computer Methods in Applied Mechanics and Engineering*, 195(1-3):179 – 201, 2006.

[71] Klinkel, S., Gruttmann, F. and Wagner, W. A mixed shell formulation accounting for thickness strains and finite strain 3d material models. *International Journal for Numerical Methods in Engineering*, 74(6):945–970, 2008.

[72] Koelbel, C. *The High Performance Fortran Handbook*. Scientific and Engineering Computation. MIT Press, 1994.

[73] Koiter, W. T. On the nonlinear theory of thin elastic shells. *Proceedings of the Koninklijke Nederlandse Akademie van Wetenschappen Royal Dutch Academy of Sciences Ser B*, 69:1–54, 1966.

[74] Kollár, L. and Springer, G. *Mechanics of composite structures*. Cambridge University Press, 2003.

[75] Krätzig, W. 'Best' transverse shearing and stretching shell theory for nonlinear finite element simulations. *Computer Methods in Applied Mechanics and Engineering*, 103(1-2):135 – 160, 1993.

[76] Lee, E. A. The problem with threads. 2006.

[77] Liu, W. K., Law, E., Lam, D. and Belytschko, T. Resultant-stress degenerated-shell element. *Computer Methods in Applied Mechanics and Engineering*, 55(3):259 – 300, 1986.

[78] Macneal, R. H. A simple quadrilateral shell element. *Computers & Structures*, 8(2):175 – 183, 1978.

[79] Macneal, R. H. Derivation of element stiffness matrices by assumed strain distributions. *Nuclear Engineering and Design*, 70(1):3 – 12, 1982.

[80] Macneal, R. H. and Harder, R. L. A proposed standard set of problems to test finite element accuracy. *Finite Elements in Analysis and Design*, 1(1):3 – 20, 1985.

[81] Manjunatha, B. S. and Kant, T. On evaluation of transverse stresses in layered symmetric composite and sandwich laminates under flexure. *Engineering Computations*, 10(6):499 – 518, 1993.

[82] Marimuthu, R., Sundaresan, M. K. and Rao, G. V. Estimation of interlaminar stresses in laminated plates subjected to transverse loading using three-dimensional mixed finite element formulation. *Technical Journal Aerospace Engineering*, 84:1–8, 2003.

[83] Marsden, J. and Hughes, T. *Mathematical foundations of elasticity*. Dover Books on Advanced Mathematics. Dover, 1994.

[84] Mittelstedt, C. and Becker, W. Interlaminar stress concentrations in layered structures, part I: A selective literature survey on the free-edge effect since 1967. *Journal of Composite Materials*, 38:1037–1062, 2004.

[85] Müller, M. *Ein Intra-Grid-System für die p-adaptive Finite-Elemente-Simulation auf Arbeitsplatzrechnern am Beispiel der Geotechnik*. Forschungsbericht, Institut für numerische Methoden und Informatik im Bauwesen, TU Darmstadt, 2006.

[86] Naghdi, P. *The theory of shells.* C. Truesdell (Ed.), Handbuch Der Physik, Mechanics of Solids II, vol VIa/2. Springer-Verlag, Berlin, 1972.

[87] Noor, A. K., Burton, W. and Peters, J. M. Predictor-corrector procedures for stress and free vibration analyses of multilayered composite plates and shells. *Computer Methods in Applied Mechanics and Engineering*, 82(1-3):341 – 363, 1990.

[88] Noor, A. K., Kim, Y. H. and Peters, J. M. Transverse shear stresses and their sensitivity coefficients in multilayered composite panels. *AIAA Journal*, 32(6):1259–1269, 1994.

[89] Patterson, D. and Hennessy, J. *Computer Organization and Design, Revised Fourth Edition: The Hardware/Software Interface.* Morgan Kaufmann Series in Computer Graphics. Elsevier Science, 2011.

[90] Pian, T. H. H. and Sumihara, K. Rational approach for assumed stress finite elements. *International Journal for Numerical Methods in Engineering*, 20(9):1685–1695, 1984.

[91] Piltner, R. and Taylor, R. L. A systematic construction of b-bar functions for linear and non-linear mixed-enhanced finite elements for plane elasticity problems. *International Journal for Numerical Methods in Engineering*, 44(5):615–639, 1999.

[92] Reddy, J. N. A simple high-order theory for laminated composite plates. *Journal of Applied Mechanics*, 51:745–752, 1984.

[93] Reddy, J. N. A generalization of two-dimensional theories of laminated composite plates. *Communications in Applied Numerical Methods*, 3(3):173–180, 1987.

[94] Reissner, E. On a variational theorem in elasticity. *Journal of Mathematics ans Physics*, 29(8):90 – 95, 1950.

[95] Rivlin, R. Large elastic deformations of isotropic materials. IV. Further developments of the general theory. *Philosophical Transactions of the Royal Society A Mathematical Physical and Engineering Sciences*, 241:379–397, 1948.

[96] Rolfes, R. and Rohwer, K. Improved transverse shear stresses in composite finite elements based on first order shear deformation theory. *International Journal for Numerical Methods in Engineering*, 40:51–60, 1997.

[97] Ruben, J. *Ein Multi-Agenten-System zur verteilten p-adaptiven Finite-Elemente-Simulation am Beispiel der Baugrund-Tragwerk-Interaktion.* Forschungsbericht, Institut für numerische Methoden und Informatik im Bauwesen, TU Darmstadt, 2005.

[98] Sansour, C. A theory and finite element formulation of shells at finite deformations involving thickness change: Circumventing the use of a rotation tensor. *Archive of Applied Mechanics*, 65:194–216, 1995.

[99] Schenk, O. PARDISO solver project. http://www.pardiso-project.org, 2012.

[100] Schenk, O. and Gärtner, K. Solving unsymmetric sparse systems of linear equations with PARDISO. *Future Generation Computer Systems*, 20(3):475 – 487, 2004.

[101] Schröder, J. and Neff, P. On the construction of polyconvex anisotropic free energy functions. In Miehe, C., editor, *Proceedings of the IUTAM Symposium on Computational Mechanics of Solid Materials at Large Strains*, pages 171–180. Kluwer Academic Publishers, Dordrecht, 2001.

[102] Schröder, J. and Neff, P. Invariant formulation of hyperelastic transverse isotropy based on polyconvex free energy functions. *International Journal of Solids and Structures*, 40(2):401–445, 2003.

[103] Schürg, M. *Agentengerechte Partitionierung von dreidimensionalen Netzen für eine p-adaptive FE-Simulation.* Vertieferarbeit, Institut für numerische Methoden und Informatik im Bauwesen, TU Darmstadt, 2005.

[104] Schürg, M. *Dynamischer Lastausgleich für die p-adaptive FE-Analyse in einem Grid-Computing System auf Basis mobiler Software-Agenten.* Diplomarbeit, Institut für numerische Methoden und Informatik im Bauwesen, TU Darmstadt, 2006.

[105] Schürg, M., Wackerfuss, J. and Gruttmann, F. Using a mixed shell formulation to compute interlaminar stresses in layered composite shell structures. In *3rd Thematic Conference on the Mechanical Response of Composites, 21st - 23rd September 2011, Hannover, Germany.* 2011.

[106] Schürg, M., Wagner, W. and Gruttmann, F. An enhanced FSDT model for the calculation of interlaminar shear stresses in composite plate structures. *Computational Mechanics*, 44(6):765–776, 2009.

[107] Schürmann, H. *Konstruieren Mit Faser-Kunststoff-Verbunden:.* VDI-Buch. Springer, 2007.

[108] Schüle, J. *Paralleles Rechnen: Performancebetrachtungen zu Gleichungslösern.* Oldenbourg Wissensch.Vlg, 2010.

[109] Simo, J. On a stress resultant geometrically exact shell model. part VII: Shell intersections with 56-dof finite element formulations. *Computer Methods in Applied Mechanics and Engineering*, 108(3-4):319 – 339, 1993.

[110] Simo, J. and Fox, D. On a stress resultant geometrically exact shell model. part I: Formulation and optimal parametrization. *Computer Methods in Applied Mechanics and Engineering*, 72(3):267 – 304, 1989.

[111] Simo, J., Fox, D. and Rifai, M. On a stress resultant geometrically exact shell model. part II: The linear theory; computational aspects. *Computer Methods in Applied Mechanics and Engineering*, 73(1):53 – 92, 1989.

[112] Simo, J., Fox, D. and Rifai, M. On a stress resultant geometrically exact shell model. part III: Computational aspects of the nonlinear theory. *Computer Methods in Applied Mechanics and Engineering*, 79(1):21 – 70, 1990.

[113] Simo, J. and Kennedy, J. On a stress resultant geometrically exact shell model. part V. Nonlinear plasticity: formulation and integration algorithms. *Computer Methods in Applied Mechanics and Engineering*, 96(2):133 – 171, 1992.

[114] Simo, J., Rifai, M. and Fox, D. On a stress resultant geometrically exact shell model. part IV: Variable thickness shells with through-the-thickness stretching. *Computer Methods in Applied Mechanics and Engineering*, 81(1):91 – 126, 1990.

[115] Simo, J. C. and Hughes, T. J. R. On the variational foundations of assumed strain methods. *Journal of Applied Mechanics*, 53(1):51–54, 1986.

[116] Simo, J. C. and Rifai, M. S. A class of mixed assumed strain methods and the method of incompatible modes. *International Journal for Numerical Methods in Engineering*, 29(8):1595–1638, 1990.

[117] Simo, J. C., Rifai, M. S. and Fox, D. D. On a stress resultant geometrically exact shell model. part VI: Conserving algorithms for non-linear dynamics. *International Journal for Numerical Methods in Engineering*, 34(1):117–164, 1992.

[118] Simo, J. C., Wriggers, P., Schweizerhof, K. H. and Taylor, R. L. Finite deformation post-buckling analysis involving inelasticity and contact constraints. *International Journal for Numerical Methods in Engineering*, 23(5):779–800, 1986.

[119] Spencer, A. *Continuum theory of the mechanics of fibre-reinforced composites*. Courses and lectures - International Centre for Mechanical Sciences. Springer-Verlag, 1984.

[120] Stein, E. and Barthold, F. J. Elastizitätstheorie. In Mehlhorn, G., editor, *Der Ingenieurbau: Grundwissen*, pages 165–428. Ernst & Sohn, 1996.

[121] Taylor, R. L., Simo, J. C., Zienkiewicz, O. C. and Chan, A. C. H. The patch test - a condition for assessing fem convergence. *International Journal for Numerical Methods in Engineering*, 22(1):39–62, 1986.

[122] Taylor, R.L. Feap - a finite element analysis program - user manual. 2011.

[123] Timoshenko, S. and Woinowsky-Krieger, S. *Theory of plates and shells*. Mcgraw-Hill College; 2 edition, 1959.

[124] Truesdell, C., Noll, W. and Antman, S. *The non-linear field theories of mechanics*. Springer, 2004.

[125] Tsai, S. and Hahn, H. *Introduction to composite materials*. Technomic Pub., 1980.

[126] von Neumann, J. First draft of a report on the EDVAC. *IEEE Annals of the History of Computing*, 15:27–75, 1993.

[127] Vu-Quoc, L. and Mora, J. A. A class of simple and efficient degenerated shell elements-analysis of global spurious-mode filtering. *Comput. Methods Appl. Mech. Eng.*, 74:117–175, 1989.

[128] Wackerfuss, J. and Gruttmann, F. A mixed hybrid finite beam element with an interface to arbitrary three-dimensional material models. *Computer Methods in Applied Mechanics and Engineering*, 198(27-29):2053 – 2066, 2009.

[129] Wackerfuss, J. and Gruttmann, F. A nonlinear Hu-Washizu variational formulation and related finite-element implementation for spatial beams with arbitrary moderate thick cross-sections. *Computer Methods in Applied Mechanics and Engineering*, 200(17-20):1671 – 1690, 2011.

[130] Wagner, W. *Zur Behandlung von Stabilitätsproblemen der Elastostatik mit der Methode der finiten Elemente*. Habilitationsschrift, Institut für Baumechank und Numerische Mechanik, Universität Hannover, 1991.

[131] Wagner, W. and Gruttmann, F. A robust non-linear mixed hybrid quadrilateral shell element. *International Journal for Numerical Methods in Engineering*, 64(5):635–666, 2005.

[132] Wagner, W. and Wriggers, P. A simple method for the calculation of postcritical branches. *Engineering Computations*, 5(2):103 – 109, 1988.

[133] Wriggers, P. *Nonlinear Finite Element Methods*. Springer, 2008.

[134] Yang, H., Saigal, S. and Liaw, D. Advances of thin shell finite elements and some applications - version I. *Computers & Structures*, 35(4):481 – 504, 1990. Special Issue: Frontiers in Computational Mechanics.

[135] Yang, H. T. Y., Saigal, S., Masud, A. and Kapania, R. K. A survey of recent shell finite elements. *International Journal for Numerical Methods in Engineering*, 47(1-3):101–127, 2000.

[136] Zienkiewicz, O. C. and Taylor, R. L. *The Finite Element Method (6th edn)*. Butterworth-Heinemann, 2005.

[137] Zienkiewicz, O. C., Taylor, R. L. and Too, J. M. Reduced integration technique in general analysis of plates and shells. *International Journal for Numerical Methods in Engineering*, 3(2):275–290, 1971.

Bisher sind in dieser Reihe erschienen

Band 1
Zur mikrorissinduzierten Schädigung spröder Materialien
B. Lauterbach, Dissertation 2001, ISBN 3-935868-01-4

Band 2
3D-Simulation der Mikrostrukturentwicklung in Zwei-Phasen-Materialien
R. Müller, Dissertation 2001, ISBN 3-935868-02-2

Band 3
Zur numerischen Simulation von Morphologieänderungen in mikroheterogenen Materialien
S. Kolling, Dissertation 2001, ISBN 3-935868-03-0

Band 4
Theoretische und numerische Untersuchung von Versagensmechanismen in Metall-Keramik-Verbundwerkstoffen
T. Emmel, Dissertation 2002, ISBN 3-935868-04-9

Band 5
On microcrack dominated problems in dynamics and statics of brittle fracture: a numerical study by boundary element techniques
S. Rafiee, Dissertation 2002, ISBN 3-935868-05-7

Band 6
Kontinuumsmechanik anisotroper Festkörper und Fluide
H. Ehrentraut, Habilitationsschrift 2002, ISBN 3-935868-06-5

Band 7
Plane unsteady inviscid incompressible hydrodynamics of a thin elastic profile
N. Blinkova, Dissertation 2002, ISBN 3-935868-07-3

Band 8
Anmerkungen zur Simulation von entfestigendem Materialverhalten
H. Baaser, Habilitationsschrift 2004, ISBN 3-935868-08-1

Band 9
Orts- und zeitadaptive DAE-Methoden zur Beschreibung elastisch-plastischen Materialverhaltens innerhalb der FEM
S. Eckert, Dissertation 2005, ISBN 3-935868-09-X

Band 10
Simulations of the Flow of the Ross Ice Shelf, Antarctica: Parameter Sensitivity Tests and Temperature-Dependent Rate Factor
A. Humbert, Dissertation 2005, ISBN 3-935868-10-3

Band 11
A Thermo-mechanical Continuum Theory with Internal Length of Cohesionless Granular Materials
Chung Fang, Dissertation 2006, ISBN 3-935868-11-1

Band 12
Modeling Dry Granular Avalanches past Different Obstructions: Numerical Simulation and Laboratory Analyses
Chiou Min-Ching, Dissertation 2006, ISBN 3-935868-12-X

Band 13
Configurational forces in defect mechanics and in computational methods
R. Müller, Habilitationsschrift 2005, ISBN 3-935868-13-8

Band 14
Hyperelastic dynamics in physical and material space
S. Kolling, Habilitationsschrift 2007, ISBN 978-3-935868-14-3

Band 15
Phenomenological modeling of ferroelectric material behavior
V. Mehling, Dissertation 2007, ISBN 978-3-935868-15-0

Band 16
Ein mischungsbasiertes Materialmodell zum Knochenumbau
R.-R. Kühn, Dissertation 2006, ISBN 978-3-935868-16-7

Band 17
Einige Erweiterungen der Rand-Finite-Elemente-Methode und deren Anwendung auf Randeffekte in ebenen Laminaten
J. Artel, Dissertation 2007, ISBN 978-3-935868-17-4

Band 18
Spannungskonzentrations-Effekte an Verstärkungspflaster-Ecken
H. Wigger, Dissertation 2008, ISBN 978-3-935868-18-1

Band 19
Rotationseffekte in der Kristallplastizität
C. Bröse, Dissertation 2007, ISBN 978-3-935868-19-8

Band 20
Finite-Element-Modelle zur Simulation von Delaminationen dünner Filme auf Substraten
V. D. Pham, Dissertation 2010, ISBN 978-3-935868-20-4

Band 21
Asymptotische Nahfeldanalysen ebener Multi-Materialverbindungsstellen mit der Methode komplexer Potentiale
C. Sator, Dissertation 2010, ISBN 978-3-935868-21-1

Band 22
Modellierung spröder Rissbildung an Spannungskonzentrationen mit der Bruchmechanik finiter Risse
J. Hebel, Dissertation 2010, ISBN 978-3-935868-22-8

Band 23
Some Contributions to the Homogenization of Macroscopically Isotropic Composites
V. Salit, Dissertation 2011, ISBN 978-3-935868-23-5

Band 24
Asymptotic Analysis of the Load Transfer on Double-Lap Bolted Joints
J. Kratochvíl, Dissertation 2012, ISBN 978-3-935868-24-2

Band 25
Spannungssingularitätsordnungen in linear-elastischen und piezoelektrischen Multimaterialkonfigurationen mit der Rand-Finite-Elemente-Methode
W. Mayland, Dissertation 2012, ISBN 978-3-935868-25-9

Band 26
Plastizität und Skaleneffekte sowie Deformations- und Versagensmodellierung dünner metallischer Schichten bei Nanoindentation
A. Trondl, Dissertation 2012, ISBN 978-3-935868-26-6

In this thesis, a contribution is made to the theoretical and numerical modeling of thin-walled structures made of fiber-reinforced composites. The global-local finite shell element presented further develops a nonlinear finite shell element emanating from a mixed variational principle. A local field equation is introduced, by which the local displacements and the interlaminar stresses are derived. The global-local finite shell element has five or six global degrees of freedom, three displacements and two or three rotational parameters, since all other fields are eliminated by numeric procedures on an element level. Additionally, an alternative possibility to derive the interlaminar shear stresses is proposed, which can be applied in shell and plate elements.
The addition of the local part of the model leads to a significant increase in computation time, due to the unknowns introduced on an element level. For this reason, the finite element software used in the implementation of the finite shell element is adapted to modern computer architectures with multiple cores and shared memory by parallelizing the implemented code.

ISBN 978-3-935868-27-3